IEKP-KA/2016-06

Karlsruhe Institute of Technology

Optical Properties and Calibration of the Pierre Auger Fluorescence Detector

Zur Erlangung des akademischen Grades eines

DOKTORS DER NATURWISSENSCHAFTEN

von der Fakultät für Physik des
Karlsruher Institut für Technologie (KIT)

genehmigte

DISSERTATION

von

Ing. Lenka Tománková
aus Prag, Tschechische Republik

Tag der mündlichen Prüfung:	3. Juni, 2016
Referent:	Prof. Dr. Dr. h.c. J. Blümer
Korreferent:	Prof. Dr. U. Husemann
Betreuer:	Dr. R. Engel

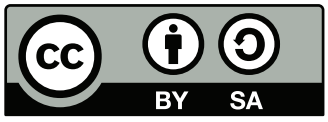

To my parents

Contents

Acronyms

AC	analog current
ADC	analog-to-digital converter
ADST	Advanced Data Structure Tree
AERA	Auger Engineering Radio Array
AGL	altitude above ground level
AGN	active galactic nucleus
AMBER	Air-shower Microwave Bremsstrahlung Experimental Radiometer
AMIGA	Auger Muons and Infill for the Ground Array
ART	Argentina Time
BG loop	BackGround loop
BLF	Balloon Launching Facility
BRM	Black Rock Mesa
CC	center of curvature
CCD	charged-coupled device
CDF	cumulative distribution function
CG	center of gravity
CLF	Central Laser Facility
CMB	cosmic microwave background
CO	Coihueco
CORSIKA	Cosmic-Ray Simulations for KASCADE
CROME	Cosmic-Ray Observation via Microwave Emission
DAC	digital-to-analog converter
DAQ	data acquisition
DC	direct current
DOP	dilution of precision
EAS	extensive air shower
EASIER	Extensive Air Shower Identification using Electron Radiometer
FD	fluorescence detector
FE	front-end electronics
FLT	First-Level Trigger
FOV	field of view
FRAM	ph(F)otometric Robotic Atmospheric Monitor
GDAS	Global Data Assimilation System
GNSS	Global Navigation Satellite System
GPS	Global Positioning System
GRB	gamma ray burst
GZK	Greisen-Zatsepin-Kuz'min
HEAT	High-Elevation Auger Telescopes

HV	high voltage
IR	infra-red
KIT	Karlsruhe Institute of Technology
LA	Loma Amarilla
LCU	LED Control Unit
LED	light-emitting diode
LHC	Large Hadron Collider
LL	Los Leones
LM	Los Morados
LR	Long Ridge
LWC	lateral width correction
MC	Monte Carlo
MD	Middle Drum
MIDAS	Microwave Detection of Air Showers
NCEP	National Centers for Environmental Prediction
NIST	National Institute of Standards and Technology
NSB	night-sky background
PMT	photomultiplier tube
PPS	pulse-per-second
PSF	point spread function
RC	radius of curvature
RMS	root mean square
SD	surface detector
SDP	shower-detector plane
SLT	Second-Level Trigger
SNR	signal-to-noise ratio
TA	Telescope Array
TIFF	Tagged Image File Format
TLT	Third-Level Trigger
UHECR	ultra-high energy cosmic ray
UT	Utah
UV	ultra-violet
VAOD	vertical aerosol optical depth
VEM	vertical-equivalent muon
VGA	Video Graphics Array
WLAN	Wireless Local Area Network
XLF	Extreme Laser Facility

1 Introduction

Ultra-high energy cosmic rays (UHECRs) are messengers from the most powerful and violent processes in the Universe. On one hand, reaching enormous energies of 10^{20} eV – many orders of magnitude higher than what is accessible to terrestrial accelerators – is by itself a major unresolved astrophysical problem. On the other hand, these particles carry information about astrophysical objects and environments that they come from, and provide an unparalleled opportunity to test the fundamental laws of physics and spacetime under extreme conditions. Research into UHECRs is one of the frontiers of astroparticle physics and aims to answer essential questions pertaining to the sources of UHECRs, of which there are no generally accepted models as of today, as well as their acceleration and propagation mechanisms.

The Pierre Auger Observatory, located in the Argentine Province of Mendoza, extends over 3000 km^2 of the vast Pampa Amarilla and is the largest UHECR observatory ever constructed. The detection mechanism utilizes the Earth's atmosphere as a gigantic calorimeter, in which an extensive air shower – a cascade of billions of particles initiated by the primary cosmic ray – deposits its energy. An array of particle detectors then samples the footprint of the air shower at ground level, while telescopes follow its longitudinal evolution by measuring the fluorescence light induced by the shower particles as they traverse the atmosphere.

Due to its calorimetric nature, the measurement of the energy with the fluorescence telescopes is essentially independent of the details of the particle interactions in the cascade and is used to set the energy scale of the entire Observatory. The energy calibration of the fluorescence detector is thus of critical importance, as it impacts all results of the Observatory and is of direct relevance to the physical interpretation of the measurements.

The absolute calibration of the fluorescence detector of the Pierre Auger Observatory is at the forefront of this thesis. The aim was to develop an improved and fully independent procedure, both in methodology and technology, to absolutely calibrate the fluorescence detector with systematic uncertainties lower than those of the currently used standard procedure and in a truly shower-like manner.

The standard absolute calibration procedure uses a large-diameter light source to illuminate the entire telescope camera simultaneously. Since this is very different from the detection of an air shower, which illuminates only a small section of the camera, great care must be taken in interpreting and applying the derived calibration constants. Moreover, because the process is very time- and manpower-consuming, it is performed rather infrequently. The calibration constants are then propagated through time by a relative calibration system, which monitors the sensitivity of the individual photomultiplier tubes (PMTs) of the camera on a

nightly basis.

As a first step, the current calibration procedures were reviewed. Aspects found to deserve increased attention include the temporal variability of the sensitivity of the PMTs on short time scales and the changing conditions of the optical components of the telescopes, neither of which are monitored by the standard calibration procedures. Also of vital importance is the understanding of the point spread function of the telescopes, and the way in which it affects the telescope response in calibration and during an actual air shower measurement. All of these topics are crucial for an accurate measurement of the energy of UHECRs and are addressed within this work.

The first point – the temporal variability in the sensitivity of PMTs over the course of one measurement night – was studied in detail and significant drifts have been found. An extended relative calibration scheme was developed, tested and implemented (Chap. 3) to compensate for those drifts and is being integrated into regular data taking.

The effect of the condition of the optical components of the telescopes, such as the aperture filters and the focusing mirrors, on image formation and air shower detection was examined in dedicated in situ measurements (Chap. 4). In particular, dust layers on the optical surfaces were found to significantly attenuate and scatter light. The understanding of those effects is of particular importance, because the current calibration procedures are sensitive to them only partially, moreover, the temporal changes are not tracked, thus affecting the energy calibration of the telescopes.

Eventually, an independent absolute calibration of the fluorescence telescopes was carried out (Chap. 5 to 6). The method, referred to as the “Octocopter method” throughout this work, is based on a remotely controlled flying platform that lifts a suitable light source into the field of view of a telescope. In this way, the telescopes can be studied and calibrated in a very natural way that resembles the measurement of an actual cosmic-ray induced air shower. The easy portability of the flying platform and the light source allows measurements to be done at different observatories, such as the Pierre Auger Observatory in the Southern and the Telescope Array in the Northern hemisphere, comparing their energy scales directly. Moreover, the generic setup of this method makes applications to a multitude of other experiments, e.g. with optical or radio-wave detectors, straightforward.

2 Ultra-High Energy Cosmic Rays at the Pierre Auger Observatory

Contents

2.1 Cosmic Rays

In the years 1911–1913, the man generally credited with the discovery of cosmic rays and winner of the 1936 Nobel Prize in Physics, Austrian Victor Hess undertook a series of high-altitude balloon flights, systematically measuring the vertical radiation profile in different conditions: during daytime, nighttime and even during a partial solar eclipse. Hess' data were in good agreement with his contemporaries [1–4], but venturing to a mighty altitude of 5300 m, he not only observed a slower-than-expected decrease in radiation flux with altitude, but even an increase above 1500 m [5,6]. Given that he found the position of the Sun to have no effect on the data, Hess ascribed the additional source of radiation to outer space, coining the phenomenon "Höhenstrahlung", which loosely translates to "radiation from above".

The term "cosmic rays" was coined around 1925 by Robert Millikan, who initially believed Hess' Höhenstrahlung to be gamma rays. Despite the evolution of the field of cosmic-ray research and the current understanding that cosmic rays are mostly protons or light nuclei, the term has held for over 90 years.

Primary cosmic rays are charged nuclei of high energy arriving at the top of the Earth's atmosphere from outer space. An extraordinary natural phenomenon, they

span twelve decades in energy and over 32 decades in flux. Those of extremely high energies in excess of 10^{18} eV are incredibly scarce and are referred to as UHECRs. They are a testament to the most powerful and violent processes in the Universe and many questions pertaining to their origin, nature, acceleration and propagation mechanisms remain unanswered even today. The energies carried by ultra-high energy cosmic rays exceed the frontiers of terrestrial particle accelerators by up to six orders of magnitude. In fact, using current technologies, an accelerator the size of Mercury's orbit would be required to accelerate protons to typical UHECR energies. As such, UHECRs can be used as probes of fundamental physical processes, such as violation of Lorentz invariance [7–9].

2.1.1 Energy spectrum

The energy spectrum of primary cosmic rays (further on also simply referred to as "primaries") bears answers to many theoretical challenges pertaining to their sources, mass, acceleration and propagation. Fig. 2.1 depicts the differential spectrum of the all-particle flux as measured by a variety of experiments covering the energy range 10^{12}–10^{20} eV. It is best approximated by a power law

$$\frac{dN}{dE} \propto E^{-\gamma}, \tag{2.1}$$

where the spectral index γ takes on different values depending on the energy range. There are three distinct features in the power law, which become more apparent when the flux is scaled by a power of the energy: The first, known as *the knee* for its resemblance to the anatomical structure of the human leg, occurs at $\sim 3 \times 10^{15}$ eV to 5×10^{15} eV, where γ changes from about 2.7 to 3.1. The spectrum hardens again at $\sim 5 \times 10^{18}$ eV – *the ankle* – and the flux is significantly suppressed beyond $\sim 4 \times 10^{19}$ eV.

To get a feeling for how quickly the flux drops with energy, consider the following approximate numbers: In the knee region, particles arrive on average once per m^2 and year. In the ankle region, this becomes one particle per km^2 and year, and at the highest energies of the order of 10^{20} eV, the average expected flux is less than one particle per km^2 per century. Clearly, direct balloon- or satellite-borne detectors with sensitive areas of $\sim 1\,\mathrm{m}^2$ no longer suffice and indirect detection methods such as air shower arrays come into play. Those experimental techniques will be discussed in more detail in Subsec. 2.2.2.

The interpretation of the spectral features is not unique. Particles in and below the knee region are believed to be of galactic origin, the prime candidates for acceleration being the shock fronts of supernova remnants (see [15] and references therein). The softening of the spectrum beyond the knee may be interpreted as the sources having reached their maximum acceleration limits, or insufficient containment of the particles by galactic magnetic fields and subsequent leakage from the Milky Way [16]. Both processes are rigidity-dependent ($\propto E/Z$, where E is the energy and Z the charge of the particle in units of elementary charge e) and consistent with the observation of light primaries in the knee-region and a gradual transition towards heavier elements up to 10^{17} eV [17].

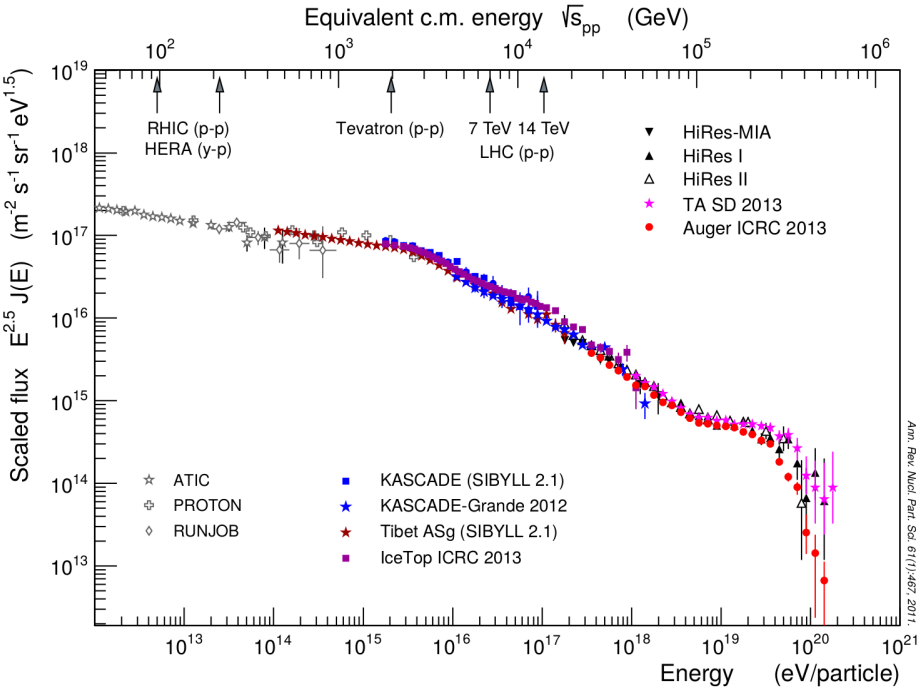

FIG. 2.1 The differential spectrum of the all-particle flux of cosmic rays above 1 TeV as measured by past and concurrent experiments. To visually enhance the breaks in the power-law behavior, the flux has been scaled by $E^{2.5}$. The equivalent center-of-mass energy (assuming proton collisions) of man-made accelerators is indicated on the top axis. Originally from [10], with updated data from [11–14].

The ankle is mostly interpreted as the onset of an extra-galactic component with a lower flux yet a harder spectrum. However, other mechanism could form an ankle-like feature. For example, protons of energies $\gtrsim 10^{18}$ eV would interact with the cosmic microwave background (CMB) to produce e^+-e^- pairs (also called the Bethe–Heitler process), naturally causing a dip in the spectrum [18, 19]. Particles beyond the ankle are generally understood to be of extra-galactic origin [15], with potential sources briefly discussed in Subsec. 2.1.3.

Similarly to the case of galactic cosmic rays in the knee region, the suppression at the highest energies could result from cosmic accelerators reaching their maximum injection energy, likely in a rigidity-dependent manner (see [20] and references therein). Furthermore, a flux suppression is expected at the highest energies for both, protons and heavier nuclei, due to propagation effects collectively termed the Greisen-Zatsepin-Kuz'min (GZK) effect. Despite the unequivocal observation of the flux suppression beyond 4×10^{19} eV by the Pierre Auger Observatory [21], the Telescope Array [22] and HiRes [23], interpretation is hindered by limited statistics and lack of composition information at the highest energies, and is ambiguous.

2.1.2 GZK effect and arrival direction anisotropy

In 1966, Greisen, and independently Zatsepin and Kuz'min, derived a theoretical upper limit on the energy of cosmic rays arriving from distant sources [24, 25]. The limit is predicated on the interactions of particles with energies exceeding $\sim 5 \times 10^{19}$ eV with photons of the CMB, which had been discovered only two years prior. For protons, the dominant interaction is photoproduction of pions with a threshold $E_p > 4 \times 10^{19}$ eV and a corresponding mean free path of $\sim$6 Mpc at this energy [26]:

$$\gamma_{2.7K} + p \rightarrow \Delta^+ \rightarrow p + \pi^0 \tag{2.2}$$

$$\gamma_{2.7K} + p \rightarrow \Delta^+ \rightarrow n + \pi^+ \tag{2.3}$$

Since substantial fluxes of neutrinos and photons are expected from those interactions [27], the observation of secondary cosmogenic neutrinos and photons would be indicative of a predominantly light cosmic-ray composition, however, no plausible candidates of such particles have been observed yet. Heavier nuclei lose energy in spallation processes on CMB as well as UV and IR photons, producing neutrons, deuterons and alpha particles in the reaction. The mean decay length of a neutron with energy 10^{20} eV is 1 Mpc [28], thus they quickly disintegrate to protons. For the case of a heavier composition, neutrinos would still be produced by neutron decay, but high-energy neutrinos from charged pion and subsequent muon decay would be lacking.

Principally, the higher the energy of the cosmic ray, the faster it will lose energy in interactions with the CMB and consequently the closer the source must be in order for the cosmic ray to have a non-negligible probability to reach the Earth. This concept is nicely visualized in Fig. 2.2, which shows the probability with which an event of a given energy comes from a source at a given distance. Roughly speaking, the GZK interaction becomes important at 8×10^{19} eV, at which energy there is only a 10 % probability that the cosmic ray has reached us from a distance greater than 100 Mpc [28].

While GZK-related energy losses are always present, it is unclear whether the shape of the spectrum in the flux suppression region is dominated by the GZK effect or the maximum energy limit of the cosmic accelerators. Detailed studies of the energy-dependent composition of UHECRs are necessary to disentangle the two aforementioned scenarios and call for an accurate and well-understood energy calibration of cosmic-ray observatories.

The GZK limit poses significant constraints on the location of UHECR sources, which are expected to be within $\sim$100 Mpc in order for the accelerated particles to have a measurable probability to reach to Earth. Given that current upper limits on the strength of cosmic magnetic fields predict deflections of a few degrees, some anisotropy in the arrival directions of UHECR would be expected at the highest energies, assuming the primaries are singly or doubly charged.

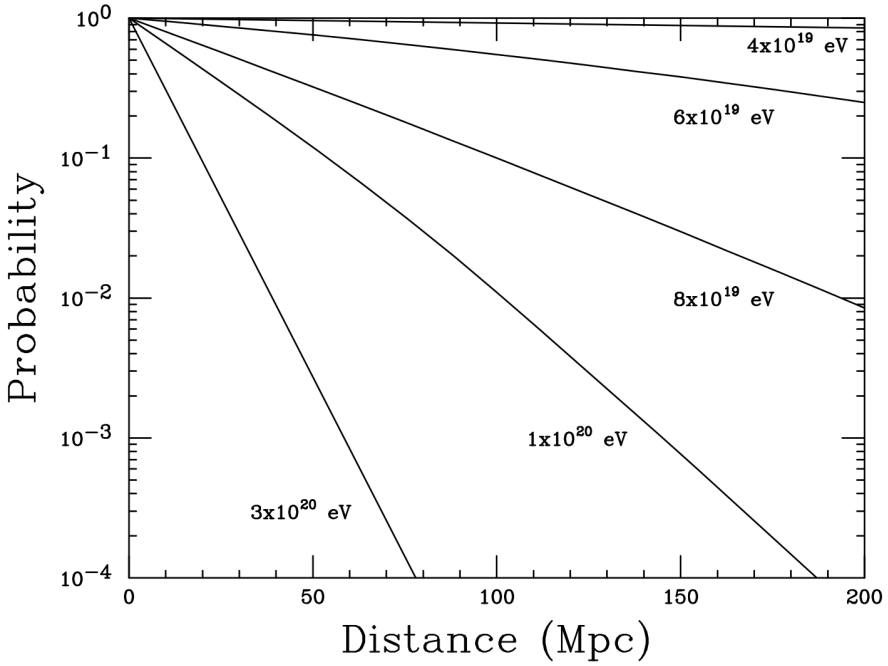

FIG. 2.2 The probability that an observed event with a given energy came from a source located at a distance greater than that indicated on the abscissa. A source spectrum proportional to $E^{-2.5}$ was assumed. From [28].

2.1.3 UHECR sources candidates and acceleration

Acceleration mechanisms of cosmic rays are not fully understood and so far, no sources of UHECR have been identified. Nevertheless, there are basic astrophysical arguments that stipulate necessary, but by no means sufficient, parameters of a UHECR source candidate: The size of the accelerator must be larger than the Larmor radius of the accelerated particle

$$r_L = 1.08 \frac{E}{ZeB}, \tag{2.4}$$

where r_L is given in units of kpc, E is the energy of the accelerated particle in units of EeV, Z its charge in units of e and B is the magnetic field strength of the accelerator in units of μG. As can be seen from the so-called Hillas diagram shown in Fig. 2.3, few objects are able to meet this basic requirement: cores, jets and lobes of active galactic nuclei (AGNs), neutron stars, large-scale shock fronts of merging galaxies or gamma ray bursts (GRBs).

Several theoretical descriptions of acceleration processes have been proposed. One of the first was Fermi's stochastic particle acceleration published in 1949 [29], according to which charged particles gain energy by repeatedly scattering on irregularities of magnetic fields in gas clouds. As the average energy gain of the particle is proportional to β^2, where β is the Lorentz velocity of the cloud, the mechanism has been coined Fermi's second-order acceleration. The original theory was extended to shock-wave environments in the late 1970s [30, 31],

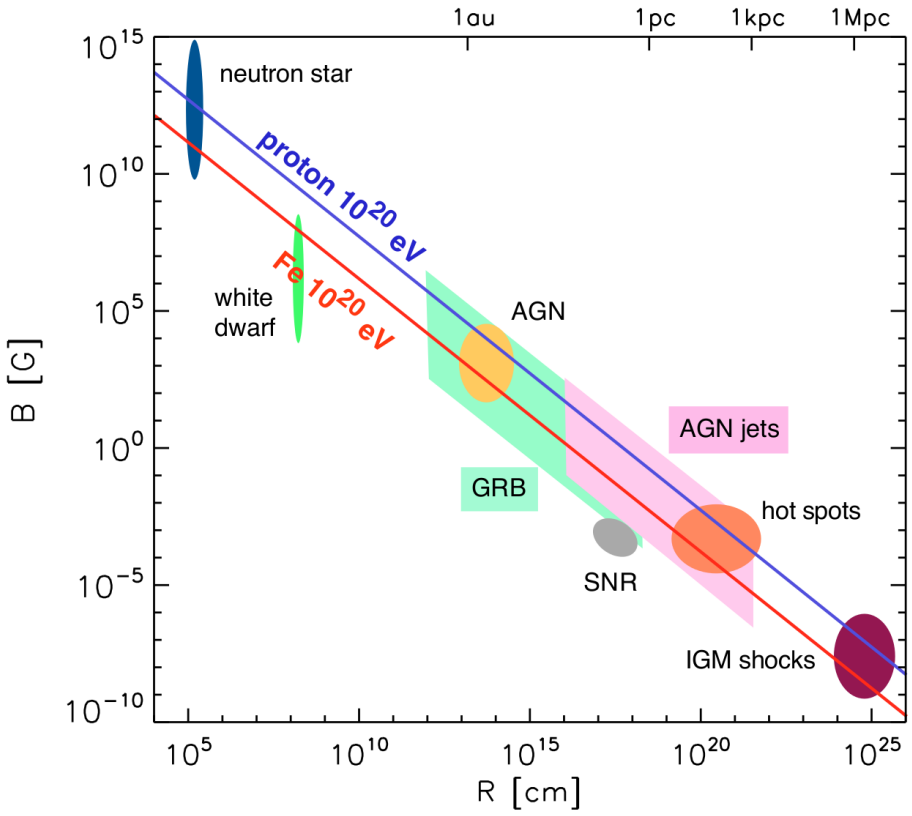

FIG. 2.3 The Hillas diagram: Astrophysical objects are positioned based on their typical size and strength of magnetic field, with the uncertainty in their parameters indicated by the size of the spot. The lines indicate the minimum combination of size and magnetic field required to confine (accelerate) protons and iron nuclei to 100 EeV (blue and red solid line, respectively). Objects located above those lines are, to first approximation, potential UHECR sources. From [20].

where acceleration is particularly efficient as the motions are not random. Since the mean energy gain is proportional to the first power of β (here the Lorentz velocity of the shock front), the mechanism is referred to as first-order acceleration. Fermi acceleration provides a power-law source spectrum compatible with the experimentally measured energy spectra of UHECR.

To bypass the difficulties associated with suitable conventional accelerators of cosmic rays, exotic top-down scenarios have been introduced by some theorists. Most postulate the existence of a super-massive, metastable particle that would decay to directly produce ultra-high energy cosmic rays. The minimum requirement on the particle are thus a mass greater than the energy of the most energetic cosmic rays ever detected and a lifetime commensurate with the age of the Universe. Topological defects, including cosmic strings and magnetic monopoles, have been suggested as candidates [32]. However, nowadays top-down scenarios are strongly disfavored by limits on the photon and neutrino fluxes posed by concurrent experiments [33–35].

2.2 Detection of Ultra-High Energy Cosmic Rays

2.2.1 Extensive air showers

Extensive air showers (EAS) are particle cascades that develop as a result of interactions of a high-energy cosmic ray with air molecules of the Earth's atmosphere, which acts as a giant calorimeter of a column density of $\sim$1030 g/cm^2. The first interaction typically occurs at 15–30 km above ground [10] and a multitude of particles is quickly produced. Three components of the cascade can be distinguished: hadronic, electromagnetic and muonic.

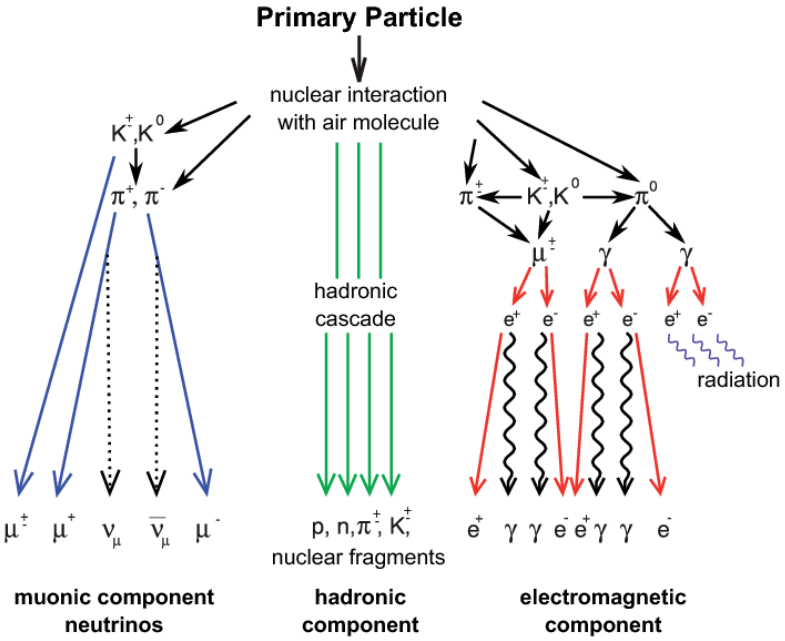

FIG. 2.4 Schematic development of a hadron-induced extensive air shower. Three components of secondary particles are distinguished: hadronic, electromagnetic and muonic. From [36].

Let us describe the development of an air shower, schematically depicted in Fig. 2.4 on the example of a proton primary. Upon striking the top of the atmosphere, the proton interacts to produce predominantly pions – the lightest existing mesons. With a lifetime of $c\tau = 25$ nm, the neutral pions quickly decay into photons, which initiate an electromagnetic sub-shower (discussed in the next paragraph). The longer-lived charged pions with a lifetime of $c\tau = 7.8$ m form the bulk of the hadronic cascade. Their fate is energy-dependent: above the critical energy of $E_\pi \gtrsim 20$ GeV [37] they are more likely to re-interact with atmospheric nuclei, thus the hadronic component continues to develop and, at the same time, feeds the electromagnetic cascade. At lower energies, decay into muons is more likely and energy is transferred to the muonic sub-shower:

$$\begin{aligned} \pi^+ &\to \mu^+ + \nu_\mu \\ \pi^- &\to \mu^- + \bar{\nu}_\mu \,. \end{aligned} \tag{2.5}$$

Other particles in the hadronic cascade are pair-produced baryons, nuclear fragments and kaons, which are produced about ten times less frequently than pions, but decay predominantly through the same channels as in Eq. (2.5). Muons of sufficient energy and thus lifetimes, as well as the simultaneously produced muon (anti-)neutrinos, reach the ground without depositing their energy in the atmosphere. This fraction of energy is then referred to as the *invisible* energy and must be properly taken into account.

The electromagnetic cascade is initiated by the rapid decay of neutral pions into photons and is additionally continuously fed by muon decays:

$$\begin{aligned} \mu^+ &\to e^+ + \nu_e + \bar{\nu}_\mu \\ \mu^- &\to e^- + \bar{\nu}_e + \nu_\mu \,. \end{aligned} \tag{2.6}$$

The development of the electromagnetic cascade can be schematically described by the Heitler model from the 1940s [38]. At each interaction step, defined by the radiation length of air of 37 g/cm^2 [39], two particles of approximately equal energies are produced. In particular, a photon interacts to pair-produce an e^+ and an e^-, which in turn each emit a bremsstrahlung photon that undergoes pair-production yet again at the next interaction step. These are the most likely interaction processes at energies of tens of MeV and the number of particles in the electromagnetic cascade grows geometrically with depth until the energy drops below the critical threshold of $E_c \sim 80\,\mathrm{MeV}$ (in air), where ionization outweighs radiation losses and the cascade begins to diminish. While the Heitler model is of course oversimplified and does not take into account the multiplicity in the emission of bremsstrahlung photons, it correctly describes the basic development of an electromagnetic sub-shower. The longitudinal development of particle abundances in a proton-induced air shower shown in Fig. 2.5.

The cascade development described here can be extended to heavier primaries using the superposition principle, according to which the interactions of a heavier primary with mass number A and energy E_0 can described as a superposition of the interactions of A nucleons, each with an energy of E_0/A [40]. Showers initiated by heavier primaries will thus develop accordingly faster and on average higher in the atmosphere, with smaller shower-to-shower fluctuations.

Most of the energy of an air shower is deposited electromagnetically. The point along the shower axis at which the energy deposit is maximal is referred to as the depth of shower maximum X_{max}, with a mean value

$$\langle X_{\mathrm{max}} \rangle = X_0 + D \log\left(\frac{E}{AE_0}\right) + \xi \ln A + \delta \ln A \log\left(\frac{E}{E_0}\right), \tag{2.7}$$

where X_0 is the mean depth of showers induced by protons with a primary energy E_0, D is the change of X_{max} per decade in energy (the so-called *elongation rate*), and the parameters ξ and δ describe deviations from the ideal superposition model. The development of an EAS in the atmosphere is a statistical process, which is best described by Monte Carlo (MC) simulations. Codes available for the simulation of electromagnetic cascades include EGS or FLUKA [41], and CORSIKA [42] or AIRES [43] for the simulation of hadronic cascades. Those codes

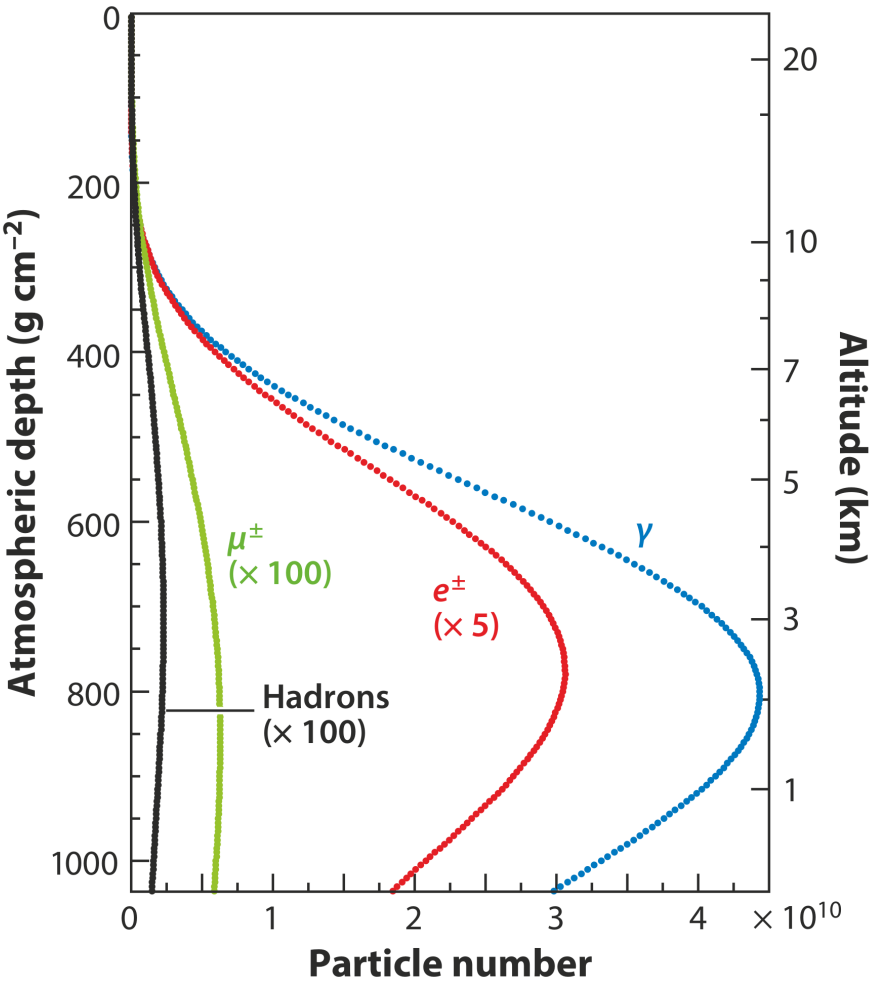

Fig. 2.5 Longitudinal profiles of different particle species in a simulated air shower initiated by a 10^{19} eV proton. From [10].

draw on various hadronic interaction models such as SIBYLL [44], QGSJET [45] or EPOS-LHC [46], which rely on the extrapolation of cross sections for hadronic interactions beyond the energy limits of particle accelerators and are thus burdened by significant systematic uncertainties [10].

2.2.2 Observational techniques

At energies exceeding 10^{14} eV, the primary cosmic-ray flux is so low that direct measurements with airborne detectors become unfeasible and are replaced by air shower measurements, based either on following the propagation of the shower through the atmosphere or sampling the secondary products arriving at ground level. Two well-established methods – air fluorescence and ground arrays – will be discussed in the following paragraphs. Other methods exist, most notably detection of EAS-induced emission in the radio range and Cherenkov

light detection, which is limited to somewhat lower energies ($\lesssim 10^{18}\,\mathrm{eV}$) by its forward-beamed nature. While those methods are not discussed within this work due to limited space, readers interested in observational techniques are referred to e.g. [47, 48].

Air fluorescence

As electrically charged particles of an extensive air shower, mainly electrons and positrons, traverse the atmosphere, they excite nitrogen molecules, which upon de-excitation emit fluorescence light. While this light – often compared to the light output of a 60 W light bulb at a distance of 30 km – is faint, it can be detected by ground-based telescopes on clear dark nights. This requirement limits the duty cycle of a fluorescence telescope to about 15 %, however, due to the isotropy of fluorescence emission, a single telescope can observe large volumes of the atmosphere and measure air showers at distances of tens of kilometers.

The amount of emitted fluorescence light is directly proportional to the calorimetric energy of the air shower, i.e. the energy deposited by the air shower in the atmosphere (∼90 %). The proportionality factor is given by the fluorescence yield in photons per unit of waveband and energy (see Fig. 2.6), and has been measured in numerous laboratory experiments [49–52]. Since the fluorescence yield is dependent on many atmospheric variables, such as air temperature, pressure and humidity, rigorous atmospheric monitoring programs are required. Moreover, photons propagating from the shower core to the telescope are subject to atmospheric attenuation and scattering, making accurate knowledge of atmospheric aerosol concentrations imperative.

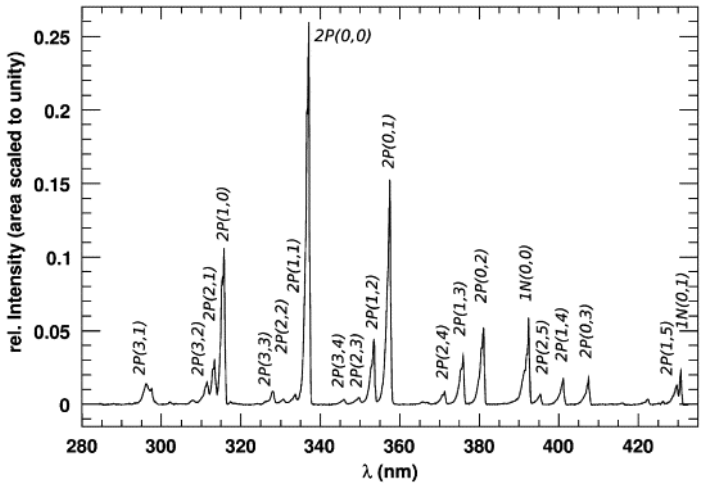

FIG. 2.6 The air fluorescence spectrum spans the wavelength range 280–435 nm, with the most prominent lines at 337 nm and 357 nm. From [53].

The distinct advantage of the fluorescence technique compared to surface arrays is its ability to observe the longitudinal energy deposit of the air shower in the atmosphere. The total calorimetric energy is obtained by integrating the

measured light profile and is additionally corrected for the so-called invisible energy carried away by muons and neutrinos to obtain the total primary energy. Most importantly, the energy measurement with the air fluorescence method is, with the exception of the invisible energy correction, independent of hadronic interaction models. Moreover, the measurement of the depth of maximum shower development X_{max} is indicative of the primary mass. However, due to shower-to-shower fluctuations, mass separation can only be performed statistically or by exploiting additional information, e.g. from muon counters.

Surface particle detectors

Secondary particle detection at ground level is the oldest technique of studying EAS. The footprint of the air shower is sampled by particle detectors, with the spacing of individual stations and the total area of the array determined by the targeted energy range. The arrival direction and total energy of the particle are reconstructed from the arrival times of the shower front at the individual stations and the lateral particle densities, respectively.

The individual detector stations are typically scintillators or water Cherenkov detectors. The latter, employed e.g. at the Pierre Auger Observatory, are large plastic vessels filled with purified water. Relativistic particles passing through the detection volume emit Cherenkov light, which is recorded by photodetectors. Large, flat, plastic scintillators are an alternative to water Cherenkov detectors and are used e.g. at Telescope Array. While they are relatively easily deployed and provide an estimate of the calorimetric energy, their effective aperture decreases promptly with the zenith angle of the air shower.

The greatest advantage of surface detectors is their high duty cycle, which is essentially 100 %. On the other hand, the technique is constrained by sampling the lateral distribution of the shower at one altitude only and, if stand-alone, relying on simulation-based calibration. In practice, the energy and mass of the primary cosmic ray are obtained by comparing measurements with the predictions of air shower simulations based on models of particle interactions in the atmosphere. As discussed on page 12, this approach is plagued by significant systematic uncertainties related to extrapolating accelerator-measured hadronic cross-sections to UHECR energies. Furthermore, the energy assignment is not only model-dependent, but also composition-dependent, whereby the primary composition is a priori unknown.

The combination of the fluorescence and ground array techniques is exceptionally powerful, with the former providing a model-independent estimate of the calorimetric energy and a direct measurement of the X_{max}, and the latter a duty cycle of almost 100 %. A set of events reconstructed from independent measurements by both detectors are used to transfer the fluorescence-detector energy scale to the surface array, as is discussed for the case of the Pierre Auger Observatory in Subsec. 2.3.5. Moreover, hybrid reconstruction, i.e. the reconstruction of air showers detected with the fluorescence detector and supplemented by timing information from one or more surface array stations, allows the lon-

gitudinal profile of the air shower to be reconstructed with considerably higher accuracy than in the case of monocular (one telescope only) detection. Both current UHECR observatories, the Pierre Auger Observatory in the Southern and the Telescope Array in the Northern hemisphere, employ a combination of the fluorescence and ground array methods.

FIG. 2.7 The Pierre Auger Observatory, indicated by the blue square, is located in the Argentine Pampa Amarilla.

2.3 The Pierre Auger Observatory

The goal of this section is to lay the foundations for understanding the research presented in this work. Emphasis is placed on selected topics that will be of importance later in the course of this study. A reader wishing a broader and in parts more detailed introduction will fare well to start with [54, 55].

The Pierre Auger Observatory, located in the vast pampa of the Argentine Mendoza Province (see Fig. 2.7), is the largest cosmic-ray observatory ever constructed. As is schematically depicted in Fig. 2.8, the Observatory combines the surface array and fluorescence techniques to achieve an unprecedented high-accuracy, model-independent measurement of EAS with energies of $10^{17.5}$ eV and higher. The following brief overview is based on [54, 55] and references therein.

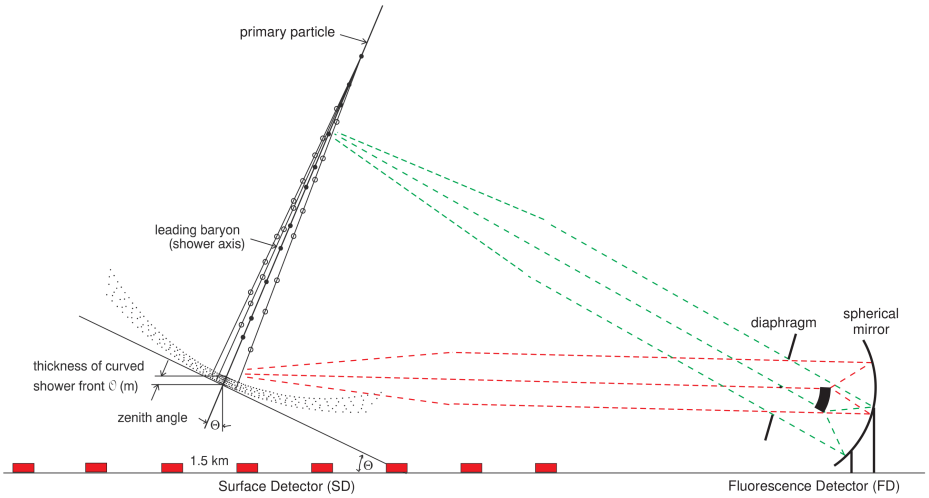

FIG. 2.8 Hybrid detection of air showers at the Pierre Auger Observatory. The telescopes measure the isotropically emitted fluorescence light induced as the shower moves through the atmosphere. The surface detector array samples the particle distribution at ground level. From [56].

Profiting from its modular design, the Observatory first began taking data in 2004, gradually adding detectors (both, surface stations and fluorescence telescopes) until its completion in 2008. The location in the vast and generally flat Pampa Amarilla is advantageous for numerous reasons: With a mean altitude of ∼1400 m and a corresponding atmospheric overburden of ∼875 g/cm^2, the Observatory is well positioned with respect to the depth of maximum development of EAS. It is far removed from large cities and the associated light pollution, and the rain shadow of the Andes provides a suitable climate for measurements with the fluorescence detector.

2.3.1 Surface detector

Over 1660 water Cherenkov stations dot some 3000 km^2 of the Pampa Amarilla (see Fig. 2.9). The regular spacing of 1.5 km and the size of the array are optimized for the detection of air showers with energies of 3×10^{18} eV and more. Each detector consists of a large plastic vessel made of highly durable polyethylene filled with 12 000 liters of purified water that act as a Cherenkov radiator for relativistic charged particles passing through the volume. The height of the vessel of 1.2 m makes it additionally sensitive to high-energy photons, which interact by pair production, and to particles arriving at large angles with respect to the vertical. To increase light collection efficiency, the inner walls are lined with a reflector and the entire volume is viewed from above by three large (9 in. diameter) hemispherical PMTs. Each station further is equipped with a data acquisition (DAQ) electronics enclosure, a GPS device, a solar panel, a battery box, and a communications and GPS antenna (see Fig. 2.10 for a photograph).

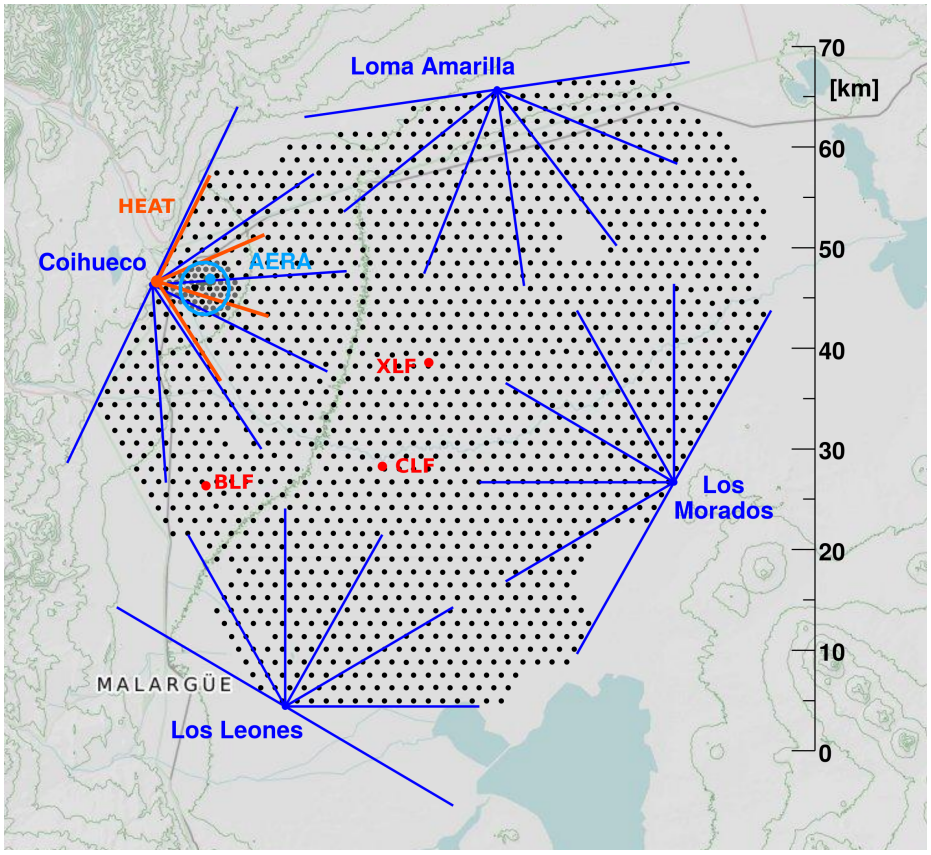

Fig. 2.9 A schematic map of the Pierre Auger Observatory. Each black dot represents a single surface detector station. Blue dots mark the location of individual fluorescence detector (FD) buildings and blue lines mark their respective azimuthal fields of view. The headquarters of the Observatory are located in the town of Malargüe, shown in the lower left corner of the map. Also indicated are the atmospheric monitoring facilities Extreme Laser Facility (XLF), Central Laser Facility (CLF) and Balloon Launching Facility (BLF).

2.3.2 Fluorescence detector

Taking advantage of the isotropic emission mechanism, a total of 27 telescopes line the perimeter of the Observatory (see Fig. 2.9) and overlook the atmosphere above the surface array. They are operated on clear dark nights with good weather conditions, reaching a duty cycle of about 15 %. The 24 baseline telescopes are evenly divided between four sites named:

- Los Leones (LL),
- Los Morados (LM),
- Loma Amarilla (LA), and
- Coihueco (CO).

The Los Leones site is depicted in the photograph in Fig. 2.11.[1]

[1] *The remaining three telescopes not listed here are part of a low-energy extension HEAT discussed in Subsec. 2.3.3.*

In the following, the viewing angles are described using a spherical coordinate system in terms of the elevation Ω, respectively zenith θ, and the azimuthal angle ϕ, which are indicated in the sketch in Fig. 2.12. Each telescope spans a field of view (FOV) of $30° \times 30°$ in elevation and azimuth, combining to an azimuthal coverage of 180° for the baseline FD buildings. The bottom edge of the FOV is elevated by about 1° with respect to the horizontal.

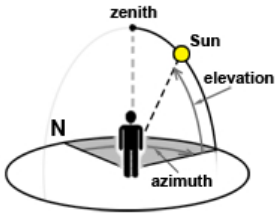

FIG. 2.12 The viewing angles are described in terms of spherical coordinates, here indicated for the position of the Sun in the sky. The elevation (Ω, not to be confused with a solid angle) and the zenith (θ) denote the angles relative to the horizontal and the vertical, respectively. They are complementary, i.e. $\Omega + \theta = 90°$. The azimuth denotes the angle in the horizontal plane. From [57].

Fig. 2.13 depicts the layout of an FD building, also referred to as an "FD site". The six telescopes, or "bays", within one building are numbered counter-clockwise and denoted using abbreviations of the form XXy, where XX is the building abbreviation and y the telescope number. LL3 would thus be the third telescope at the Los Leones site, and CO1 the first telescope at Coihueco.

Since the understanding of the operation of the fluorescence detector is of prime importance to this work, the optical design and to a lesser extent the triggering system are discussed in the following (pages 18 to 23).

Optical design

A schematic depiction of the modified Schmidt design of the telescopes and a photograph of a telescope bay are shown in Fig. 2.14. Light enters through a circular 2.2 m aperture equipped with a UV filter made of MUG-6 glass [58], which transmits in the wavelength range 290–410 nm and serves to cut the background in the visible range. The spectral efficiency curve for the MUG-6 filter, as well as other optical components, is shown in Fig. 2.15.

A segmented corrector ring with an inner and outer radius of 0.85 m and 1.1 m, respectively, positioned concentrically just on the bay-side of the filter, reduces coma and spherical aberrations. The resulting increase in effective aperture, compared to a design without a corrector ring and with a correspondingly smaller aperture to keep aberration at an acceptable level, is a factor of 1.7 [55].

A spherical segmented mirror with an area of $\sim$13 m^2 and a radius of curvature (RC) of 3.4 m focuses light onto the photodetector. Two different mirror designs are in use:

Fig. 2.10 One of 1660 surface detector stations of the Pierre Auger Observatory. The 1.2 m high vessel is filled with 12 000 liters of purified water, viewed from above by three large hemispherical PMTs. Mounted on top are a solar panel, and a communications and GPS antenna on a small mast. Photo courtesy of Radomír Šmída.

Fig. 2.11 The telescopes at the Los Leones site overlooking the atmosphere above the surface array from atop a small elevation. The telescopes are of course only operated on clear dark nights, but here the shutters were opened for the special occasion of taking this photograph. The communications tower is visible in the background. Photo courtesy of Radomír Šmída.

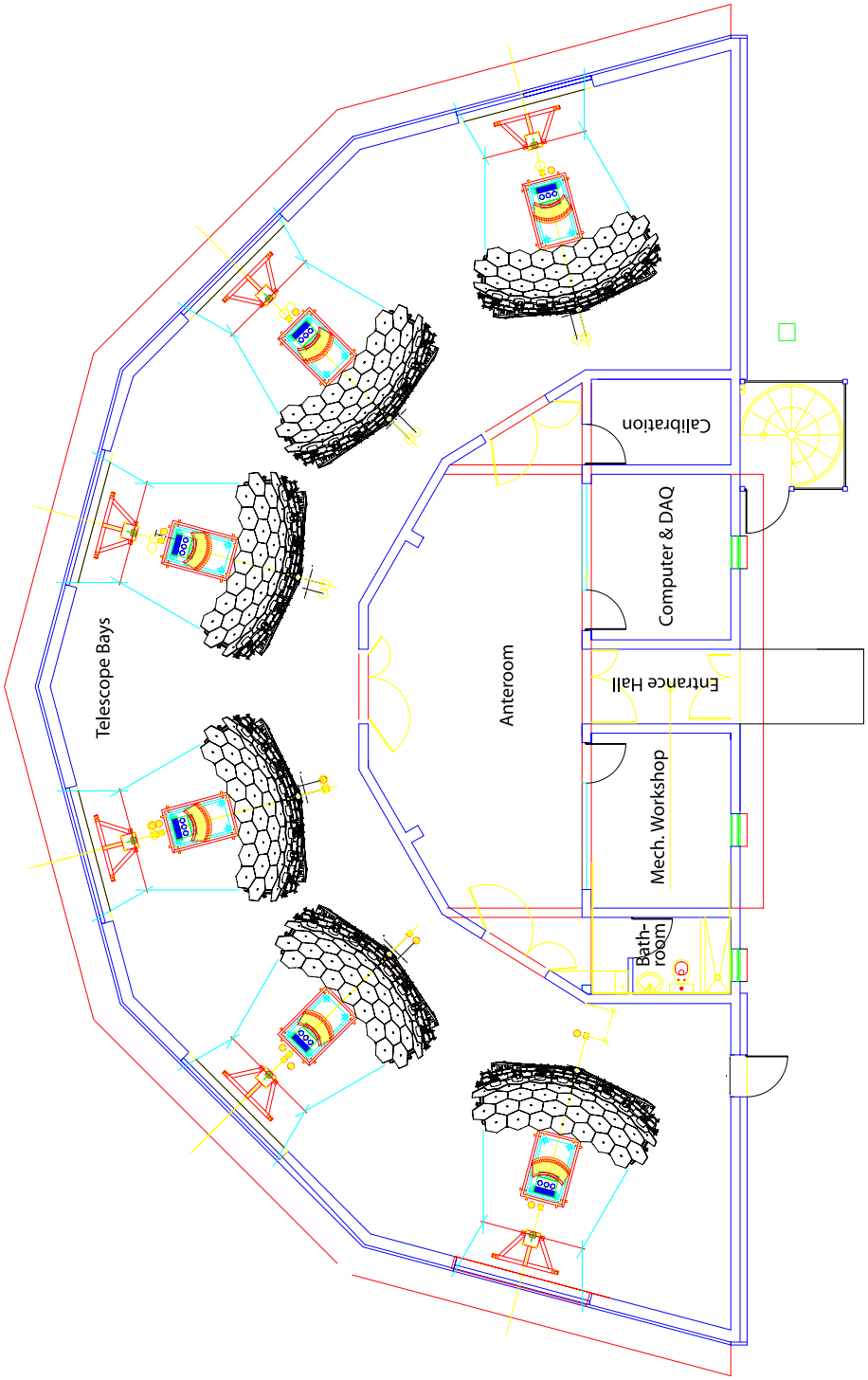

FIG. 2.13 A schematic layout of an FD building housing six telescopes. From [55].

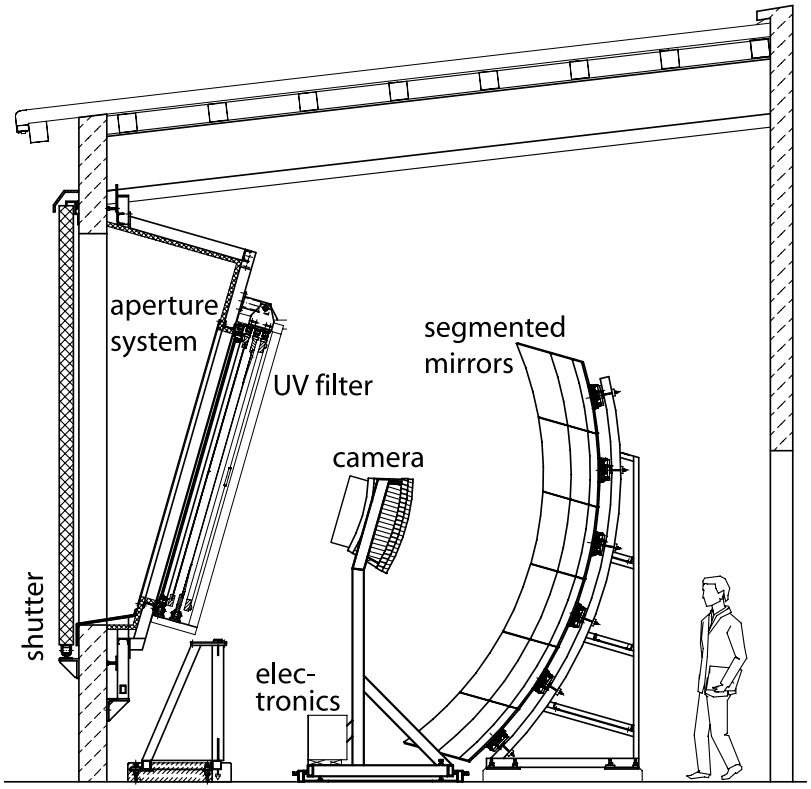

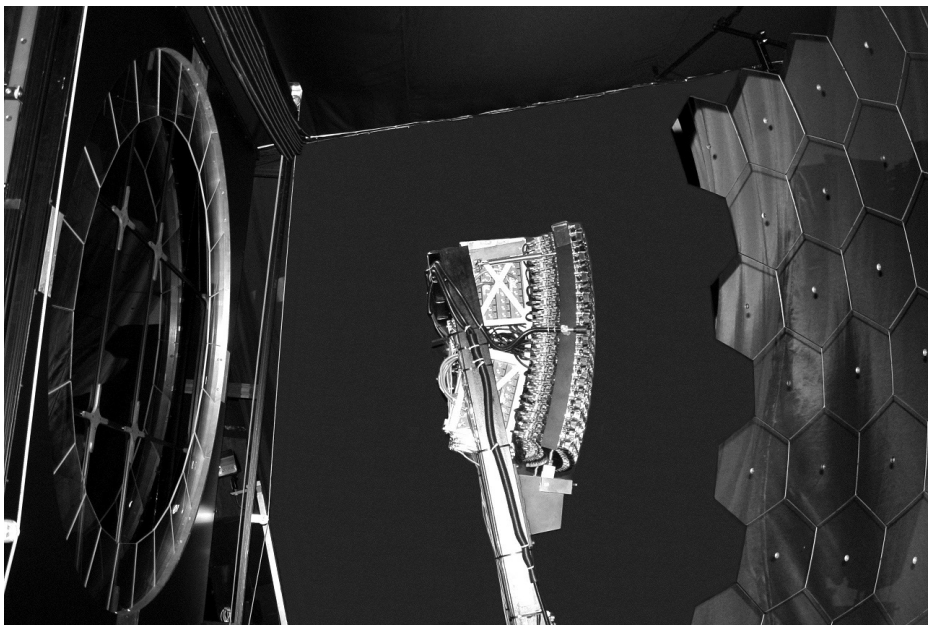

FIG. 2.14 Top: A schematic depiction of a telescope bay. Light enters through a circular aperture and is focused by a large spherical mirror onto a camera of PMTs. From [55]. Bottom: A photograph shot from a similar perspective. The annular structure in the aperture on the left is the segmented corrector ring. Photo courtesy of Radomír Šmída.

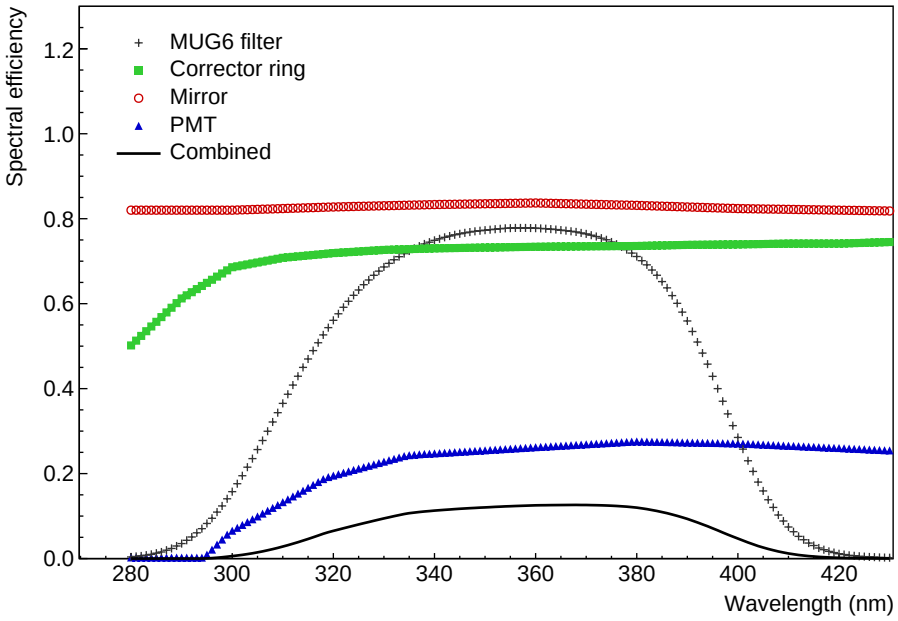

FIG. 2.15 The spectral efficiency of individual FD optical components, to be understood as transmissivity for the MUG-6 filter (gray plus signs) and the corrector ring (green squares), reflectivity for the mirror (red circles) and the quantum efficiency for the photomultipliers (blue triangles). Data from [59].

1. Glass mirrors with an aluminum reflective layer and a protective silicon oxide layer, and

2. aluminum mirrors with an aluminum alloy reflective coating and a protective aluminum oxide layer.

The first type is installed in buildings LA and CO, the second in LL and LM. While the mirrors share a common geometrical design, the tesselation differs. The glass mirrors are composed of a matrix of 8×8 hexagonal segments, whereas the aluminum mirrors use larger rectangular segments in a 6×6 arrangement.

The spherical focal surface is comprised of a camera of 440 bi-alkali, 8-dynode, hexagonal PMTs manufactured by Photonis, model XP3062 [60], arranged in a 22×20 row-column matrix [61]. Each PMT views a different part of the sky. The nominal viewing direction is defined by the vector perpendicular to the PMT face and passing through its center, and is given in terms of the elevation Ω measured relative to the horizontal and the azimuthal angle ϕ. The solid angle of the sky subtended by one PMT is proportional to the opening angle of its FOV of $\sim$1.5°, nominally measured from side to side. Due to the hexagonal shape of the PMTs, the opening angle is naturally somewhat larger (1.73°) vertex-to-vertex (see Fig. 2.16. left).

Light collectors shaped like Mercedes stars, see Fig. 2.16 (right), fill the small gaps between adjacent PMTs. MC simulations have shown that, assuming a

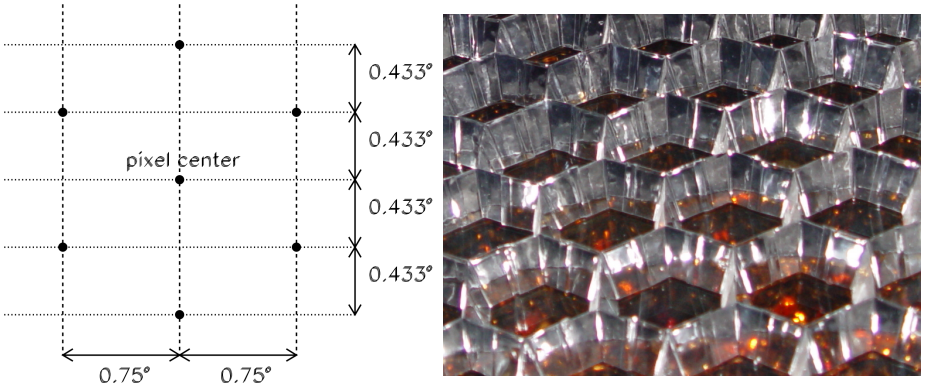

FIG. 2.16 Left: The positioning of pixel (PMT) vertices (marked by black points) relative to the pixel center. The nominal opening angle of the FOV of a PMT is 1.5° as measured from side to side. Vertex-to-vertex it is naturally somewhat larger. From [61]. Right: A close-up of the FD camera. The small insensitive gaps between individual PMTs are filled with light collectors called "Mercedes stars" due to their shape. Photo courtesy of Radomír Šmída.

reflectivity of 85 % for these reflectors, the light collection efficiency of the camera is boosted from 70 % to 94 % [55, 62].

Electronics and trigger system

The FD electronics is optimized to handle the large dynamic range of air fluorescence measurements and provide strong background rejection, all the while accepting any physically plausible event. Each PMT is connected via its head electronics to a distribution board located at the back of the camera body, with one board serving 44 PMTs. The adjacent front-end electronics (FE) houses analog boards that provide a 15-bit dynamic range which is later adapted to the 12-bit analog-to-digital converter (ADC) with 100 ns sampling. In addition to receiving, shaping and digitizing signals, the FE is also responsible for generating the first two firmware triggers. The flexible trigger system comprises three levels:

First-level threshold trigger (FLT): This is a firmware trigger that works on the level of a single pixel.[2] The pixel threshold is dynamically adjusted such that the resulting hit rate is about 100 Hz. In this way, the individual sensitivities of the pixels and spatial variations of the night-sky background (NSB) are taken into account.

[2] *The terms pixel and PMT are used synonymously.*

Second-level geometry trigger (SLT): Also a firmware trigger located at the FE, the SLT searches for groupings of at least five pixels forming track-like patterns on the camera (see Fig. 2.17 for the fundamental patterns). By requesting that only four out of those five pixels actually have an FLT, this trigger allows for pixels with sub-threshold signals that are in fact part of a real air shower event, but are located too far off the main shower track to trigger at the first level, or potential dead pixels. At this point, each event with an SLT is assigned a time stamp by the building's GPS clock that is later used to merge the signals

of individual telescopes within one FD building. Typically, the SLT rate is in the range 0.1–10 Hz [54].

Third-level timing trigger (TLT): This software trigger examines the time sequence of the pixels that have passed the first- and second-level triggers. Background events such as lightning or direct cosmic-ray impacts are eliminated this way.

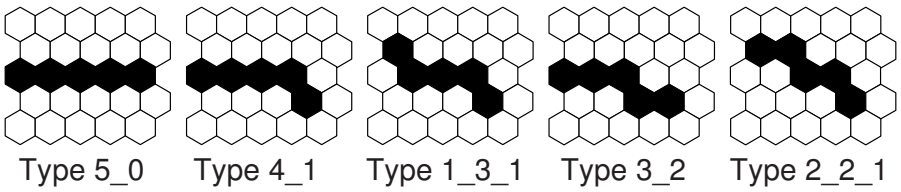

FIG. 2.17 Fundamental five-pixel patterns regarded as shower-track segments. The second-level trigger allows for one of the five indicated pixels to not have triggered at the first level. From [55].

To reduce electronics readout time, data volume, and to allow for higher triggering rates, only the ADC traces of pixels with a TLT and those located within ± 2 rows or columns are read out. This is an important point that will be revisited in Sec. 3.3 as well as later chapters.

An event that has survived all three levels is sent to the main computer of the respective FD building, where the events from different telescopes having an SLT within a time window of 2 ms are combined and a hybrid trigger (T3) is generated for the surface array. At this point, the impact time of the air shower at ground level is computed in a preliminary, on-the-fly analysis of the FD signals, and an updated GPS timestamp is assigned to the T3 trigger. The main purpose of the T3 is to obtain an surface detector (SD) signal for air showers below 3×10^{18} eV, in which energy range the array is not fully efficient and consequently may not self-trigger. Even though in many cases the shower will not be reconstructed by the SD, the arrival timing from one or two stations is a critical piece of information for high-quality hybrid reconstruction. The final T3 rate of the baseline telescopes is about 0.012 Hz [54].

There are several scenarios in which external triggering is employed. In particular, a full-camera readout is triggered during calibration runs (Sec. 3.1), Octocopter flights (Chap. 5 and Chap. 6) and laser beam detection.

2.3.3 Enhancements and planned upgrade

Throughout the course of its operation, the Observatory has been complemented by various enhancements, mostly aimed at lowering the energy threshold for the detection of air showers and the research and development of radio- and microwave detection.

A part of the ground array (23.5 km^2) was literally filled in with additional surface stations, and is thus appropriately named the “infill array”. There has been an ongoing effort to complement the infill stations with muon counters

buried 2.3 m underground (AMIGA). The reduced spacing of 750 m is optimized for the detection of air showers in the range 10^{17}–10^{18} eV, which is of interest for a variety of reasons. The isolation of the muonic component with dedicated counters supplies additional information for the determination of the primary mass composition in the energy region where the dominant contribution to the flux presumably transitions from galactic to extra-galactic sources. Furthermore, with the infill particle interactions at LHC-equivalent energies can be studied. The fluorescence detector was correspondingly enhanced with three additional telescopes – the High-Elevation Auger Telescopes (HEAT) – capable of viewing higher altitudes above the infill array, and thus have the X_{max} of lower-energy showers in their field of view.

On the radio-detection development front, the Observatory features the Auger Engineering Radio Array (AERA), and in the microwave range the Air-shower Microwave Bremsstrahlung Experimental Radiometer (AMBER), the Microwave Detection of Air Showers (MIDAS) and the Extensive Air Shower Identification using Electron Radiometer (EASIER). An overview of the enhancements listed here is given in e.g. in [54] or [63].

Within the planned upgrade of the Pierre Auger Observatory (AugerPrime) [64, 65], the existing SD stations will be complemented with scintillator detectors to determine the muonic and electromagnetic components of air showers. In this way, the mass composition sensitivity of the Observatory will be extended to the flux suppression region, where only limited data from the FD are available due the extremely low flux of particles and a limited duty cycle of 15 %. An extension of the FD uptime by up to 50 % is also foreseen and is further addressed in Subsec. 3.1.2.

2.3.4 Atmospheric monitoring

The amount of fluorescence light reaching the telescope apertures is considerably affected by atmospheric attenuation and scattering, and must be properly taken into account in order to reconstruct the calorimetric energy correctly. Interactions of UV photons with air molecules are described analytically by the wavelength-dependent Rayleigh scattering cross section, which is affected by basic atmospheric state variables, such as temperature, pressure and humidity [66]. Scattering on aerosols is described by Mie scattering theory. However, the final amount of attenuation and scattering strongly depends on real-time conditions, with aerosol concentration and mean size being of vital importance. Dynamic, time- and space-dependent monitoring of the atmosphere is thus required.

Two distant laser facilities are situated in the central part of the array: the Central Laser Facility (CLF) and the Extreme Laser Facility (XLF) (see Fig. 2.9). Ideally, one facility positioned roughly equidistantly from all sites would serve the entire fluorescence detector. Since this is not possible due to the elongated shape of the array, the CLF, in operation since 2004, serves Los Leones, Los Morados and the Coihueco and HEAT site. Loma Amarilla, which sees a rather faint signal from the CLF, uses predominantly the XLF. Sets of 50 vertical shots, with an

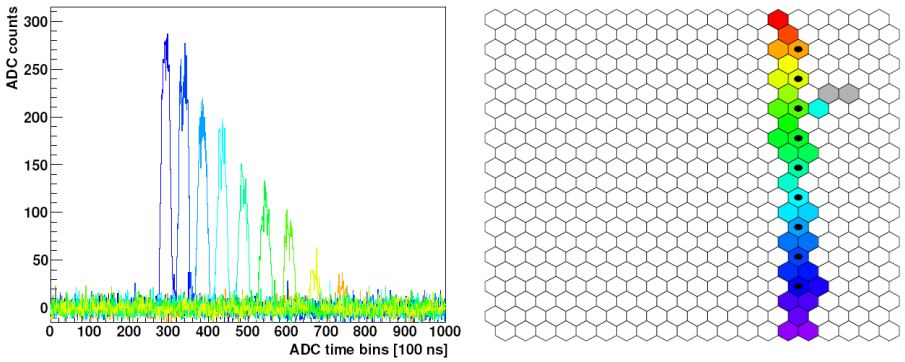

FIG. 2.18 A CLF laser shot observed by an FD camera. Side-scattered light moves across the FOV of the telescope, producing a track on the FD camera (right). Each hexagon represents one PMT and the color coding carries time information. The ADC traces for individual PMTs marked by a black dot are shown in the left panel.

example shown in Fig. 2.18, are observed by at least one telescope at each FD site at 15-minute intervals and are used to determine the vertical aerosol optical depth (VAOD) [67], defined as the integral of the aerosol extinction from ground level to a particular altitude h observed at an elevation angle Ω.

Two different procedures are used to extract the aerosol optical depth profiles from the CLF and XLF measurements. The mean signal of 50 shots is either compared to the mean signal measured under clean conditions (referred to as the *data-normalized* analysis) or to signals simulated with different aerosol conditions (*laser simulation* analysis) [67]. The obtained VAOD values are filled into a database used during FD data reconstruction. Preferentially, the data-normalized values are used. The Mie-related transmission factor is then computed as

$$\tau_{\text{Mie}} = \exp\left(\frac{-VAOD(h)}{\sin\Omega}\right), \tag{2.8}$$

where h is the altitude above ground level and Ω the elevation angle. If no VAOD measurement is available for a particular time, a default value based on an all-time average is used.

Other atmospheric transmission monitoring systems and cloud installations include the aerosol phase function monitors [66], the horizontal attenuation monitor [66], infrared cameras for cloud identification [68], FD lidar stations [69, 70] and the optical telescope FRAM [71, 72]. Each FD site and additionally the CLF are equipped with a ground-based weather station.

2.3.5 Hybrid detection and energy calibration

The hybrid detection principle of the Pierre Auger Observatory is schematically depicted in Fig. 2.19.

The cross-calibration is achieved by analyzing a high-quality data set of air showers reconstructed by both, the FD and the SD, and relating the FD-measured energy to an energy estimator of SD. The SD energy estimator S_{38} describes the

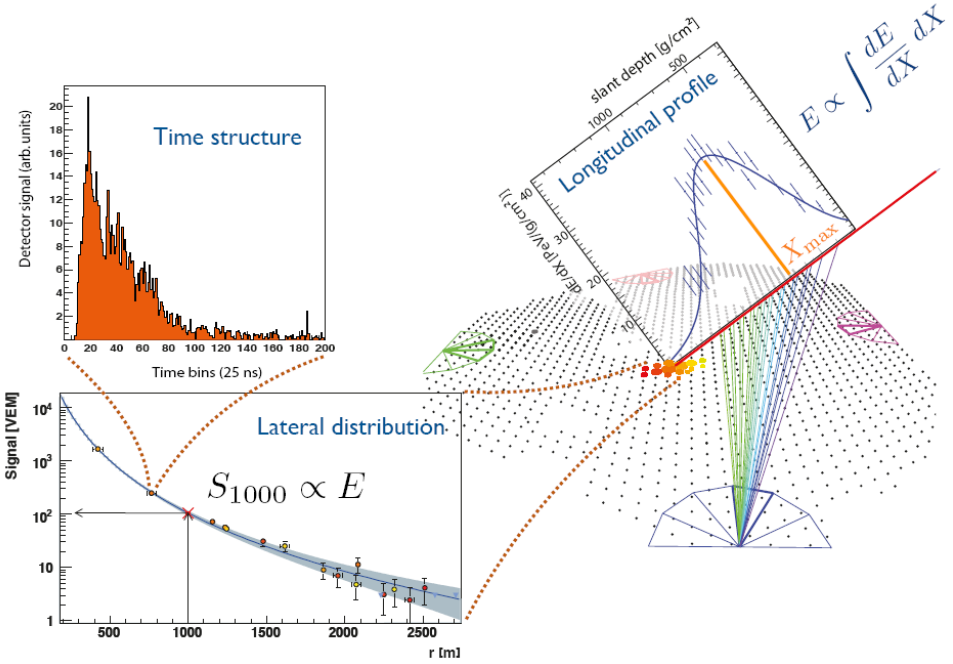

FIG. 2.19 The hybrid detection of an air shower at the Pierre Auger Observatory. The FD (right panel) measures the longitudinal energy deposit profile as a function of the atmospheric slant depth, the integral of which provides an estimate of the calorimetric energy. The determination of the shower X_{max} is direct. The SD (left panels) samples the lateral distribution of particles at ground as a function of distance from the shower core. The particle density is proportional (measured in units of vertical-equivalent muon (VEM)) to the primary energy, and due to minimized signal fluctuations the value S_{1000} at 1000 m is used as the energy estimator. The timing information contained in the ADC traces of individual surface stations may provide additional composition information. From [73].

shower size in terms of the signal S_{1000} it would produce at a distance of 1000 m from the shower core. Since this estimator is dependent on the zenith angle θ of the shower, the observed S_{1000} is additionally converted to a reference zenith angle of 38°. The final energy estimator S_{38} can thus be interpreted as the signal a shower of size S_{1000} would have produced if it had arrived at a zenith angle $\theta = 38°$.[3] The dependence of S_{38} on reconstructed FD energy is shown in Fig. 2.20 and well described by a simple power-law

$$E_{FD} = A S_{38}^{B}\,, \tag{2.9}$$

where $A = (0.187 \pm 0.004)$ EeV and $B = 1.023(006)$ [74].

The total systematic uncertainty of the FD energy scale is 14 %, the most dominant contribution being the absolute calibration of the fluorescence detector of 9.9 %. Other prominent sources of uncertainty include folding with the point spread function (5 %, see Secs. 3.2 to 3.3), the temporal stability of the energy scale (5 %) and the aerosol optical depth (3–6 %) [76]. The largest uncertainty of the SD energy scale comes from the uncertainties of the FD energy scale, which are correlated between individual air showers, and the SD thus shares the full 14 % uncertainty of the FD energy scale.

[3] *The S_{38} is used as the energy estimator for vertical showers (defined as those with zenith angles θ greater than 60°) detected with the standard SD array. The infill array with reduced spacing uses the energy estimator S_{35} and yet another energy estimator is used for inclined showers (defined as those with zenith angles θ in the range 60–80°).*

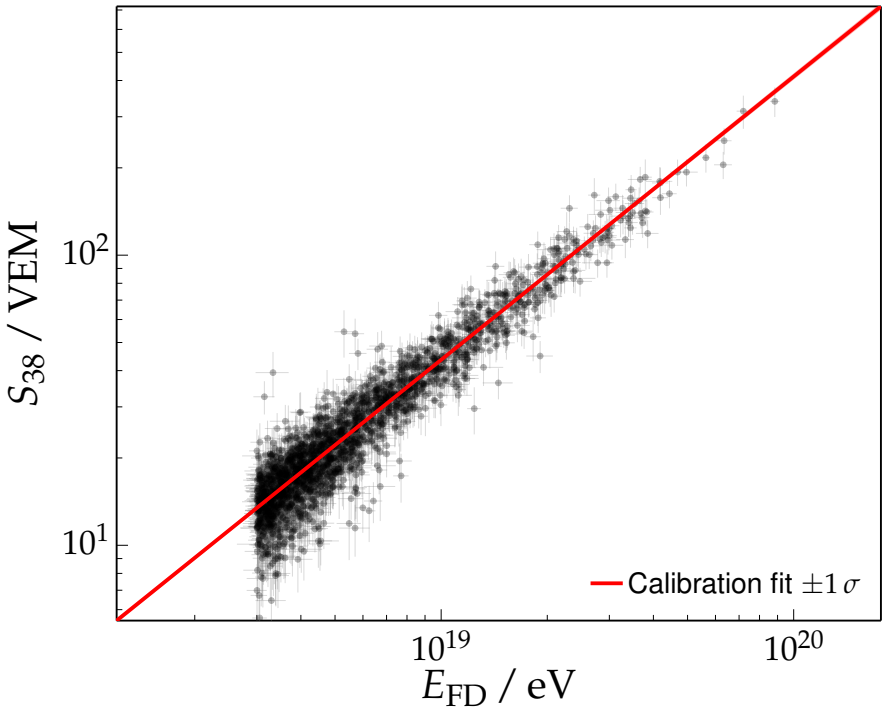

FIG. 2.20 The correlation between the SD energy estimator S_{38} and the energy E_{FD} measured by the fluorescence detector. From [75].

2.4 Selected Results

In this section, results that have motivated and are directly related to the research presented in this thesis are discussed. In the following, a comparison of results of the two currently operating UHECR observatories – the Pierre Auger Observatory and the Telescope Array (TA) – will be drawn, thus a brief introduction to the latter is provided first.

The TA site is located in the high desert of Milard County in Utah, USA. Similarly to the Pierre Auger Observatory, TA also utilizes a hybrid approach, combining the air-fluorescence technique with a surface array. Instead of using water Cherenkov detectors, each surface station is made up of two slabs of plastic scintillator with an area of 3 m^2 and thickness of 1.2 cm [77] (see Fig. 2.21 for a photograph). Over 500 surface stations are evenly spaced at 1.2 km on an area of 762 km^2. A schematic of the layout of the observatory is shown in Fig. 2.21.

The fluorescence detector of the Telescope Array comprises three sites[4] located about ∼30 km apart on the vertices of a triangle, each housing 12–14 telescopes spanning a range of 3–33° in elevation. While the general idea of the fluorescence detection is the same, the telescope optics are different. As can be seen from the photograph in Fig. 2.23, the aperture is without a UV filter and fully open. Photons are reflected on the mirrors and focused onto a camera of 256 PMTs, which itself is covered by a UV filter.

[4] *The individual sites are called Black Rock Mesa (BRM), Long Ridge (LR) and Middle Drum (MD).*

The Pierre Auger Observatory and the Telescope Array function fully independently, together providing full sky coverage, albeit with different exposures. The former overlooks a wide declination range from $-90°$ to $+25°$ (up to $+46°$ if inclined events with zenith angles greater than $60°$ are used), the latter a range from $-6°$ to $+84°$. There is thus a small overlap in the observed declination ranges between the two observatories containing a limited set of events.

A comparison of the energy spectra reported by both observatories is shown in Fig. 2.24. There is a striking difference in flux, which appears particularly pronounced in the flux suppression region. At the time of writing of this thesis, the origin of this discrepancy was not clear: On one hand, it could be an artifact of systematic uncertainties of the energy scales of the two experiments (14 % for the Pierre Auger Observatory and 21 % for TA). On the other hand, it could be an indication of the observation of an anisotropy in the arrival directions of UHECRs due to a local distribution of sources, or of course a combination of both.

The GZK effect, discussed in Subsec. 2.1.2, significantly limits the probable distance of UHECR sources to about 100 Mpc. Assuming a cosmic ray composition with a component of singly or doubly charged particles, a correlation with the underlying baryonic matter and thus anisotropy in arrival directions at the highest energies is expected, and could be responsible for the difference seen in the Auger and TA spectra.

Both, the Pierre Auger Observatory as well as TA report some level of anisotropy at highest energies. While no significant departure from isotropy in the energy range 4–8 EeV is observed in the data of the Auger Observatory [79, 80], for energies above 8 EeV a dipole with an amplitude of 0.073 ± 0.015 is observed [80]. TA reports the presence of a "hotspot" with a 3.4σ significance in the distribution of events with energies above 57 EeV [81]. Such anisotropy is likely to affect the flux of UHECRs in different regions of the sky.

As each of the observatories views only a limited part of the sky, combining their data sets can considerably increase the sensitivity to large-scale anisotropies. This has been done [82], however, at the current stage the combined sensitivity is severely limited by the differing energy scales of the two experiments. Although

Fig. 2.21 A surface scintillator station at the TA site in Milard County, UT. The scintillator is protected by an iron housing, which also supports a solar panel, a battery and electronics box just underneath, and a small mast with a WLAN antenna. Photo courtesy of Ralph Engel.

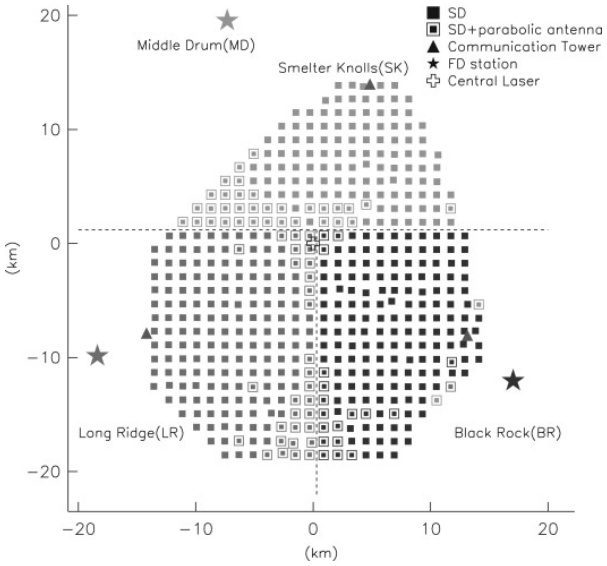

FIG. 2.22 The layout of the Telescope Array. Solid squares denote the 507 deployed scintillator stations. The array is divided into three subarrays, each controlled by one communications tower denoted by a solid triangle. The locations of the three FD sites are marked by stars. From [77].

the energy scales are compatible within systematic uncertainties, a common energy scale must be used for anisotropy searches, else false dipoles will occur. A common scale was determined in [82] by comparing the fluxes in the overlapping declination band of the two observatories, effectively limiting the power of the combined data set to the statistics in this limited overlap region. A direct cross-calibration of both experiments is expected to improve the sensitivity of large-scale anisotropy searches considerably, even if the absolute energy scale should remain uncertain.

Primary cosmic ray composition is of critical importance in the interpretation of the observed flux features and anisotropies. The first two central moments of the X_{max} distribution measured by the Pierre Auger Observatory are shown in Fig. 2.25 for energies of $10^{17.8}$ eV and higher. Comparison with predictions of air shower simulations suggests a predominantly light composition at 2×10^{18} eV that becomes increasingly heavier up to 4×10^{19} eV. The observed correlated

FIG. 2.23 Left: The Black Rock Mesa FD site at the Telescope Array. In contrast to the Auger fluorescence telescopes, here the aperture is fully open and photons impinge directly on the mirrors. Right: A UV filter covers the telescope camera directly. Photos courtesy of Radomír Šmída.

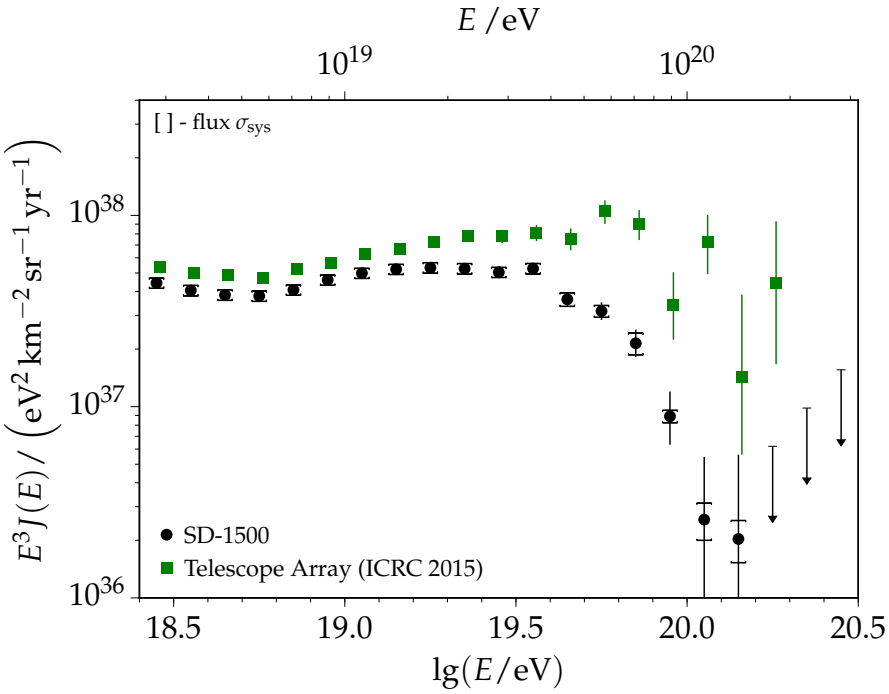

FIG. 2.24 The flux of cosmic rays as a function of energy measured by the Pierre Auger Observatory (standard SD with 1500 m spacing) and TA. From [78].

changes in composition hint at an alternative interpretation of the flux suppression above 5×10^{19} eV. Rather than originating from GZK energy losses, the suppression may result from the sources of UHECR reaching the maximum energy limit to which they can accelerate particles. Not only the composition, but also an accurate determination of the position and shape of the flux suppression are key to distinguishing between the two different model scenarios.

Finally, it shall be mentioned that there has been a long-standing discrepancy between the signal recorded by the surface detectors of the Pierre Auger Observatory and the signal predicted by simulations, shown in Fig. 2.26. The discrepancy is present for any composition assumption – here illustrated for protons and iron nuclei – as well as both tested hadronic models, QGSJET-II and EPOS-LHC, and ranges from approximately 1.25 to 1.5 depending on the zenith angle of the shower, the primary mass and the hadronic model [84].[5] It may be explained in part by a systematic offset in the FD energy scale, in particular to lower values, or the hadronic interaction models not providing a realistic description of the interaction of shower particles in the atmosphere. A combination of both is likely: A significant offset in the FD energy scale was found in this work (Chap. 6), but at the same time the dependence of the observed discrepancy on zenith angle hints at a shortcoming of the simulation of the muonic shower component.

All of the aforementioned points call for an improved understanding and accuracy of the energy scale of the Pierre Auger Observatory, that is the energy scale of the fluorescence detector.

[5] *A similar discrepancy is observed by Telescope Array [84].*

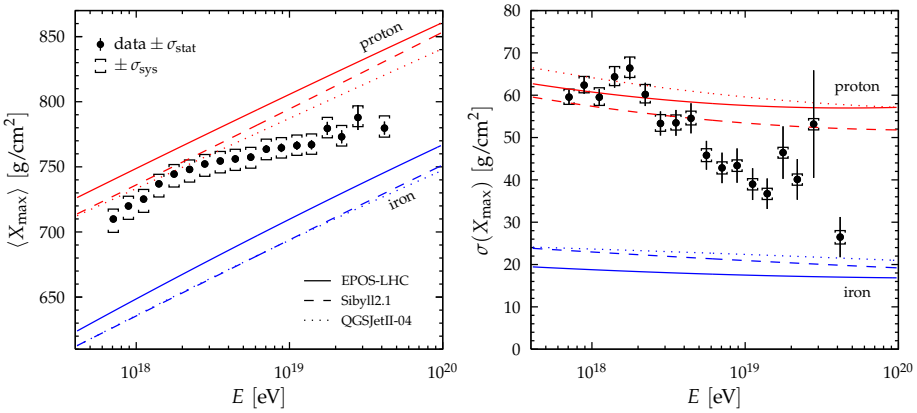

FIG. 2.25 The first two central moments of X_{max} as a function of the logarithm of energy measured by the Pierre Auger Observatory. The lines represent predictions by different hadronic models (solid for EPOS-LHC, dashed for Sibyll2.1 and dotted for QGSJET-II-04) for a pure proton (blue) and iron (red) composition. The measured composition is predominantly light up to $10^{18.3}$ eV and becomes heavier at higher energies. From [83].

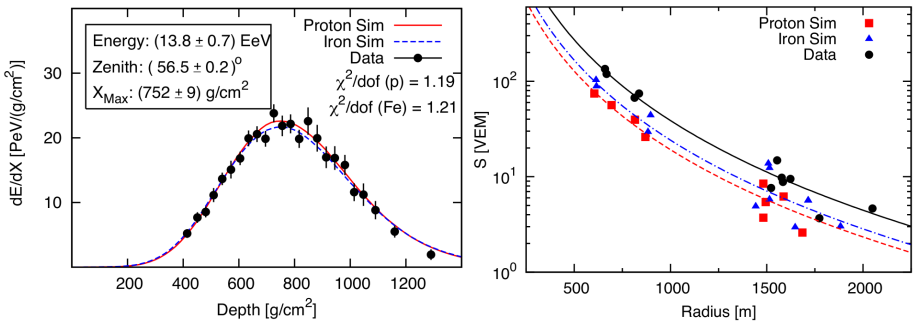

FIG. 2.26 Left: The measured longitudinal profile (black solid points) of an example air shower with matching longitudinal profiles of showers simulated (using QGSJET-II-04) for a proton (red solid) and an iron primary (blue dashed line). Right: The observed (black solid circles and line) and simulated ground signals for the same event (proton: red squares, dashed line, iron: blue triangles, dash-dotted line), shown as a function of the distance from the shower core. The points represent the signal in the individual SD stations and the curves are the resulting lateral distribution function fit. From [85].

3 Fluorescence Detector Calibration and Imaging Properties

Contents

This chapter focuses on the different calibration systems and the imaging properties of the fluorescence detector. The absolute calibration (Subsec. 3.1.1) and the relative calibration type A (Subsec. 3.1.2) are of particular importance, as they will reoccur throughout the course of this work. Also included is a description of the design, implementation and performance of an extended calibration scheme capable of monitoring significant drifts in telescope sensitivity throughout the course of one night – something that was previously not possible within the standard framework. While this is part of the author's contributions, it is part of this overview chapter for continuity reasons. The imaging properties of the telescopes are a common theme connecting all aspects of this work and are introduced in Sec. 3.2. Their role in hybrid event reconstruction is discussed in Sec. 3.3.

3.1 Calibration Systems

The calibration of the fluorescence detector is of utmost importance, as it is used to set the energy scale of the entire surface array. Any systematic uncertainties or offsets in the FD energy scale will not only affect hybrid events, but also events registered only by the surface detector.

The sensitivity of the fluorescence telescopes changes on different time scales. First, there is a seasonal modulation with a period of about one year and a peak-to-peak amplitude of $\sim$10 % [86–88]. Second, there are intra-shift[1] and intra-night variations related to the exposure of the PMTs to the NSB, both of the order of 5 % [86–88, 90, and this work].

[1] *The term shift refers to the monthly dark period of on average 17 nights [54, 89] during which the FD is operated.*

Standardly, one calibration constant is generated for each measurement night. This is achieved by combining two calibration systems: the absolute and the relative one. Since the former, described in detail in Subsec. 3.1.1, is quite labor-intensive and thus performed rather infrequently, the obtained telescope response is propagated through time via a considerably less demanding relative calibration, which is performed nightly and is discussed in Subsec. 3.1.2.

Ideally, the calibration constants would fully reflect the variations in the sensitivity of the telescopes, yet the standard approach of producing one calibration constant per night succeeds only partially. As can be seen from the time progression of calibration constants in Fig. 3.1, it corrects for the seasonal and the mean night-to-night variations, but fails to account for potentially significant changes occurring throughout the course of one night. Therefore, we have developed and implemented an extended relative calibration scheme capable of following those sensitivity changes throughout the night. This extension is presented in Subsec. 3.1.2.

3.1.1 Absolute calibration

The standard FD absolute calibration procedure [91, 92] is widely known under the affectionate alias "drum calibration", so chosen for the resemblance of the large-aperture light source to a giant drum (see Fig. 3.2 for a photograph). As schematically depicted in Fig. 3.3, the drum is mounted onto the aperture from the outside and pulsed at 1 Hz, thus allowing for an end-to-end absolute calibration of the telescope. The resulting drum calibration constant gives the conversion from the electronic signal (in ADC counts) detected by the FD camera to the number of 375 nm-equivalent photons at the aperture.

Fig. 3.4 illustrates the basic construction of the drum. A 365 nm LED [93], thermally stabilized by a Peltier controller, is mounted on the front face of the drum. It illuminates the Tyvek-coated[2] back and side walls, and photons eventually exit through the 0.38 mm-thick Teflon face and strike the MUG-6 filter of the aperture. The absolute calibration of the drum is performed in the dark room at the headquarters of the Observatory in Malargüe and is described in detail in [92]. The uncertainty of the drum intensity is given as 9.0 % in [54], although recent improvements in the calibration procedure indicate that 5 % [92, 94, 95] may be a more realistic estimate. The final distribution of emitted photons is Lambertian and uniform within 4 %.

[2] *Tyvek is a lambertially reflecting plastic.*

The critical point is the following: As the mounted drum is pulsed, *all* PMTs of the FD camera are illuminated simultaneously with a roughly identical photon flux. This simultaneous illumination of the entire camera causes the drum to be insensitive to certain imaging properties of the telescopes. Consider this scenario: Photons striking the aperture at an angle corresponding to the FOV of a given pixel – the target pixel – scatter on optical interfaces out of the FOV of the target pixel. When they arrive at the camera (unless they are scattered off the camera completely), they are simply detected by neighbors of the target pixel.[3] To put it shortly: In drum calibration, photons lost by one pixel are to a large extent detected by neighboring pixels and vice versa. This mechanism is potentially problematic, because it does not necessarily hold in the detection of air showers, where only photons within a limited region of the camera are considered (more on this in Sec. 3.3). This critical distinction between drum calibration and air shower detection will be discussed at relevant places of this work.

[3] *Recall that the opening angle of the FOV of one pixel is 1.5° and therefore also the viewing directions of two neighboring PMTs are separated by 1.5°.*

One may, and ought to, ask the following question: What happens when

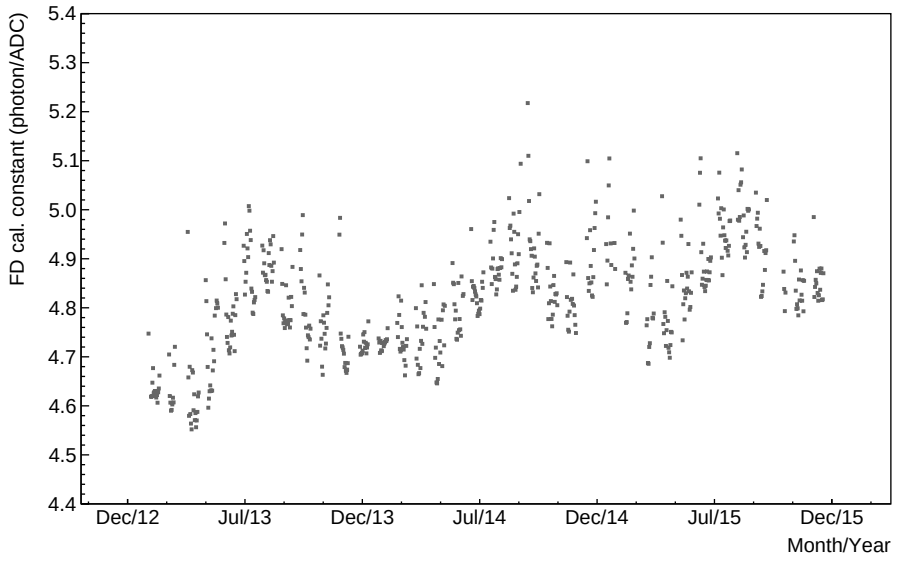

(A) From January 2013 to December 2015.

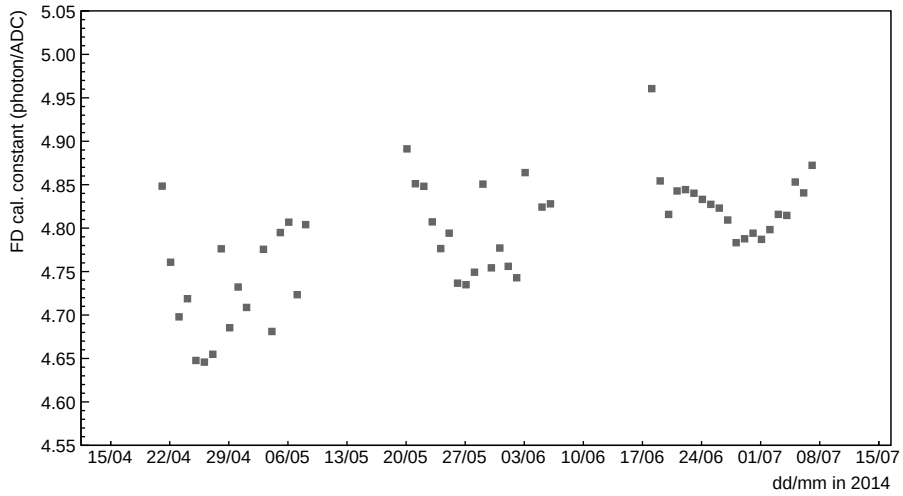

(B) During three shift periods in mid 2014.

FIG. 3.1 The time progression of standard absolute FD calibration constants (one value per measurement night). Shown is the all-camera mean for LL3.

FIG. 3.2 The large-aperture light source used to absolutely calibrate the Auger fluorescence telescopes end-to-end is, for obvious reasons, referred to as the drum. Photo courtesy of Julia Bäuml.

photons emitted by the drum are reflected on the aperture? Sure enough, such photons are lost during air shower measurements to the outside environment, but not so for the drum. Let N_{drum} be the number of photons emitted by the drum within one pulse as measured in the dark room. Given the reflectivity R_{MUG} of MUG-6 glass of 8.5 % (assuming normal incidence and no additional surface defects such as a dust layer on the filter), the fraction of photons returned to the drum will be $R_{\text{MUG}} N_{\text{drum}}$. Depending on the efficiency ϵ_{drum} of the drum, meaning the transmissivity of its front face and the reflectivity of the interior, a portion of those photons

$$N_{\text{reinjected}} = \epsilon_{\text{drum}} R_{\text{MUG}} N_{\text{drum}} \tag{3.1}$$

will be re-injected into the telescope.

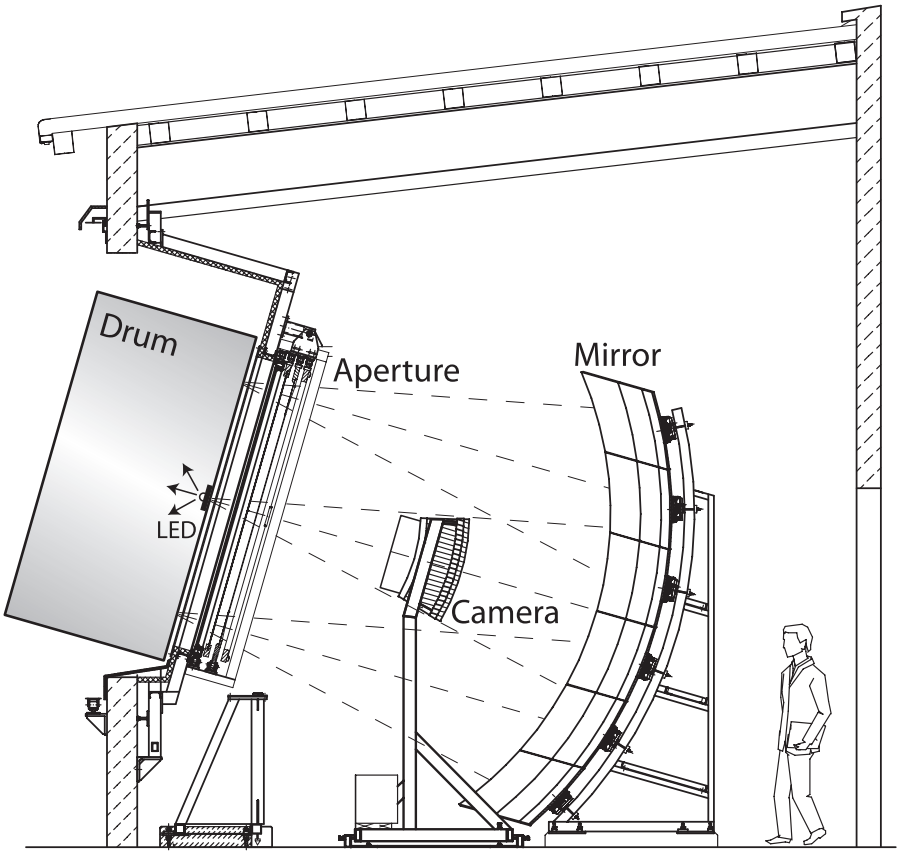

FIG. 3.3 A schematic depiction of the drum mounted in the aperture. From [55].

Since the value of ϵ_{drum} is difficult to compute, $N_{\text{reinjected}}$ was measured as follows [96]: An independent monitoring PMT was placed inside the drum, facing towards the back. The drum was first pulsed in the dark room and next when mounted in the aperture. The signal measured by the PMT was 4 % higher when mounted in the aperture, thus $N_{\text{reinjected}} = 0.04 N_{\text{drum}}$ [97]. However, the value of $N_{\text{reinjected}}$ was quantitatively determined only once [96] and, given that the filter condition changes over time and is not tracked by any calibration system, it may have limited validity. Furthermore, an additional reflections-related factor is applied, but is discussed in connection with the imaging properties in Sec. 3.2.

Besides absolute calibration, the drum can also be used for relative multi-wavelength measurements of the end-to-end spectral efficiency. The original LED is replaced by an optical fiber connecting to a Xenon lamp positioned at the back of the drum. Using notch filters [98] or more recently a monochromator [99] different wavelengths spanning the spectral range of the telescopes are supplied. Fig. 3.5 shows the default spectral efficiency curve used for FD data reconstruction as of April 2016, as well as the most recent measurement for Los Leones.

The end-to-end spectral efficiency of the telescopes is not only needed for air shower reconstruction, but also to correct for the finite spectral width of the drum LED and specify the absolute calibration constant as a 375 nm-equivalent.

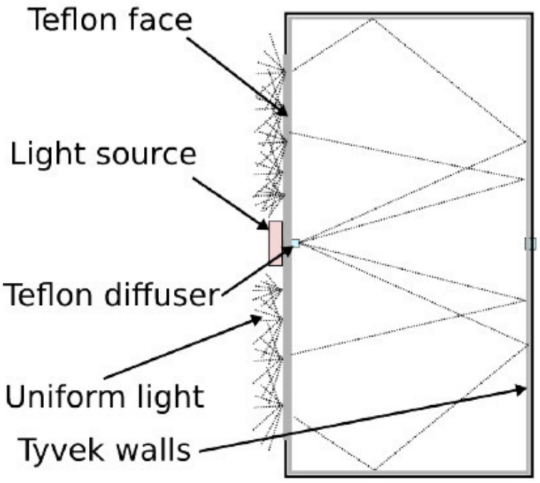

FIG. 3.4 The basic construction of the drum: The LED mounted on the front of the drum illuminates the Tyvek-coated interior. Photons exit through the diffusive Teflon face with a Lambertian distribution. From [95].

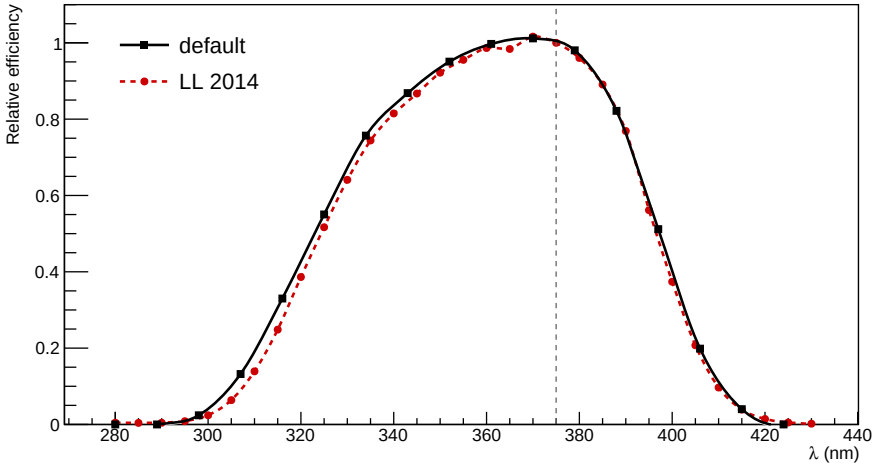

FIG. 3.5 The end-to-end FD spectral efficiency, shown relative to the reference value at 375 nm indicated by the gray dashed line. The default curve for all telescopes [98] (black solid) and the most recent measurement for Los Leones [99] (red dashed line) are shown.

Before 2010, the drum was equipped with a 375 nm LED and this wavelength has become the reference wavelength at which the spectral efficiency curve is scaled to unity. In 2010, as lower-wavelength LEDs of sufficient power became increasingly more available, the drum LED was replaced with one of wavelength 365 nm [94], yet the reference wavelength remained unchanged.

While drum calibration is the standard absolute calibration procedure of the Auger fluorescence telescopes, other options exist, each with their own pros and cons. External light sources such as absolutely calibrated laser beams may be used [100], provided that atmospheric attenuation and scattering are properly accounted for. A unique and novel method – and a topic of the last two chapters of this work – uses a remotely controlled drone to lift a light source into the FOV of a telescope. In the following, this method is referred to as the “Octocopter”.

3.1.2 Relative calibration

A rather time- and manpower-consuming process, drum calibrations are performed rather infrequently. The most recent campaign took place in 2013 [101], and before that in 2010 [94] and 2005. A relative calibration procedure called calibration A (further on CalA for short) is used to propagate the drum calibration constants through time. This approach works very well, as was demonstrated by comparing the calibration constants propagated from 2010 to the freshly measured ones in 2013: the average difference for all telescopes was only 0.8 % [101]. There are two other relative calibration systems, called calibration B and calibration C (further on simply CalB and CalC), which will be discussed briefly in the second part of this section (from page 44 onward). In the first part, however, we shall focus on CalA, for it is the only one of the three currently standardly used for data reconstruction.

Calibration A

The CalA system is used to monitor changes in PMT sensitivity, i.e. changes in PMT gain, on each measurement night.[4] Light pulses are fired from the center of the mirror directly onto the FD camera and, as can be seen from Fig. 3.6, no other optical components are in the direct path of the CalA photons. The light source itself, a 370 nm LED located in the calibration room (c.f. Fig. 2.13), is coupled to seven optical fibers, six of which transport light to the individual telescopes and one to a monitoring photodiode (UV100 by UDT Sensors), referred to as the LED Control Unit (LCU) [102]. Each baseline FD building is thus equipped with one LED–LCU pair. Unlike the other FD sites, HEAT is equipped with three LED–LCU pairs, one for each telescope.

[4] *The terms PMT sensitivity and gain are synonymous in the context of this work and will be used as such. Note that the calibration constant in photons per ADC count is inversely related to the sensitivity.*

Standard CalA runs are performed with shutters closed at the beginning and end of each measurement night. Fifty pulses are fired at a rate of $1/3$ Hz ($1/2$ Hz at HEAT), a full-camera read-out is triggered externally and the response of each PMT is recorded and analyzed. Due to its design, CalA is performed in all telescopes of one FD building simultaneously, but the time interval with respect to the opening/closing of shutters, and hence exposure of the PMTs to the NSB, is not fixed: it may differ from night to night and even from telescope to telescope within one building and one night, as some telescopes will stop running sooner e.g. due to having the Moon in their FOV.

The absolute telescope calibration is propagated in time by relating the CalA response on a given night to the reference run performed immediately after drum calibration, which is no different from any other run, except for the fact that 400 pulses are fired to achieve superior precision. The final absolute calibration constant C_{abs} for a given pixel on a given night combines the drum calibration constant C_{drum}, the CalA reference run response Q_{ref} and the nightly run response Q_{night} [104]:

$$C_{\text{abs}} = \frac{Q_{\text{ref}}}{Q_{\text{night}}} \cdot C_{\text{drum}}. \tag{3.2}$$

The advantage of this approach is that the CalA LED does not need to be absolutely

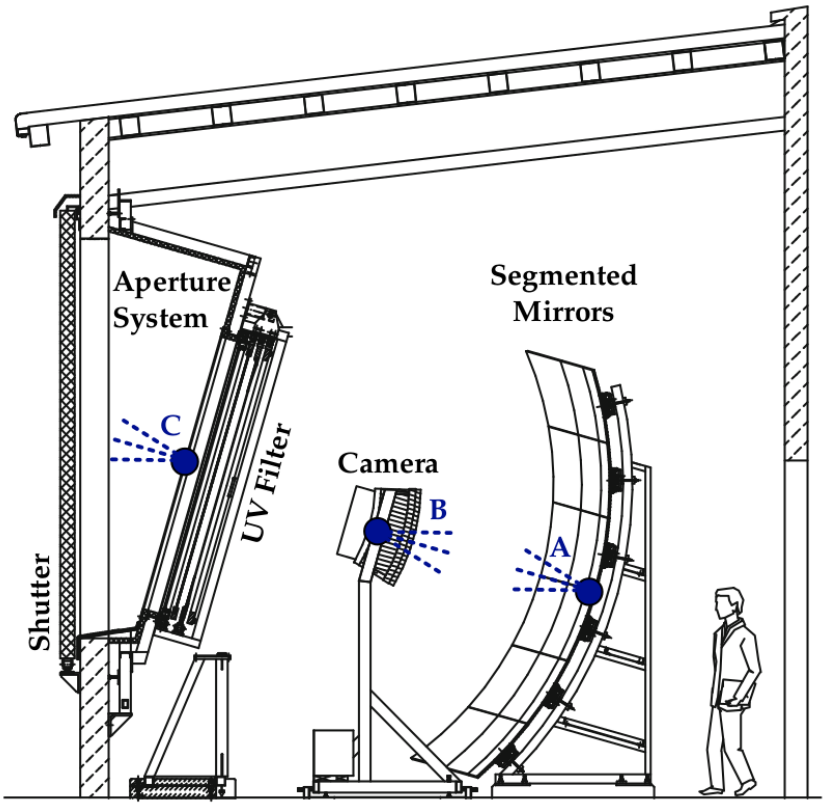

Fig. 3.6 The photon injection points of CalA, CalB and CalC, marked by blue circles, in the telescope bay. The emission direction of photons is indicated by blue dashed lines. In particular, photons in CalC are emitted towards the shutter, where they reflect on Tyvek patches. From [103], originally from [55].

calibrated; relative knowledge of the photon output measured by the LCU and subsequent comparison to previous runs are sufficient. Reproducibility, however, is of prime importance. For example, the camera is not evenly lit in CalA, partially due to the radiation pattern of the diffuser-capped optical fiber, and partially due to the curvature of the camera. This in itself is not a problem, as long as the setup is fixed and the illumination pattern remains constant.

Interestingly, the response of the camera to CalA pulses has been found to be different in the evening and the morning runs. In particular, the morning response is on average 2 % higher [86, 88, 105]. Based on the presumption that the PMT response to the morning run is more indicative of the behavior throughout the night than the response to the evening run, the morning calibration run is used preferentially for reconstruction. If not available, the evening run is used; if not available, the most recent available CalA constant is used.

The standard CalA procedure suffers from a weakness: It fails to account for PMT gain changes occurring over the course of each night. Those gain changes, resulting from exposure of the PMTs to the NSB, have been studied under laboratory conditions [106] as well as on-site by taking additional CalA runs throughout

the night [86, 90, 107–109] and were found to reach up to 6 % relative to the evening standard CalA constant. Neglecting such significant effects will surely worsen the energy resolution, and may even introduce an overall bias or a seasonal modulation of the FD energy scale [105, 110], as the magnitude of the drift positively correlates with the length of the measurement night and is thus larger during winter nights.

While the behavior of individual PMTs may be quite variable, the average sensitivity of the camera tends to increase throughout the night, reaching a maximum just before the measurement period ends and shutters are closed [107]. Recall that the standard CalA run is taken with shutters closed, whereat the delay between the shutter closing and the calibration run is not fixed but depends on the conditions of the particular night, such as the level of the NSB (in particular the presence of the Moon in the FOV), weather conditions and cloud cover or potential hard- and software malfunction. The calibration constant – the inverse of the detector response – will thus decrease throughout the night, leading to a systematic underestimation of the light flux at the aperture when only the morning CalA constant is used. The problem cannot be easily remedied by using the evening run as well, because the telescope response depends on many circumstances, including the time interval between the calibration run and opening or closing the shutters, the individual characteristic of a given pixel and its NSB exposure history throughout the night (and even the entire FD shift).

In early 2013, as part of this thesis project, we began work on an extended CalA scheme that would account for the nightly gain drifts – a continuous CalA, so to speak. The aim is the acquisition of short CalA runs at fixed intervals throughout the night, however, in stark contrast to the standard procedure, with shutters open and real-time NSB exposure. The development, implementation and testing of this extension is described on the following pages.

Continuous calibration A

The key features of continuous CalA are:

- Periodic monitoring of PMT response throughout the measurement night,
- performed with shutters open and with real-time NSB exposure,
- without interrupting the DAQ mode, thus with minimum interference to the operation of the FD.

Before the advent of continuous CalA, nightly gain drifts had been studied by performing additional standard CalA runs at different times of the night [86, 90]. The major downside of this approach is the long execution time caused by having to complete the following steps:

- closing the shutters ($\sim$45 s),
- terminating DAQ and subsequently initializing calibration mode (20–30 s),
- performing the actual calibration run (180 s for 50 pulses),

- terminating calibration and initializing DAQ mode (20–30 s), and
- opening the shutters (∼45 s).

This multi-step procedure originates from the fact that the DAQ mode, in which air shower detection happens, and the calibration mode, reserved for performing relative calibration runs with shutters closed, are completely disjoint. The loss of data acquisition time resulting from the overhead associated with closing/opening shutters and switching modes is entirely unacceptable (save for isolated studies) and the approach was quickly ruled out. The obvious idea of running CalA in DAQ mode with shutters open flew in the face of just about all FD operational procedures, but for its sheer attractiveness deserved a second look.

The execution time of a continuous CalA run in DAQ mode with open shutters is simply the length of the ADC trace multiplied by the number of pulses per run. Between pulses data taking proceeds uninterrupted and showers continue to be detected. Not so in calibration mode, even with shutters still open, where this time is lost and the total amount of deadtime will depend on the pulsing rate. Assuming a rate of 0.3 Hz and a run of 10 pulses, the total deadtime will be 30 s. In the most pessimistic case of switching to calibration mode as well as closing the shutters, the execution time per run will be about two minutes, largely driven by the time it takes to open or close the shutters (45 s each way). A summary of the discussed execution times is given in Tab. 3.1. Furthermore, it was later realized that following the closing of shutters, the PMTs undergo short-term (of the order of tens of seconds) transient gain changes, thus performing a calibration with open shutters during full NSB exposure is key for a realistic capture of the PMT responsivity.

The number of pulses per run is a compromise between run time, data volume and precision. We chose to prioritize precision, requiring 1 % or better. As can be seen from the spread of responses plotted in Fig. 3.7, the standard deviation of the response to one pulse is about 0.6 % and in principle one pulse is enough to meet the precision requirement. At last, 10 pulses were chosen for redundancy. However, should the need arise, e.g. due to data volume issues, the number of pulses per run can still be reduced.

Eventually, and requiring quite some effort, the continuous CalA scheme was fully implemented within DAQ mode. More information as well as technical

Tab. 3.1 Approximate execution times associated with performing continuous CalA for three different configurations: calibration mode with open or closed shutters, and DAQ mode with open shutters. A run is assumed to consist of 10 pulses, delivered at a rate of 0.3 Hz. In the last row, a long winter night of 10 hours fitting 20 runs spaced 30 minutes apart is assumed.

Mode	DAQ	Calibration	
Shutter status	open	open	closed
Per bunch	$10 \times 100\,\mu\text{s} = 1\,\text{ms}$	$10 \times 3\,\text{s} = 30\,\text{s}$	$30\,\text{s} + 90\,\text{s} = 120\,\text{s}$
Per night	20 ms	10 min	40 min

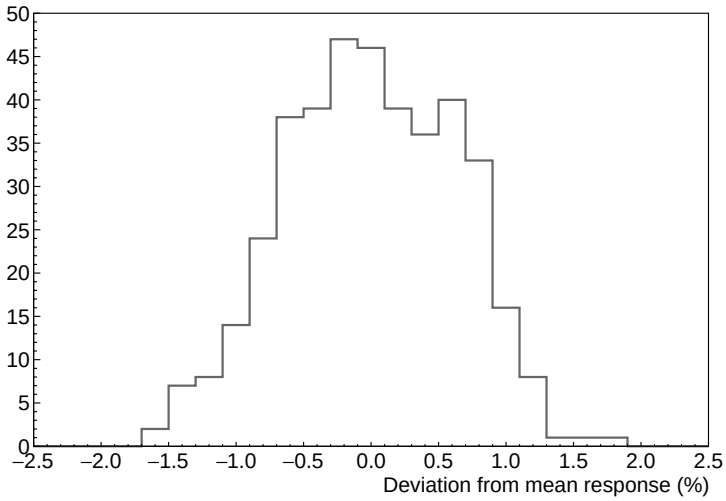

FIG. 3.7 The distribution of responses to individual CalA pulses relative to the mean has an RMS of 0.6 %. A 400-pulse reference CalA run was used here.

details of the implementation are available in [111]. Runs of 10 pulses (as opposed to the standard 50 pulses) are performed every 30 minutes starting 300 s after shutters were opened and for each pulse a full-camera read-out is triggered by the GPS clock of the respective FD building.[5] Standard evening and morning CalA runs are performed as previously.

The pulse-to-pulse interval of 7 s, at first sight a somewhat odd pick, was carefully chosen to minimize the collision probability with NSB monitoring data. The so called "BG loop" (where BG stands for background) reads and saves one ADC trace of NSB every 30 s. The data are used in real time to assess whether the current background levels are safe to continue data taking; if not, an automatic shutter closure is forced. Offline, direct studies of the NSB aim to track stars moving across the FOV of the telescopes and have been used to cross-check the pointing [112, 113] as well as the calibration of the FD [114, 115]. In addition, the data are used to indirectly study cloud coverage (clouds scatter light, thus increasing the NSB), shutter status (the background drops sharply when shutters are closed) and for MC shower simulations with realistic NSB conditions. In the unlikely event of a CalA pulse falling within the BG loop trace, the maximum safety limits may be exceeded and an automatic shutter closure could occur. To prevent this behavior and subsequent loss of data taking time, special pattern recognition scripts were implemented [111]. They exploit the fact that the distribution of the signal on the camera is different for a CalA light pulse and the typical night sky, and shutter closure commands following CalA-resemblant patterns in the BG loop are automatically vetoed.

Initial proof-of-principle tests of the continuous CalA scheme took place in February 2013. A close-to-final implementation was completed in mid 2014, followed by extensive testing. Since November 2014, a full final implementation

[5] *In this sense, "continuous CalA " is a misnomer, since the runs obviously occur at discrete intervals throughout the night. Nevertheless, the name was chosen to emphasize the considerably higher frequency of acquisition than in the standard CalA scheme.*

has been running in all telescopes including HEAT.

The camera-averaged continuous CalA response of LA3 during the FD shift in August/September 2014 is shown in Fig. 3.8 (top). The maximum gain drift of 7 % occurs during the first night of the shift. This behavior is typical for PMTs after a prolonged period of no exposure, in this case about 14 days between two adjacent shifts. The smallest observed variations within one night are about 1 %. Another example, this time for CO1, is shown in the bottom panel of Fig. 3.8. Here, the $\sim$2 % systematic shift between the morning and evening CalA runs becomes apparent. The drift during the first night is a typical 3 % and a quite extraordinary 7 % during the second-to-last night. Clearly, the variations and drifts in PMT sensitivity are complex in nature and depend on many external factors. Therefore, only a direct measurement such as continuous CalA is able to properly correct for these effects.

Calibrations B and C

Relative CalB and CalC [59, 116] each use a xenon lamp [117] to study the linearity and spectral efficiency of the telescopes. The setup of both systems, schematically depicted in Fig. 3.9, is to a large degree identical: First, the light pulses are split by a pick-off mirror between an intensity monitoring device [118] and a filter wheel equipped with five calibration-specific filters. Past the filter wheel, the light beam is focused onto a bundle of seven optical fibers. Just like in CalA, six of the fibers distribute the light pulses to the individual bays and one terminates at an intensity monitor, which is shared by the two calibration systems. The CalB setup additionally incorporates a UG-1 filter to produce a similar spectrum as the MUG-6 filter.

The CalB and CalC systems differ in the type of filters they use and in the positioning of the termination points of the fibers inside the telescope bays, as can be seen in Fig. 3.6. Each CalB fiber is yet again split in two and the diffuser-capped ends are affixed to either side of the FD camera, pointing at the center of the mirror. This geometry is very particular: Light rays emitted from the focal surface are reflected parallel to the optical axis, hence only photons reflecting on the central $\sim$1 m^2 of the mirror strike the camera, considerably limiting the suitability of CalB for the study of the condition of the mirror.

The CalB filter wheel holds five neutral density filters providing a dynamic range of 100. While the system is not standardly used for data reconstruction, it proved incredibly useful for studying the linearity of the telescope response at standard and reduced high voltage (HV). The Auger Upgrade [64] namely foresees a 50 % increase in the current FD uptime, i.e. from 15 % to 21 %, to considerably expand the hybrid data set. Currently, suitable times for the operation of the FD require that the Sun be at least 18° below the horizon, the illuminated Moon fraction less than 70 %, and that the Moon be at least three hours below the horizon on any given night meeting the two aforementioned criteria [54, 89].

Extending the duty cycle requires relaxing those criteria and measuring during higher NSB levels, leading to increased anode currents and consequently larger

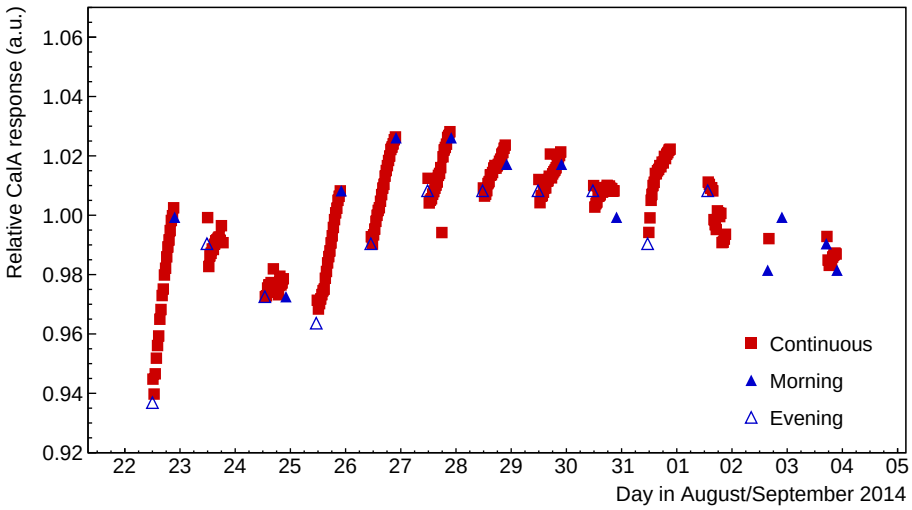

(A) LA3

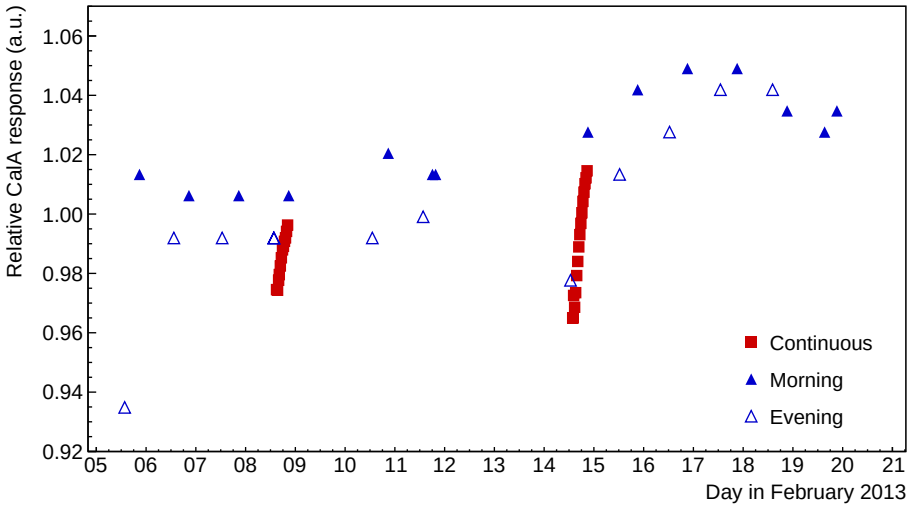

(B) CO1

FIG. 3.8 The camera-averaged response to CalA pulses over a period of one FD shift. Shown are the standard CalA runs taken in the evening (open blue triangles) and morning (solid blue triangles), as well as the continuous CalA runs (solid red squares). The response on the y-axis is shown relative to the mean of all responses to allow the reader to estimate the magnitude of the drifts and fluctuations.

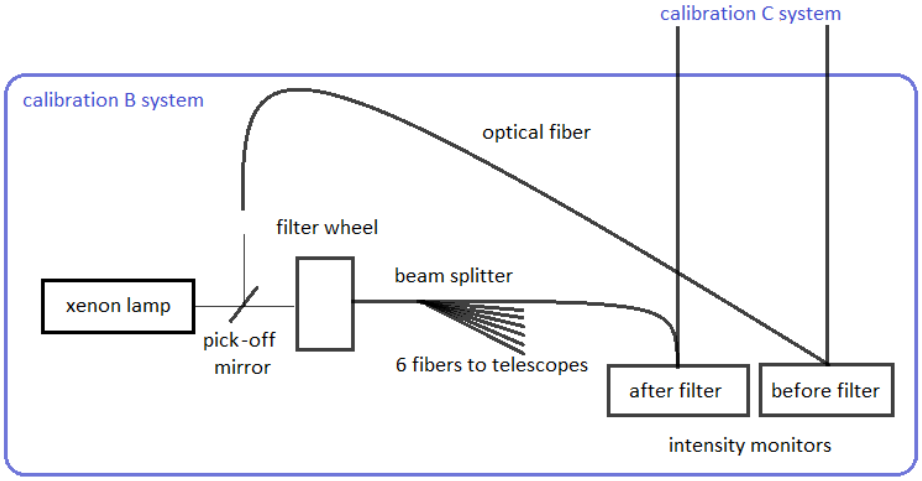

FIG. 3.9 The schematic layout of the CalB system. While the CalB and CalC systems are separate and use different filters, the flow is identical and they share the same intensity monitors.

cumulative charge, which are associated with PMT aging and decrease of performance [119]. While the NSB level is given, the anode currents can be kept at a safe level by operating the FD at a reduced HV; this is precisely the idea behind the FD uptime extension. Many studies and test measurements are necessary before the FD can be operated in the extended mode [107], including studies of the linearity of response, which can be conveniently probed with the otherwise obsolete CalB system.

Within the calibration studies performed in the scope of this work, the telescope response to CalB was analyzed at nominal and reduced HV. In particular, sequences of back-to-back CalB runs were acquired, one run at the nominal, the successive at a reduced HV setting, and the responses recorded at different CalB intensities were compared. The response of the FD was found to be equally linear at both HV settings, with an example of a typical response-intensity curve shown in Fig. 3.10.

The injection points of CalC are located further upstream than those of CalB. Two glass-capped optical fibers terminate on either side of the shutter box and point at two 61 cm $\times$ 61 cm Tyvek sheets attached to the inside of the shutters (c.f. Fig. 3.6). Photons are first diffusely reflected off the Tyvek patches before passing through the MUG-6 filter. The geometry of CalC is such that only parts of the aperture are probed; in particular, the corrector ring is not part of the typical path of the light rays [59]. The CalC filter wheel is equipped with five spectral interference filters, the wavelengths of which span the FD spectral acceptance range as well as the nitrogen fluorescence spectrum (330 nm, 350 nm, 370 nm, 390 nm and 410 nm). CalC can thus be used to monitor the combined changes in spectral sensitivity of all components downstream from the filter, with the exception of the corrector ring.

While CalA is performed in the evening and in the morning of each measurement night, and since November 2014 also during data taking, CalB and CalC

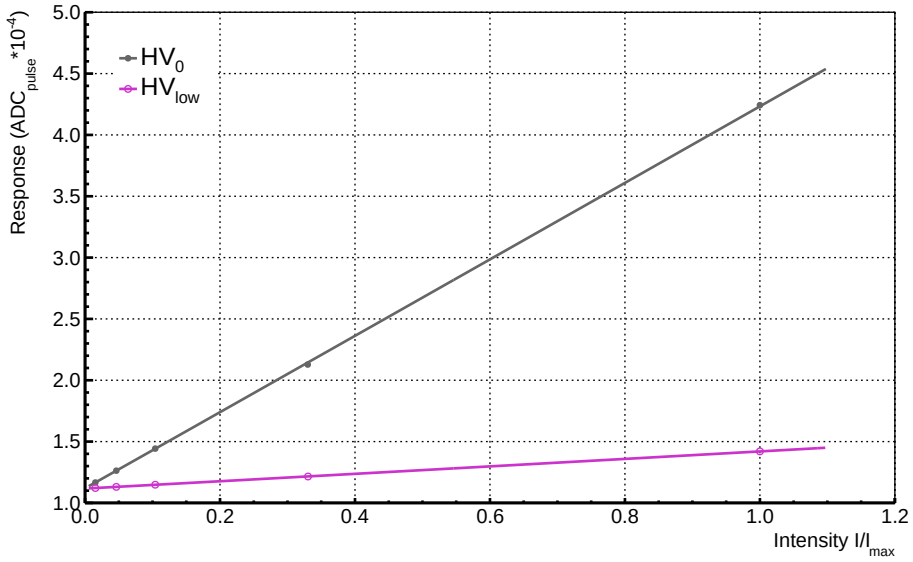

FIG. 3.10 Response to CalB light pulses (in ADC counts per pulse, scaled by a factor of 10^{-4}) as a function of relative CalB light pulse intensity for two HV settings: nominal (HV_0) and reduced (HV_{low}).

are only run in the mornings. The procedure is identical for both: a total of 150 light pulses, 30 per filter.

3.2 Point Spread Function

The imaging properties of an optical detector can be described by its response to a point source – the PSF. The Auger telescopes are complex instruments and their PSF is a convolution of the contributions from the individual optical components. Some contributions are purely geometrical, such as spherical aberration, albeit greatly reduced by the corrector ring, resulting from the use of a spherical mirror. In fact, the minimum spot size of a point source imaged on the camera is about 0.5° due to spherical aberration only [120]. Other contributions to the PSF may come from potential misalignment or imperfections of the shape or surface of the optical components, including deposited aerosols. Those are difficult to describe theoretically and must be measured experimentally.

The optical halo of the fluorescence telescopes – a term used to describe the apparent widening of the final image – had been an open problem since the initial measurements performed in 2005, when a tethered balloon was used to lift a light source into the FOV of the telescopes [121]. Unexpectedly, the observed PSF was much broader than what simulations had predicted, and the findings were repeatedly confirmed by follow-up measurements [122, and this work].

There are different approaches to measuring the PSF of a fluorescence telescope. In this work, a remotely controlled drone, which we refer to as the Octocopter,

[6] The details of this measurement are presented in Chap. 5 and Chap. 6.

was used to lift a light source into the FOV of the telescope.[6] Alternatively, the images of laser beams fired from the CLF or the XLF can be studied, however, this approach is complicated by the contribution from multiple scattering in the atmosphere, which may be minimized by using roving lasers at close distances to the telescopes [123].

Being a spherical focal surface, distances on the camera are best described in terms of angles in a spherical coordinate system. The origin of the system is fixed at the center of curvature (CC) of the telescope, i.e. in the center of the plane of the corrector ring, and the polar angle relative to the axis connecting the CC to the centroid of the image on the camera is denoted by ζ. The azimuthal angle in this coordinate system would describe the variation of the signal for a particular value of ζ, but is rarely used explicitly, as radial symmetry of the image on the camera is often present or assumed.

Fig. 3.11 shows the image of a point source in the FOV of an Auger telescope as measured with the Octocopter method. In spite of the 1.5° opening angle of the FOV of a single pixel, the image is considerably spread out, moreover, a satellite image appears center-symmetrically to the main image and shall be discussed in a few paragraphs.

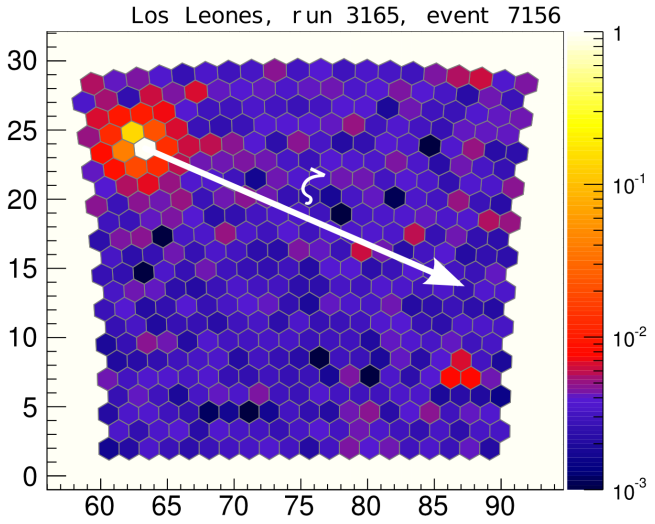

Fig. 3.11 The image of a point source (the Octocopter) on the FD camera. The color scale is proportional to the logarithm of the signal detected by each pixel and the distance of a particular pixel from the center of the main image is given in terms of the angle ζ (indicated by the arrow) on the spherical focal surface. Note the satellite image in the lower right corner.

For our purposes, the PSF is conveniently expressed in terms of the amount of light detected per solid angle $\mathrm{d}N/\mathrm{d}\Omega(\zeta)$ at a particular distance ζ from the center of the image, defined by the superposition of signal-weighted viewing directions of individual pixels in the region of interest, i.e. the center of gravity (CG).[7] There are various approaches to computing the CG, differing in the size of the region of interest and use of additional weighting factors. Those are discussed in detail in the relevant analysis sections in Chap. 6.

[7] The terms CG and centroid of an image are used interchangeably.

Three examples of the PSF are shown in Fig. 3.12. For now, let us focus only on these two: the experimentally measured and the basic ray-tracing PSF. The former is considerably wider with a flat tail extending to large angles, while the latter is very steep and fluctuates about zero from 2° out. For many years, the

difference between the measured and simulated PSF remained a riddle. The ray-tracing code used for this simulation is the module TelescopeSimulatorKG [124][8] of Offline [125–127], the official C++ based analysis and simulation framework of the Pierre Auger Observatory. The TelescopeSimulatorKG module is, in fact, the default telescope simulation code used by the Pierre Auger Collaboration. Implemented are refraction on the filter, the corrector ring and the camera surface, as well as specular reflection on the mirror. No multiple reflections between individual optical elements are allowed and ideal shapes and surfaces are assumed.

[8] *The suffix KG is short for the "Karlsruhe group."*

The dominant mechanism shaping the tail of the PSF was identified in 2010, when dedicated laboratory measurements revealed that reflections on the PMT faces are about 20 % [128], i.e. four times higher than what had been assumed based on the refractive index $n = 1.52$ at 380 nm of the entrance window made of lime glass. However, as can be seen from Fig. 3.14 (left), other structures, most notably the photocathode, contribute to the reflectivity of the PMT surface. The combined reflectivity of the PMT face was measured in the relevant wavelength range and found to increase from 7.5 % at 250 nm to a maximum of 24.5 % at 400 nm for a light beam incident at 45° [128]. An example of the measurement is depicted in Fig. 3.14 (right).

The mechanism responsible for the formation of the flat tail of the measured PSF works as follows: Photons that reflect on the camera travel back to the mirror, where they are reflected yet again, striking the camera in a broad beam. Some of those photons pass the camera and reflect on the aperture, forming the center-symmetric satellite image appearing in Fig. 3.11, often referred to as the "ghost". Of course, since in the TelescopeSimulatorKG module photons that are reflected on the PMT faces are terminated and no multiple reflections occur between the camera and the mirror, the characteristic tail of the measured PSF is not formed.

Multiple reflections were enabled and enhanced PMT reflections implemented in the development version of the code, the TelescopeSimulatorKG_DEV. The improvement in the agreement of the measured and simulated PSF is shown in Fig. 3.12 and may be better appreciated in the cumulative plot in Fig. 3.13. The remaining discrepancy below 15° resisted explanation for another three years. Clearly, dedicated measurements were required to identify the main mechanisms at play and have become the topic of Chap. 4.

Looking at the differential PSF plotted in Fig. 3.12, one can immediately see that the tails of the distributions do not match perfectly even when multiple reflections are enabled. However, the corresponding cumulative plot (Fig. 3.13) clearly shows that beyond 15° the mismatch is less than 1 %. The current implementation of the reflections on PMT faces in the TelescopeSimulatorKG_DEV modules relies on the Fresnel equations and the fraction of reflected photons is defined by an effective wavelength-independent index of refraction $n_{\text{eff}} = 2.58$. While this approach describes the reflections on the lime glass window well, it is inappropriate for the description of the reflections on the photocathode, the thickness of which is smaller than the wavelength of the incident fluorescence light.

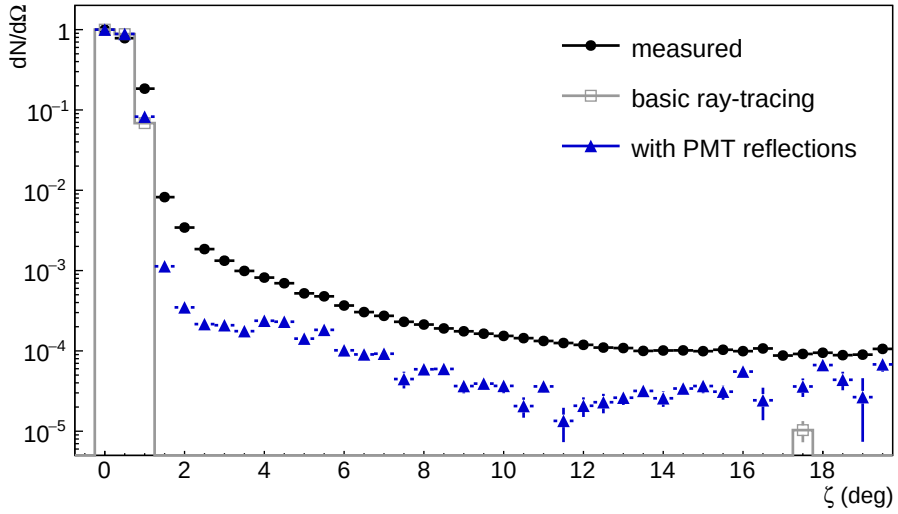

FIG. 3.12 The PSF as measured with the Octocopter in this work (black solid circles) and simulated using basic ray-tracing (gray open squares). Note that the lone point at 17.5° is a mere fluctuation of the signal and not a contribution from the satellite image, which arises due to multiple reflections in the telescope that are not permitted in the basic ray-tracing. The agreement between the measured (black solid circles) and simulated PSF (blue solid triangles) improved considerably after reflections on the camera were implemented.

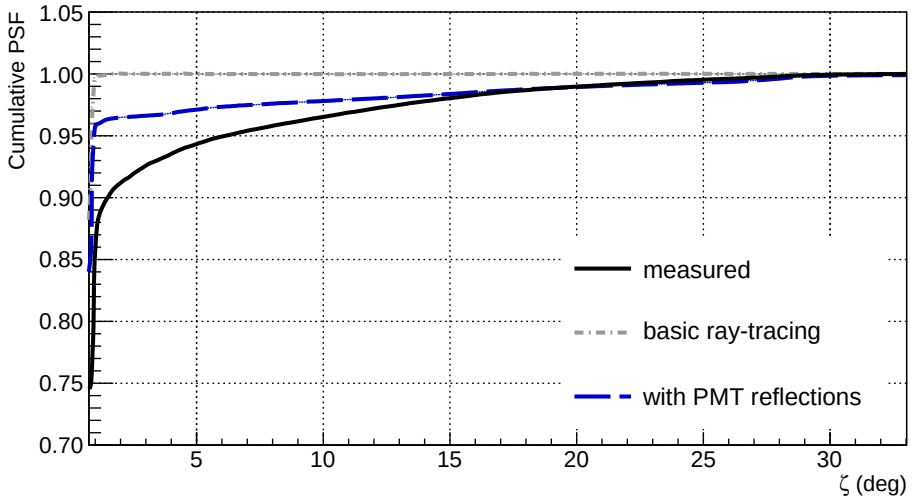

FIG. 3.13 The cumulative PSF as measured with the Octocopter in this work (black solid line), simulated using basic ray-tracing (gray dash-dotted) and simulated with increased reflections on the PMTs (blue dashed line). All curves are scaled to 1.0 at 33°.

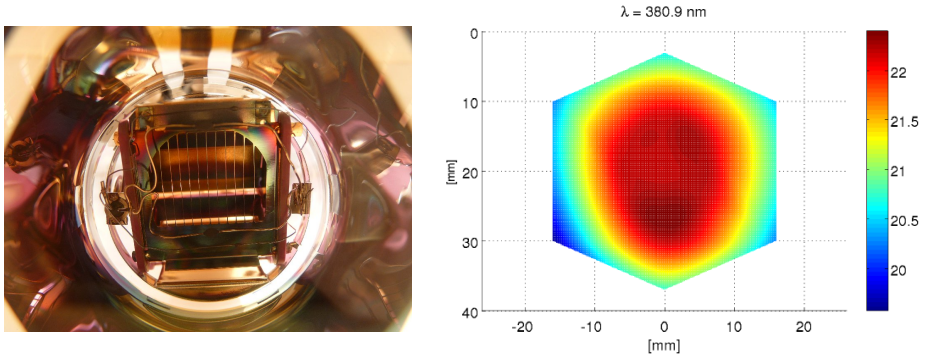

FIG. 3.14 Left: A view through the entrance window of an FD PMT. The parallel wires in the center are part of the focusing electrode. The photocathode itself is directly adjacent to the entrance window, but being only about 90 nm thick, it is semi-transparent. Photo courtesy of Radomír Šmída. Right: A reflectivity map of the PMT surface measured at 381 nm and an incident angle of 45°. The reflectivity, indicated by the color scale in %, is both position- and wavelength-dependent. From [128].

In this situation, a thin-film approximation is more appropriate (see e.g. [129]). Nevertheless, given the level of complexity of the internal reflective structures of the PMT shown in Fig. 3.14 (left), the most realistic description would be achieved by implementing wavelength-dependent look-up tables based on the reflectivity maps such as the example shown in Fig. 3.14 (right).

It was soon realized that the flat tail of the PSF will bias the drum calibration constants towards lower values (of photons per ADC count), because a fraction of photons contributing to the signal of a given PMT will have come from the reflections on other PMTs, possibly located in quite distant parts of the camera. This does not happen during air shower detection, where only a narrow track of pixels is lit. A correction was designed to account for this effect [97], resulting in an increase of calibration constants, and by extension reconstructed energies, of 3.5 %. The value of the correcting factor for a particular pixel depends on its viewing angle and ranges from 2.6 % to 4.0 % across the camera.

3.3 Shower Image and Light Collection

For a given geometry, the deposited calorimetric energy of an air shower per slant depth $\mathrm{d}E/\mathrm{d}X$ is proportional to the light flux at the aperture, which is in turn proportional to the signal recorded by the PMTs. At any instance in time, the image of an air shower on the camera (Fig. 3.15) is that of an extended point source. Not only does the shower have an intrinsic lateral width, but also the imaging properties of the telescopes – the PSF – and multiple scattering on the path to the telescope contribute to the widening of the image. Moreover, because the signal is effectively integrated over 100 ns, very close showers (< 5000 m) can move across the telescope FOV with sufficient angular speed to add some smearing in the longitudinal direction.[9] In general, the farther away the shower, the smaller its angular size relative to the telescope and the narrower the image on the camera.

[9] *A shower moving in the plane perpendicular to the optical axis of a telescope at a distance of 3000 m will cross about one third of the pixel FOV in 100 ns.*

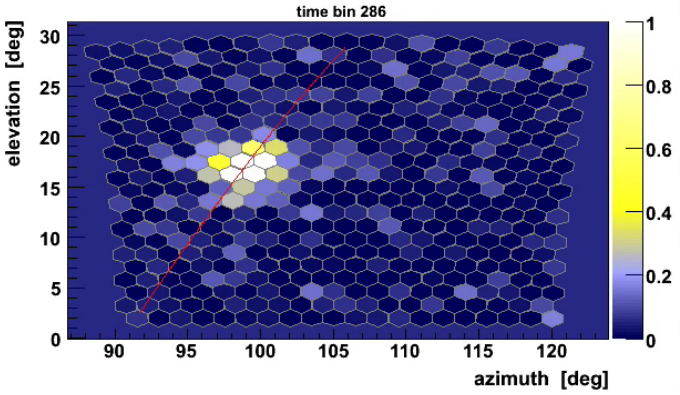

FIG. 3.15 The image of an air shower on the FD camera at one instance in time. The red line marks the shower-detector plane (SDP), along which the image moves. From [130].

In regular DAQ mode, only a narrow stripe of pixels adjacent to the triggered core track is read out, about 4° to either side of the SDP. Given the experimentally measured PSF introduced in the previous section, some photons will inevitably strike outside this boundary and will be lost from reconstruction. If not properly corrected for, the light flux at the aperture will be underestimated.

The optimum light collection region on the camera, also referred to as the integration region, is chosen for each event individually so as to minimize the signal-to-noise ratio (SNR) [131]. Its size is quantified in terms of the angle ζ_{opt} from the SDP: If the nominal viewing direction of a pixel falls within the circle defined by ζ_{opt}, that pixel's signal is included. Fractional contributions proportional to the area of a pixel encompassed by ζ_{opt} are not implemented. The value of ζ_{opt} for a particular shower depends on many parameters, such as distance to telescope, energy, age, viewing angle and the contribution from multiple scattering.[10] Fig. 3.16 shows a distribution of ζ_{opt} for over 20 000 measured showers, with typical values in the range 1–2° and a mean of $(1.3 \pm 0.2)°$. Exceptionally large values of ζ_{opt} are found for nearby showers of high energy, as can be seen in Fig. 3.17.

The fraction of light arriving outside of ζ_{opt} must be properly compensated for to avoid a reconstruction bias. A phenomenological correction, referred to as the lateral width correction (LWC), was derived by analyzing the amount of light falling between ζ_{opt} and 4.0° for a sample of thousands of measured showers [76, 132]. The angle of 4.0° is not arbitrary, but reflects the typical width of the camera region that is read out to either side of the main shower track.[11]

A function of ζ_{opt} and parametrized in terms of the shower distance R_p and age s, the LWC gives a multiplicative factor used to scale up the light flux at the aperture. In general, the closer and the more developed the shower, the higher the value of the correction. The resulting energy shift ranges from 6 % to 10 percent. Due to the age-dependence, the depth of shower maximum X_{max} is affected too, on average by $+8\,\mathrm{g/cm^2}$ [132]. The impact on both, energy as well as X_{max}, are depicted in Fig. 3.18 as a function of energy.

While the LWC phenomenologically corrects for the light falling between ζ_{opt} and $\zeta_{\mathrm{LWC}} = 4.0°$, it does not provide any microscopic explanation of the origin of that light. It is expected that the dominant contribution stems from the PSF of

[10] *The age* s *of a shower describes its stage of development with respect to the depth of the shower maximum* X_{max}*, at which* $s = 1$*, and the distance refers to the distance of closest approach of the shower axis to the telescope.*

[11] *Note that due to statistical noise, the signal cannot be integrated up to 4.0° on a shower-by-shower basis.*

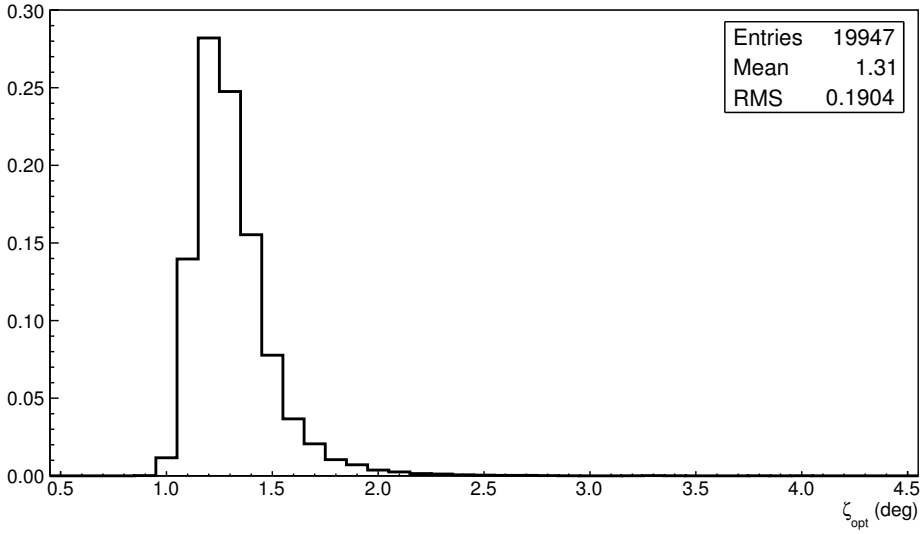

FIG. 3.16 A normalized distribution of the values of ζ_{opt} for a sample of nearly 20 000 measured showers passing standard quality cuts. The mean value is $(1.3 \pm 0.2)°$. Data from [83].

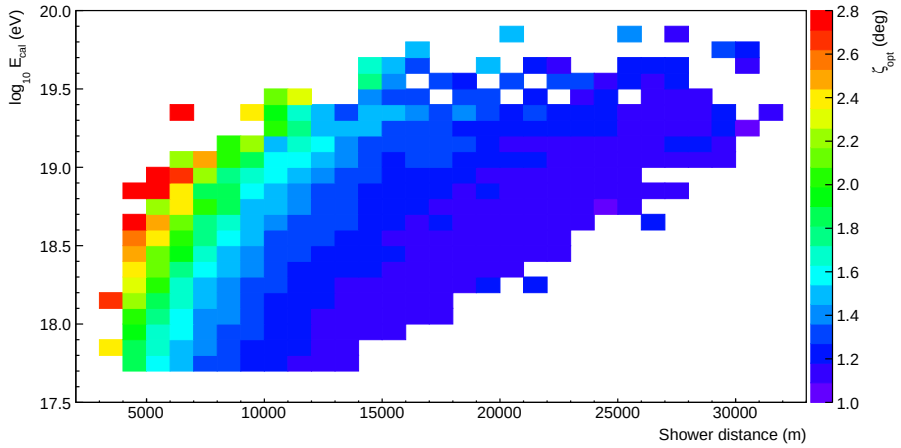

FIG. 3.17 The radius of the optimum integration region ζ_{opt}, indicated by the color scale, as a function of shower distance and energy. The data set shown here consists of nearly 20 000 measured air showers passing standard quality cuts. Data from [83].

the telescopes, but other contributions may be involved. As of the time of writing this work, multiple scattering has been ruled out, since no dependence on shower distance was observed [132]. We shall revisit the topic of the LWC in Sec. 6.6, where it will be relevant to the interpretation of the results.

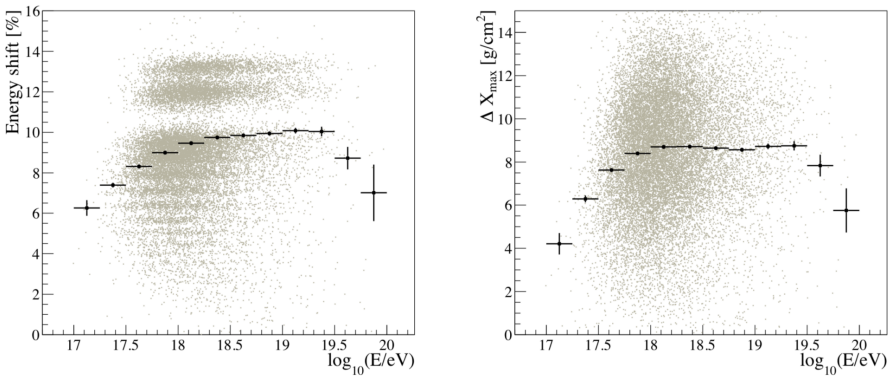

FIG. 3.18 Resulting shifts in reconstructed shower energy (left) and X_{max} (right) after applying the LWC. Shown are the shifts for individual showers (scattered gray points), as well as the mean value per energy bin (black points with bars), where the error bars indicate the statistical spread within a given bin. The horizontal bands in the left panel are a result of discrete values of the angle ζ_{opt}, which changes in 0.1° steps. The top-most band corresponds to the lowest possible value of $\zeta_{\mathrm{opt}} = 1.1°$. A sample of over 20 000 showers was used for the analysis. From [132].

4 Point Spread Function

Contents

While the mechanism responsible for shaping the point spread function (PSF) at large angles – enhanced reflections on the PMT faces – was identified in 2010 [122, 128], the small-angle region resisted explanation for another three years. Clearly, targeted measurements were required to figuratively and literally shed light on the issue. In 2013 and 2014 we took to studying the distributions of mirror-reflected and filter-transmitted light in numerous dedicated measurement campaigns, and compared those major optical interfaces in clean and dusty conditions. The results were surprising, providing an unprecedented understanding of not only the PSF, but also the unexpectedly large attenuation occurring on the MUG-6 filter.

The measurement of the mirror is discussed first, with Subsecs. 4.1.1 to 4.1.4 covering the experimental setup, data acquisition and analysis. The found distributions of mirror-reflected light, reported in Subsec. 4.1.5, were subsequently implemented in telescope simulations to achieve more realistic ray-tracing. This is described in Sec. 4.2 and the impact on the shape of the simulated PSF, drum calibration constants and reconstructed shower variables is presented in Subsecs. 4.2.2 to 4.2.4. Sec. 4.3 describes the methodology and results of the filter measurement, and comparison to results obtained via other approaches is done in Subsec. 4.3.4.

Both measurements presented in this chapter are relative comparisons of a clean versus a dusty aperture or mirror, with much of the systematic uncertainties canceling and no need for absolute normalization. The emphasis lies on understanding the shape of the PSF qualitatively and semi-quantitatively. A rigorous quantitative description is not the goal, especially since it will depend on the exact condition of the optical interfaces, which is variable in time and not tracked by CalA.

At the outset, let us clarify some terms used throughout the text. The term "aerosol" refers to fine solid particles or liquid droplets dispersed in a gas, and for our purposes air. Dust is also a type of aerosol. Larger aerosols with diameters exceeding 1 μm tend to have significant settling speeds, especially in the absence of turbulence, and are often distinguished as suspensions. We will keep it simple and stick to the term "aerosol" for airborne particles and will reserve the term "dust layer" for aerosols deposited on a surface. Furthermore, the terms "scattering" and "absorption" will occur throughout this text. With regards to the fluorescence detector, we define "absorption" as the shifting of the wavelength of a photon outside of the spectral acceptance of the telescope (c.f. Fig. 2.15). "Scattering" refers to the deviation of a photon from its specular direction, either during transmission on the filter or reflection on the mirror.

4.1 Distribution of Mirror-Reflected Light

4.1.1 Idea of the measurement

Photons impinging on a hypothetical ideal mirror would be reflected altogether specularly. A non-specular component may, however, be present due to imperfections of the reflector, such as microscopic defects, small particles deposited on the surface, misalignment of individual mirror segments or deformation of the segment shapes, leading to a deviation from the nominal radius of curvature of 3.4 m.

Aerosol deposition on the mirror surface is of particular interest to us for two reasons:

1. It may scatter photons, thus widening the PSF.
2. It may introduce an elevation dependence to the signal, because the 16° tilt of the optical axis causes aerosols to preferentially accumulate in the bottom bowl-like part of the mirror.

The condition of the bottom part of the CO5 mirror in November 2013, shown in Fig. 4.1, testifies that aerosol deposition is an issue, even in the somewhat protected atmosphere of the FD buildings.[1] Uneven accumulation of dust on the mirror is not only visible by eye, but has been studied in the laboratory as well as using relative CalC data.

In 2010, two mirror segments were removed from the CO6 mirror for investigation and cleaning: one from the top-most, the other from the bottom-most row [133]. The reflectivity and roughness of both segments were measured

[1] *Most mirrors are in a considerably better condition than CO5 shown in the photo, where cleaning was postponed until all studies were completed.*

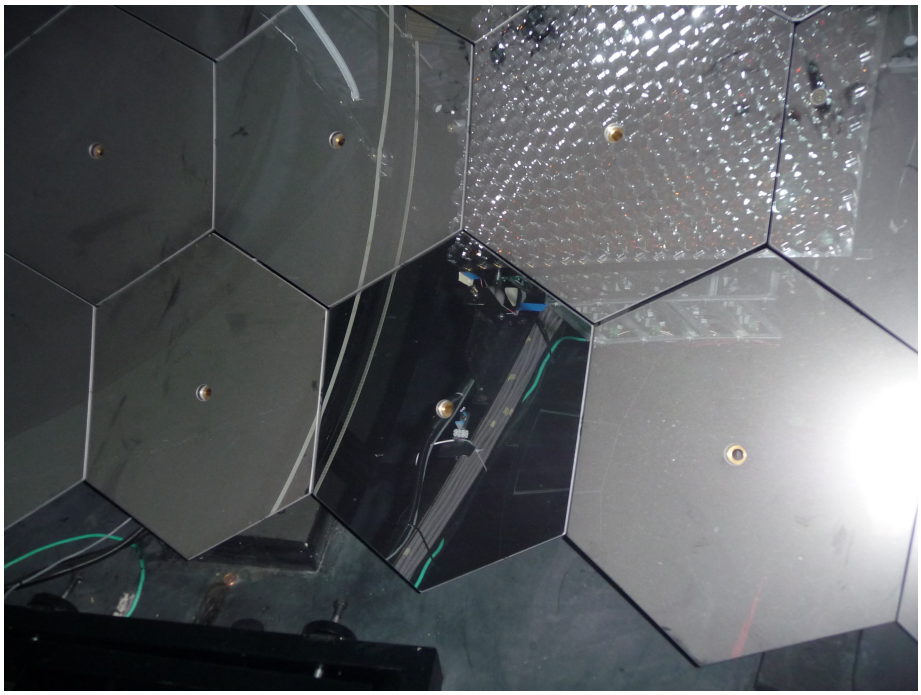

FIG. 4.1 The bottom rows of the mirror are most prone to aerosol deposition. Shortly before this photograph was taken in CO5 in November 2013, the bottom central segment was removed for a special measurement and replaced by a clean one. The measured difference in reflectivity is about 6 % at 375 nm [133]. Photo courtesy of Radomír Šmída.

before and after cleaning. After five years of operation, the reflectivity of the top segment at 375 nm had not changed significantly and accordingly cleaning had little effect. On the other hand, the reflectivity of the bottom segment had dropped by 6 %, but was restored to 99 % of the initial value after cleaning. A before-and-after comparison of macro images of the mirror surface is shown in Fig. 4.2.

The uneven deterioration of the mirror surface can also be seen in relative CalC data. In [88], the ratio of CalC signals recorded by the PMTs in the upper and lower third of the camera was tracked in time. This approach takes advantage of the very specific geometry of CalC, where photons traveling from close to the CC are reflected from the upper/lower part of the mirror to the upper/lower part of the camera, i.e. unlike in air shower detection the image is not vertically inverted. As expected, the signal in the lower part of the camera, corresponding to photons reflected on the lower, dustier part of the mirror, was found to decrease faster with time, and to recover more following cleaning than the signal from the upper part of the camera.

The goal of the measurement described in this section is to determine the angular distribution of photons reflected on the mirror and to compare the distributions obtained for the upper clean and the lower dusty parts of the mirror. Primarily, we seek to understand how a dust layer on the mirror affects the PSF, but the measurement of course encompasses the general quality of the

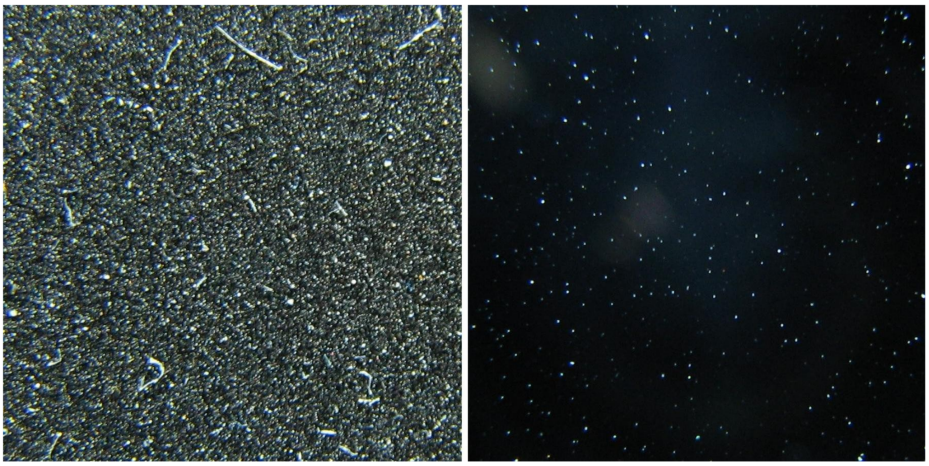

FIG. 4.2 Macro images of the mirror surface before (left) and after (right) the cleaning procedure. From [134]. While the exact size of the photographed region is not known, it is estimated to be less than 1 cm^2 [135].

reflector, including e.g. aging effects. There are two key features that make this measurement unique: First, it took place in situ, i.e. the scattering on a real mirror with an authentic dust layer of the Pampa Amarilla was studied. Second, several segments of the mirror were illuminated by the light source so, in contrast to laser beam measurements, an extended surface area of the mirror was studied in a realistic way.

4.1.2 Experimental setup

The setup takes advantage of the special geometrical properties of the CC of the mirror: All light rays emitted from the CC hit the mirror at a right angle and are reflected back into themselves, returning to the emission point (assuming a perfect reflector). By shifting the light source a little to the side of the CC, the image is focused symmetrically onto a detector positioned just to the other side. This geometry is schematically depicted in Fig. 4.3.

In practice, a semi-diffuse UV light source is placed 5.5 cm to the side of the CC of the telescope[2] and directed at the mirror. The reflected photons are intercepted at the focal plane by a target screen, which in turn is viewed by a CCD camera that records the resulting image.

[2] *Note that the CC is not located in the filter plane, but in the plane of the corrector ring, which is offset by 12 cm inward.*

Fig. 4.4 shows the complete setup in bay 5 of Coihueco. The paper-covered target screen is located in the aperture to the left of the CC, while the light source appears as a black tube just to the right. The CCD camera is mounted on a custom-made bracket attached to the side of the actual FD camera at the point where normally the calibration B fiber terminates and views the target screen roughly head-on. To suppress multiple reflections, the left part of the aperture and all sides of the FD camera were covered with black cloth.

Having three degrees of freedom and a limited opening angle, the light source can be adjusted to illuminate different regions of the mirror, thus enabling a

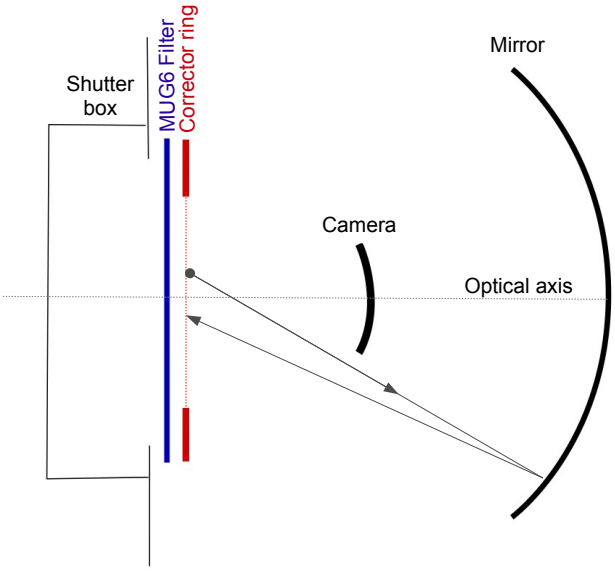

FIG. 4.3 The geometry of the mirror measurement viewed from the top: The light source (gray solid circle) is positioned 5 cm to one side of the CC in the plane of the corrector ring, and the image is focused symmetrically just to the other side. The CC is at the point where the optical axis (gray dashed line) and the plane of the corrector ring (red dashed line) intersect. Adapted from [116].

comparison of images recorded with the source pointing at the upper clean and lower dusty part of the mirror, respectively. Since we are predominantly interested in the angular distribution of reflected light, no absolute normalization and thus no absolute calibration of the light source is required. Furthermore, the absolute reflectivity of mirror elements can be easily and regularly measured with a hand-held reflectometer [133, 134, 136].

The first measurements took place in March 2013 and served mainly as proof of principle. The positive news of this campaign was that, using this general setup, it would be possible to measure the angular distribution of mirror-reflected light. At the same time, numerous shortcomings were identified, both on the equipment and data quality fronts. Once resolved, the second and final measurement campaign was carried out in November 2013. In the following paragraphs, the properties of the main components of the final setup are discussed.

Light source: Different combinations of wavelength, radiation pattern and output power were tested throughout the design stage. The ultimately used light source is based on a UV LED manufactured by Roithner LaserTechnik [137], model UVLED370-110E. The peak wavelength of 375 nm matches that of CalA and is close to the peak drum wavelength. Three different amplitude settings provide an output power range of 3.02–8.56 mW. The LED is housed in a rectangular plastic holder and photons first pass through a plastic diffuser before exiting through a 3 mm circular aperture. The housing is surrounded by a tunnel of black flock paper to loosely collimate the beam and intercept any potential photons emitted at large angles due to multiple reflections at the exit aperture. The resulting beam

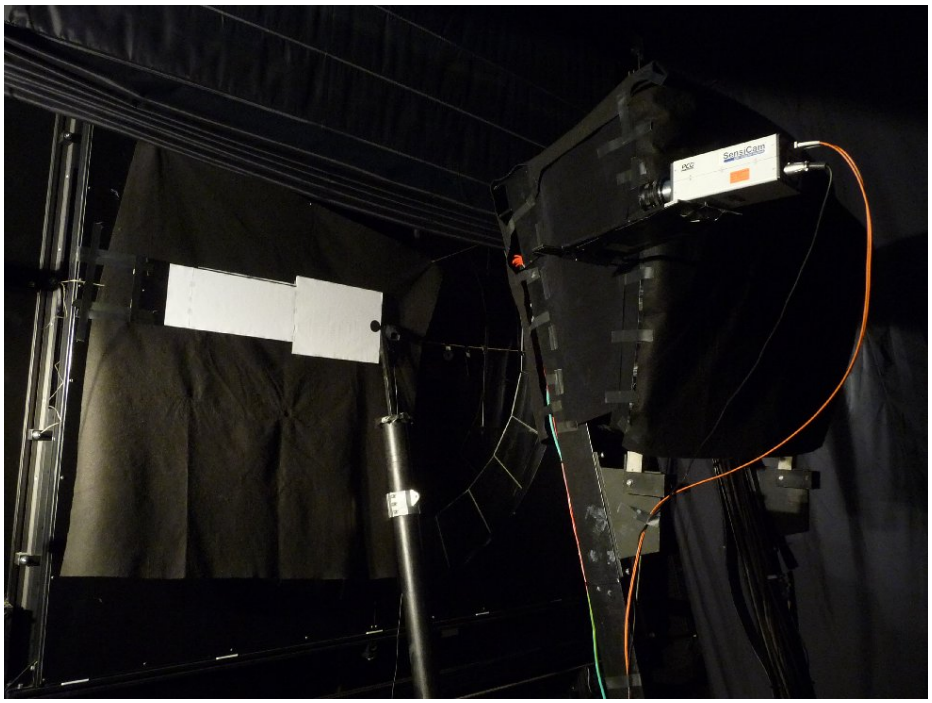

FIG. 4.4 The setup for the mirror measurement in CO5. The screen is positioned to the left of the CC, the light source just to the right. The CCD camera is mounted on the side of the actual FD camera. Both, the aperture and the FD camera are covered with black cloths to minimize multiple reflections.

is semi-diffuse, with an opening angle of about $\pm 8°$, covering an area of $\sim 1\,\mathrm{m}^2$ on the mirror. The mounted light source is shown in Fig. 4.5 (left). To avoid having to enter the telescope bay every time the light source needed to be turned on or off, a remote control was built.

[3] *Paper is a good diffuse reflector.*

Target screen: The target screen is a paper-covered[3] plastic plate with a bracket that attaches to the fixed-point structure at the CC – a mountable mast used for mirror alignment at the time the telescopes were built. There is a built-in light trap on one side of the screen, shown in Fig. 4.5 (left), that is uncovered during long exposure measurements of the order of 100 s to reduce the light intensity in the center of the image. Black flock paper, which is a good light absorber, was used to line the surfaces of the light trap. The cylindrical body[4] with a diameter of 20 mm protrudes out of the back of the target screen. The opening on the screen is taped with a flock paper annulus with an inner and outer diameter of 20 mm and 50 mm, respectively, positioned concentrically on the light trap. The resulting reduction in intensity is a factor of roughly 1000. The target screen is positioned such that the image is focused on the center of the light trap 5.5 cm to the left of the CC, corresponding to the position of the light source 5.5 cm to the right of the CC.

[4] *The typical conical shape is not required, as the light source is diffuse and photons arrive at various angles.*

Note on under-surface scattering and paper fluorescence: Translucent materials, such as paper or human tissue, exhibit under-surface scattering. Photons may propagate sideways through such materials and be re-emitted at some distance

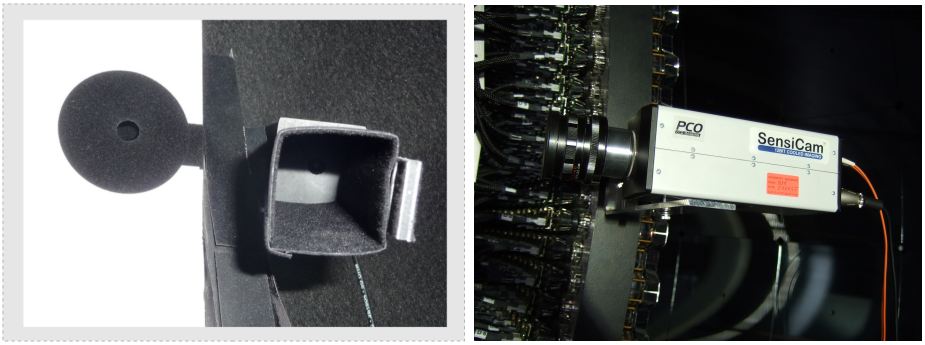

FIG. 4.5 Left: A close-up of the light source attached to the mounting bracket of the target screen. The light trap is also visible. Right: The CCD camera viewing the target screen is mounted to the side of the FD camera.

from the point of incidence. Paper enriched by fluorescence whitening agents, which act as wavelength-shifters, absorbs wavelengths below 370 nm and re-emits in the visible range at about 475 nm. Hence, the amount of scattering will depend on the concentration of whitening agents. To assess the magnitude of under-surface scattering, we tested several types of paper, the naked target screen (black plastic) and a screen coated with titanium dioxide (white diffusively reflecting surface) in the laboratory. The size of the spot produced by the light source on each of the tested surfaces was examined and no significant difference was found. Moreover, test measurements performed in situ in March 2013 using a 375 nm and a 475 nm light source gave comparable results. In conclusion, under-surface scattering does not observably affect the measurement and the resulting distribution functions.

CCD camera: The light detector is a long-exposure, UV-enhanced CCD camera by PCO Sensicam, model 360 KL Long Exposure [138], with VGA resolution (640×480 pixels) and 12-bit gray-level sensitivity. Two-stage Peltier cooling with forced air flow is used to cool the CCD sensor from the ambient electronics temperature of 40 °C to −15 °C. Possible exposure times range from 1 ms to 3600 s, providing a wide dynamic range. Images are saved as 16-bit TIFF files or in the internal file format (denoted by the extension *b16*). They may be converted into number matrices using e.g. Mathematica or processed with dedicated scripts, as was done in this case. For the final campaign in November 2013, version 3.11 of the camera operating software *CamWare* was used.

4.1.3 Pre-studies and data acquisition

Mirror re-alignment

Before starting the actual measurement, the mirror under investigation was re-aligned. In practice this means that each individual segment was rotated ever so slightly until a laser beam fired from the CC was focused upon, or very close to,

itself. In this way we ensure that the observed distribution of reflected light is due to the surface properties of the mirror, and not due to potential misalignment.

Next the light source was pointed at the lower right part of the mirror (as viewed from the position of the light source) and its position was fine-adjusted until the return image hit the center of the light trap. While fiddling with the setup, a fascinating photograph was taken showing the process of image formation, see Fig. 4.6. It shows the out-of-focus image of the light source on a sheet of paper held about 10 cm in front of the target screen. The individual lit mirror segments are clearly visible, as is their small misalignment resulting in either gaps or overlaps.[5] The dark point in the center of each segment is the mounting hole to the frame.

[5] *In fact, the effective misalignment comes mainly from the very slightly different radii of curvature of the individual segments.*

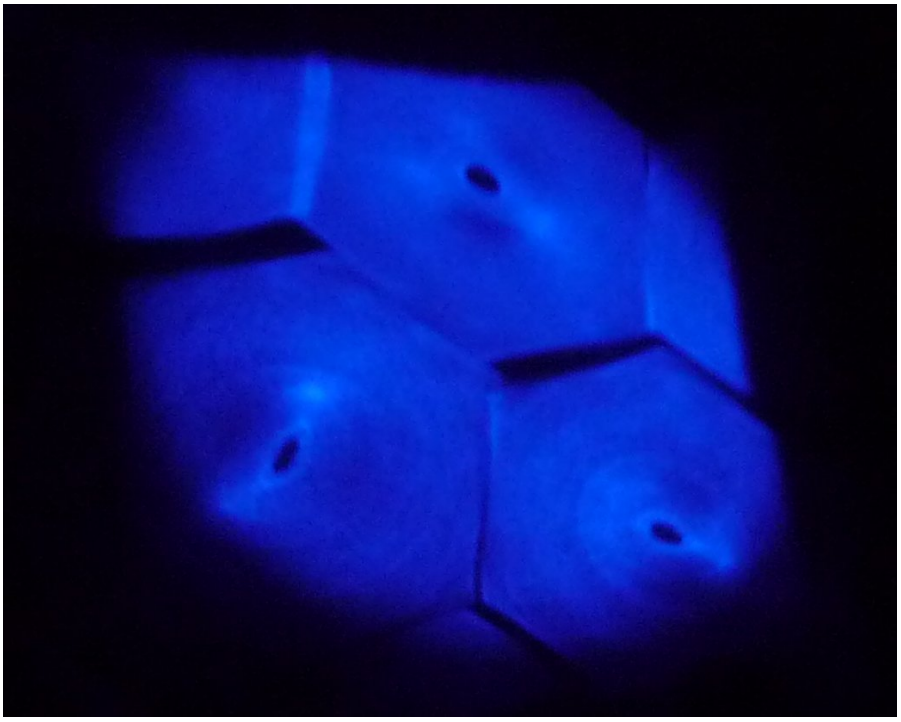

FIG. 4.6 The out-of-focus image of the light source on a sheet of paper held about 10 cm in front of the target screen. Photo courtesy of Radomír Šmída.

Background studies

In the following, we shall distinguish between the following three terms:

- *Dark frames* are images taken with the light source turned off and the camera lens covered by a cap. They capture the thermal noise of the CCD chip.
- *Background frames* are taken with the camera lens uncapped, but the light source still off. They are used to correct for background light in the telescope bay.
- *Signal frames* are images taken with the light source switched on.

Long-exposure dark frames, such as the one shown in Fig. 4.7, were studied first. The typical number of counts per pixel is in the range 50–60 and there appears to be a spatial pattern in the image. Conceivably, the efficiency of the Peltier cooling varies across the chip and is at its lowest in the top right and bottom left corners.

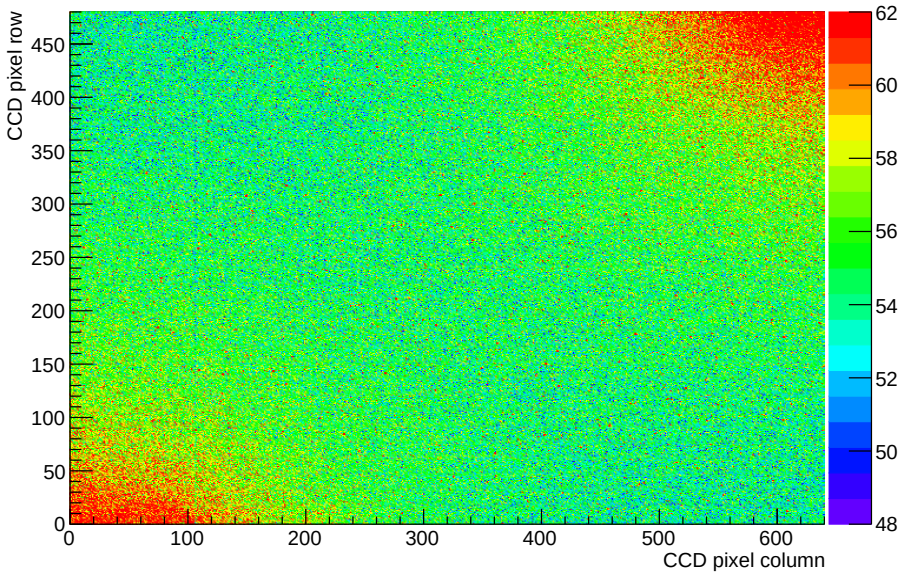

FIG. 4.7 A dark frame taken with an exposure time of 1000 s. Each point represents one pixel on the 640 × 480 CCD chip. Pixels in the upper right and lower left corners are characterized by higher thermal noise.

Fig. 4.8 shows the distribution of the number of counts per pixel for the very same dark frame. The main peak at 55 counts corresponds to standard, well-cooled pixels located in the central parts of the chip. The tail extending to larger values comes from pixels located in the corners of the chip, which have more thermal noise. The small peak at 260 counts may be due to cosmic rays passing through the chip. Not pictured are 23 noisy pixels with the number of counts in the range 500–4000.

Hot and cold pixels were identified by their concurrent occurrence in two different 1000 s dark frames. Using the criterion of more than 85 and less than 45 counts to define a hot and cold pixel, respectively, 1011 hot (a mere 0.3 %) and no cold pixels were found. The hot pixels were flagged and excluded from the analysis.

Test measurements with long exposure times of 15 min indicated the presence of stray light in the bay. First, all LED control lights were covered with black tape. While they were very faint to start with, they may still contribute significantly to long-exposure images. Next, it was found that the shutter box is not perfectly light-tight and the relevant part was covered with a large black cloth. Comparing background and dark frames taken with exposure times of 1000 s in Fig. 4.9, one

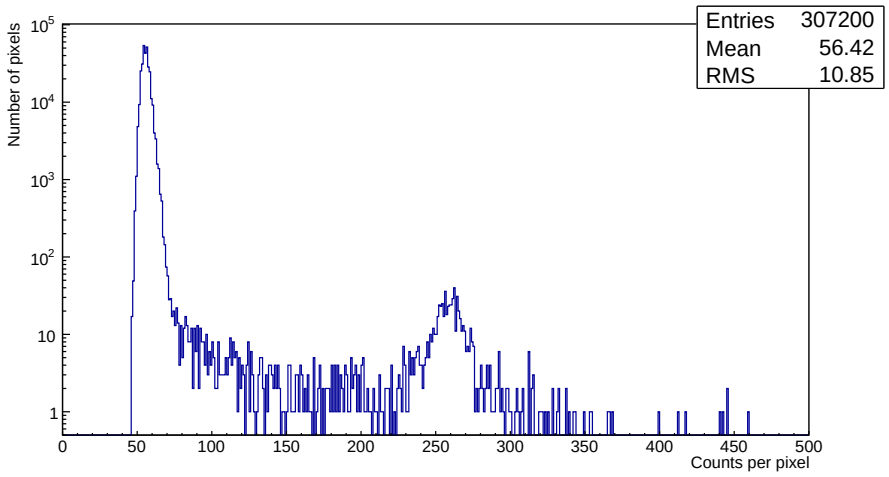

FIG. 4.8 The distribution of the number of counts per pixel in a 1000 s dark frame has a mean of 56.4 and a suppressed tail extending to higher count values. The small peak around 260 is probably due to cosmic ray hits. Notice the logarithmic scale of the y-axis.

sees that the background in the right half of the frame matches, save for statistical fluctuations, the thermal background, but there appears to be additional light in the left part of the frame. The presence of this parasitic light source is only observable in long-exposure frames with $t_e > 300\,\mathrm{s}$ and was accounted for by taking a corresponding background frame just before or after acquiring the signal frame. This was done for every single frame, including those with very short exposures of the order of ms.

Dynamic range, exposure times and non-linearity

Test frames revealed a steeply falling lateral intensity distribution of the light source image on the target screen – about five orders of magnitude across the FOV of the CCD camera. Such a large dynamic range cannot be covered with one single exposure time. Therefore, signal and corresponding background frames were taken with exposures times ranging from 8 ms to 1000 s, spanning a dynamic range of 1.25×10^5.

A complication in the form of charge loss arises for long exposure times and is best explained using an example. Fig. 4.10 shows the ratio of two frames taken with exposure times of 1000 s and 300 s, respectively. With the exception of the area of the light trap, which is clearly visible on the right as a dark orange circle with a blue spot in the center, one would naively expect to see a ratio of $3.\overline{3}$. Although this is the case for regions about 260 pixels away from the center of the image, the near regions have considerably lower ratios, down to $\sim$1. Note that those regions are not saturated, only the center of the light trap is.

In the case of our PCO Sensicam, charge loss was observed only for pixels holding large amounts of charge (about 40 % of the saturation level and more) for long exposure times $t_e > 300\,\mathrm{s}$. Clearly, if not handled correctly, charge loss

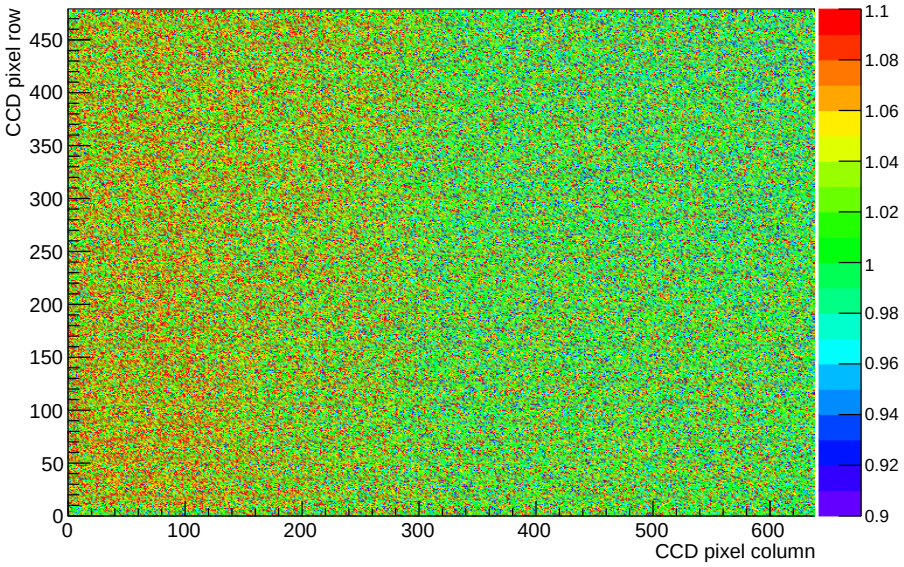

FIG. 4.9 A comparison of a background and a dark frame, both taken with a 1000 s exposure time. Each point represents the ratio of background- and dark-frame counts (indicated by the color scale) in one CCD pixel. The numbers on the axes correspond to the row- and column-coordinate of the pixel on the chip (here, as well as in subsequent plots of this type). While the ratio fluctuates about unity in the right part of the frame, there appears to be parasitic light contributing to the left part of the frame.

will introduce serious non-linearities. To circumvent the problem, each image was compared to the image taken with the next shorter exposure time as in Fig. 4.10, and only regions not affected by charge loss were used for analysis.

Studied mirror parts

Two complete data sets were acquired at CO5: one with the light source pointed at the upper (cleaner), the other with the light source pointed at the lower (dustier) right corner of the mirror. The orientation of the long axis of the light source was approximately $\pm 20°$ vertically and 23° horizontally with respect to the optical axis of the telescope. About three mirror segments were illuminated simultaneously (c.f. Fig. 4.6), corresponding to an area of $\sim 1\,\mathrm{m}^2$. The exposure times for the upper clean part of the mirror were generally slightly shorter than for the lower dusty part, as otherwise the higher reflectivity lead to saturation of the CCD pixels in the central region of the image.

4.1.4 Data analysis

Analyzing the CCD frames

The viewing direction of the CCD camera was purposely chosen such that the center of the image (also the center of the light trap) was close to the edge of the

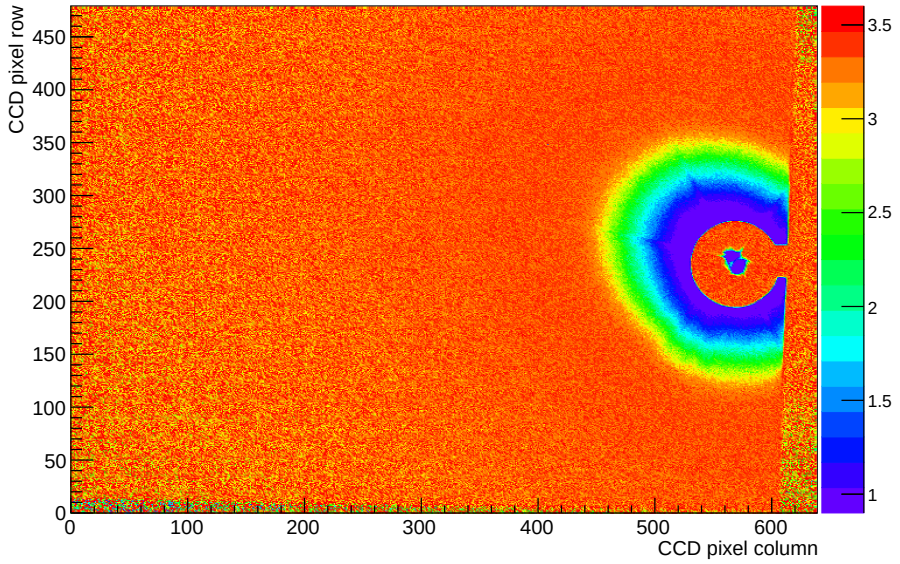

FIG. 4.10 A comparison of two signal frames taken with exposure times of 1000 s and 300 s. Each point represents the ratio of counts (indicated by the color scale) in one pixel on the CCD chip accumulated during the longer and shorter exposure time, respectively.

target screen. With this arrangement the light distributions could be evaluated over nearly the entire FOV of the camera, about 34 cm on the target screen, corresponding to scattering angles up to $\sim 6°$ on the mirror.

The basic CCD image analysis procedure is as follows:

1. Subtract the corresponding background frame from the signal frame.
2. Flag the hot pixels identified (see page 62) and exclude them from the analysis.
3. Identify invalid regions of the frame, in particular those that are off the target screen or within the area of the light trap (if activated), and exclude them from the analysis.
4. Compute the CG of the image using only short-exposure frames in which the light trap was not activated. Since only the exposure times are varied and the FOV remains fixed, the position of the found CG is applicable to all frames. Two procedures were used:
   a) The frame is scanned with a 3×3 square, each time summing the signal of the 9 pixels contained within the square. The CG is taken as the position of the central pixel of the square, whose mean signal is maximized.
   b) The image is projected along the x-direction, and the projection is fitted with a Gaussian. The mean of the distribution marks the x-coordinate of the CG. The procedure is repeated for the y-direction.

   The difference in determining the CG using the described methods is ± 1 pixel in either direction.

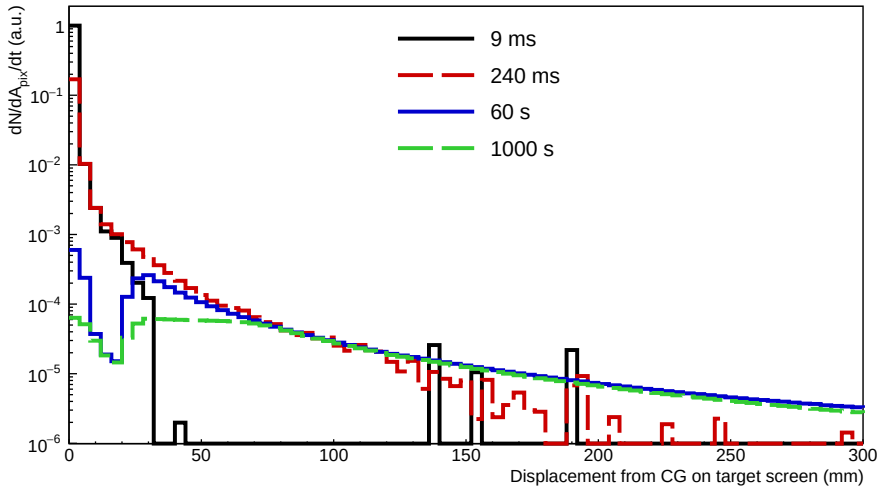

FIG. 4.11 Four differential distributions taken with exposure times ranging from 9 ms to 1000 s. All are shown per unit of exposure time and pixel area, and scaled by a common factor so that the shortest-exposure distribution is 1.0 in the first bin.

5. Each image is analyzed in concentric annuli centered on the CG, i.e. radial symmetry is assumed, and the mean number of counts per pixel as a function of distance from the CG is plotted. Initially, the distance is given in terms of pixels on the CCD chip, but is later converted to physical distance on the screen and eventually to the scattering angle on the mirror (see next section). Statistics is excellent, as already at small distances from the CG, corresponding to scattering angles of $\sim$0.2° on the mirror, thousands of pixels are averaged over within one annulus.

6. A combined distribution is pieced together from about 16 distributions obtained with different exposure times. In particular, the individual distributions overlap in regions of linearity, where no charge loss is suffered, and great care was taken to make sure that the overlapping regions span the entire FOV. An example of four distributions taken with exposure times in the range 0.009–1000 s is shown in Fig. 4.11. If more than one distribution describes a particular distance range, the distribution with the longer exposure time is used to gain better statistics.

Distance calibration and conversion to angle

Ultimately, we are interested in the angular distribution of photons reflected on the mirror. Since photons strike the mirror at different points, each characterized by a different normal, it is convenient to express the angle of reflection relative to the specular direction of reflection (see sketch in Fig. 4.12). In the following, we refer to the difference between the actual and specular angles of reflection as δ.

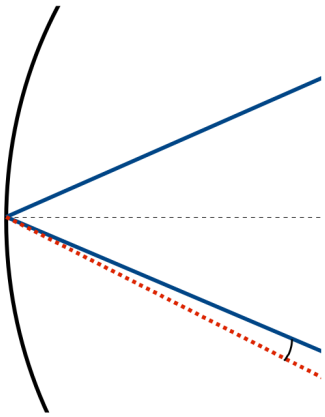

FIG. 4.12 The angular deviation δ from the specular direction of reflection: The incoming and specularly reflected light ray is indicated by the solid blue line, the scattered light ray be the red dashed line. The angle δ is marked with an arc.

Two steps are required to arrive at the angle δ starting with the CCD frames: a conversion from the distance on the CCD chip in pixels to the physical distance on the target screen, followed by a conversion to the angular deviation δ.

Images of a graph paper on the screen, see Fig. 4.13, were taken to complete the first step. The following conversion factors k_x and k_y were found for the horizontal and vertical directions on the CCD chip:

$$k_x = 0.62\,\mathrm{mm/pix}, k_y = 0.61\,\mathrm{mm/pix}. \tag{4.1}$$

The uncertainty in reading the position of the grid lines is ± 1 pixel. Both conversion factors remain constant across the entire FOV within this uncertainty, indicating that the CCD camera viewed the target screen sufficiently head-on for the images not to be observably skewed. The conversion equation from distance d_{CCD} on the CCD chip in pixels to distance d_{ts} on the target screen in mm is then

$$d^i_{\mathrm{ts}} = k_i d^i_{\mathrm{CCD}}, \tag{4.2}$$

where the index i denotes the x- or y-directions.

Conversion from distance on the target screen to the angle δ is non-trivial, as the semi-diffuse light source leads to each photon covering a slightly different distance on the way from the mirror to the screen. In first approximation, we can assume that each photon is reflected from exactly the same point on the mirror, which would be the case for a collimated light source, and the center of the image would correspond to the specular direction of reflection. The approximated angular deflection is then computed as

$$\delta_{\mathrm{app}} = \arctan \frac{d_{\mathrm{ts}}}{R_{\mathrm{ts}}}, \tag{4.3}$$

where d_{ts} is the distance of the investigated region from the spot center on the target screen, and R_{ts} is the distance from the point of reflection on the mirror to the spot center. This distance was measured with a laser distancemeter as 3396 mm, i.e. nearly the same as the nominal radius of curvature of the mirror 3400 mm. Using the small-angle approximation and evaluating, Eq. (4.3)

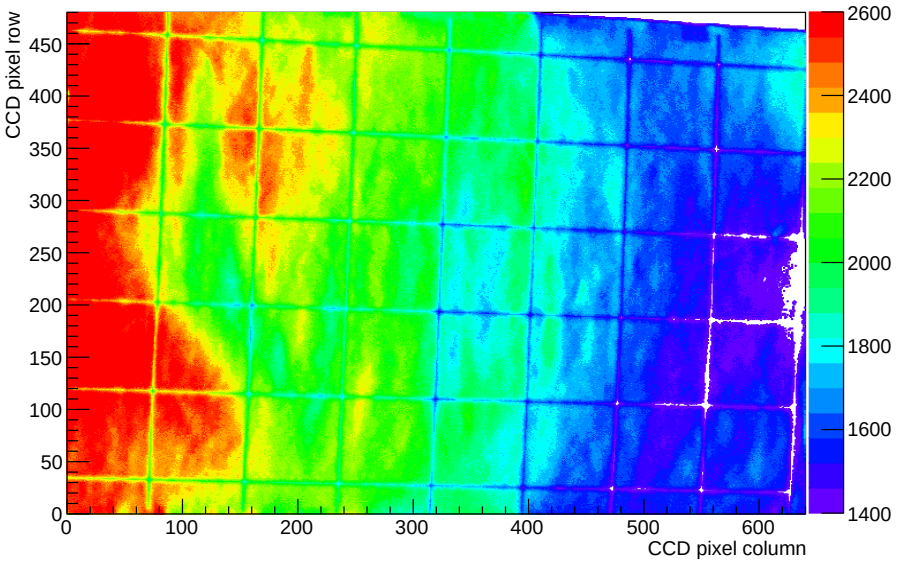

FIG. 4.13 An image of a sheet of a graph paper taped to the target screen as used for the distance calibration. Neighboring parallel lines are separated by 5.0 cm in both directions. Each point on the plot corresponds to one pixel on the CCD chip and the color scale shows the number of counts per pixel, but is not needed for the distance calibration.

becomes

$$\delta_{\text{app}} \simeq \frac{d_{\text{ts}}}{R_{\text{ts}}} = 0.169 d_{\text{ts}}, \tag{4.4}$$

where δ_{app} is in degrees and d_{ts} in cm.

The exact path length of the photon depends on its reflection point on the mirror and the value of δ, both of which are a priori unknown, since we cannot trace individual photons striking the screen back to the mirror. It is thus impossible to find a one-to-one relationship between the position on the target screen and δ. In order to assess the effect of different path lengths, the geometry of the measurement was simulated. The following input is required:

- **The position of the light source,** which is known to be 55 mm to the side of the CC.
- **The angular distribution of photons emitted by the light source,** which is known to be quite flat with an opening angle of $\pm 8°$, and was approximated with a cosine distribution. In the simulation, photons exit the light source from one point as opposed to a 3 mm circular aperture.
- **The distribution of** δ, which is a priori unknown. As an initial estimate, the distribution obtained with Eq. (4.4) was used.

The simulated relationship between the angle δ_{sim} and the distance d_{ts} on the target screen, depicted in Fig. 4.14, is very linear and fitting a first-order

polynomial in the measured range 0–5.7° yields

$$\delta_{\mathrm{sim}} = 0.001 + 0.168 d_{\mathrm{ts}}, \tag{4.5}$$

where δ_{sim} is in degrees and d_{ts} in cm again.

The approximated and fitted conversion functions are nearly identical and start to deviate only at large angles. At 5.7°, the angular range of our measurement, this deviation is a negligible 0.03°. As such, the final distributions were, for simplicity, computed using Eq. (4.4).

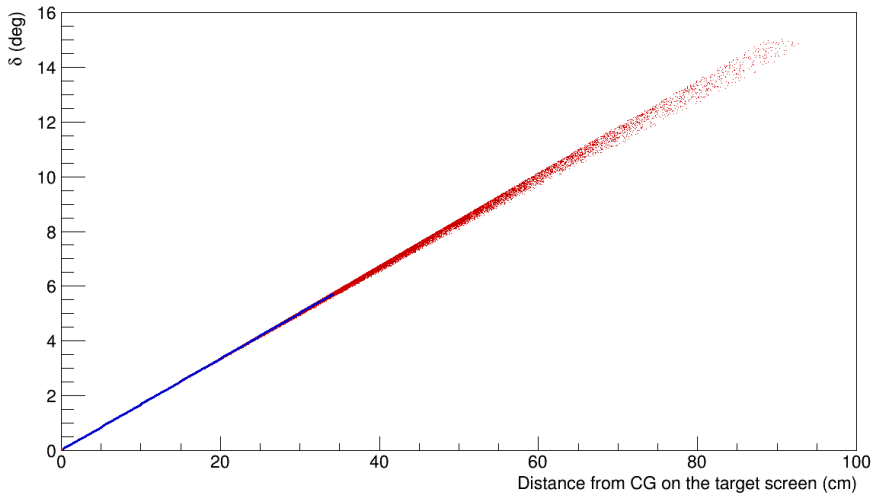

FIG. 4.14 The simulated conversion function from distance d_{ts} on the target screen to the angle δ_{sim}. A linear fit up to 5.7° is shown in blue.

4.1.5 Final distribution functions

The final distribution functions of mirror-reflected light for the upper and lower parts of the mirror are presented here. For purely specular reflection, the differential distribution would be a 3 mm-wide box function, yet the non-specular component adds some widening.

The differential functions, depicted in the top panel of Fig. 4.15, are given in relative counts per solid angle $\mathrm{d}\Omega_{\mathrm{pix}}$, which is proportional to the area $\mathrm{d}A_{\mathrm{pix}}$ subtended by one pixel of the CCD chip on the target screen (about 0.38 mm^2 or 3.3×10^{-8} sr). Since the distance conversion factors given by Eq. (4.1) are constant across the entire FOV, so is $\mathrm{d}A_{\mathrm{pix}}$, and with the distance R_{ts} from the mirror to the target screen being virtually constant, $\mathrm{d}\Omega_{\mathrm{pix}}$ is a linear function of $\mathrm{d}A_{\mathrm{pix}}$. To allow for easy comparison of the shapes, the differential functions were scaled to 1.0 in the first bin.

There is an evident difference in the distributions obtained for a clean and a dusty part of the mirror: the latter is considerably wider as a result of photons scattering at larger angles from the specular direction. Clearly, deposited aerosols

on the mirror significantly affect the quality of reflection. Nonetheless, both distributions drop by about four orders of magnitude over the initial 0.74° and 1.2° for the upper and lower parts of the mirror, respectively. Because the measured data only cover an angular range up to 5.7°, the tails of the distributions were extrapolated to 15.0° using an exponential function.

The corresponding cumulative distributions are shown in the bottom panel of Fig. 4.15. We shall refer to the value of the cumulative function evaluated at a particular δ as the "encircled energy" – an optics term that describes the concentration of energy in an optical image relative to the centroid of the PSF or, in this case, the CG of the image. Since the measurement is only relative and the total number of reflected photons is unknown, both distributions were scaled to 1.0 at 15.0°. In this representation, the effect of the dust layer on the PSF becomes more tangible: For a dusty mirror segment, the encircled energy within one FD camera pixel with a radial FOV of 0.75° is 92.9 % and the remaining 7.1 % of light are scattered into neighboring pixels. In comparison, for a clean segment only 0.7 % of light are scattered out of target pixel.

4.2 Telescope Simulation

Scattering on the dust layer on the mirror is likely to affect shower variables such as reconstructed energy, especially since drum calibration is – due to the simultaneous illumination and read-out of the entire camera – blind to this effect. In fact, the elevation-dependence of the PSF caused by the uneven deposition of aerosols on the mirror may even bias the depth of the shower maximum X_{max}. For this purpose, the distribution functions of the last section were implemented in the telescope simulation code, which is briefly described in Subsec. 4.2.1. The improvement in the agreement of the measured and newly simulated PSF was evaluated first (Subsec. 4.2.2). Next, drum calibration and air showers were simulated with and without a dust layer on the mirror. It turns out that the extent to which scattering on the mirror affects drum calibration constants, discussed in Subsec. 4.2.3, determines just how much reconstructed shower variables will be affected. Changes in reconstructed energy, the depth of the shower maximum X_{max}, as well as the radius of the optimum integration region ζ_{opt} are studied in Subsec. 4.2.4.

4.2.1 Implementation of realistic mirror properties

The cumulative distribution functions describing the scattering on the upper and lower parts of the mirror[6] were implemented in the ray-tracing module TelescopeSimulatorKG_DEV. Depending on the height of the point of incidence on the mirror, photons scatter according to one or the other distribution function, or an interpolation of the two.

[6] *listed in App. A for completion*

Let us define the vertical position on the mirror as follows: Consider a vertical plane defined by the optical axis. In this plane, let v be the angle between the optical axis and the imaginary line connecting the CC to a point at a given height

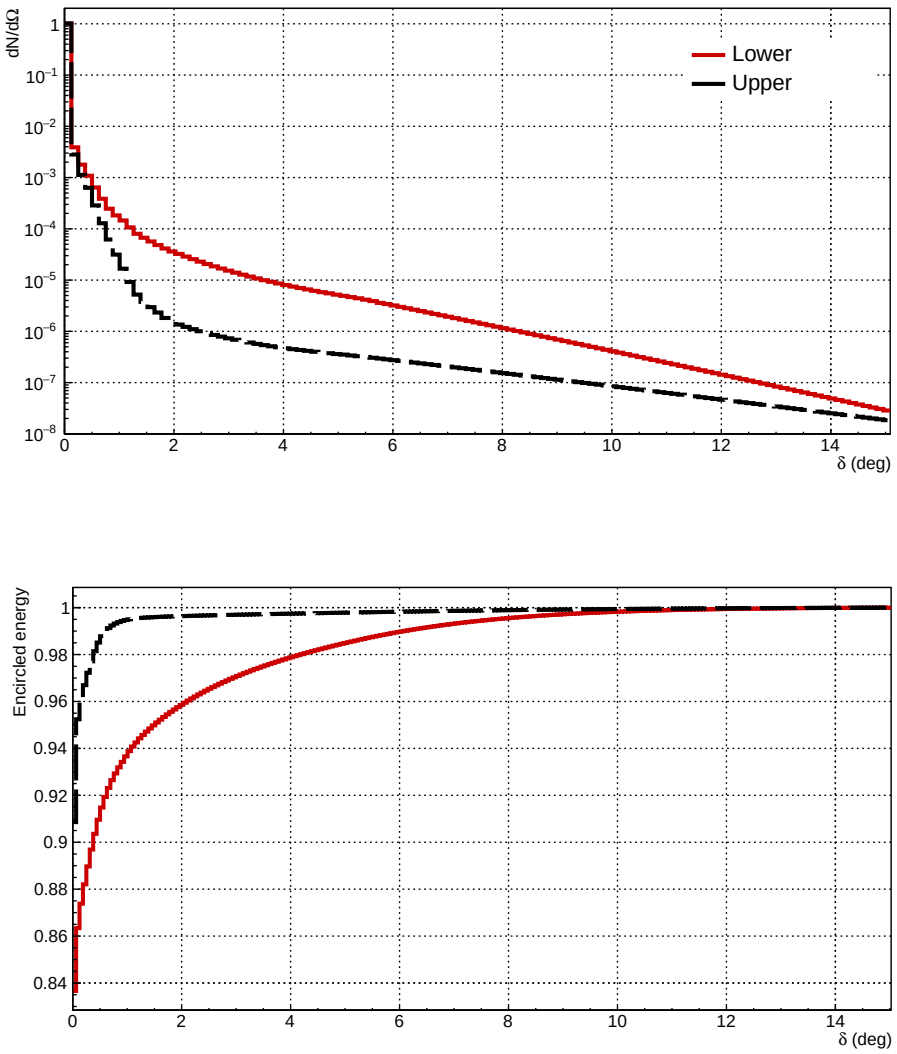

FIG. 4.15 Top: The differential distributions of mirror-reflected light as a function of the angular deviation δ from the specular direction of reflection. Both distributions are shown per unit solid angle and are scaled to 1.0 in the first bin to allow for easy comparison of their shapes. The labels "lower" and "upper" refer to the dustier and the cleaner parts of the mirror, respectively. Bottom: The corresponding cumulative distributions, scaled to 1.0 at 15°.

on the mirror. In this representation, the upper and lower edge of the mirror are defined by $v_{\text{edge}} = \pm 33°$, with positive values corresponding to the upper parts of the mirror and vice versa, and the following regions of validity emerge for the measured distribution functions:

1. $v > 18°$: The distribution for the upper part of the mirror is used.
2. $v < -18°$: The distribution for the lower part of the mirror is used.
3. $v \in (-18°, 18°)$: The two *cumulative* distributions are linearly interpolated.

The first two regions correspond to the upper and lower areas of the mirror that were illuminated by the semi-diffuse light source. Linear interpolation was chosen for the central mirror region [139], although a cosine function would also be a good candidate. One can imagine that the rate of aerosol deposition at a given height of the mirror is proportional to the projection of the corresponding mirror area $\mathrm{d}A$ onto the horizontal, which in turn is proportional to the cosine of the angle between the tangent to $\mathrm{d}A$ and the horizontal. However, the gradient of the cosine is, for our purposes, rather constant in the relevant range 0–0.5, thus a linear interpolation was chosen for simplicity. The two measured distributions and one interpolated distribution for $v = 0°$, i.e. the height of the intersection point of the optical axis with the mirror, are plotted in Fig. 4.16.

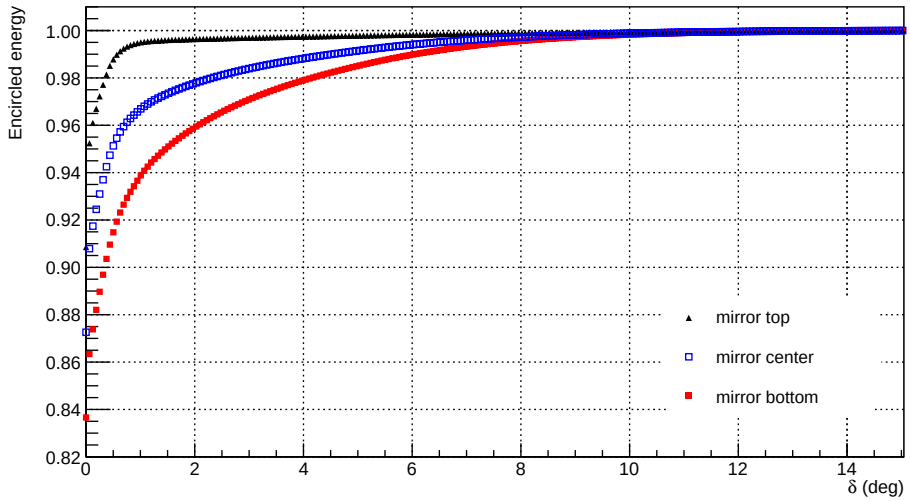

FIG. 4.16 Examples of cumulative distributions used in simulations: upper clean mirror part (black solid triangles) and lower dusty part (red solid squares). The interpolated function for $v = 0°$ (blue open squares) is shown as well.

4.2.2 Effect on point spread function

The change in the shape of the PSF was investigated first. Clearly, scattering on the dust layer on the mirror will widen the PSF, the question is only by how much.

The PSF was simulated similarly as described in Sec. 3.2. On top of enabling enhanced reflections on the camera surface, the dust layer on the mirror was activated. The former configuration is referred to as the "clean mirror", the latter as the "dusty mirror", and results for both are shown in Fig. 4.17.

Although there is significant improvement in the small-angle region below 5°, the width of the simulated PSF is, even with added scattering on the mirror dust, not sufficient to match the experimental data. This is, however, consistent with the expectation that qualitatively similar dust layers (or other types of dirt layers) cover other optical surfaces of the telescope, i.e. the filter, the corrector ring and the PMT entrance windows. The critical realization here is that scattering on dust widens the PSF in the appropriate angular range. The mirror is the only optical surface for which a dust layer was implemented in the simulation code, and the results obtained therewith ought be understood as proof of principle.

4.2.3 Effect on drum calibration

The drum is implemented as a simple photon injector in the $\overline{\text{Off}}\underline{\text{line}}$ module DrumPhotonGeneratorOG. The angular distribution of emitted photons is perfectly Lambertian, with a maximum emission angle of 25°.[7] Unlike the real-world drum, the simulated drum is not a physical object and cannot pick up photons traveling through the aperture outward.

[7] *This is a free parameter and the chosen value represents the properties of the real drum.*

The ray-tracing was done with the TelescopeSimulatorKG_DEV using three different mirror configurations:

1. A hypothetical ideal mirror with purely specular reflection, further on referred to as simply the "ideal mirror".

2. A mirror with a height-dependent dust layer resulting in non-specular reflection described by the distributions detailed in Subsec. 4.2.1, further on referred to as the "measured mirror".

3. As in the previous point, with an additional absorption of 3 % and 9 % along the top and bottom edges of the mirror, respectively, and linear interpolation between the two extremes.[8]

[8] *A 6 % difference in absorption between the top and bottom parts of the mirror was found in [133] and a comparable result was obtained in [140]. A +3 % offset in absorption across the entire mirror surface is simply equivalent to overall lower mirror reflectivity.*

Regardless of configuration, all simulated drum calibration constants shown in Fig. 4.18 share a common trend: A large-scale modulation spanning across all pixels and a smaller-scale modulation with a period of 20 pixels. The latter is related to stepping through a column of 20 pixels, each seeing a different projection of the aperture. In fact, the farther away from the optical axis a pixel looks, the smaller the projection of the aperture it sees. Notice that the calibration constant is always highest for the $(20n_{\text{col}})^{\text{th}}$ pixel in a given column n_{col}. This is because those bottom-most pixels on the camera, corresponding to maximum elevation angles, are additionally shadowed by the camera support.

Comparing the absolute values of the simulated drum calibration constants, there is little difference between the ideal and the measured mirror. This is, in fact, expected because photons scattered away from the specular direction of

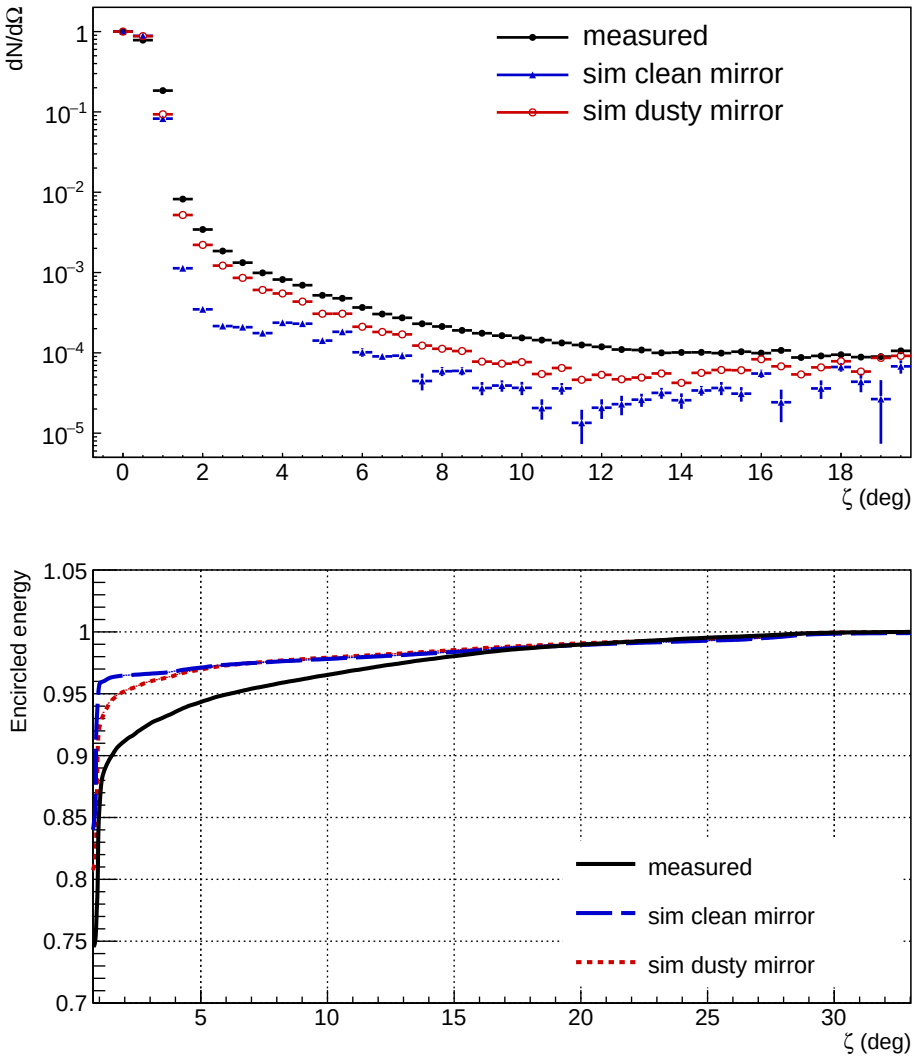

FIG. 4.17 The differential (top) and cumulative (bottom) PSF as measured by the Octocopter in this work (black solid circles/line), simulated with enhanced PMT reflections and a clean mirror (blue upward triangles/dashed line), and as before but with a height-variable dust layer on the mirror (red open circles/dotted line). The differential curves are scaled to be 1.0 in the first bin, and the cumulative ones are normalized to 1.0 at 33°.

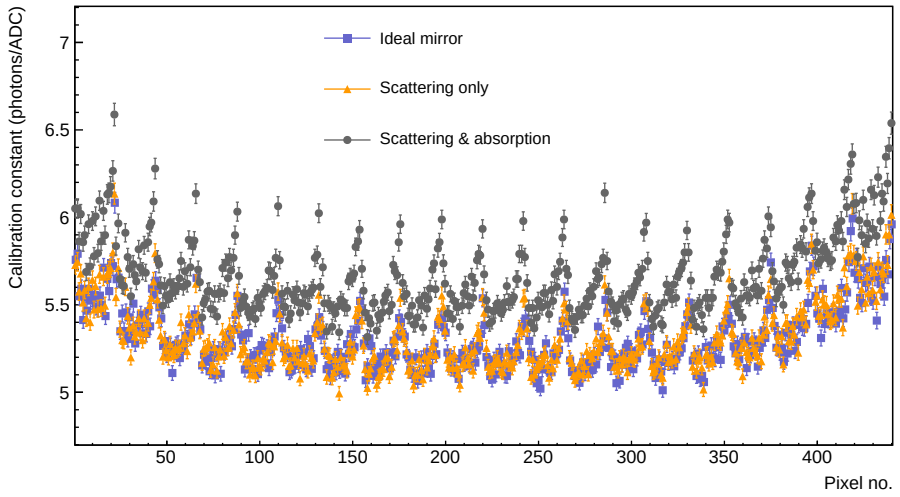

FIG. 4.18 Drum calibration constants simulated with three different mirror configurations: the ideal mirror (cyan squares), the measured mirror (orange triangles), and the measured mirror with additional absorption (gray circles). Only statistical errors are shown.

reflection are simply detected by neighboring PMTs, save for at the very edges of the camera. Absorption, on the other hand, does affect the calibration constants. For one, there is a global shift to higher values indicative of a lower detection efficiency. Moreover, the amplitude of the intra-column modulation increases in accordance with the height-dependent absorption.

Those differences are best understood by examining the ratios of calibration constants simulated with different mirror configurations shown in Fig. 4.19. The ratio for the ideal and measured mirror fluctuates about 1.0, with an average value of 0.999 ± 0.001 for the entire camera. It is thus compatible with unity and we conclude that drum calibration constants do not change significantly if photons scatter on the dust on the mirror.

In contrast, the camera-averaged ratio of calibration constants for the measured mirror without and with additional absorption is 0.938 ± 0.001. Moreover, the ratio systematically varies by $\sim$4 % within any given column. The 6 % overall shift corresponds to the average absorption on the mirror (3 % and 9 % along the upper and lower edge, respectively, with an interpolation for the central region) and the modulation reflects the height-dependence of the absorption coefficient. Notice that the amplitude of the intra-column modulation is by about 2 % smaller than the difference in absorption coefficients across the mirror. This can be traced back to the fact that each pixel receives light from slightly different regions of the mirror, although those regions largely overlap. In particular, as is shown in Fig. 4.20, the illuminated area of the mirror is defined by the projection of the aperture onto the mirror along the viewing direction of the target pixel. Given a 2.2 m circular aperture, about $^2/_3$ of the mirror are illuminated vertically. While the central region of the mirror is always illuminated, the illumination of the

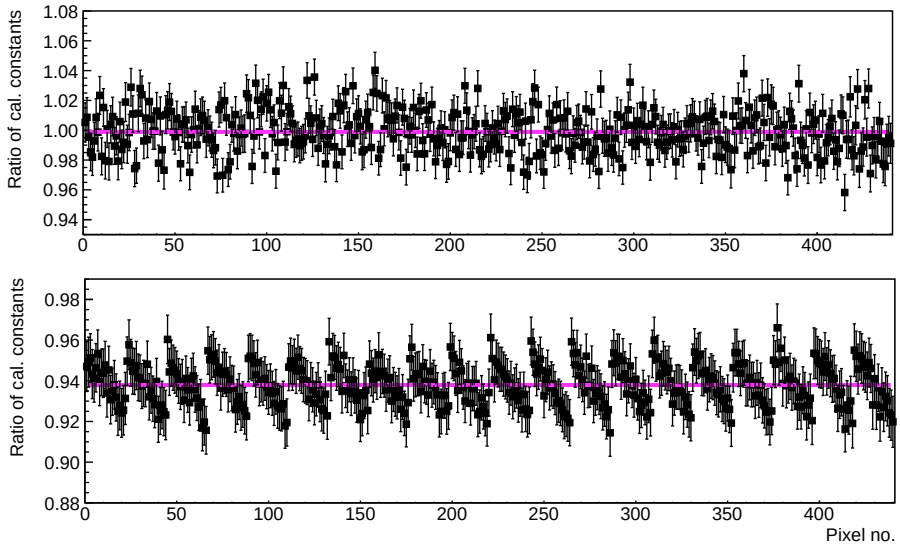

FIG. 4.19 Ratio of drum calibration constants simulated with different mirror configurations. Top: the ideal mirror relative to the measured one, bottom: the measured mirror relative to measured with additional absorption. The magenta lines indicate the mean ratio for the camera. Only statistical errors are shown.

peripheral parts is pixel-dependent. It is this averaging that causes the calibration constants to reflect the full range of the absorption coefficients only partially.

In summary, we have learned that drum calibration constants are sensitive to absorption but in first approximation not to scattering on the mirror, or more generally the PSF. This finding has important implications for the detection of air showers, which are investigated in the upcoming section.

4.2.4 Effect on reconstructed shower variables

The extent to which deposited aerosols on the mirror affect shower detection is closely related to how they enter into drum calibration constants. As was shown in the previous section, absorption is to a large extent taken into account, whereas non-specular reflection goes unnoticed. Therefore, in the following we focus on the effect of non-specular reflection on reconstructed shower variables.

Over 50 000 showers were simulated in the energy range $10^{17.5}$–$10^{19.5}$ eV, half protons and half iron nuclei, using CONEX, v2r4.44[9] [141], and the hadronic interaction model SIBYLL [44]. Basic geometry- and profile-related quality cuts listed in App. B were applied, leaving about 1500 events in each of the five energy bins. No fiducial FOV cuts were applied.

[9] *CONEX is an EAS simulation program based on a one-dimensional hybrid approach.*

Two different mirror configurations were used: the ideal and the measured mirror (see Subsec. 4.2.1 to review the definition). Very importantly, what we refer to as “consistent scenarios” were simulated. This means that both, the drum calibration constants as well as the air showers were simulated using the same mirror configuration, which is equivalent to the mirror condition being

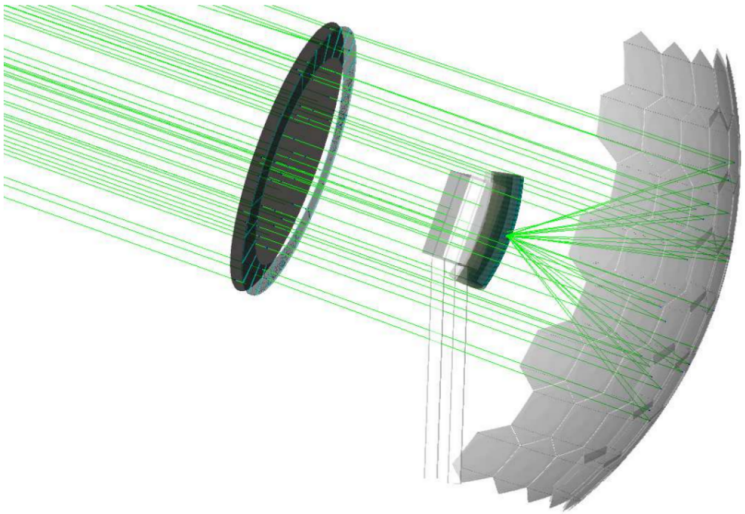

FIG. 4.20 The illuminated region of the mirror is defined by the projection of the aperture along the viewing direction of the target pixel. From [55].

frozen in time. Since we are merely interested in a comparison of the two mirror configurations, no lateral width correction (LWC) was applied during reconstruction.[10]

[10] *Reminder: The LWC is a data-based correction that accounts for the light falling between ζ_{opt} and $\zeta_{\text{LWC}} = 4.0°$.*

Calorimetric Energy

Let us first investigate the effect on reconstructed calorimetric energy, which, for the sake of clarity and unless stated otherwise, is referred to simply as "energy" for the remaining part of this section.[11] Plotting the relative difference of the reconstructed and generated energies as a function of generated energy in Fig. 4.21, we immediately see a reconstruction bias even for the ideal-mirror curve. This energy-dependent bias is well-known and is standardly corrected for, however, since we are simply interested in the comparison of the two curves, the correction is irrelevant here and not applied.

[11] *The reconstructed calorimetric energy is a better estimator than the total reconstructed energy, which may be biased by the invisible energy correction that accounts for muons and neutrinos not depositing their full energy in the atmosphere.*

To be able to better appreciate the change due to the dust on the mirror, the difference of the reconstructed energies for the two mirror configurations relative to the generated energy is plotted in Fig. 4.22. Rather flat across all energies, the mean difference is -0.033 ± 0.001, i.e. the reconstructed energy of an air shower detected with the measured mirror is on average 3.3 % lower than that of one detected with an ideal mirror. The magnitude of the effect is in good agreement with expectations based on the distribution of mirror-reflected light (c.f. Subsec. 4.1.5): 0.7 % and 7.1 % are scattered out of the target pixel by the upper and lower parts of the mirror, respectively, so 3.9 % on average. Provided that the LWC is dominated by the telescope PSF and given that the resultant shift in reconstructed energies ranges from 6.2 % to 10.1 % depending on energy (see Fig. 3.18), the observed bias due to scattering on the mirror will be compensated for in reconstruction.

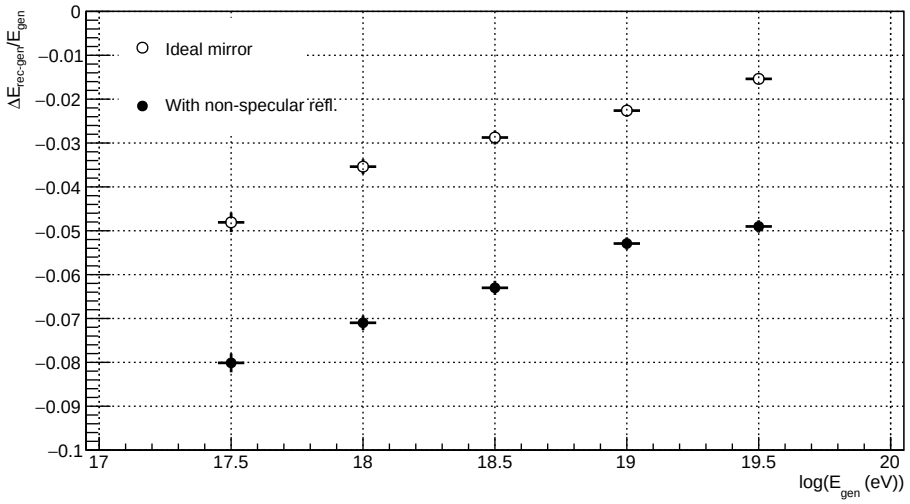

FIG. 4.21 The difference between the reconstructed and generated energies as a function of the logarithm of the generated energy for two different mirror configurations: the ideal (open) and the measured mirror (solid circles).

Depth of Shower Maximum $X_{\max}$

A similar study was performed for the depth of shower maximum $X_{\max}$. The absolute difference in reconstructed and generated values of $X_{\max}$ for both mirror configurations is depicted in Fig. 4.23. By differentiating between protons and iron nuclei, naturally deeper and shallower showers are selected. Fig. 4.24 shows the corresponding difference in reconstructed $X_{\max}$ for the measured and the ideal mirrors. Above 10^{18} eV, the difference is a minuscule (1.6 ± 0.5) g/cm^2 and (1.7 ± 0.5) g/cm^2 for protons and iron nuclei, respectively. Compare this to $\sim$795 g/cm^2 for protons and $\sim$700 g/cm^2 for iron nuclei predicted by simulations at 10^{19} eV [142].[12] In the lowest energy bin at $10^{17.5}$ eV, the difference is (4.2 ± 1.2) g/cm^2 for both species. This comparatively larger difference arises due to a cut that requires the $X_{\max}$ to be within the FOV of the telescope: Some of the shallow showers that just do not make the cut for the ideal mirror are pushed slightly deeper by the measured mirror, just barely clearing the cut.

[12] *The predictions differ somewhat depending on the used hadronic model, but generally agree within approximately* $\pm 10\,g/cm^2$*, see e.g. Fig. 2.25.*

The mean shift across all energies amounts to (2.9 ± 0.9) g/cm^2 and is an additional systematic uncertainty of the measurement of $X_{\max}$, currently estimated to be less than 10 g/cm^2 for all energies [83]. However, this systematic shift resulting from a height-dependent dust layer on the mirror would be difficult to observe in measured data, e.g. by comparing air showers detected within a time period before and after cleaning a mirror, for it is small in comparison to the currently achieved resolution of $X_{\max}$ in hybrid reconstruction, ranging from 26 g/cm^2 at $10^{17.8}$ eV to 15 g/cm^2 at $10^{19.3}$ eV [83].

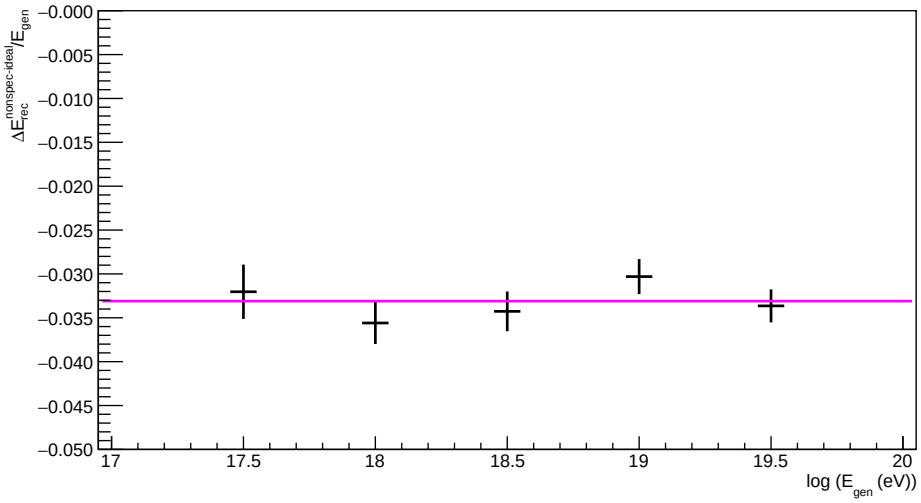

FIG. 4.22 The difference in the reconstructed energies of an air shower detected by the measured and the ideal mirror, respectively, shown as a function of the logarithm of the generated energy. The horizontal line represents the mean value of $-3.3\,\%$.

Optimum Integration Region ζ_{opt}

One may ask the following question: How does the optimum integration region defined by ζ_{opt} change when the ideal mirror is covered with a dust layer? A comparison of ζ_{opt} values obtained for the ideal and measured mirror is shown in Fig. 4.25. Averaged over all energies, ζ_{opt} increases by a negligible 0.02° when photons are made to scatter on the mirror. It follows that ζ_{opt} is a rather robust parameter with respect to the PSF of the mirror and is dominated by the intrinsic lateral width of the air showers or by the PSF of other telescope components than the mirror.

Inconsistent scenarios

So far we have only discussed consistent scenarios in which the simulated telescope is in the same configuration during drum calibration and the detection of air showers. In reality, however, inconsistent scenarios are bound to occur. Surely, the dust layer on the mirror and other optical elements changes with time, and since no calibration system currently tracks those dust layers (although cleaning procedures are logged [143]), their effect will propagate into reconstructed variables, particularly energy.

Because the extent to which reconstructed shower variables are affected is directly proportional to the sensitivity of the drum calibration to the effect under investigation, the outcome of inconsistent scenarios can be reasonably well predicted. There are two extreme cases – performing drum calibration with a dusty mirror and detecting showers with a perfectly clean mirror and vice versa – both of which we shall compare to a clean-telescope consistent scenario.

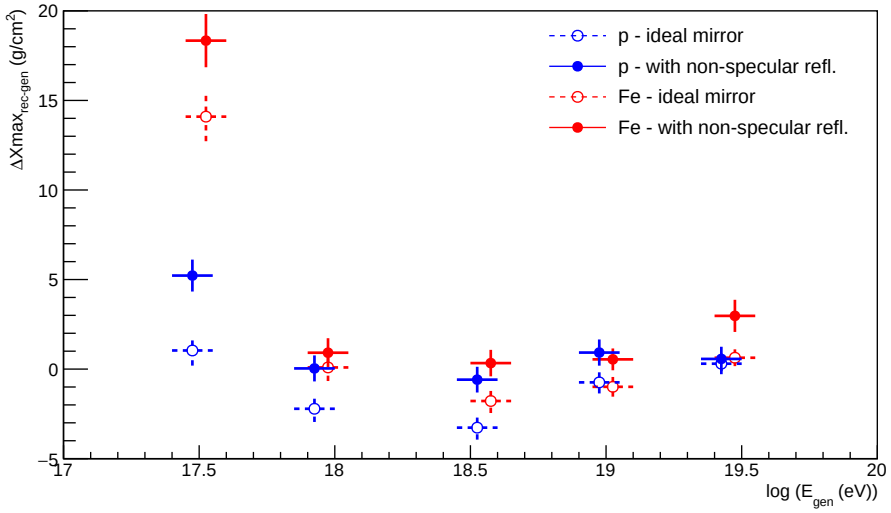

FIG. 4.23 The difference of reconstructed and generated $X_{\max}$ values simulated with the ideal (open) and the measured mirror (solid circles) as function of the logarithm of the generated energy, shown for protons (blue) and iron nuclei (red circles) separately.

In the first case, i.e. dusty during drum calibration and clean during shower detection, shower energies will be overestimated in proportion to the mean absorption coefficient of the dust layer on the mirror. For the specific simulation input used here, this amounts to +6.2 %. In the second case, shower energies will be underestimated in proportion to the mean absorption coefficient as well as the amount of scattering. Again, for this specific simulation, by −9.5 %. However, this scenario is rather unlikely to occur, for dedicated cleaning procedures are generally not performed before drum calibration. It is important to point out that while a PSF-dominated LWC will compensate for the impact of scattering on the mirror, it will not – and by design does not – correct for absorption, as the absolute level of the signal within ζ_{opt} remains unchanged. Additional absorption on the optical components will thus always cause the energies to be underestimated.

4.3 MUG-6 Filter Transmittance

Once it was clear that the dust layer on the mirror led to substantial scattering, naturally the question arose: Does the same behavior occur on the MUG-6 filter? The filters are fully exposed to the outside environment and can accumulate substantial dust layers, as is evident from the photograph in Fig. 4.26. To answer the posed question, a dedicated in situ measurement of the filter properties was needed. Again a relative measurement was done, this time designed to determine the effect of a dust layer on filter transmittance and the transmission function.

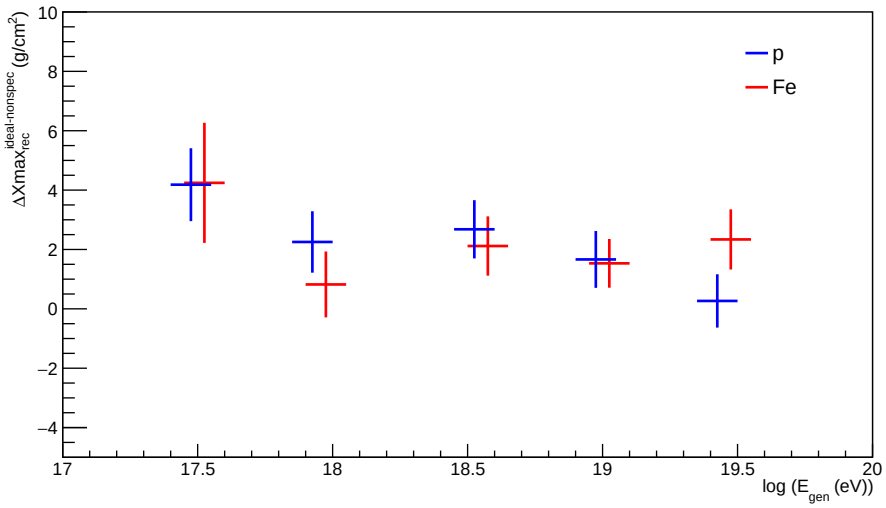

FIG. 4.24 The difference of reconstructed $X_{\max}$ values simulated with the ideal and the measured mirror as a function of the logarithm of the generated energy, shown for protons (blue) and iron nuclei (red) separately.

4.3.1 Idea of the measurement

The basic idea of the measurement is as follows:

1. Attached a collimated light source to the outside of the MUG-6 filter such that the beam neither passes through the corrector ring, nor hits the back of the FD camera.

2. Position a screen inside the telescope bay, about halfway between the mirror and the FD camera, with the beam striking roughly head-on.

3. Record the image of the beam on the target screen with a light detector. In our case, we used a CCD camera mounted close to the CC of the mirror.

4. "Rinse and repeat." Without changing anything, carefully clean the part of the filter through which the beam passes and repeat the measurement.

The beauty of this measurement lies in the fact that, just like in the mirror measurement, systematic uncertainties cancel in the comparison, if properly carried out.

4.3.2 Experimental setup, data acquisition and analysis

Experimental setup

As this measurement shares many features with the mirror measurement described in Sec. 4.1, several of the proven analysis methods and pieces of equipment were re-used. The CCD camera and the target screen were the same as

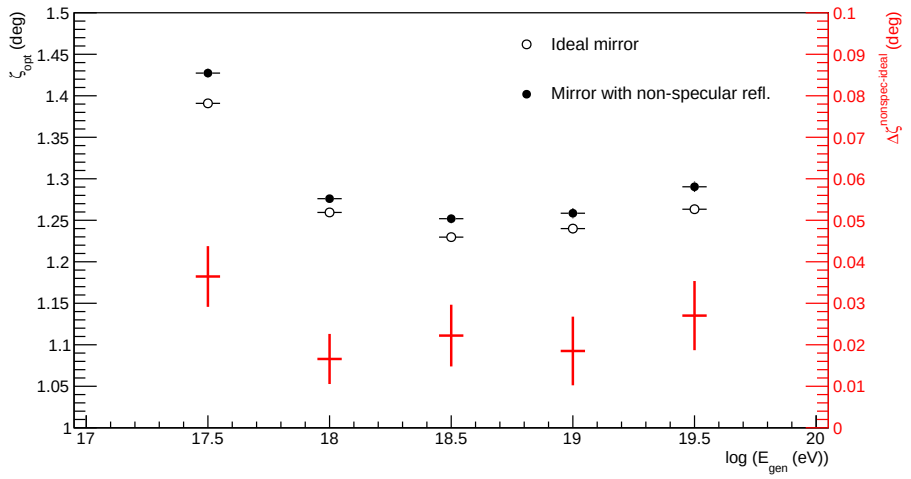

FIG. 4.25 ζ_{opt} obtained for the ideal (open) and the measured mirror (solid circles) as a function of the logarithm of the generated energy. The difference between the latter and the former is indicated by red crosses with the corresponding scale on the right-hand side of the plot.

detailed in Subsec. 4.1.2. The light source – a custom-modified laser pointer – was of course different.

The original laser pointer, model GLS-405 from Roithner LaserTechnik [137], has a peak wavelength of 405 nm and an output power of 20 mW. Even though the quoted beam divergence is below 0.5 mrad, the 2 mm diameter exit aperture does not produce a sufficiently parallel beam, so a custom-made cylindrical aluminum casing, 20 cm long and 2.5 cm in diameter, was constructed to provide further collimation.

Photons emitted by the laser pointer first pass through a 2 mm pinhole and are focused by a lens with a focal length $f = 150$ mm. The larger focal length, the narrower the resultant beam profile. Finally, photons exit the aluminum housing through a window 20 mm in diameter made of MUG-6 glass. Photos of the light source mounted on the outside of the LA1 filter are shown in Fig. 4.27.

The target screen was mounted on a tripod positioned at a distance of 2333 mm from the filter, facing towards the aperture, and was viewed by the CCD camera mounted on the fixed-point structure close to the CC of the mirror. The setup is photographed in Fig. 4.28. The alignment of the individual components was such that the beam struck the filter and the target screen roughly perpendicularly ($\pm 5°$) and the CCD camera viewed the target screen as head-on as possible.

Data acquisition and analysis

Three different positions on the MUG-6 filter were measured to make sure that the narrow light beam was not passing through some anomalous part. In two cases, a series of measurements was done before and after cleaning, and in one case only the uncleaned filter was measured. As with the mirror measurement, a large

Fig. 4.26 The condition of the MUG-6 filter at LA1 in March 2014 before (left) and after (right) cleaning. The white spots on the uncleaned filter are bat droppings. Photos courtesy of Kai Daumiller and Hans Klages.

Fig. 4.27 The custom-modified laser pointer mounted on the outside of the aperture of LA1 in March 2014. Left: The beam passes through the dusty filter, making sure not to hit a patch of bat excrement. Right: The very same setup, after the relevant filter part had been cleaned. Photos courtesy of Hans Klages.

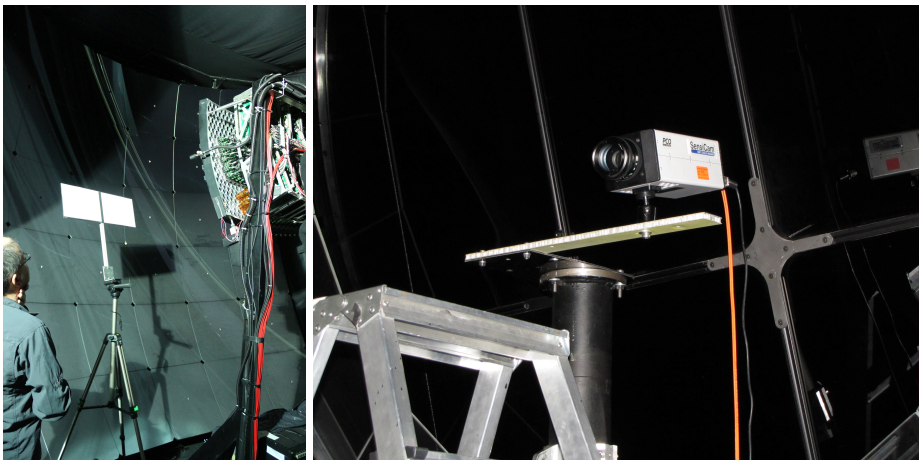

FIG. 4.28 Left: The paper-covered target screen mounted on a tripod in the telescope bay. Right: The CCD camera, viewing the target screen, was mounted on a custom-made aluminum bracket screwed onto the fixed-point plate. After finalizing the setup, the ladder seen in the foreground was of course removed. Photos courtesy of Kai Daumiller.

dynamic range of signal must be covered, and all combinations of position and filter condition were acquired with three different exposure times: 4 s, 40 s and 400 s. An example of a 400 s background-subtracted frame is shown in Fig. 4.29.

Each point represents the ratio of background- and dark-frame counts (indicated by the color scale) in one CCD pixel. The numbers on the axes correspond to the row- and column-coordinate of the pixel on the chip (here, as well as in subsequent plots of this type).

With a few exceptions, the CCD image analysis was adapted from the mirror measurement. In particular, the background, hot pixels, the distance calibration, non-linearity due to charge loss, and determination of the image CG were handled in the same way as detailed on pages 62 to 70.

The factors for converting distances on the CCD chip in pixels to physical distances on the target screen were found to be

$$k_x = 0.6003\,\mathrm{mm/pix}, k_y = 0.6061\,\mathrm{mm/pix}. \tag{4.6}$$

Again, as in the mirror measurement, both were found to be constant across the FOV of the camera, meaning that the viewing angle was perpendicular enough not to skew the images observably.

The conversion from distance on the target screen to the scattering angle at the aperture is straight-forward in this case. The angular deviation from the specular direction of transmission

$$\delta = \arctan \frac{d_{\mathrm{ts}}}{R_{\mathrm{ts}}}, \tag{4.7}$$

where d_{ts} is the distance from the CG of the image on the screen, and $R_{\mathrm{ts}} = 2333\,\mathrm{mm}$ is the distance from the point on the MUG-6 filter through which the

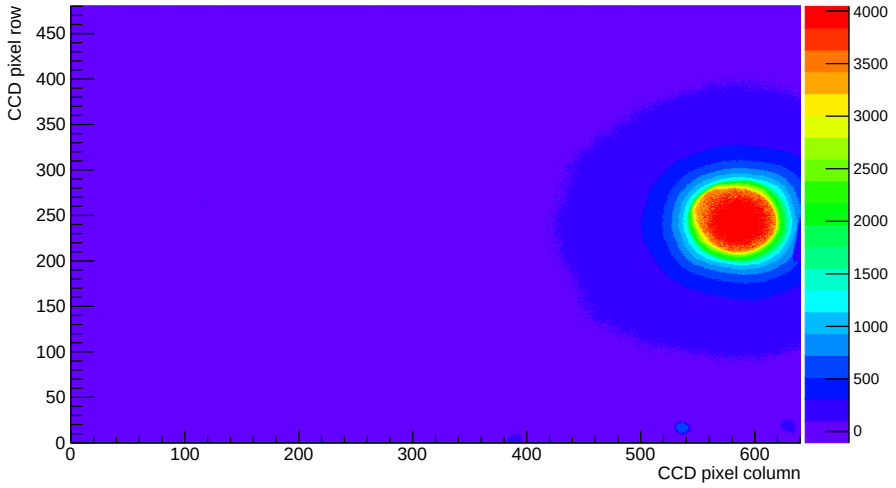

FIG. 4.29 A background-subtracted signal frame showing the image of the light beam passing through an uncleaned MUG-6 filter. The number of counts in each pixel is indicated by the color scale.

beam passes to the target screen. Accordingly, the size of one pixel on the CCD chip corresponds to $\sim$0.015°.

4.3.3 Final distribution functions

The final distributions were again stitched together (c.f. Subsec. 4.1.4) from three frames taken with exposure times ranging from 4 s to 400 s. Within statistical fluctuations, the same results were obtained for all three positions on the filter and their average is used henceforth.

Fig. 4.30 depicts the cumulative distributions for the cleaned and uncleaned filter scaled by a common factor, such that the former is 1.0 at 4.6°, i.e. the angular range of the measurement. There is a substantial difference between the curves: The total amount of light detected within $\delta = 4.6°$ is 11 % lower for the uncleaned filter. The missing 11 % are absorbed, scattered at large angles or even back-scattered.

This finding has important implications for shower measurements, because they are affected differently by large-angle scattering at the aperture than drum calibration. In particular, air shower photons that back-scatter on the aperture will be permanently lost, whereas drum photons will re-enter the drum and be re-emitted with a probability proportional to the reflectivity of the drum interior and transmittance of the front Teflon face. A 4 % correction is applied to the drum intensity measured in the dark room to compensate for reflections in the aperture (c.f. Subsec. 3.1.1), however, while this correction is frozen in time, the dust layer is not. Whether any large-angle scattering on the aperture will be properly accounted for depends on the difference in the condition of the filter at the time the correction was devised and the time of the actual air shower (or CLF, or Octocopter) measurement.

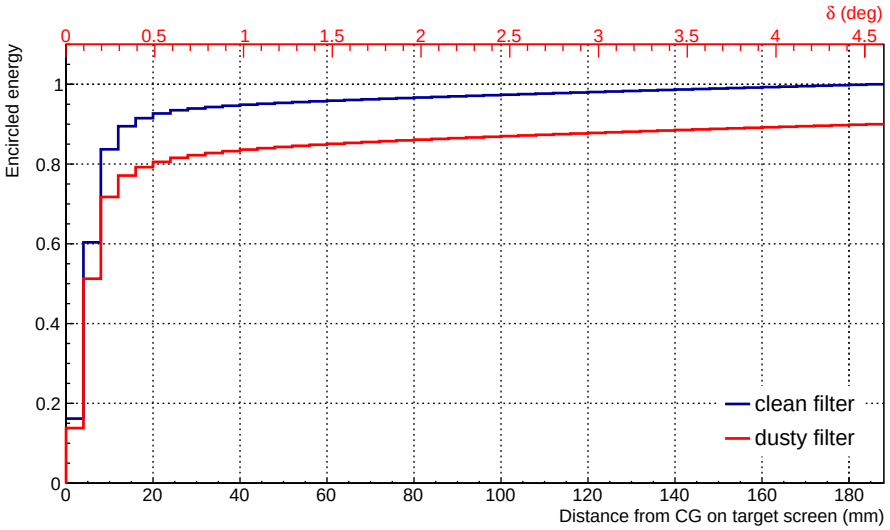

FIG. 4.30 The cumulative distribution functions for the cleaned (blue) and uncleaned (red) filter, both scaled by a common factor such that the clean-filter curve is 1.0 at 4.6°. The difference in the total amount of detected light is 11 %.

The interpretation of the shape of the final distributions, shown in Fig. 4.31 in their differential form, is more complicated than in the mirror measurement, where the image is focused into one point and any widening results from imperfections of the reflector. In this case, the quasi-parallel light beam has an intrinsic angular distribution, which must be unfolded from the final measured distributions. Because previous studies of clean filter segments in the laboratory have found the scattering component to be negligible [144, 145], we make the simplifying assumption that a clean filter transmits light perfectly specularly and thus the clean-filter intensity profiles simply reflect the divergence (albeit small) of the light beam. Only the difference between the distributions measured before and after cleaning arises due to scattering on the dust layer.

The effect of the dust layer was isolated by forward-folding the clean-filter distribution with various potential smearing functions. The best results were obtained for a Gamma distribution with a shape parameter $k = 0.8$ and a scale parameter $\alpha = 0.1$:

$$\mathrm{d}N/\mathrm{d}\delta = \frac{1}{\Gamma(k)\alpha^k}\delta^{k-1}\exp\left(-\frac{\delta}{\alpha}\right) = \frac{6.31}{\Gamma(0.8)}\delta^{-0.2}\exp\left(-10\delta\right), \tag{4.8}$$

where δ is the angular deviation from the specular direction in radian and α was chosen to replace the customarily used θ for the scale parameter to avoid any confusion with the angles used to describe the telescope viewing directions.

Fig. 4.32 shows the differential smearing function for an uncleaned MUG-6 filter. Integrating over a phase space of 2π up to the range of the measurement of 4.6° and interpreting the distribution with respect to the center of a given pixel, 2.5 % of all photons arriving from within the FOV of that pixel are scattered and detected by other pixels. At the contrary to the mirror measurement,

the smearing function was not interpolated to larger angles here, because it is qualitatively different: it has a flat tail in $\mathrm{d}N/\mathrm{d}\delta$, hence the integral of a simple flat extrapolation would not converge. In the following paragraphs, a plausible explanation for the differing scattering distributions of the filter and the mirror is given in terms of aerosol size.

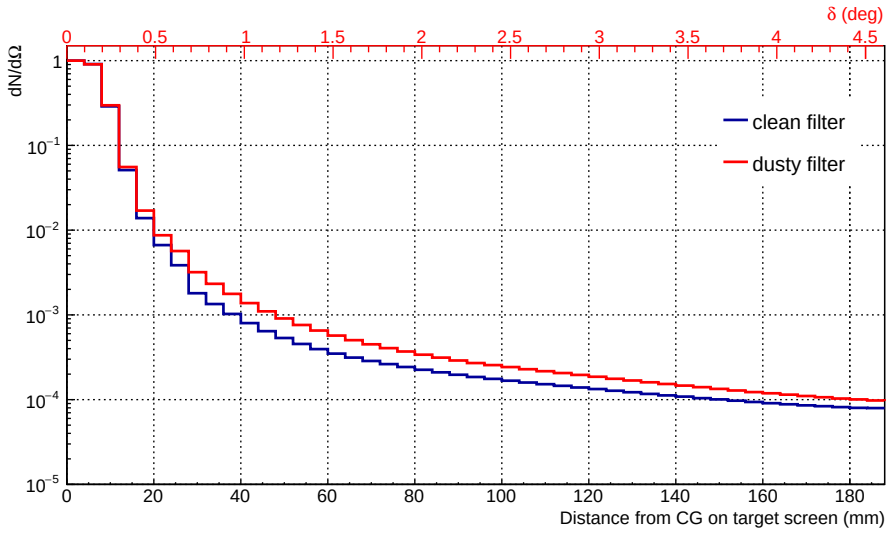

Fig. 4.31 The differential distribution functions for a clean and dusty MUG-6 filter. Both are scaled to be 1.0 in their first bin to allow for easy comparison.

Aerosol size

Scattering on the dust layer on the filter and the mirror can be interpreted as Mie scattering on aerosols. In this sense, those dust layers are no different to the aerosols dispersed in the atmosphere, except they are confined to a thin layer. The angular distribution of Mie-scattered light depends on the ratio of the aerosol size d_a to the photon wavelength λ, and will generally be strongly forward-peaked for $d_a \gg \lambda$. The angular pattern gradually becomes more isotropic as the ratio d_a/λ approaches unity.

The distributions of mirror-reflected and filter-transmitted light indicate that, within the overlapping measured range of 4.6°, more scattering occurs on the dust on the mirror than on the uncleaned filter. It is conceivable that the dust layer on the mirrors and the filters is different in granularity. The mirrors are housed inside the FD buildings and are protected from the outside environment even during data acquisition, as the aperture is fully closed off by the MUG-6 filter. Aerosols get into the buildings through doors as staff enter, or through the air conditioning system, which filters large particles. The MUG-6 filters, on the other hand, are fully exposed to the outside atmosphere during shower detection.

In November 2013, immediately after the mirror measurement campaign, the aerosol size distribution inside the bay LL5 was measured using a portable laser

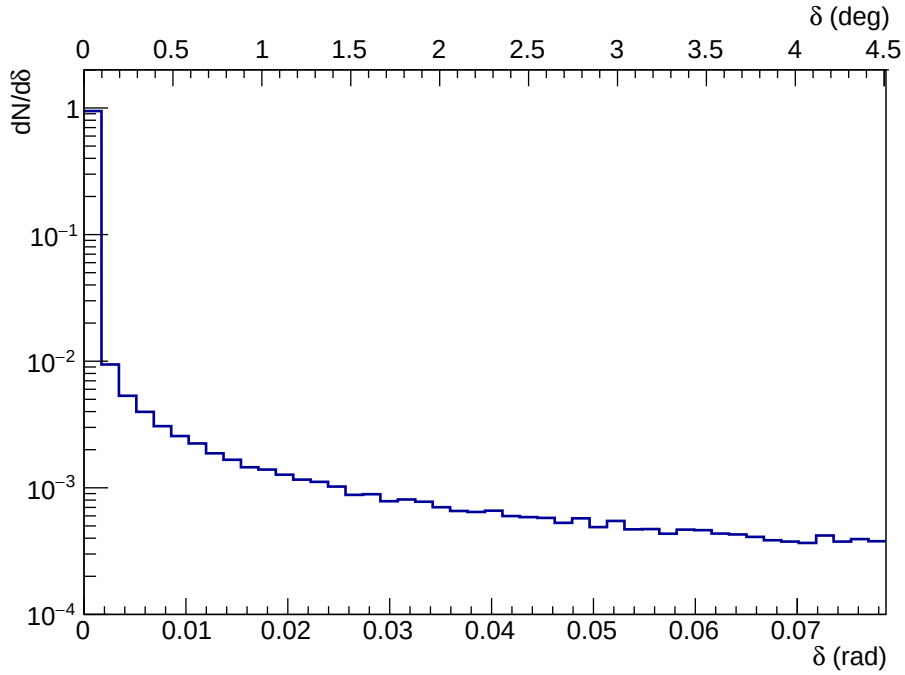

FIG. 4.32 The normalized differential smearing function for a dusty MUG-6 filter is best described by a Gamma distribution.

Mirror part	Mean aerosol size (μm)
Top	0.298
Center	0.311
Bottom	0.326

TAB. 4.1 The mean diameter of aerosols detected close to the top, center and bottom of the LL5 mirror in November 2013.

aerosol spectrometer and dust monitor Grimm 1.109 [146].[1] To characterize the aerosol sizes at different heights from the ground, the instrument was put in three positions: close to the top edge of the mirror, roughly in the center and close to the bottom edge. The obtained aerosol size distributions are depicted in Fig. 4.33. Interestingly, the larger aerosol sizes are found closer to the ground. The mean size for all three positions is 311 nm, which is commensurate with the wavelength of 375 nm used in the mirror measurement. The average sizes for the different positions are broken down in Tab. 4.1. While no data set of comparable quality is available for the outside environment, it is plausible that the grain size of the filter dust layer is larger, leading to the different, potentially more asymmetric, angular distribution of scattered light on the uncleaned MUG-6 filter.

[1] The device and data read-out was kindly provided by M. Micheletti of the Institute of Physics Rosario, Argentina.

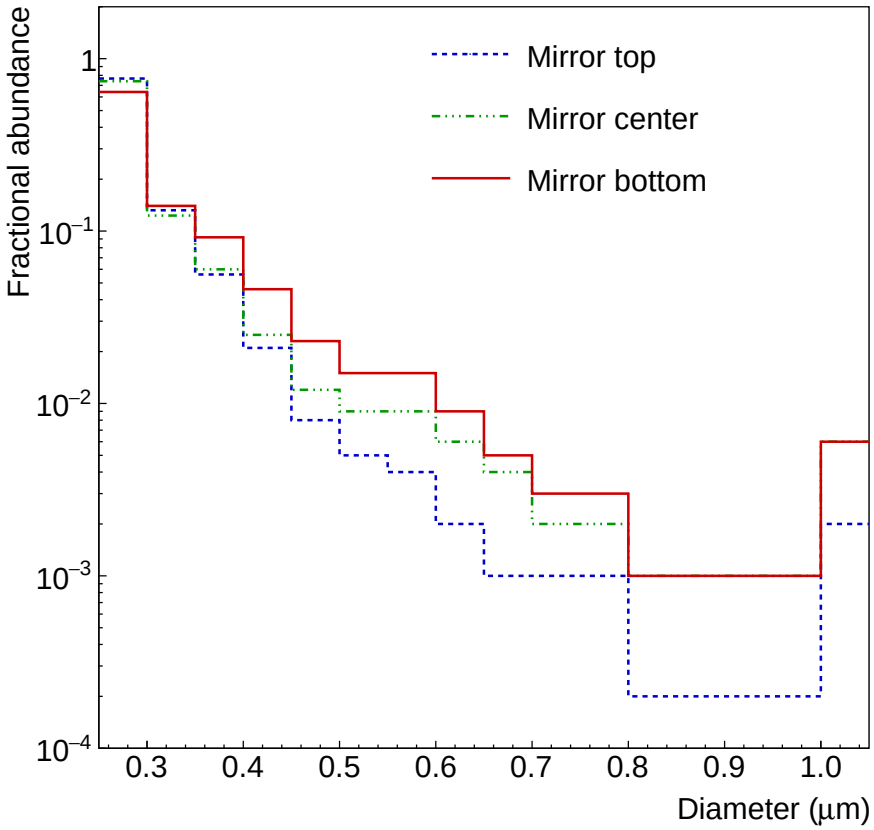

FIG. 4.33 The size distribution of aerosols detected close to the top, center and bottom parts of the LL5 mirror in November 2013. All curves are normalized to the total number of particles detected. The last bin of the histograms contains all aerosols with sizes greater than 1.0 μm.

4.3.4 Comparison to other measurements

Independent measurements were sought to confirm the results of the filter measurement, in particular in relation to the large observed attenuation on the dust layer. They include:

- CLF laser shots,
- drum calibration, and
- CalC.

The first measurement – detection of laser shots fired by the CLF – is a shower-like method in the sense that any photons back-scattered on the aperture will be permanently lost. In contrast, the second and third measurements are both performed with some kind of a reflector in the telescope aperture that is capable of feeding photons scattered at large angles back into the telescope (e.g. the drum, the CalC Tyvek patches or simply the aluminum shutters).

Integration region ζ (°)	Effect (%) HE1	CO3
1.0	14.5	11.6
2.0	12.8	10.1
3.0	12.1	9.7

TAB. 4.2 The effect of filter cleanings based on the change in the ratio of CLF signals detected by CO3 and HE1. From [140].

Detection of CLF laser shots

The CLF probes the atmosphere above the ground array with several hundred pulses on each measurement night. Roughly equivalent to an air shower with an energy of 10^{19} eV, the laser tracks are detected by one telescope at each FD site and the aerosol content in the atmosphere can be deduced. As is shown in Fig. 4.34, Coihueco and HEAT view the CLF laser beam from nearly the same position. If the filter of one telescope is cleaned, the other can be used as a reference, with atmospheric effects and other variations canceling.

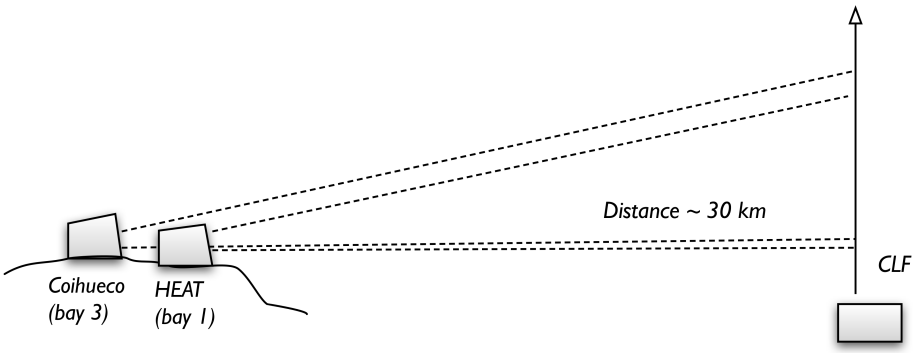

FIG. 4.34 The telescopes CO3 and HE1 measure the same CLF shots from nearly the same position. Variations in laser energy and atmospheric conditions are thus practically identical. From [147].

A dedicated filter cleaning campaign was carried out in March 2014 with HEAT in the downward position, i.e. having an overlapping FOV with Coihueco . Filters at HE1 and CO3 (last previous documented cleanings of both in January 2011 [143]) were cleaned on the 4^{th} and 7^{th} of March, respectively, and the associated changes in the relative detected signal from the CLF were studied [140]. Fig. 4.35 shows that the ratio of detected signals dropped by nearly 13 % following the cleaning of the HE1 filter, only to be restored almost to its original value once the CO3 filter was cleaned as well. Due to the apparently different PSFs of the telescopes, the magnitude of the step depends on the radius of the integration region. The results for three different integration regions are listed in Tab. 4.2.

As the size of the integration region increases, gradually more scattered photons are summed and the effect of the dust layer decreases. At 3.0°, it is 10.9 %, which is in excellent agreement with the 11 % at 4.6° found in Subsec. 4.3.3.

To assess how quickly the dust layer forms, the measurements were repeated in November 2014, but this time only the filter of HE1 was cleaned. The observed

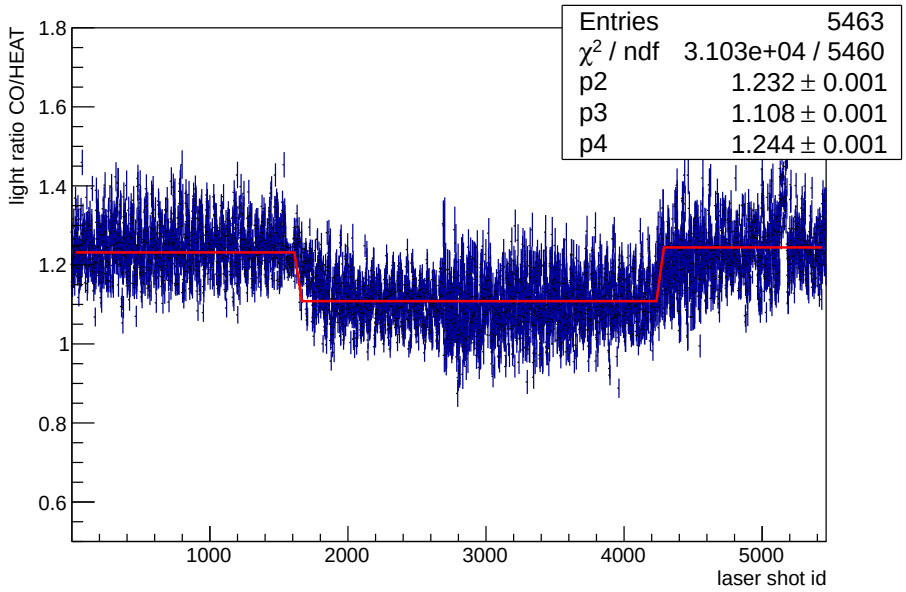

FIG. 4.35 Ratio of CLF signals detected by the telescopes CO3 and he1 over eight days in March 2014. The two steps correspond to the filter cleanings, first at he1, then at CO3. From [140].

change in the ratio was only 1–2 % lower than in March 2014, meaning that the dust layer has rebuilt almost completely over only nine months of operation. Following this realization, a strict cleaning schedule was implemented, with the filters of each FD site being cleaned once every four months [148].

Drum calibration

During the absolute FD calibration campaign of April 2014, a particularly dusty filter (LM1) was cleaned (last previous documented cleaning in June 2006 [143]). Drum calibration was performed before and after the cleaning and the response of the clean aperture was found to be 5 % higher [101]. However, based solely on the drum measurement it is not possible to disentangle enhanced transmittance of the cleaned filter from potential enhanced back-reflections, as both would result in an increase of the light flux at the FD camera. Therefore, this seemingly small effect of 5 % cannot be directly compared with the shower-like laser pointer measurement and the CLF shot reconstruction results.

Since about 12 % of light is lost on a dusty aperture in shower-like measurements and the drum observes only a 5 % loss, there must be mechanisms at play, large-angle scattering being the prime candidate, which feeds photons back into the telescope. Ultimately, unlike shower-like measurements, the drum is only partially sensitive to the dust on the aperture and does not appear to see 7 % of the total attenuation caused by the dust layer.

CalC

Another way to study the effect of a dusty aperture is to compare the CalC response before and after cleaning. To ensure that the changes in the response are not driven by gain changes of the PMTs, the ratio of the response to CalC at 375 nm and CalA, denoted with CalC/A in the following, was investigated, too.

The time progressions of the different responses, averaged over all pixels of the LA1 camera, are shown in Fig. 4.36. At first sight, there is no striking jump between the March and April 2014 shifts, when the cleaning procedure took place. Notice that this is the very same cleaning procedure at LA1 that was studied in the dedicated laser pointer measurement described at the beginning of this section and saw an 11 % effect.

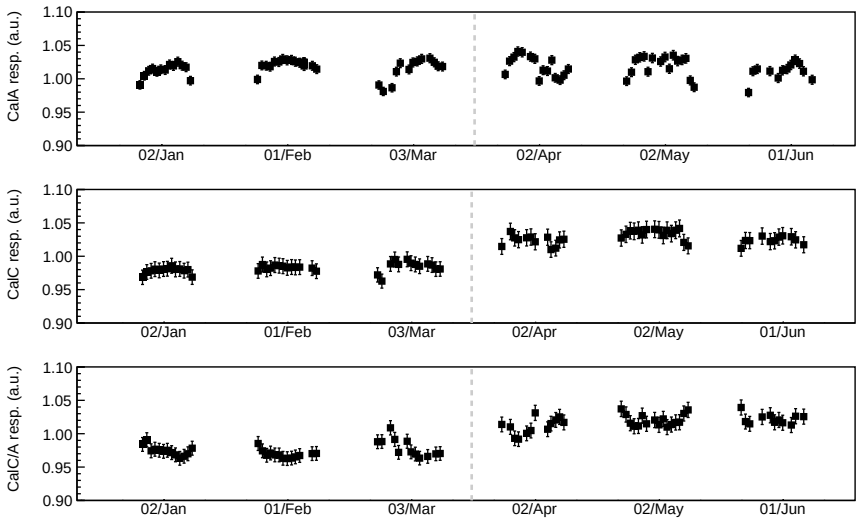

FIG. 4.36 Top to bottom: The mean camera response to CalA, CalC, and their ratio CalC/A shown for the time period of three months before and after the cleaning of the filter. Recall that CalA monitors only the PMT response and is shown as a reference. The LA1 filter was cleaned between March and April 2014 (indicated by the gray dashed line). Being relative calibration systems, all responses are shown relative to their mean response.

Comparing the ratio CalC/A averaged over the shift immediately preceding and following the cleaning reveals a minuscule change of (3.8 ± 0.3) %.[13] In [88], the complete relative calibration data set up to 2012 had been analyzed and the change in the ratio of the CalC and CalA response following filter cleanings was found to range from 0.5 % to 5 %, even for excessively dusty filters.

[13] *The average response over one complete shift is used for stability reasons.*

Similarly to drum calibration, the cleaning effect seen in CalC data is nowhere near to that seen in the shower-like measurements. Interestingly, the magnitude of the change increases when a cut is imposed on the region of the camera from which the CalC signal is collected. When the peripheral four and eight rows and columns of pixels are excluded, the change in the ratio increases from (3.8 ± 0.3) % to (4.8 ± 0.4) % and (5.9 ± 0.5) %, respectively. While this effect was not further investigated, it is clear that just like the drum, CalC is at best only half as sensitive to a dusty aperture as shower-like measurements.

TAB. 4.3 The increase in detected signal following the cleaning of a dusty MUG-6 filter for different measurement methods. The laser pointer measurement specifies the encircled energy at 4.6°. The range for the CLF measurements reflects different integration regions on the FD camera.

Measurement method		Increase in signal (%)
Shower-like	Laser pointer	11
	CLF shots	9.7–14.5
Non-shower-like	Drum	5
	CalC	3.8–5.9

Shower- vs. non-shower-like measurements

Two different types of MUG-6 filter measurements were discussed in this section:

1. **Shower-like:** Just as in an actual air shower measurement, photons scattering on the aperture at large angles are lost to the outside atmosphere and do not enter the telescope. Such measurements include
   a) the dedicated laser pointer measurement described at the beginning of this section,
   b) the detection of CLF laser shots, and
   c) any other measurement, where the light source is located outside of the aperture, which is free of any reflectors.

   The last point encompasses all airborne light sources. A prototype of such a light source carried by a remotely flown drone – the Octocopter – is the main topic of Chap. 5 and 6.

2. **Non-shower-like:** The light source is based on a reflector located directly in the aperture. Photons that are scattered at large angles on the aperture are "recycled" by the reflecting part of the light source and re-injected into the telescope. Such measurements include
   a) the drum, and
   b) CalC.

The sensitivities of different measurement methods to the attenuation and scattering on the dust layer on the filter are summarized in Tab. 4.3. Overall, non-shower-like methods are about half as sensitive to the dust layer as shower-like methods. This finding is expected to have significant implications for the energy calibration of the FD.

5 The Octocopter

Contents

Since 2004 tethered Helium-filled balloons were used to lift light sources into the field of view (FOV) of the Auger telescopes to probe their optical properties [121, 122, 149]. Although relatively inexpensive and capable of sufficiently long flight times, the obvious disadvantage was, of course, that the balloon was gripped by winds and could not be steered into the FOV of individual camera pixels to systematically examine their response. Clearly, a more sophisticated approach was desired. It was in recognizing the need for a more stable and controllable airborne platform that the idea of the Octocopter was conceived.

An octocopter is a remotely controlled eight-rotor drone, which, when equipped with a special light source and refined by numerous hardware and software add-ons, becomes a high-precision tool for studying the fluorescence telescopes – *the Octocopter* (with a capital "O"). Throughout the text, when used in its capitalized

form, the term Octocopter refers to the highly enhanced prototype developed and used at the Karlsruhe Institute of Technology (KIT).

Sec. 5.1 gives an overall description of the airborne platform itself. The subsequent sections deal extensively with the light source, covering its design and construction (Subsec. 5.2.1), the absolute calibration (Sec. 5.3) as well as various properties (Sec. 5.4) such as the emission spectrum or isotropy. Somewhat more mathematical, Sec. 5.5 lays out the procedure for computing the actual number of photons arriving at the telescope aperture. This value is used in all subsequent analyses and is critical for the absolute calibration of the telescopes. Performance aspects of the Octocopter in the field, such as in-flight positional and temperature stability, are discussed in Sec. 5.6. The chapter closes by summarizing all known systematic and statistical uncertainties of the method and establishing its sensitivity in Sec. 5.7.

5.1 Airborne Platform

The concept and realization of the Octocopter was pioneered at KIT. The large team effort initiated in 2009 was headed by Felix Werner and Kai Daumiller, both accomplished pilots. Information on the design, assembly, and hard- and software modifications is available in Felix Werner's Master thesis [103]. The following two subsections (5.1.1 and 5.1.2) provide a brief summary.

5.1.1 Requirements

The requirements on the airborne platform itself are determined by the task at hand: a high-precision, systematic examination of the response of individual camera pixels to light pulses.

Payload: The airborne platform must be able to carry a mechanically compatible (light) source.[1] A platform open for modifications is strongly desired, as the possibility of interfacing the source with existing on-board electronics (wireless communication, batteries etc.) will keep the design simple and the weight of the payload low.

[1] *Other sources have been used, e.g. a microwave emitter for the experiment CROME [150].*

Flight time: Within one flight, the platform must reach the FOV of a selected pixel and remain there for a time interval long enough to collect sufficient statistics, at least 5–15 minutes. The flight time is limited by the capacity of commercially available batteries and further reduced by the payload.

Positional accuracy and stability: The platform must be able to hover in the FOV of a fluorescence telescope (or parts of it) for several minutes. Inescapably, deviations from the target position will occur, e.g. due to GPS position uncertainty or sudden wind gusts. In practice, the extent to which the image on the camera will be affected depends on the flight distance from the telescope. At a nominal distance of 1000 m, a pixel with an opening angle of 1.5° appears 26 m wide, so at minimum the platform must stay contained within this area to probe this pixel.

Even better positioning is required if parts of the FOV of individual pixels are to be probed.

Moreover, there is a trade-off between positional accuracy and flight time. Consider a pixel with an elevation of 16°, translating to 276 m above the FD building level at 1000 m flight distance. If we were to double this distance to reduce the effect of off-target deviations, the altitude would also double, adding to the flight time needed to reach the target position and consequently decreasing the on-target time. In addition, the risk of strong gusts of winds increases with altitude.

5.1.2 Design

A well-established commercial platform by Mikrokopter was chosen [151]. The modular design allows the user to assemble a multicopter with 4–12 engines and optimize for aspects such as flight speed, time and stability, payload or redundancy. Eventually, an octocopter (with eight engines arranged coplanarly on the perimeter of a circle) was chosen [103], as it has the potential to meet all the requirements listed in Subsec. 5.1.1 and is in addition easily portable. In fact, the disassembled octocopter easily fits into an airplane carry-on luggage, opening the possibility of employing it at and even cross-calibrating different observatories [152].

The Octocopter is powered by commercial Lithium polymer batteries with a capacity of about 6500 mA h and a weight of roughly half a kilogram.[2] Given the approximate current consumption of 20 A and up to 60 A when hovering and rising, respectively, the maximum flight time works out to about 20 minutes.

[2] *Two models are in use: Hyperion Vx G3 4S1P with 6500 mA h and 14.8 V, and SLS APL 4S1P with 6750 mA h and 14.8 V.*

The Mikrokopter platform is composed of separate electronic modules interconnected via independent bus systems (see Fig. 5.1 for a schematic). At the heart of the system lies the flight control (see FlightCtrl on Fig. 5.1) module. Its 3-axis accelerometer and three gyroscopes continuously monitor the attitude[3] and angular velocities of the platform. An additional pressure sensor aids altitude stabilization by storing the pressure at the moment the altitude controller is activated as a reference and any spontaneous changes in altitude are automatically compensated to match this reference value. The flight control module further receives commands from the remote control operated by the pilot, converting them to setpoint values for the individual engine controllers (see the BlCtrl module in Fig. 5.1, where “Bl” stands for “brushless”).

[3] *Attitude: the orientation of an aircraft with respect to the horizon.*

GPS-assisted positioning of the platform is accomplished via a GPS device (u-blox [153]) housed on the position controller board (see NaviCtrl on Fig. 5.1) and allows us to steer the platform to the FOV of a particular camera pixel. A 3D-compass aids the pointing of the platform. If the flight option “heading lock” is activated, the orientation at take-off is stored and may be used to correct for drifting accelerometers and gyroscopes.

In flight dynamics, the orientation of an aircraft is described in terms of angles of rotation with respect to three principal axes indicated in Fig. 5.2:

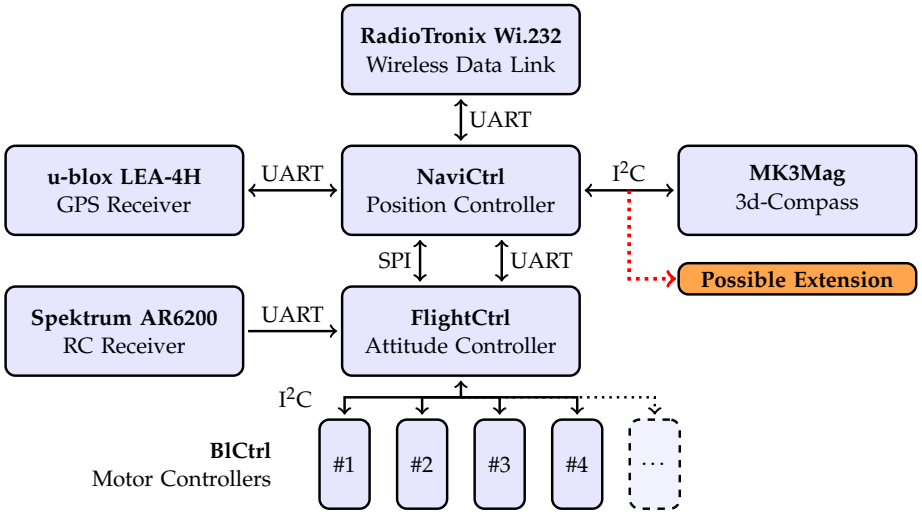

FIG. 5.1 The individual electronic modules of a fully equipped Mikrokopter. From [103].

1. Yaw (also called nick): rotation with respect to the vertical axis. The geomagnetic north corresponds to 0°.

2. Roll: rotation around the longitudinal axis of the aircraft, i.e. the front-back axis.

3. Pitch (also called nick): rotation around the transverse axis, i.e. the side-to-side axis perpendicular to the roll axis.

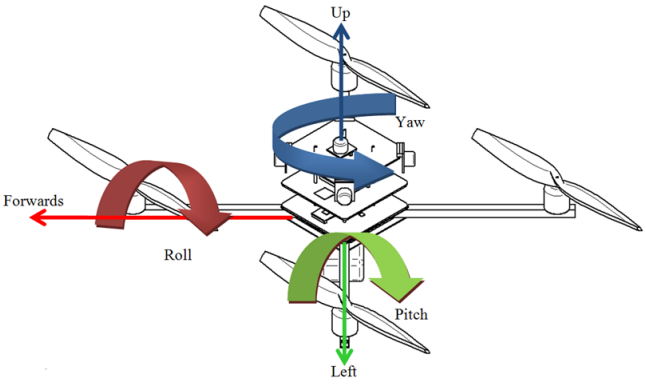

FIG. 5.2 The orientation of an aircraft is described in terms of rotation around three principal axes: yaw, pitch and roll. From [154].

The light source is mounted at the bifurcation of the two front arms as is shown in the photograph in Fig. 5.3, and is driven by a dedicated electronics board connected to the NaviCtrl module via the spare I^2C bus (indicated in Fig. 5.1). In order to avoid potential shadowing effects and ensure data reproducibility, the heading lock flight mode was extended [103] to allow the light source to always point directly at the telescope. The pointing uncertainty is difficult to estimate, but less than 5°. It originates mainly from the superposition of the geomagnetic

FIG. 5.3 Hovering Octocopter. The light source is mounted at the bifurcation of the two front arms (red), and the green and orange LED strips allow a visual cross-check of the orientation in the dark. All electronic boards are housed in the plastic dome. The black "brick" attached just below is the thermally isolated battery pack. Photo courtesy of Radomír Šmída.

field with that produced by the Octocopter as large currents flow from the battery to the electronic boards.

To be able to visually cross check the position and orientation of the Octocopter against the dark night sky, strips of LEDs were glued to the underside of all eight arms – green on the two front ones, orange on the remaining ones. Those wavelengths are absorbed by the MUG-6 filter in the telescope aperture and are still far enough from the infra-red range, in which the filter becomes transmissive again.

Before a flight, the Octocopter is programmed with a list of GPS waypoints corresponding to target positions within the FOV of the studied telescope as well as hold times at each position. Bi-directional communication with the Octocopter is facilitated by a radio telemetry link and vital diagnostic data, including remaining battery voltage, vertical and lateral speeds, and attitude are transmitted at a rate of 5 Hz.

Furthermore, a dedicated Python- and Qt4-based ground control software was developed [103] to facilitate using the platform for the purpose of studying the optical properties of the fluorescence telescopes. The main functionalities include:

- ▷ display of diagnostic information (flight speed, distance from target, attitude and orientation, remaining battery voltage etc.)
- ▷ programming or loading of 3D waypoints with fixed orientation
- ▷ graphical representation of the Octocopter's position in the telescope FOV

▷ configuration of the light source (intensity and pulse width, total number of pulses to be delivered etc.)

▷ data logging (navigational and temperature data, light source configuration, number of visible satellites etc.)

5.2 Light Source Basics

The Octocopter method aims to mimic a snapshot of an air shower traversing the atmosphere. In accordance with this philosophy, the light source shares three critical properties with air-shower-induced fluorescence light:

1. **Emission in the UV:** The emission spectrum of the light source falls in the range covered by nitrogen fluorescence and is well-matched to the FD spectral responsivity.
2. **Isotropy:** Due to the isotropic emission of the light source, the telescope response is probed in much the same manner as by air showers and the same basic signal reconstruction procedures can be applied.
3. **Point source:** At the nominal flight distance of 1000 m, the angular diameter of the light source is only $21''$. Similarly to an air shower, it appears almost point-like to the telescope.

The development of the light source proceeded in stages, which are described in [103, 122, 149]. In the following section, a brief overview of the final design is presented.

5.2.1 Construction

Two main components make up the light source: the body – a regular dodecahedron[4] with one LED on each face, and the diffuser sphere, which serves as mechanical protection and enhances isotropy.

[4] *A dodecahedron is any polyhedron with twelve faces. A regular dodecahedron is composed of twelve pentagons.*

InGaN-based LEDs of type H2A1-H375 by Roithner LaserTechnik [137] are used. The spectrum peaks sharply at 376.5 nm and the wide emission angle of 130° is achieved by capping the LED with a silicon lens. Providing 55 mW of optical power at a driving current of 350 mA, the LEDs originally came mounted on a hexagonal heat sink 2 cm in diameter (see Fig. 5.4), which was later removed to reduce size and save weight. The LED light output was compared before and after the heat sink removal using 64 μs pulses at 1 kHz and no significant differences were observed below driving currents of 500 mA [103].

The final combination of the dodecahedron edge length of 16 mm and the sphere radius of 50 mm was chosen to yield the best isotropy. The body, depicted in Fig. 5.5 (left), was 3D-printed out of plastic (acrolynitrile butadiene styrene) and weighs a mere 25 g. Each face has a socket and a canal to accommodate one LED plus its cabling. The axis of the light source functions as a cable holder and at the same time as the mounting bracket for the diffuser sphere. The sphere itself is made from polysterene and diffusive transmission was achieved by etching in

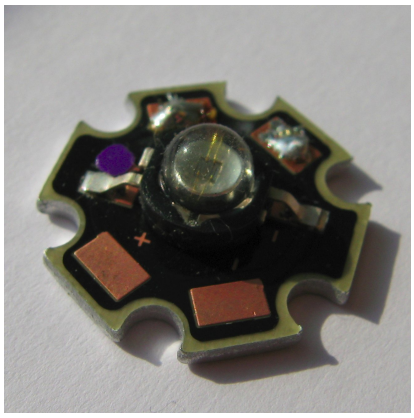

FIG. 5.4 An Octocopter LED capped with a lambertian silicone lens, still soldered to its hexagonal heat sink, which was later removed to reduce size and save weight. Photo courtesy of Felix Werner.

acetone. Moreover, the entire body is covered with Tyvek[5] to facilitate multiple reflections inside the sphere (see Fig. 5.5, right). The complete light source weighs 150 g and may be easily packed into a small box for measurements at different laboratories and even different observatories.

[5] *a lambertially reflecting plastic*

The driving electronic board of the light source is interfaced with the NaviCtrl. Twelve current-stabilized output channels are used to drive each LED separately with a slightly different current to match its individual light output vs. driving current characteristics, and thus achieving supreme isotropy (see Subsec. 5.4.3). The light source is triggered by the pulse-per-second (PPS) signal of the GPS device and may be configured to emit light pulses of variable amplitudes and widths with a delay of 50–1000 μs.

Two additional temperature sensors and a photodiode for monitoring the light output are interfaced with the light source electronic board. The two temperature sensors monitor the temperature directly on the driving electronic board and in the diffuser sphere, and are used to account for the temperature dependence

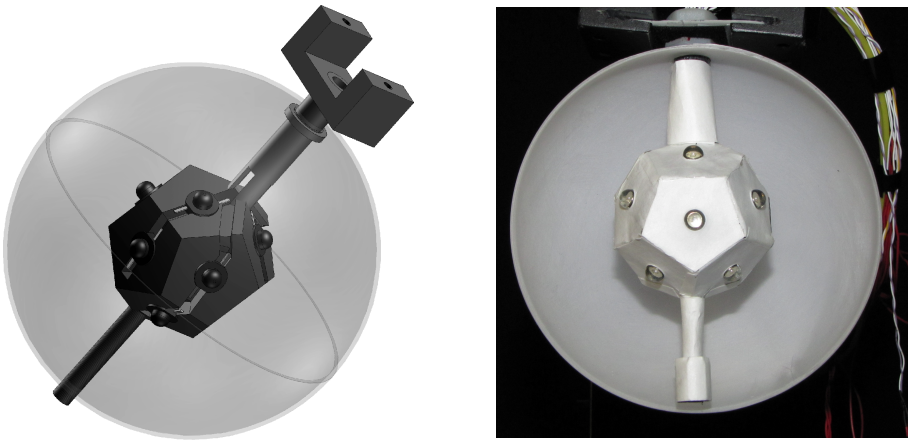

FIG. 5.5 Left: The body of the light source is a regular dodecahedron with a an edge length of 16 mm. Picture courtesy of Michael Riegel. Right: The assembled, Tyvek-coated body holding all 12 LEDs. Photo courtesy of Kai Daumiller.

of the light source discussed in Subsec. 5.3.2. The monitoring photodiode is attached to the central cable tube and looks towards the "back" of the diffuser sphere, i.e. always away from the telescope. The initial idea was to use the photodiode for post-flight intensity corrections, but even though data for each light pulse are available, they have been found to be largely unstable [155] and are not currently used for analysis. Nevertheless, for stability reasons the assembled light source is not opened unless absolutely necessary, and the photodiode was left in place. The data from those additional sensors are digitized and stored during flight, and are read out only after landing.

5.2.2 Generations and standard configuration

Three light source generations have been conceived since the first Octocopter test measurements in January 2010. The very first prototype, let us call it *L1*, was in use until the end of 2011, when a new light source of the same type (let us refer to it as *L2a*) was constructed. Flown only in the March 2012 campaign, the diffuser sphere of the *L2a* was soon replaced, as there were doubts about the homogeneity of the acetone etching. Since the body and the LEDs remained unchanged, we refer to the resulting light source as *L2b*. The *L2b* was first flown in the November 2012 campaign and was still in use at the time this work was composed. An overview of the different light sources is shown in Tab. 5.1. Unless otherwise stated, in the following the term "light source" refers to the *L2b*, which was in use for most of the campaigns presented in this work.

Tab. 5.1 Overview of the three light source generations used from 2010 to 2016.

Light source	Change w.r.t to previous generation	Used from–to
L1		01/2010–01/2012
L2a	new LEDs and diffuser sphere	02/2012–07/2012
L2b	new diffuser sphere (front hemisphere only)	09/2012–01/2016

Multiple aspects of the light source may be configured: driving current, operation mode (pulsed vs. direct current (DC)), pulse width, pulsing rate and PPS delay. In the following paragraphs, the individual options as well as the standard configuration of the *L2b* are discussed.

The driving current of the LEDs is determined by setpoint values passed to the 12-bit digital-to-analog converter (DAC). For simplicity, six amplitudes ranging from 0 to 5 were preconfigured and the amplitude–DAC conversion is given in Tab. 5.2. The highest amplitude $A = 5$ was chosen to produce a strong signal in the target pixel ($\sim$75 % of the saturation level) from a flight distance of 1000 m and was used for the absolute calibration campaigns from 2012 to 2015. In principle, any value up to 4095 may be used, however, very high values are not recommended as they were observed to cause oscillations in the driver circuit [156].

Amplitude	DAC value	Rel. light output (%)
5	997	100
4	851	82
3	705	64
2	552	45
1	354	22
0	223	8

TAB. 5.2 Nominal amplitude settings of the light source *L2b* with corresponding DAC values and relative intensities.

TAB. 5.3 Light source configuration: possible range of values and the *L2b* standard configuration.

	Range of values	Standard *L2b* configuration
Amplitude	0–5	5
Current mode	pulsed/DC	pulsed
Pulsing rate	1–1000 Hz	
during flight		1 Hz
during calibration		1000 Hz
Pulse width	2–64 μs	8 μs
Delay after PPS trigger	50–1000 μs	350 μs

The light source is normally (and always during data taking at the Pierre Auger Observatory) operated in pulsed mode, but may be operated in DC mode for special purposes, heat capacity permitting. Pulses 2–64 μs long can be delivered at rates from 1 Hz to 1 kHz. The standard configuration of the *L2b* during the 2012–2015 absolute calibration campaigns was 8 μs long pulses delivered at a rate of 1 Hz, which is closely tied to the full read-out speed of the FD camera. For comparison, the duration of a shower pulse within a single pixel is typically a few microseconds, and of course depends on the distance and orientation of the shower. The delay of the pulse following the PPS trigger is customarily set to 350 μs and is synchronized with the external triggering of the telescope. Tab. 5.3 summarizes the configuration options and the standard values for the *L2b*. Unless specified otherwise, the standard configuration of the light source is assumed.

5.3 Absolute Calibration

The absolute calibration of the light source comes down to measuring the light output produced in one pulse. Since the calibration measurement is based on a photodiode operated in DC mode, the basic measured quantity is the charge collected within one pulse. This is later, through a series of steps, converted to radiant energy of the light source and subsequently the absolute number of photons arriving at the telescope aperture. This subsection focuses on the first step: the measurement of the pulse charge. The procedure for computing the number of photons on the aperture is outlined in Sec. 5.5.

5.3.1 Measurement of the pulse charge

Two main instruments are used to measured the pulse charge: a NIST-calibrated photodiode and a Keithley 6514 electrometer. The general measurement procedure is described here and the details of the measurement instruments follow on pages 106 and 108.

A photograph of the calibration setup is shown in Fig. 5.6. The light source is mounted on an optical bench at a distance of (2.436 ± 0.002) m from the photodiode and centered on its optical axis.[6] The special mounting bracket permits the sphere to be rotated along two axes (effectively changing the heading and the nick angle) and moved along and perpendicularly to the optical bench. The uncertainty of the light source orientation is approximately 2°. To replicate the conditions during flight, the light source is facing the photodiode just as it would face a pixel in the central part of the FD camera. The entire setup is located in a dark room, with the optical bench surrounded by black, non-reflective curtains, and much of the setup covered by black flock paper. In addition, the main reflection paths are blocked by a 6.6 cm-diameter baffle positioned about half way on the optical bench.

[6] *The optical axis of the photodiode is an imaginary line perpendicular to and passing through the center of the photodiode aperture.*

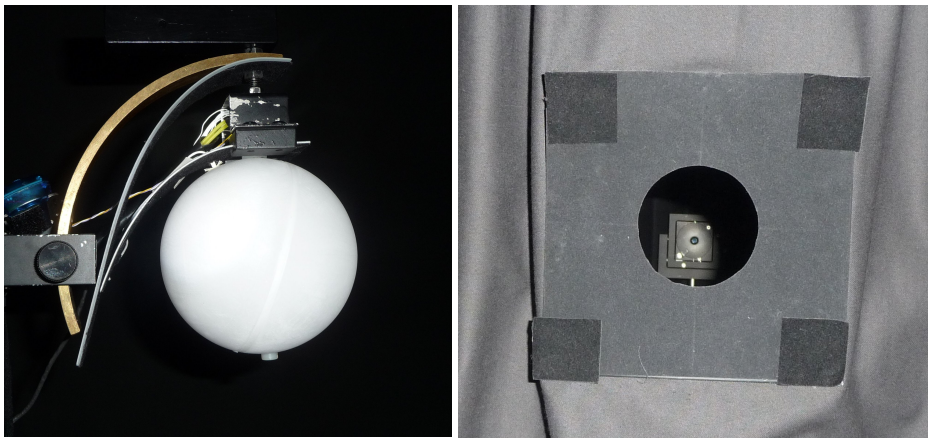

FIG. 5.6 Left: The Octocopter light source mounted on the optical bench in the dark room. Right: A look through the large-diameter baffle at the photodiode. Photos courtesy of Radomír Šmída.

With the setup described above in place, the light source is triggered by the Keithley electrometer at a rate of 1 kHz to deliver 8 μs pulses. The NIST-calibrated photodiode responds with a current proportional to the impinging radiant power, which is integrated by the electrometer in 100 ms intervals.

At this point, let us spend a few moments on the pulsing rate. As previously mentioned, the light source is flashed at 1 Hz during measurements at the Observatory to allow for a full read-out of the FD camera. The calibration instruments, on the other hand, are not as limited in their read-out rates, so higher pulsing rates are possible, even desired. One obvious reason for a higher pulsing rate is the acquisition of a large number of pulses during short time intervals throughout which the light source and ambient conditions remain stable. The other reason is

related to the noise floor of the Keithley electrometer. Regardless of the actually measured charge, a constant-offset uncertainty is associated with each measurement. Since this offset is commensurate with the charge of one pulse (of the order of 100 fC), it is advantageous to measure the cumulative charge of a bunch of pulses. For the combination of a pulsing rate of 1 kHz and a standard-length integration interval of 100 ms, this boils down to 100 pulses per bunch. A typical measurement contains 20 bunches, and the charge is continuously summed. The relationship between measured charge at a set amplitude and pulsing rate is investigated in Subsec. 5.3.2.

Next, the charge per integration interval, i.e. the difference between successive data points, is plotted as a function of time as is shown in Fig. 5.7. The background sections are simply fitted with a constant to obtain the mean background charge per integration interval Q_{bgd}. The signal section, on the other hand, is fitted with a first-order polynomial $p_0 + p_1 t$ to account for a weak warm-up effect when pulsing at 1 kHz, which is well described by a constant slope. In particular, the charge per interval increases ever so slightly with the pulse number, so that $\frac{p_1}{p_0} \sim 10^{-6}$. Since the warm-up effect is not observed at the 1000 times lower flight pulsing rate, the contribution from p_1 is discarded and the gross charge per integration interval Q_{bunch} is taken to be p_0. The mean net charge per light pulse Q_{pulse} is then obtained as

$$Q_{\mathrm{pulse}} = \frac{Q_{\mathrm{bunch}} - Q_{\mathrm{bgd}}}{100}, \tag{5.1}$$

where 100 is the number of pulses in one integration interval of 100 ms. It is noteworthy that the background is four orders of magnitude lower than the signal.

Since the measurement lasts only a few seconds, we assume that the light source, the measurement apparatus and the ambient conditions (particularly the temperature) are stable. The statistical uncertainty of Q_{pulse}, obtained by combining the uncertainties of the fit parameters in the background and signal regions, is at the per mill level and negligible in comparison to the systematic uncertainty of the Keithley measurement of the order of 2 %. More in-depth characteristics (including systematic uncertainties) of the photodiode and Keithley electrometer used for the light source calibration are given in the following paragraphs.

NIST-calibrated photodiode

We use a UV-enhanced, NIST-calibrated silicon photodiode manufactured by OSI Optoelectronics, model UV-100 [157, 158], S/N U1062 (further on referred to as simply photodiode). The calibrated range 200–500 nm spans the entire light source spectrum. The wavelength-dependent 1σ-uncertainty of the spectral power responsivity ranges from 0.13 % to 1.9 % and amounts to 0.45 % at the peak wavelength of the light source.

The radius of the aperture and the photosensitive area of the photodiode is 6 mm and 4 mm, respectively. As can be seen on the contour plot in Fig. 5.8, the

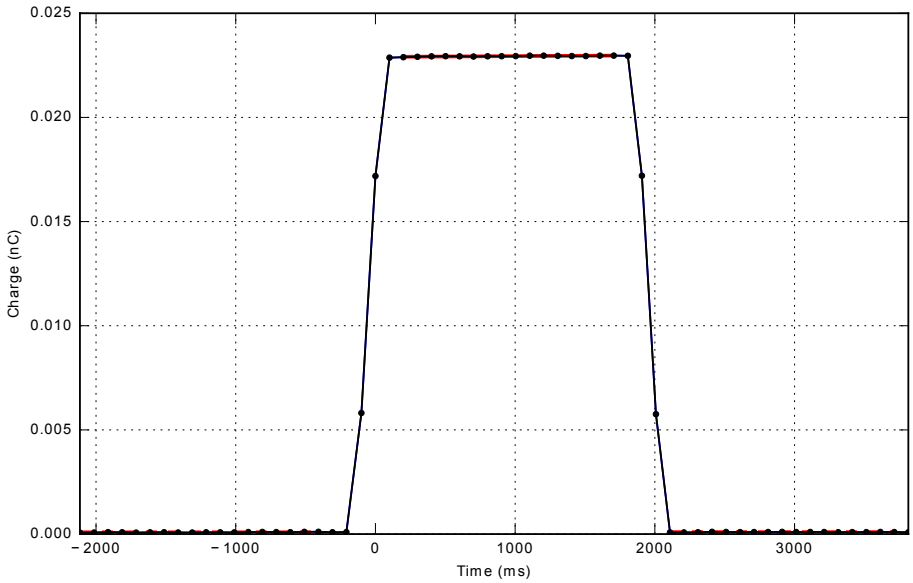

FIG. 5.7 The charge per time interval plotted as a function of measurement time. Each point signifies the charge measured during one integration interval of 100 ms. The pre- and post-pulse background regions are fitted with a constant, the pulse plateau with a first-order polynomial (all fits are indicated by red lines). From [156].

spatial responsivity is not fully uniform and drops by 1.6 % when moving from the center to the periphery of the photosensitive area. In order to illuminate a well-defined part of the aperture, a dedicated baffle was crafted out of a 0.1 mm thick sheet of high-grade steel using electrical discharge machining, and positioned directly in front of the aperture. The edges of the baffle were mapped using a microscope and a circle was fitted to the points (see Fig. 5.9), allowing the area of the opening A_{PD} to be determined with high accuracy as $(50.096 \pm 0.067)\,\mathrm{mm}^2$. The uncertainty in the sensitivity of the active photodiode area with the custom-made baffle in place was estimated to be 0.5 %.

Keithley electrometer

The Keithley 6514 is a highly sensitive programmable electrometer capable of measuring charges as low as 10 fC [159]. The manufacturer specifies the accuracy in terms of a multiplier error of ± 0.4 % and an offset of ± 50 counts, which corresponds to ± 500 fC and is the dominant contribution to the uncertainty in the relevant measurement range. Typical values of the cumulative charge Q_{bunch} for a bunch of 100 pulses detected within a 100 ms integration interval are of the order of 100 nC. The statistical uncertainty is four orders of magnitude smaller than the signal measurement, the uncertainty of which is dominated by the Keithley electrometer.

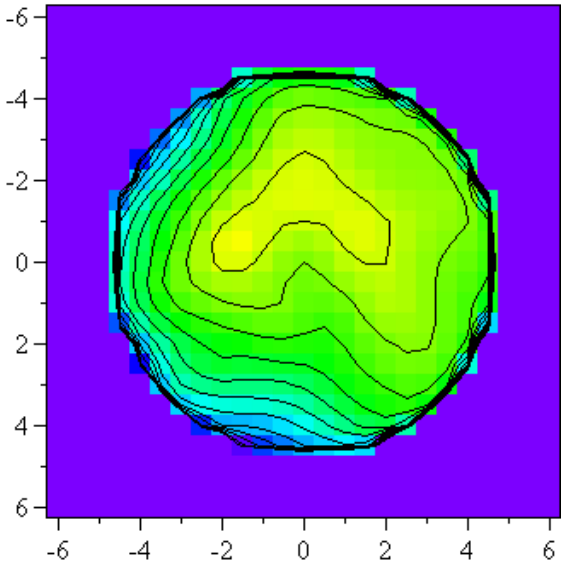

FIG. 5.8 Spatial uniformity of the OSI Optoelectronics silicon photodiode in 0.2 % contour lines. The color scale corresponds to the level of responsivity and the axes are shown in mm. The measurement was performed at 350 nm with 1.5 mm resolution and 0.5 mm/step. From [158].

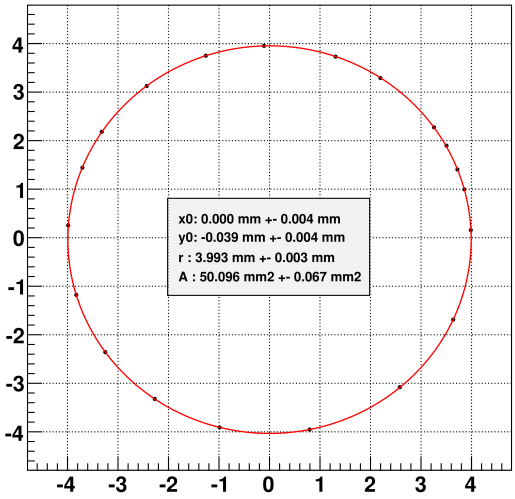

FIG. 5.9 Positions of points along the edge of the custom-made baffle were measured with a microscope and fitted with a circle. The x- and y-axis are shown in units of mm. The fit parameters and the corresponding area are also given. From [156].

TAB. 5.4 Relative difference between the light output measured at KIT at the end of February 2013 and the University of Utah in March 2013 for different DAC settings of the light source.

DAC value	Difference (%) at	
	22.0 °C	23.3 °C
997	1.29	0.60
851	1.31	0.58
705	1.21	0.40
552	1.03	0.07
354	0.76	−0.50
223	0.60	−0.91
155	1.54	−0.09
150	1.72	0.07
140	2.32	0.66

Comparison to measurements at TA

In March 2013, an Octocopter campaign was staged at the TA site in UT [152,160]. Part of this campaign was an absolute calibration of the Octocopter light source *L2a* in the optics laboratory of the University of Utah in Salt Lake City [161]. The measurement setup was completely different and consisted of a photodiode read out by a picoammeter in a dark tunnel. Relative differences of the values recorded at KIT and the University of Utah [161] are listed in Tab. 5.4 and plotted in Fig. 5.10 for temperature values of 22.0 °C and 23.3 °C.

Those fully independent measurements are in excellent agreement. The largest observed difference is 2.3 %, and the average differences are 1.3 % and 0.1 % at

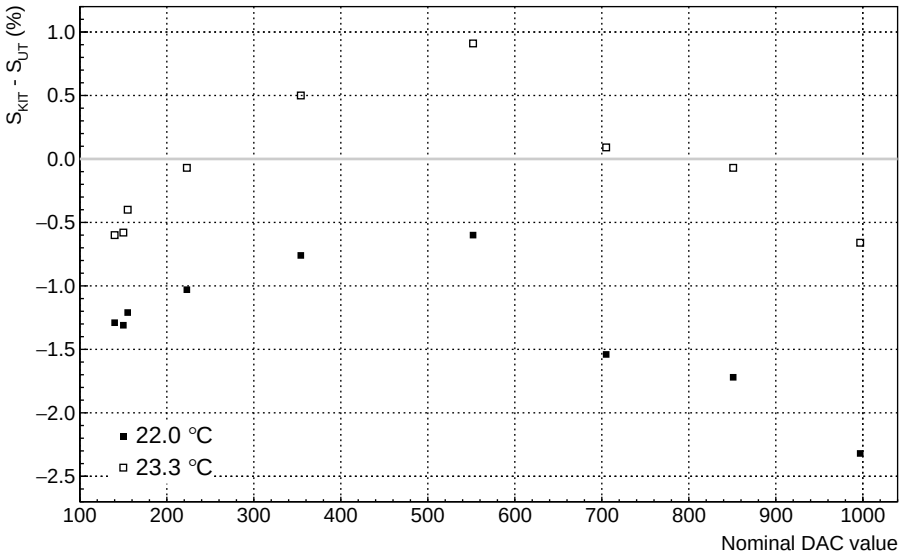

FIG. 5.10 Relative difference between the light output measured at KIT at the end of February 2013 and the University of Utah in mid March 2013 as a function of DAC value.

22.0 °C and 23.3 °C, respectively. The parabolic shape of the curve hints at small non-linearities in one or both measurements.

5.3.2 Corrections

The configuration of the light source and the ambient conditions during calibration in the laboratory differ from those in the field, and consequently a number of corrections must be applied to properly account for those differences. Most importantly, the charge measurement for a given nominal amplitude is affected by the ambient temperature and the rate at which the light source is pulsed. Furthermore, the pulse width is affected by the pulse amplitude.

The magnitude of the corrections is about 5 % and up to 10 % for the ambient temperature, so they are of immense importance to the systematic uncertainty and the sensitivity of the method, and by extension to the absolute calibration of the fluorescence detector. To preserve the conciseness of the main text, in the following only a brief quantitative statement is made about each of the three corrections. The technicalities, including a description of the dedicated measurements, interpretation of the findings, and error propagation are detailed in App. C.

Temperature

The light output of LEDs is known to vary inversely with the junction temperature and the Octocopter light source is no exception. Since it is calibrated in the laboratory at a temperature $T_{\text{cal}} = 22\,^{\circ}\text{C}$, but the ambient flight temperatures are typically in the range 0–10 °C, the actual pulse charge during flight will be higher than measured in the laboratory.

The light output vs. ambient temperature dependence was measured for the complete light source, i.e. the sphere and its driving electronics, using a climate chamber. The observed decrease in light output at the standard amplitude $A = 5$ is about $-0.6\,\%/^{\circ}\text{C}$ (see Fig. C.1) and the corresponding multiplicative correction factor to the calibration pulse charge is

$$C_{\text{temp}} = p_1 T_{\text{offset}} - p_2 T_{\text{offset}}^2 \tag{5.2}$$

$$= -6.158 \times 10^{-3} T_{\text{offset}} - 5.413 \times 10^{-5} T_{\text{offset}}^2\,, \tag{5.3}$$

where $T_{\text{offset}} = T - T_{\text{cal}}$ is the difference between the actual and calibration ambient temperatures, and $p1$ and $p2$ are the parameters of the second-order polynomial fit to the light output–ambient temperature curve.[7]

[7] *The temperature dependence of the light source is amplitude-dependent.*

At flight temperatures of 10 °C and 0 °C, the correction factors will be 1.07 ± 0.02 and 1.11 ± 0.01, respectively. The quoted uncertainty results from the propagation of the uncertainty of the fit parameters. An additional term arises from the uncertainty in the temperature measurement and will be discussed in Subsec. 5.6.2.

Pulsing rate

For a multitude of factors, including the full read-out speed of the FD camera and the uncertainty and stability of the absolute pulse charge measurement, the Octocopter light source is pulsed at 1 Hz during flight but 1000 Hz during calibration. We cannot a priori assume that the actual pulse charge is unaffected by the pulsing rate.

This dependence was investigated by performing measurements at nine different rates in the range 1–1000 Hz at the standard amplitude $A = 5$ and was found to be roughly linear with a slope of $\sim$3.5 %/kHz (see Fig. C.2). In particular, the multiplicative correction factor C_{rate} to the calibrated charge, arising from the warm-up of the light source driving electronics, is $C_{\text{rate}} = 0.966 \pm 0.001$. The actual light output during flight is thus lower than measured in the laboratory.

The temperature and pulsing rate corrections C_{temp} and C_{rate} compensate to some degree, and the combined correction factor C_{total} will depend on the ambient temperature during flight. For example, $C_{\text{total}} = 1.030$ at a temperature of 10 °C and increases to $C_{\text{total}} = 1.07$ as the temperature drops to 0 °C.

Pulse width

Unlike the previous two corrections, the actual width of the light pulse does not affect the total photon number arriving at the aperture, although it does affect the photon flux. Just as the light source calibration works with integrated charge, so does the analysis of the FD pulses work with integrated ADC traces, and the correction to the pulse width is thus only relevant for achieving a realistic simulation of the Octocopter light pulses. The difference between the nominal and actual pulse width measured with an oscilloscope is amplitude-dependent and amounts to 0.358 μs for the standard nominal settings of 8 μs and amplitude $A = 5$ (see Fig. C.3).

5.4 Light Source Properties

5.4.1 Emission spectrum

Fig. 5.11 shows the relative emission spectra of the light source *L2b* and that of a single LED obtained with an Ocean Optics SD2000 array spectrometer [162]. We observe a slight difference between 380 nm and 400 nm, plausibly due to the preferential absorption of the diffuser sphere or the Tyvek in this region. No dependence of the spectral shape on amplitude was observed. As shown in Fig. 5.12, the wavelength range emitted by the Octocopter is fully contained within the FD spectral acceptance.

The uncertainty of the spectrometer wavelength scale is rather small, 0.32 nm at maximum, but must be propagated in the calculation of the number of photons arriving at the telescope aperture nonetheless (Sec. 5.5). Fig. 5.13 shows the difference between the true and measured wavelengths over the entire spectrometer bandwidth 200–850 nm as given by the manufacturer Ocean Optics [163].

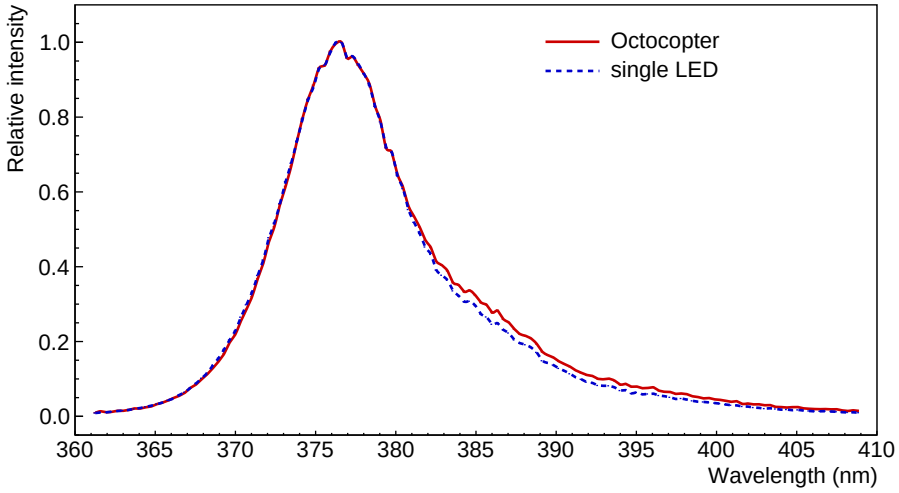

FIG. 5.11 The emission spectrum of the Octocopter light source *L2b* (red solid) and that of a single LED (blue dashed line) measured at the standard amplitude $A = 5$. Both curves are shown relative to their peak intensity.

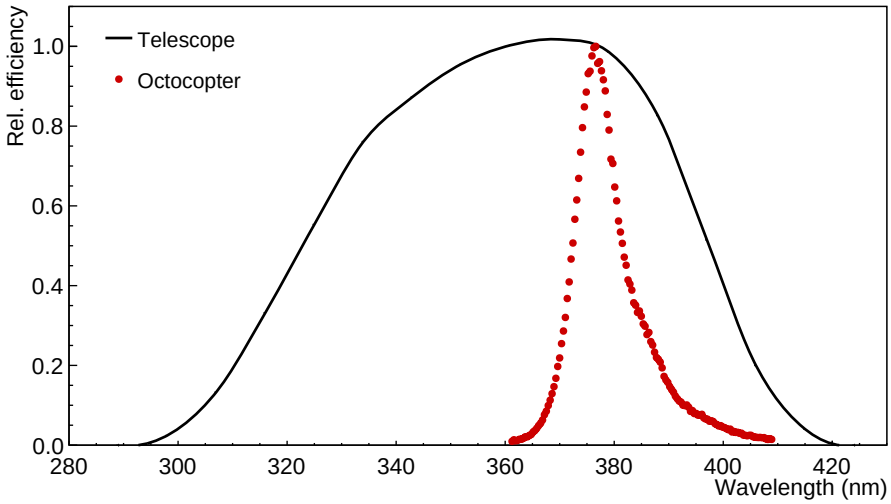

FIG. 5.12 The emission spectrum of the Octocopter light source *L2b* (red points) falls within the FD spectral acceptance (black curve). Both curves are scaled to be 1.0 at the FD reference wavelength of 375 nm.

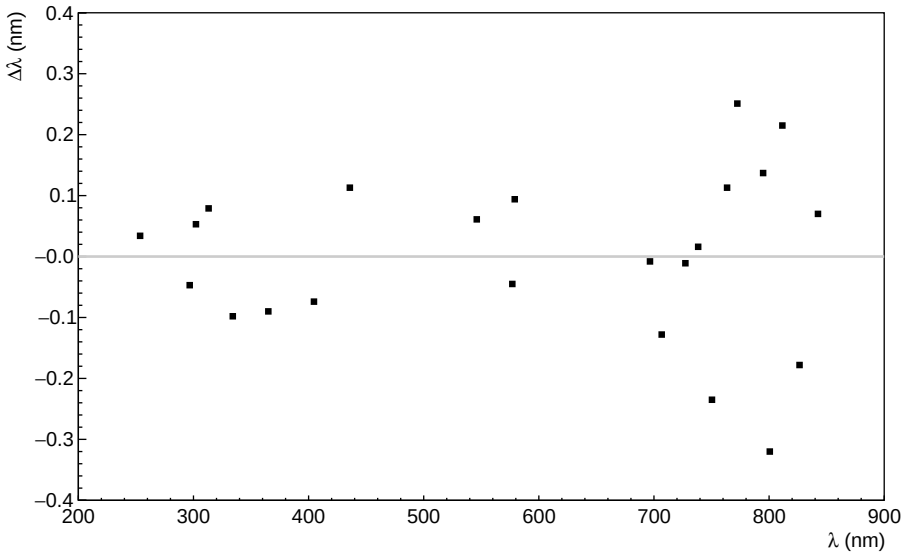

FIG. 5.13 Difference between the true and measured wavelengths $\Delta\lambda$ over the entire spectrometer bandwidth (from [163]).

5.4.2 Inverse-square law behavior

Much of the Octocopter data analysis, including the calculation of the number of photons arriving at the telescope aperture in one light pulse, rests on the assumption that the light source is isotropic and obeys the inverse-square-law. The former property is discussed in Subsec. 5.4.3, the latter here.

The light output was measured for five different source–photodiode distances using standard configuration settings. Potential stray and multiply reflected light reaching the photodiode aperture could severely deteriorate the measurement, and consequently the absolute calibration, but ought to be blocked by the baffle system. Fig. 5.14 shows the measured data fitted with a simple inverse-square function

$$y = C + Ar^{-2}, \tag{5.4}$$

where C represents a constant background of stray and multiply scattered light.

The residuals, shown in the bottom panel of Fig. 5.14, are at the per mill level. The constant light background C is three orders of magnitude lower than the signal and in all cases compatible with zero at the 2σ level. The baffle system thus effectively blocks multiple reflections and stray light during calibration and the light source obeys the inverse-square law to a very high degree. Implicit is the assumption – a reasonable one, we believe – that this behavior can be extrapolated to large distances, e.g. the standard flight distance of 1 km from the telescope.

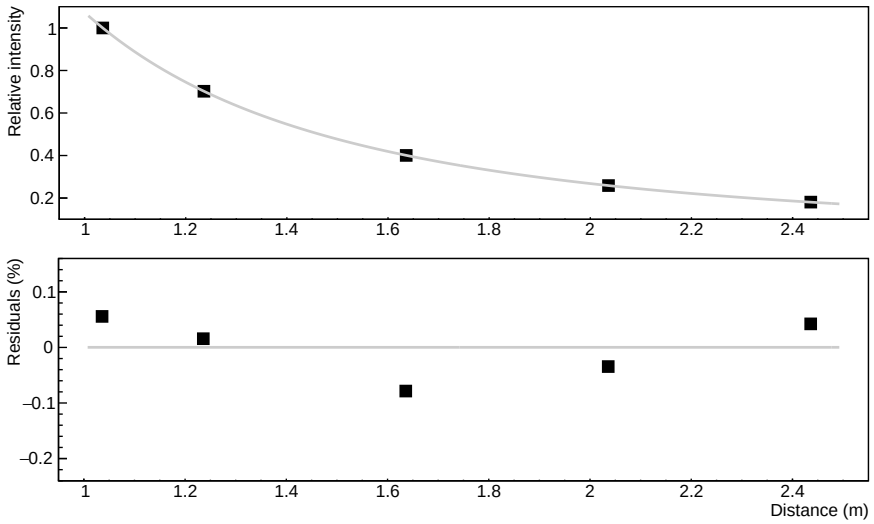

FIG. 5.14 Relative light output as a function of the light source–photodiode distance fitted with a simple inverse-square law $C + A/r^2$ (top) and the corresponding residuals (bottom).

5.4.3 Isotropy

Each LED is to a certain degree unique and can be characterized by its own light output–current curve. In order to achieve maximum isotropy, the light sources were constructed in the following way: First, the light output–current curve of each LED in the initial batch of 36 pieces was measured. Next, twelve LEDs with the closest characteristics were selected for the *L1*. The LEDs for the *L2* were selected in much the same way from the remaining 24 LEDs. On top of this careful matching, each LED is being driven at a slightly different current to compensate for any differences still left.

To understand the geometries and scales at which isotropy becomes important, we first investigate the stability of the orientation of the Octocopter during flight (refer to Fig. 5.2 for a definition of the individual angles).

Heading: The Octocopter is programmed so that the light source always faces the FD pixel under investigation head-on. It is thus never shadowed by the landing gear or other structures.

Pitch: In a stable position, the pitch angle fluctuates about zero, and the pixel views the light source at an angle proportional to its elevation. This geometry was taken into account when positioning the seam of the diffuser sphere such that it would not deteriorate the isotropy. In particular, the seam was rotated away from the horizontal by 16° (c.f. Fig. 5.6), and thus a pixel in the central row of the FD camera views the “pole” of the sphere, the seam being the equator.

Roll: The roll angle is also close to zero in stable conditions. However, in contrast to the pitch, the target pixel always sees the same area of the light source, albeit rotated, regardless of the roll.

When in the air, the Octocopter balances stable winds and sudden gusts by adjusting its attitude. Fig. 5.15 shows the distribution of heading and pitch angles during several flights in pixel 70 in LL3 on a typical campaign night in November 2014. The RMS of the distributions is 1.9° and 2.4° for heading and pitch, respectively. Isotropy is thus important on small scales of several degrees.

Picture the light source mounted on the optical bench and being viewed by the photodiode. A pixel in the center of the camera would see the light source from the same angle. To make the description of the geometry more intuitive, let

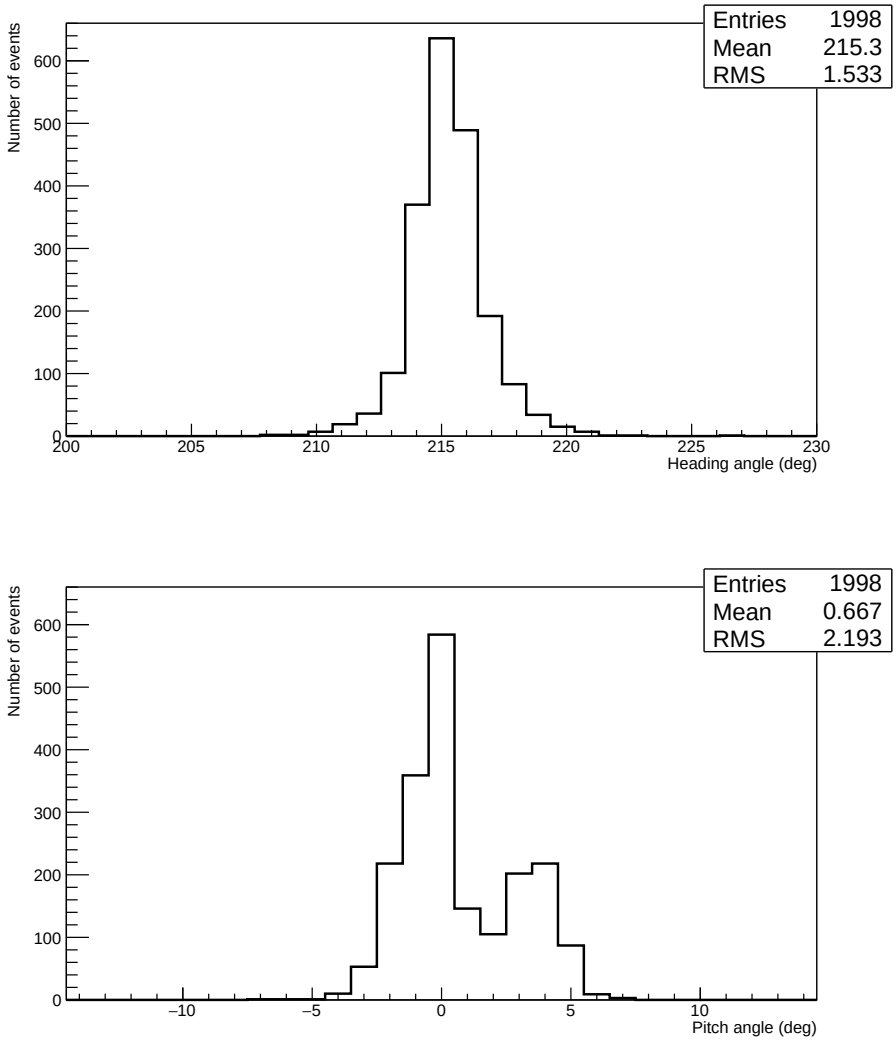

FIG. 5.15 The distribution of heading (top) and pitch angles (bottom) during several typical flights spread over two measurement nights in November 2014. Each data point corresponds to the orientation of the Octocopter at the moment a light pulse (event) was emitted in the FOV of pixel 70 in LL3.

us switch from the pitch and heading angles to latitude and longitude, with the point on the sphere viewed by the photodiode head-on corresponding to $(0°, 0°)$. The light output was measured for a range of latitudes and longitudes of $\pm 10°$ and $\pm 8°$, respectively, stepping through at 2.5°. The isotropy was found to be excellent, the largest difference between any two measured positions being 0.7 %. The results of the scan are plotted in Fig. 5.16.

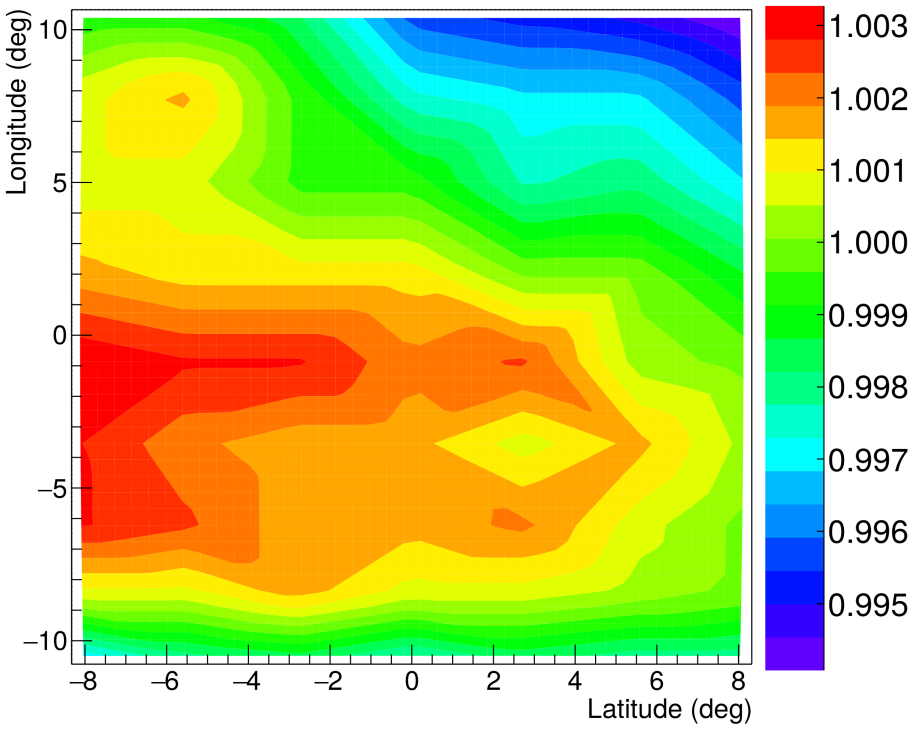

FIG. 5.16 Light source isotropy. Different colors correspond to fractional deviations from the mean intensity (1.0) at various points on the surface of the diffuser sphere. The maximum difference in intensity between any two points is 0.7 %. The coordinate $(0°, 0°)$ marks the point on the sphere that the photodiode or a pixel in the center of an FD camera views head-on.

5.4.4 Temporal stability

Long-term stability

The *L2b* has been in use since November 2012. It is natural to suspect that the light source ages with time, maybe due to dust accumulation inside the diffuser sphere or the deterioration of its surface. To follow such changes, the light source is calibrated in the laboratory before and after each campaign, and the calibration measurements that are closest in time to the actual campaign are used in the analysis. Fig. 5.17 depicts how the relative signal dropped from 100 % to 84 % over 3.5 years of operation, about 4 % per year on average.

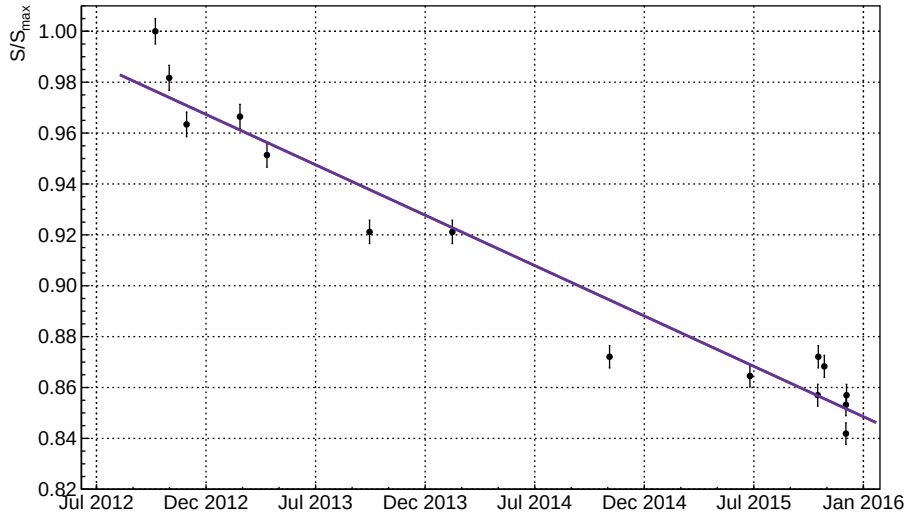

FIG. 5.17 Long-term stability of the *L2b*: The signal S relative to the all-time maximum value $S_{\max}$ over 3.5 years of operation. The linear fit estimates an average decrease in light output of 4 % per year.

Inter-campaign stability

Comparison of pre- and post-campaign calibration measurements indicates that the light source intensity drops slightly during the course of one campaign. The average decrease observed in the 2012 and 2015 campaigns amounts to 1.8 %. Since there is no way of knowing at what point during the campaign the decrease occurred, we use the average of the pre- and post-campaign measurements for analysis, with one half of the difference (0.9 %) contributing to the systematic uncertainty.

Short-term stability

In this context, the term short-term stability refers to the agreement of two or more calibration measurements performed within one day that, given a perfectly stable light source and measuring instruments, should yield the same intensity. The observed discrepancy in the 2015 data ranges from 0.5 % to 1.8 %, with a median of 1.4 %. Note that the light source was not moved and the electronics were left running during those measurements. A similar level of stability (± 1 %) over the period of a few days was observed in the light source *L1* [103]. This type of instability is not fully understood and is probably related to some hidden source of systematic uncertainty. We account for it by including half of the median value ± 0.7 % in the systematic uncertainty budget.

5.5 Number of Photons at the Aperture

In this section, we lay out the mathematical procedure for computing the number of photons arriving at the aperture in one pulse, which is later used for the absolute calibration of the fluorescence detector.

5.5.1 From pulse charge to photon number

The absolute spectral responsivity of a photodiode R_{PD} describes the amount of current it generates in response to a unit of impinging radiant power. The units of R_{PD} are thus A/W or, in our case, C/J since we integrate over time.

The responsivity R_{PD} as a function of wavelength λ is known from the NIST calibration [158]. The effective responsivity R_{eff} in a given measurement, however, always depends on the spectrum of the impinging light. Convoluting the normalized Octocopter light source spectral emissivity $\hat{\epsilon}(\lambda)$ in J/nm with the absolute spectral responsivity of the photodiode R_{PD}, we obtain

$$R_{\mathrm{eff}} = \sum_{\lambda} \hat{\epsilon}(\lambda) R_{\mathrm{PD}}(\lambda) \Delta\lambda, \tag{5.5}$$

which evaluates to $(0.136\,15 \pm 0.000\,71)$ C/J for our specific source–detector combination. The sum runs over the entire wavelength range of the light source spectrum measured in steps of $\Delta\lambda = 0.35$ nm and the responsivity of the photodiode, provided by NIST in coarser steps, was linearly interpolated.

The uncertainty of R_{eff} was computed numerically by shifting the light source emissivity $\hat{\epsilon}(\lambda)$ in wavelength and the responsivity of the photodiode $R_{\mathrm{PD}}(\lambda)$ in intensity by $\pm 1\sigma$ (the error of the wavelength scale is negligible), and selecting the combination producing the largest error of 0.52 %, which is dominated by the uncertainty of the photodiode responsivity, equal to 0.45 % at the peak wavelength of the light source.

To compute the energy E_{pulse} radiated by the light source in one pulse, the pulse charge Q_{pulse} is divided by the effective responsivity R_{eff} and adjusted for the solid angle Ω_{PD} subtended by the photodiode aperture:

$$E_{\mathrm{pulse}} = \frac{Q_{\mathrm{pulse}}}{R_{\mathrm{eff}}} \cdot \frac{1}{\Omega_{\mathrm{PD}}} = \frac{Q_{\mathrm{pulse}}}{R_{\mathrm{eff}}} \cdot \frac{4\pi d_{\mathrm{PD}}^2}{A_{\mathrm{PD}}}, \tag{5.6}$$

where $A_{\mathrm{PD}} = (50.096 \pm 0.067)\,\mathrm{mm}^2$ is the aperture of the photodiode defined by the custom-made baffle (see page 106) and $d_{\mathrm{PD}} = (2.346 \pm 0.002)$ m is the distance from the photodiode to the center of the light source. The solid angle Ω_{PD} then evaluates to (1.699 ± 0.003) msr.

To convert the radiant energy E_{pulse} to the total number of photons emitted in one pulse, we first introduce the energy-weighted equivalent frequency of the light source

$$\nu_{\mathrm{eqv}} := \frac{\sum_i (E_i \nu_i)}{\sum_i E_i} = (790.83 \pm 0.17)\,\mathrm{THz}, \tag{5.7}$$

where the sum runs over the individual measured entries of the emission spectrum of the Octocopter light source and E_i is the energy radiated at the frequency ν_i.

The corresponding energy-weighted equivalent wavelength

$$\lambda_{\mathrm{eqv}} = \frac{c}{\nu_{\mathrm{eqv}}} = (379.35 \pm 0.08)\,\mathrm{nm}, \tag{5.8}$$

with c the speed of light, is very close to the peak wavelength of the emission spectrum of 376.5 nm. The total number of photons emitted in one light pulse is then calculated as

$$N_\gamma = \frac{E_{\mathrm{pulse}}}{h\nu_{\mathrm{eqv}}}, \tag{5.9}$$

where h is Planck's constant. The number of photons emitted at a given wavelength λ is then

$$N_\gamma(\lambda) = \frac{\lambda E}{\sum_i \lambda_i E_i} N_\gamma\,. \tag{5.10}$$

Here, the sum again runs over all entries of the emission spectrum of the light source and E is the energy radiated at the wavelength λ. Taking into account the position of the Octocopter with respect to the telescope, the number of photons reaching the telescope aperture is

$$N_\gamma^{\mathrm{ap}} = N_\gamma \Omega_{\mathrm{ap}} = N_\gamma \frac{A_{\mathrm{ap}}}{4\pi d_{\mathrm{Oct-tel}}^2} \cos\theta, \tag{5.11}$$

where $A_{\mathrm{ap}} = 3.801\,33\,\mathrm{m}^2$ is the area of the telescope aperture and Ω_{ap} is the subtended solid angle at a flight distance $d_{\mathrm{Oct-tel}}$ and an angle θ with respect to the telescope optical axis. Note that $A_{\mathrm{ap}} = \pi r_{\mathrm{ap}}^2$ is simply computed as the geometrical area of the MUG-6 filter of radius $r_{\mathrm{ap}} = 1.1\,\mathrm{m}$.

5.5.2 Atmospheric attenuation

Photons from the Octocopter are both Rayleigh- and Mie-scattered on the path to the telescope. The number of photons arriving at the aperture given by Eq. (5.11) is thus modified by wavelength-dependent Mie and Rayleigh transmission factors $\tau_{\mathrm{Mie}}(\lambda)$ and $\tau_{\mathrm{Rayleigh}}(\lambda)$:

$$\begin{aligned} N_\gamma^{\mathrm{ap}} &= \Omega_{\mathrm{ap}} \sum_\lambda N_\gamma(\lambda)\tau_{\mathrm{Rayleigh}}(\lambda)\tau_{\mathrm{Mie}}(\lambda) \\ &= \frac{A_{\mathrm{ap}}}{4\pi d_{\mathrm{Oct-tel}}^2} \cos\theta \sum N_\gamma(\lambda)\tau_{\mathrm{Rayleigh}}(\lambda)\tau_{\mathrm{Mie}}(\lambda), \end{aligned} \tag{5.12}$$

and $N_\gamma(\lambda)$ is the total number of photons of wavelength λ emitted by the light source in one pulse.

The typical attenuation due to Rayleigh scattering at 1 km flight distance is 4.4 %. Since the process is well understood and described [164, 165], we consider the uncertainty of the Rayleigh attenuation coefficient to be negligible.

Mie scattering, however, is a different story. It is highly dependent on the concentration of aerosols in the atmosphere, as well as their size, both of which are difficult to determine. The transmission coefficients are based predominantly on CLF of XLF data, and the attenuation is effectively integrated over the optical

path from the origin of the laser beam to the respective FD building – 26 km in case of Los Leones.

Because the FOV of the telescopes does not extend below $\sim$1.5° with respect to the horizontal, only the integral of the attenuation in the bottom-most 700 m of the atmosphere is measured, i.e. the height-dependence is not known. The relevant altitudes for the Octocopter are up to 400 m, and it is thus unclear to what degree the CLF-based Mie transmission coefficients accurately represent the situation at one particular position close to the ground.

At the time this manuscript was taking shape, no aerosol database had been released for the years 2014–2015. When measured aerosol data are missing, the reconstruction falls back on default values that are averages over many years. Because aerosol conditions are seasonally modulated and can be highly variable in semi-arid environments, those default values could be significantly off. For example, the Mie transmission coefficients for the Octocopter nights in November 2012 range from 0.925 to 0.980 at the nominal flight distance of 1 km. Compare this to the default value of 0.982.

In an attempt to get a feeling for the possible uncertainty of the atmospheric attenuation, CLF-measured Mie and Rayleigh transmission coefficients were averaged over six years from 2007 to 2013. Since the aerosol concentration is seasonally modulated, peaking in the summer and hitting a minimum in the winter, only data from the months of November were used. Moreover, only CLF-based values were accepted; default values were excluded.

The distribution of Mie and Rayleigh transmission coefficients for the Octocopter positioned at a distance of 1 km from LL3 in the FOV of a pixel in row 4 (e.g. pixels 70 and 202) is shown in Fig. 5.18. The mean values and corresponding RMS are: 0.973 ± 0.030 for Mie and 0.956 ± 0.001 for Rayleigh transmission, where the quoted uncertainty is the standard deviation of the distribution.

Excellent agreement of the default and the mean Rayleigh transmission coefficient (0.956) was expected, as the default value is based on monthly models, similar by design to the mean value computed here. The mean Mie transmission coefficient, on the other hand, is by 0.009 lower than the default value. In this case, some disagreement was anticipated, since the default Mie value is a global and not a monthly average. Since the distribution of Mie transmission coefficients depicted in Fig. 5.18a is skewed, with a tail stretching to lower transmission values, asymmetric uncertainty bands are appropriate. Integrating the distribution in the lowest and highest 15.87 % quantiles yields asymmetric one-sigma error bars of -0.012 and $+0.016$. The mean Mie transmission coefficient in the month of November from 2007 to 2013 is thus $0.973\,^{+0.016}_{-0.012}$. For pixels in row 10 (e.g. pixels 76 and 208), the result is $0.977\,^{+0.018}_{-0.006}$ for Mie and exactly the same as for row 4 for Rayleigh transmission.

In the analysis in Chap. 6, the six-year averages quoted here will be used. We account for the limited knowledge of the aerosol concentrations by including one half of the mean Mie attenuation coefficient (1.25 %) in the combined systematic uncertainty of the number of photons at the aperture. However, it must be stressed that sizable variations of the aerosol concentration over the course of

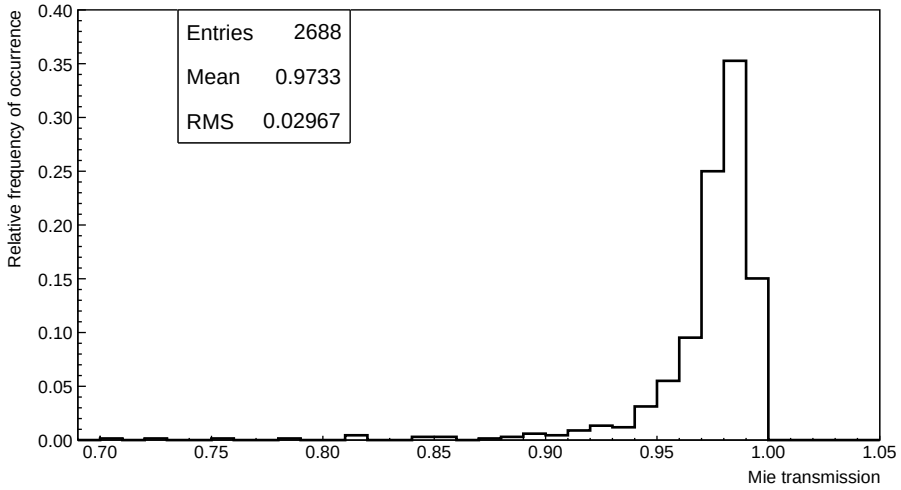

(A) Mie transmission

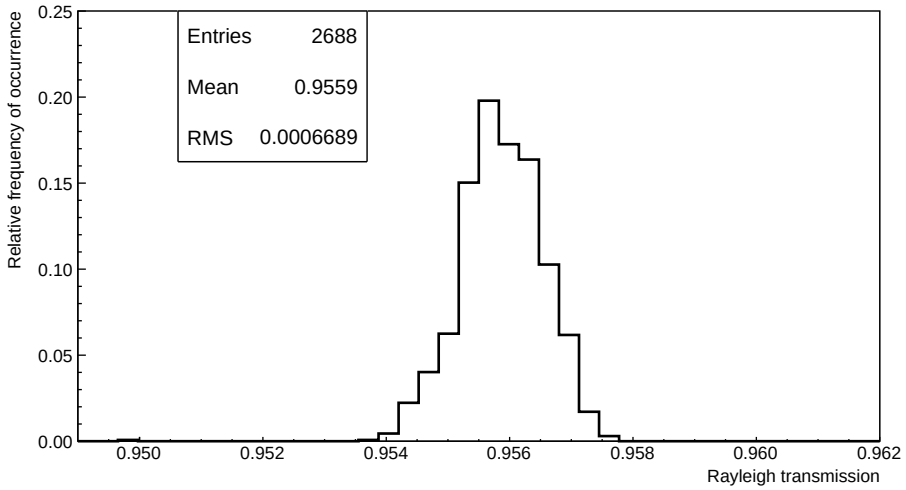

(B) Rayleigh transmission

FIG. 5.18 The distribution of CLF-measured transmission coefficients for the months of November in the years 2007–2013. The data shown are for the Octocopter in the FOV of a pixel in row 4 in Los Leones and the nominal flight distance of 1 km.

one Octocopter campaign cannot be excluded and a re-analysis of the relevant data sets once the aerosol data become available for the years 2014–2015 is desirable.

5.5.3 FD spectral efficiency

To relate the number of ADC counts recorded by the PMTs to photons at the aperture, the end-to-end spectral efficiency of the telescope is needed. Because the standard absolute FD calibration constant provides a conversion factor from ADC counts to a 375 nm-photon equivalent, we shall also express the photon number arriving at the aperture from the Octocopter N_γ^{ap} in this way:

$$N_{\gamma 375}^{\mathrm{ap}} = \frac{1}{\epsilon_{FD}(375)} \sum_\lambda N_\gamma^{\mathrm{ap}}(\lambda)\epsilon_{FD}(\lambda) \tag{5.13}$$

where $\epsilon_{FD}(\lambda)$ is the spectral efficiency of the FD at a wavelength λ and $\epsilon_{FD}(375)$ is the reference efficiency at the reference wavelength $\lambda_{\mathrm{ref}} = 375\,\mathrm{nm}$ (refer to Fig. 3.5 for the FD spectral efficiency curve).

The effective conversion factor from the total number of photons emitted by the light source to a 375 nm-equivalent

$$\epsilon_{Oct-FD} = \frac{\sum_\lambda \epsilon_{FD}(\lambda)}{\epsilon_{FD}(375)} = 0.929. \tag{5.14}$$

This value is based on the standard end-to-end FD spectral efficiency used for reconstruction as of April 2016 [98]. However, a newer measurement is now available [99] and results in $\epsilon_{Oct-FD} = 0.924$. Throughout the analysis, the mean of the two measurements is used, with the difference of 0.3 % included in the combined systematic uncertainty of the method.

In addition to the above discussed uncertainties, there is also an uncertainty on the Octocopter–telescope distance, which combines effects such as the GPS position uncertainty and the Octocopter on-target stability. These are discussed in the following section.

5.6 Performance in the Field

When flying in the field, the Octocopter is exposed to a variety of navigational and meteorological effects, which act as additional sources of uncertainty. In the following, we examine the GPS position uncertainty and the on-target stability of the platform, which combine to give an overall uncertainty of the Octocopter–telescope distance. Subsec. 5.6.2 discusses the temperature measurement in the field, which is necessary to properly apply the temperature correction, and the related uncertainties. Both, the flight distance as well as the ambient temperature significantly affect the number of photons arriving at the aperture, and thus results of the absolute calibration performed with the Octocopter method.

Before we delve into the specifics, let us briefly review the general sequence of affairs during a night of flying the Octocopter. A crew of at least three members

is required: Two persons are needed to handle the Octocopter in the field, while one person holds down the fort in the respective FD building. First, a provisional "octopad" is set up in the pampa, ideally at a distance of about 1 km from the FD building and just below the FOV of the camera pixels to be probed. This is not always possible because of fences, wet areas and power lines, but of course the better the location, the shorter the flight time to the target position.

The integral parts of the octopad are the steering laptop and the Li-Po battery charger, both powered by a gasoline generator, radios for communicating with the FD building and the headquarters in Malargüe, as well as a large toolbox. Additional items include a camping table, two camping chairs and a fluorescent lamp. Besides performing standard FD shift duties, the crew member in the FD building is responsible for activating the "Octocopter mode", in which a full-camera read-out is trigged synchronously with the emission of light pulses by the Octocopter, and verifying that the Octocopter is indeed visible in the FOV of the target pixel.[8]

[8] *The real-time event display software called the "FDEyeDisplay" is used for this purpose.*

To protect the Octocopter, in particular the light source and the dome-capped electronics, from the ever-present pampa dust, it is started from either the camping table or the large toolbox. During landing, the Octocopter is caught manually by the landing gear, to avoid having to land on the uneven ground dotted by shrubberies. The battery is changed after each flight, with re-charging taking place nearly nonstop. A total of four batteries is mostly sufficient to keep a continuous supply of full batteries throughout the night.

5.6.1 Octocopter–telescope distance

GPS position

To determine the flight distance $d_{\mathrm{Oct-tel}}$ of the Octocopter from the telescope, we rely solely on the GPS data.[9] Because the flight distance enters into the calculation of the number of photons in quadrature, it is imperative that the relevant systematic uncertainties are understood.

[9] *In contrast, the position of the Octocopter in the plane perpendicular to the Octocopter–telescope axis can be calculated from the center of gravity of the image on the FD camera.*

A multitude of causes contribute to the total uncertainty of the GPS position, providing for a complex topic. For the interested reader, a short treatise on the main sources of error, satellite coverage and dilution of precision is provided in App. D. Within the scope of the main text, it is sufficient to state that, given an average of eleven visible satellites and relatively low satellite shadowing in the Pampa Amarilla, the estimated uncertainty in GPS position is 6 m.

The Octocopter is currently equipped with a non-differential GPS device, which is fully interfaced with the NaviCtrl (position controller) module. While it is in principle possible to mount an additional hand-held differential GPS device, the total weight of the platform would then increase by nearly one kilogram [166], leading to a considerable reduction in flight time. Therefore, only the currently interfaced GPS device was used and potential systematic offsets in the measured GPS position were handled offline by advanced analysis methods (see Sec. 6.4). An upgrade to a differential device is foreseen for future measurements.

TAB. 5.5 Standard deviation of the off-target distance for two flights *F1* and *F2*, during which the Octocopter was hovering at the target position.

	xy–plane (m)	Altitude (m)
F1	0.6	0.8
F2	1.0	0.7

On-target stability

The flight distance is further affected by the on-target stability of the Octocopter. In other words, how stable is the position of the platform when it has been programmed to hover still at a given GPS waypoint? Fig. 5.19 portrays the stability in the xy–plane and the altitude (in a reference frame centered on the FD building) during three successive flights. As can easily be recognized from the altitude curve, the Octocopter hovered in the FOV of one pixel during the first two flights *F1* and *F2*, and covered two different pixels in the last flight *F3*. The sharp drop in the xy–coordinate just before the Octocopter begins to ascend steeply results from a special take-off maneuver referred to as "parking", during which final in-air checks and preparations are performed.

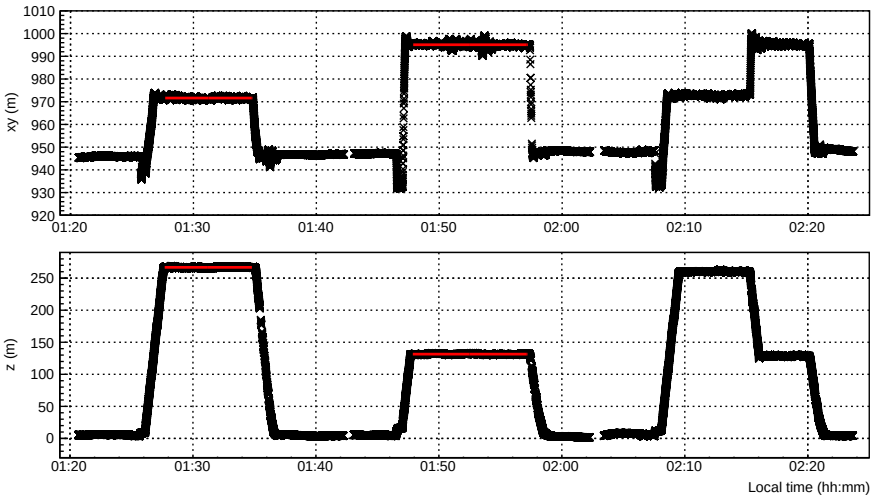

FIG. 5.19 Distance from the LL building in the xy–plane (top) and altitude above the building level (bottom) during three successive flights on November 6, 2012. The times are shown in local Argentina Time (ART). The red lines are fits of the stable regions when the Octocopter was hovering on-target.

Under perfect conditions, the Octocopter would stay completely still at its target position. This is of course not the case and flights like these allow us to study off-target deviations. Fitting the stable regions of flights *F1* and *F2* with a constant, we find that the standard deviation from the mean position is around 0.8 m and does not differ significantly for the xy–plane and the altitude. A breakdown of the fit results is given in Tab. 5.5.

The combined uncertainty of the Octocopter position resulting from GPS error and off-target deviations is taken to be 6.1 m. However, only displacement along the Octocopter–telescope axis $\mathcal{O}_{Oct-tel}$ affects the number of photons arriving at

the aperture. Assuming that excursions in all directions are equally likely and are normally distributed, they can be described with three-dimensional Gaussian curve. We can picture a 1σ-uncertainty as the Octocopter moving on the surface of a sphere of radius $\rho = 6.1\,\mathrm{m}$. The mean displacement $\langle \Delta d_{\mathrm{Oct-tel}} \rangle$ along the axis $\mathcal{O}_{Oct-tel}$, say in the direction away from the telescope, is

$$\langle \Delta d_{\mathrm{Oct-tel}} \rangle = \frac{\int \Delta d_{\mathrm{Oct-tel}} \mathrm{d}A}{\int \mathrm{d}A} = \frac{\rho^2 \int_0^{2\pi} \int_0^{\pi/2} \cos\theta \sin\theta \mathrm{d}\theta \mathrm{d}\phi}{\rho \int_0^{2\pi} \int_0^{\pi/2} \sin\theta \mathrm{d}\theta \mathrm{d}\phi} = \frac{\rho}{2} = 3.05\,\mathrm{m}, \tag{5.15}$$

where θ and ϕ are the polar and azimuthal angles, respectively, and the integration runs over one hemisphere.

The number of photons reaching the aperture $\Delta N_\gamma^{\mathrm{ap}}$ goes with the square of the Octocopter–telescope distance $d_{\mathrm{Oct-tel}}$, and the mean relative distance uncertainty $\langle \Delta d_{\mathrm{Oct-tel}} \rangle$ propagates as

$$\frac{\Delta N_\gamma^{\mathrm{ap}}}{N_\gamma^{\mathrm{ap}}} = 2 \left(\frac{\Delta d_{\mathrm{Oct-tel}}}{d_{\mathrm{Oct-tel}}} \right). \tag{5.16}$$

For the nominal flight distance of 1000 m this becomes

$$\frac{\Delta N_\gamma^{\mathrm{ap}}}{N_\gamma^{\mathrm{ap}}} = 2 \left(\frac{3.1}{1000} \right) = 0.006. \tag{5.17}$$

Excursions in the plane perpendicular to the Octocopter–telescope axis are also immensely important to the analysis, as they can shift the image of the light source within the target FD pixel or even to the neighboring pixels. Advanced techniques exploiting the distribution of the signal on the FD camera have been developed for this purpose and are presented in detail in Sec. 6.4 in the next chapter.

5.6.2 Temperature considerations

In Subsec. 5.3.2, we saw that the intensity of the light source changes with ambient temperature at a rate of approximately $-0.6\,\%/^\circ\mathrm{C}$. Careful temperature monitoring is thus required. Ideally, data from the temperature sensor located inside the diffuser sphere would be available for all flights. This is, however, not always the case, and for instance the 2014 absolute calibration campaign lacks this per-pulse temperature information completely. In such situations, we must draw on other available data sources: the weather stations of the Pierre Auger Observatory or the Global Data Assimilation System (GDAS) [167].

Weather stations: Each FD building as well as the CLF are equipped with a commercial weather station, recording temperature, humidity, pressure, and wind speed and direction at five-minute intervals. In the following discussion, we limit ourselves to data from the LL weather station, which is the closest to the flying site ($\sim$1 km), and the CLF, which is the second closest and best approximates the conditions of the open pampa.

GDAS Run by the United States National Centers for Environmental Prediction (NCEP), GDAS combines surface observations, balloon and wind profiler data, aircraft reports, and buoy, radar and satellite observations to produce altitude-dependent profiles of the main atmospheric state variables. The data are freely available in three-hour intervals on a 1° latitude-longitude grid, the closest reference point being near LA over 60 km from the flying site. Due to good large-scale agreement, GDAS replaced weather station data for shower reconstruction in 2011 [168].

GDAS and weather station temperatures are plotted in Fig. 5.20 for five successive days in November 2012. The weather stations appear to be more sensitive to local conditions than GDAS, exhibit larger day-to-night amplitudes and the LL and CLF temperature curves copy each other closely.

Fig. 5.21 shows the agreement, or lack thereof, with the temperature measured in the diffuser sphere over two nights in November 2012 (5–6 and 11–12).[10] Notice that although spaced only six days apart, the temperature difference between the two nights reaches nearly 10 °C, translating to about 6 % in intensity and underlining the importance of the temperature correction. We observe that the weather station data agree with the sphere temperatures better than GDAS, and for proximity reasons (in both, space and time) choose to use weather station data in lieu of missing Octocopter temperatures.

[10] *Since the light output is determined by the ambient temperature of the LEDs, only the temperature inside the diffuser sphere, and not that on the electronics board, is considered henceforth.*

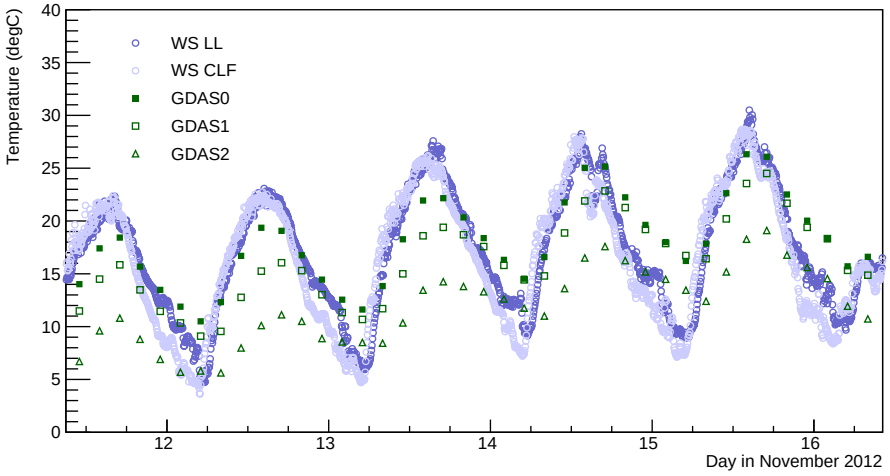

Fig. 5.20 Comparison of weather station (LL and CLF) and GDAS data over five days in November 2012. The legend labels GDAS0–GDAS2 refer to the surface, and the first and second altitude points (approximately at 120 and 600 m above ground level, respectively).

Let us now investigate the sphere temperatures in more detail. At first sight, the weather station temperatures are consistently higher than the sphere temperatures. The difference ranges from 1 °C to 6 °C and depends on the night, as well as the phase of the Octocopter's flight cycle. The global offset is not fully understood. Both, the weather station and sphere temperatures were checked

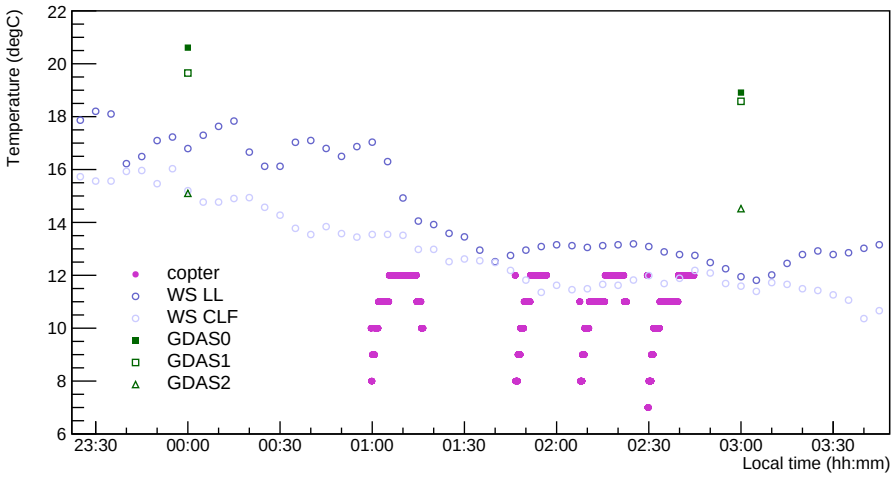

(A) 05–06 November 2012 at LL

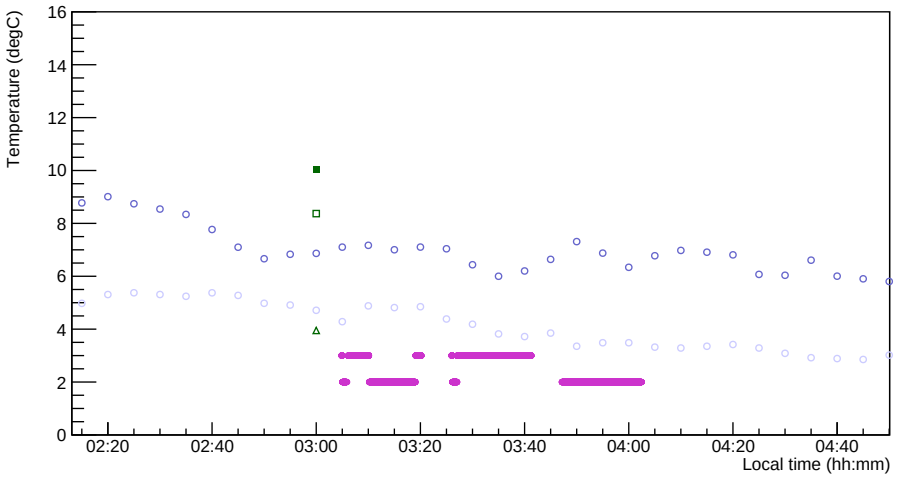

(B) 11–12 November 2012 at LL

FIG. 5.21 Temperatures in the light source sphere (magenta solid circles), from the weather stations (open light and dark blue circles for CLF and LL, respectively) and from GDAS (dark green symbols for different altitudes) plotted for two nights of the November 2012 campaign.

against other temperature sensors and no significant deviations were found. We can only speculate that structures in the vicinity of the weather stations, in the case of LL the concrete pedestal and the FD building itself, store heat during daytime, releasing it throughout the night. To take into account the observed global difference between the weather station and sphere temperatures, the mean deviation of 3 °C enters into the systematic uncertainty budget whenever weather station data are used (November 2014 campaign).

Second, there is a characteristic trend in the sphere temperatures during each flight on the first night (Fig. 5.21a). To better understand how the temperature in the sphere develops, both the temperature and the platform altitude above ground level (AGL) were plotted as a function of pulse number. An example of one flight is shown in Fig. 5.22. As the Octocopter climbs to and hovers at the first target altitude of 250 m, the temperature monotonically increases by 3 °C, and keeps climbing, albeit at a lower rate, even as the Octocopter descends 150 m to the next target altitude. Cooling begins only after landing, and the sphere temperatures appear to lag behind the Octocopter motion.

There is an important conclusion to be drawn from this: The temperature–altitude behavior is not dominated by a change of the atmospheric temperature, assuming a monotonic temperature profile. It also does not result from the total radiated energy of the light source, which translates to a temperature increase of the order of μK per pulse. It appears that the heat originates outside the sphere, perhaps from the electronic modules. Interestingly, the characteristic temperature shape is not visible in the second measurement night in November 2012 (Fig. 5.21b), when the ambient temperature was 10 degrees lower.

Additional temperature data were collected during a series of test flights at LA in March 2012 [156, 169] using an independent MSR145 datalogger [170] attached on the outside of the Octocopter. In this case, as Fig. 5.23 illustrates, the temperature follows the Octocopter motion closely with little latency, confirming the suspicion that the heat originates outside of the diffuser sphere.

Whenever sphere temperatures are available, they are applied on a pulse-by-pulse basis. While it is has been understood that air inside the sphere is heated from the outside with some latency, it is unclear how quickly the LEDs adapt to this temperature. This uncertainty is represented in the combined error analysis by an additional uncertainty of 2 °C and is treated as fully correlated with the 3 °C uncertainty of the weather station temperatures, if used. The combined uncertainty of the temperature correction factor C_{temp} is computed using equation Eq. (C.7).

5.7 Combined Error Analysis

The individual sources of systematic uncertainty discussed throughout this chapter combine to form the uncertainty of the number of photons arriving at the aperture. This uncertainty defines the sensitivity of the Octocopter method as well as the accuracy with which the absolute calibration of the fluorescence detector can be performed. An overview of the systematic uncertainties is given in Tab. 5.6.

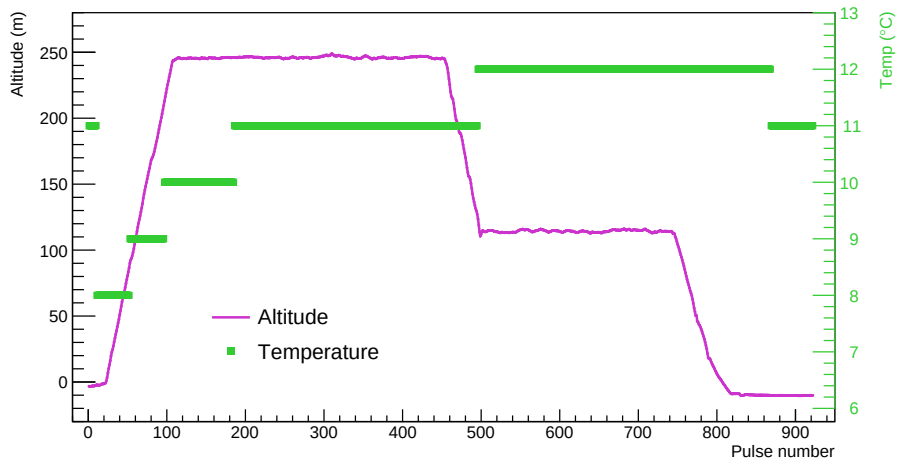

FIG. 5.22 The altitude of the Octocopter above ground level (magenta solid circles, left-hand scale) and diffuser sphere temperatures (green rectangles, right-hand scale) plotted as a function of pulse number, the pulse rate being 1 Hz. The abrupt change in the AGL at pulse number 460 corresponds to the Octocopter moving from a mid- to a low-elevation pixel. Note that due to data volume restrictions the temperatures are stored in steps of 1 °C.

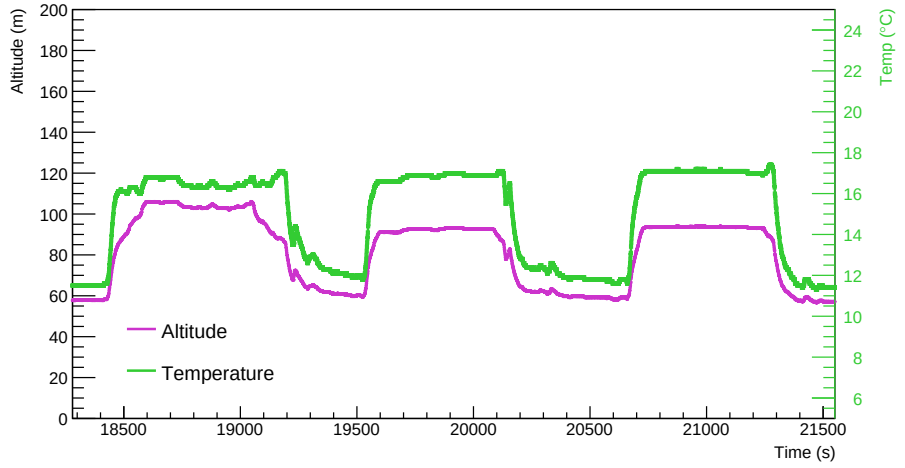

FIG. 5.23 Temperatures (green rectangles, right-hand scale) recorded by the MSR datalogger during three successive flights at LA in March 2012 plotted as a function of time. Also shown is the relative altitude of the Octocopter (magenta solid circles, left-hand scale). Data were logged at a rate of 1 Hz.

TAB. 5.6 Individual sources of the systematic uncertainty of the number of 375 nm-equivalent photons arriving at the telescope aperture from the Octocopter.

Source of uncertainty	Rel. uncertainty (%)
Charge measurement in the laboratory	
Solid angle of photodiode Ω_{PD}	0.2
Spatial non-uniformity of photodiode sensitive area	0.5
Charge measurement Q_{pulse}	2.5
Correction for pulsing rate C_{rate}	0.1
Stray light and multiple reflections	0.1
Conversion of pulse charge to number of photons N_γ	
Effective source–photodiode responsivity R_{eff}	0.5
Energy-weighted wavelength equivalent λ_{eqv}	0.0
Stability and other light source properties	
Inter-campaign stability	1.0
Short-term stability	0.7
Isotropy	0.4
Actual number of photons on the aperture N_γ^{ap}	
Octocopter–telescope distance $d_{\mathrm{Oct-tel}}$	0.6
FD spectral acceptance	0.3
Temperature correction C_{temp} at $T_{\mathrm{offset}} = -17\,^\circ\mathrm{C}$	1.4
Mie attenuation	1.3
TOTAL	3.5

The chosen temperature offset $T_{\text{offset}} = -17\,^{\circ}\text{C}$ corresponds to the typical November night temperatures in the Pampa Amarilla of 5 °C. Availability of sphere temperatures was assumed. If weather station data were to be used, the uncertainty of C_{temp} would increase to 2.3 % and the total consequently to 4.0 %. Note that this is only the combined systematic uncertainty of the number of photons arriving at the aperture per pulse. Additional sources of systematic uncertainty occur further downstream in the analysis chain and will be discussed at the relevant places in the next chapter.

There are two dominant contributions to the total systematic uncertainty of the photon number: the measurement of the pulse charge (2.5 %) and the temperature correction (1.4 % and 2.3 % for sphere and weather station temperatures, respectively). While the former is difficult to improve due to limitations of the instrumentation, the latter may be approached from two different angles. Part of the temperature-related uncertainty comes from the determination of the ambient temperature, part from the fit parameters to the light output–temperature curve. Both could be minimized by stabilizing the temperature inside the diffuser sphere via thermoelectric cooling.

Another welcome and significant improvement of the Octocopter would be a differential GPS device. Although the uncertainty of the Octocopter–telescope distance is only about 0.6 % at 1 km, the data quality would be considerably enhanced by more accurate positioning within the FOV of the telescope, as shall become apparent in the upcoming chapter.

6 Absolute Calibration of the Fluorescence Detector

Contents

This chapter presents the results of the FD absolute calibration using the Octocopter method. Sec. 6.1 outlines the fundamental differences between the drum and the Octocopter light source in terms of their angular photon distribution, timing and the resultant image on the camera. This understanding is imperative for a meaningful comparison of the two, and defines the design of the absolute-calibration Octocopter campaigns described in Sec. 6.2. The technicalities of the FD data analysis, in particular the event selection and processing, as well as methods to accurately determine the Octocopter position on the camera, are discussed in Secs. 6.3 and 6.4. The final results of the calibration are presented and compared to simulations in Sec. 6.5, and discussed from different angles in Sec. 6.6.

6.1 Drum Calibration vs. Octocopter

Drum calibration is the standard absolute calibration procedure of the Auger fluorescence telescopes, aptly named for the resemblance of the used large-diameter light source to a giant drum (see Sec. 3.1 for a thorough description). During calibration, the drum is mounted onto the aperture, covering it entirely,

and pulsed light is emitted. The whole camera is illuminated fairly uniformly (save for minor inhomogeneities of the drum) and the signals of all pixels are read out simultaneously. The absolute calibration constant thus describes the mean response of a pixel, averaging over its spatial non-uniformities.

The advantage of the drum light source is the ability to calibrate all 440 pixels of one camera simultaneously, however, at the price of a very non-shower-like measurement insensitive to the point spread function (PSF) of the telescopes. In contrast to the drum, an air shower passing through the field of view (FOV) of a telescope produces a track on the camera, the width of which depends on many parameters, including the energy and the distance of the shower from the telescope, the viewing angle, the imaging properties of the telescope or atmospheric conditions. At any given point in time, i.e. for any 100 ns bin of the ADC trace, the image of an air shower on the camera resembles that shown in Fig. 3.15 on page 52.

The Octocopter, designed to mimic a snapshot of an extensive air shower (EAS) in time, is a categorically different light source than the drum. Only 10 cm in diameter, its geometric size at the nominal flight distance of 1 km is a mere 0.006°. The final image on the camera is effectively broadened to 0.6° [121] by spherical aberration and further by the PSF.[1] Nonetheless, as can be seen from the example in Fig. 3.11 on page 48, the majority of photons strike the target pixel and the lateral distribution of the image is rather steep, with the intensity dropping by two orders of magnitude when going from the target pixel to a pixel within the first crown of pixels surrounding the target pixel (see Fig. 6.1).

[1] *See Sec. 3.2 and Subsec. 4.2.2 for a discussion of the PSF.*

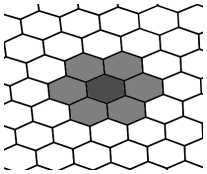

FIG. 6.1 The hottest pixel is surrounded by six pixels in the first crown.

The relatively small size and steep lateral distribution of the Octocopter image cause the method to be sensitive to the spatial non-uniformities of the camera, dominated by the lower efficiency of the light collectors and varying PMT surface sensitivity. Let us describe the position of the image on the camera in terms of the signal-weighted viewing directions of the participating pixels:

$$\vec{n}_{\mathrm{CG}} = \frac{\sum_i S_i \vec{n}_i}{\sum_i S_i}, \tag{6.1}$$

where $\vec{n}_i$ is the nominal viewing vector of pixel i defined by the central line of its FOV, S_i the signal detected by this pixel (in 375 nm-equivalent photons at the aperture) and $\vec{n}_{\mathrm{CG}}$ is the effective viewing vector of the position of the image on the camera. The sum runs over a number of pixels grouped symmetrically around the target pixel, in practice limited to the first crown of pixels, as the outer crowns are dominated by noise. Depending on the application, the hottest pixel may or may not be included in the calculation. If included, $\vec{n}_{\mathrm{CG}}$ will be heavily pulled towards the viewing direction $\vec{n}_{\mathrm{hottest}}$ of that pixel. If not included, the true position of the image can be reconstructed from $\vec{n}_{\mathrm{CG}}$ using advanced procedures described in Sec. 6.4. For now, suffice it to say that it is indeed possible to determine the position of the image on the camera to a few tenths of a degree.[2] Note that the GPS position of the Octocopter cannot be used due to potentially large systematic offsets.

[2] *Compare this to the 1.5° opening angle of the FOV one pixel.*

The varying photon detection efficiency of the camera is clearly visible in

Octocopter data. Fig. 6.2 demonstrates how the detected signal changes with angular distance of the CG of the image from the center of the hottest pixel center. Note that rotational symmetry with respect to the nominal pixel viewing vector is assumed, i.e. we do not distinguish between moving towards the side or the vertex of the light collectors. The signal was integrated over three regions: the hottest pixel only, the hottest pixel and the surrounding crown of six pixels, and the entire camera.

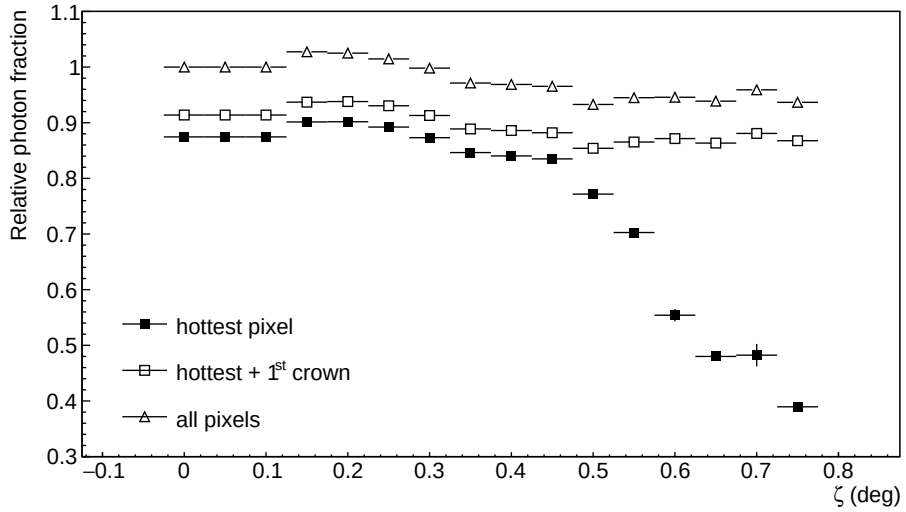

FIG. 6.2 The spatial sensitivity of a camera pixel measured with the Octocopter method. The relative reconstructed photon fraction is shown as a function of the angular distance ζ from the center of the hottest pixel. Three different integration regions were used: hottest pixel only, hottest pixel and the pixels within the first crown, and the entire camera. The abscissa shows the number reconstructed photons relative to that at the center of the pixel ($\zeta = 0°$) when summing over the entire camera. The flat response in the first three bins results from the inability of the position determination procedures (discussed in detail in Sec. 6.4) to resolve the position in this angular range.

In the first case, the signal drops sharply for $\zeta > 0.5°$ simply because parts of the image begin moving out of the integration region. The distance from the pixel center to the border of a neighboring pixel is 0.75° when moving perpendicularly towards a side of a light collector and 0.866° when moving towards a vertex. Once pixels in the first crown are included in the integration region, the effect is largely compensated and the signal curve stabilizes. The all-camera curve follows a similar trend, albeit on average 8 % higher. The magnitude of the response variation for the two larger integration regions is about 10 %, and is comparable with the results obtained in direct laboratory measurements using a spot with a diameter of 0.56° and a similar angular distribution [62].

Returning to the subject of rotational symmetry, it must be noted that there is a qualitative difference between the image moving towards the side of a Mercedes star and towards its vertex. In the former geometry, the spot smoothly rolls over the Mercedes arm, while in the latter, it is "squeezed" in the corner of the light collector. It is hard to identify this pattern in measured data, because stringent

cuts on position are required and the position determination is insufficient for this purpose. However, as we shall see soon in Sec. 6.4, this asymmetry is clearly visible in simulation.

With regards to the spatial inhomogeneity of the PMT surface, the key to performing an absolute calibration of the FD that can be realistically compared to the drum method lies in applying the Octocopter in a way that effectively does the same as the drum, that is in uniformly sampling the response of a pixel across its surface. To this end, two dedicated measurement campaigns have been conducted and are described in the following section.

6.2 Dedicated Measurement Campaigns

To be able to compare the Octocopter absolute calibration to that obtained with the drum method, the pixel surface ought the be sampled uniformly with light pulses. Two specially designed campaigns were flown for this purpose, one in November 2014, the other in November 2015. Selected pixels were scanned using a regular grid of GPS waypoints with a step size of approximately 0.25° – roughly one third of the effective spot size – and about 30 pulses were fired from each position. Moreover, to compensate for a potential systematic offset in GPS position of up to 6 m, a 0.3° safety margin was added to the scanned pixel's boundary in each direction. An example of a such a flight pattern is shown in Fig. 6.3. Due to constraints imposed by flight time and the number of programmable waypoints, the pattern for each pixel was split between five flights.

Tab. 6.1 lists the pixels studied in each campaign, including the November 2012 test campaign, during which only one position per pixel was flown. The pixel numbering convention is shown in Fig. 6.4. There are a few standard pixel positions on the camera that are of particular interest and convenient to study:

Pixel 208 (row 10, column 10) is one of the three pixels positioned around the center of the camera through which the optical axis of the telescope passes. The ghost image is directly adjacent to the main image and the solid angle of the pixel is maximum.

Pixel 70 (row 4, column 4) and 356 (row 4, column 17) are lower-elevation pixels close to the corners of the camera. We always study pixels that are at least four pixels away from either side of the camera to limit border effects and allow for reasonably large and symmetric integration regions. The advantage of low-elevation pixels is increased on-target time, however, they may be more affected by the uncertainty of the aerosol concentration and subsequent Mie scattering in the lowest levels of the atmosphere.

Other studied pixels include pixel 369 (row 10, column 17) located close to the camera side at mid-elevation, and pixel 202 (row 4, column 10) close to the bottom of the FOV. Unless desired for dedicated elevation studies, we do not venture above 250 m (the approximate height of the optical axis at the standard flight distance). In the following, pixels will often be denoted by their absolute

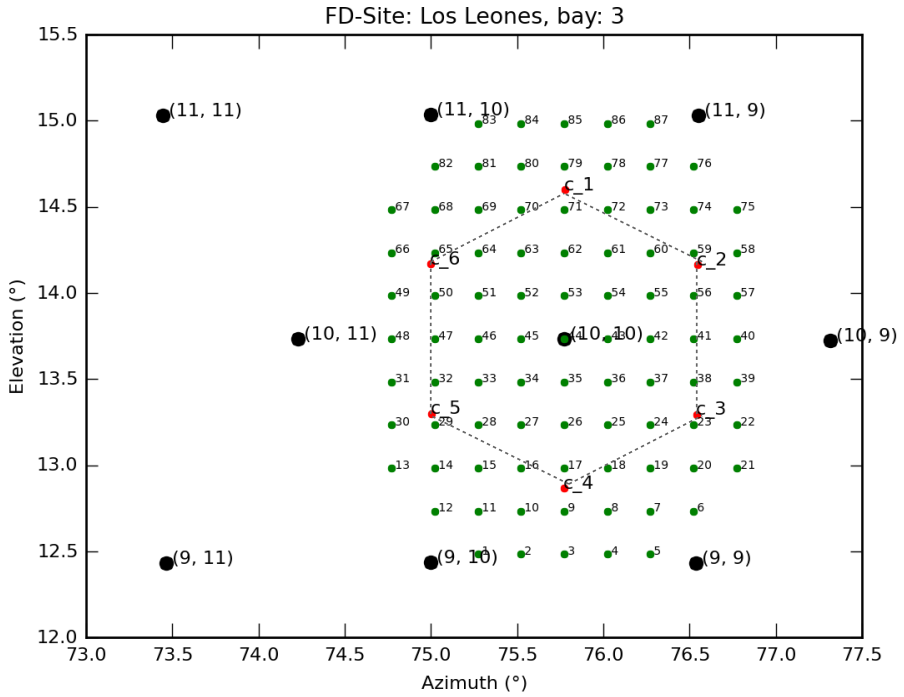

FIG. 6.3 An example of a flight pattern of the Octocopter in the November 2014 and 2015 campaigns. The large black points labeled with (x, y) denote pixel centers in terms of row and column numbers x and y, the smaller red points labeled with c_z the pixel corners. The outline of the hottest pixel is traced with a gray dashed line. The small green numbered points are the pre-programmed Octocopter GPS waypoints projected onto the camera.

number (c.f. Fig. 6.4) complemented by the row and column coordinates r and c on the camera. For example, the description r10/c10 p208 refers to pixel 208 in row 10 and column 10.

Octocopter measurements are performed on clear dark nights with calm atmospheric conditions. We require no (or very low) cloud coverage to minimize scattered light, wind speeds below 10 km/h for stability and safety reasons, and obviously no rain. Basic atmospheric state variables are recorded by the ground weather stations at each FD site and at the CLF in 5-minute intervals. The average values for all Octocopter measurement nights in November 2014 and 2015 are listed in Tab. 6.2. It is interesting to note that the humidity during the second and third night are considerably higher than during the first night (by 18 % and 37 %, respectively). While these data are not used for analysis, they are useful to get an idea of the conditions on a given measurement night.

It shall be pointed out that pixel scans are incredibly time-consuming. Under favorable conditions (wind- and cloudless nights with no lightning on the horizon), five flights may just be completed in one night. Such conditions are rather rare, and occur on average every fourth night. For proximity reasons, flights are generally conducted at Los Leones, about half an hour's drive from the central campus in Malargüe. In the past, flights were also conducted at Coihueco,

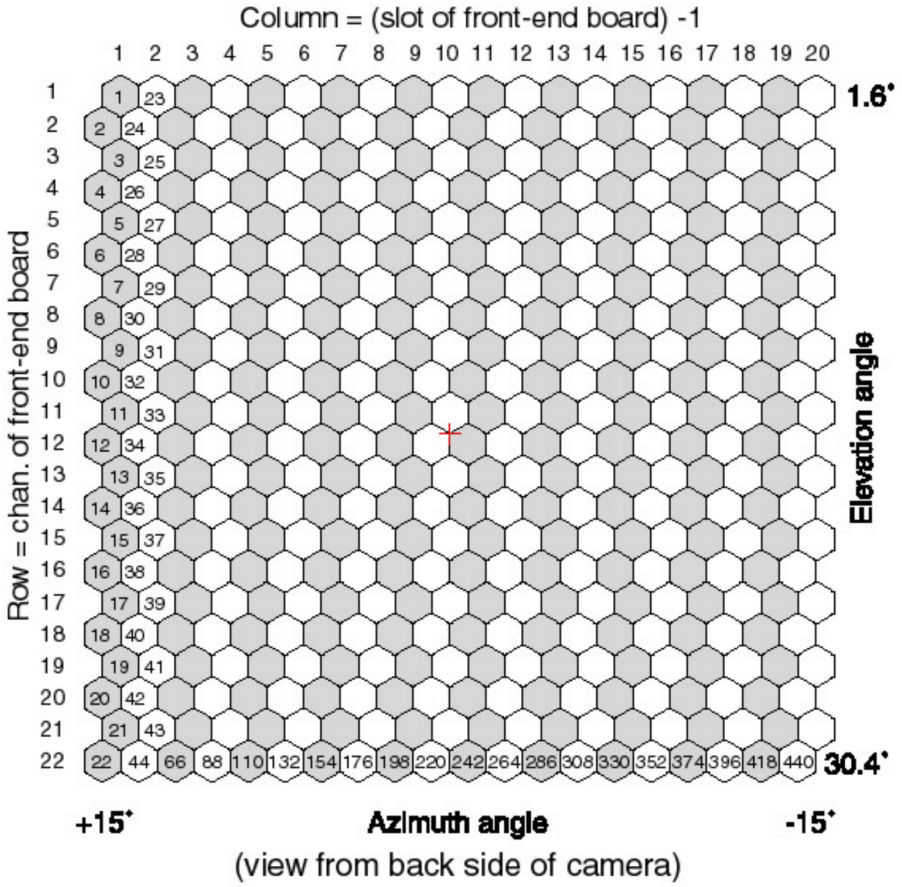

FIG. 6.4 The pixel numbering convention: Viewing the camera from behind, pixels are number from the top left moving first down, then right across the camera, starting at 1. The image of the Octocopter or an air shower on the camera is vertically inverted, so pixels in the upper part of the sketch correspond to low elevations and vice versa. The red cross marks the optical axis of the telescope. From [171].

about as far as Los Leones in terms of driving time, but were perpetually plagued by problems with the Octocopter compass, possibly due to local magnetic field anomalies, and frequent high winds. Furthermore, the octopad had to be set up quite inconveniently across the National Route 40, about 300 m below the level of the FD site, considerably increasing the flight time to the target position and the AGL of the Octocopter.

Fig. 6.5a and Fig. 6.5b show the achieved pixel coverage in November 2014 and 2015. In particular, each point represents the projection of the Octocopter GPS position onto the FD camera at the moment a light pulse was fired. During the 2015 campaign, a dedicated elevation scan was flown, and is clearly visible in Fig. 6.5c as a line of points reaching up to row 14. The idea of this exercise was to investigate a potential elevation dependence of the signal that could be effected e.g. by the stratification of aerosols in the bottom-most layers of the atmosphere, the albedo of the ground or the optical characteristics of the telescopes.

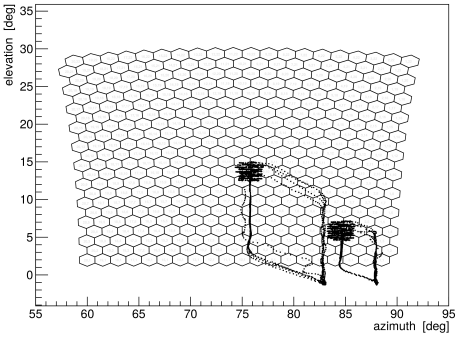

(A) November 2014

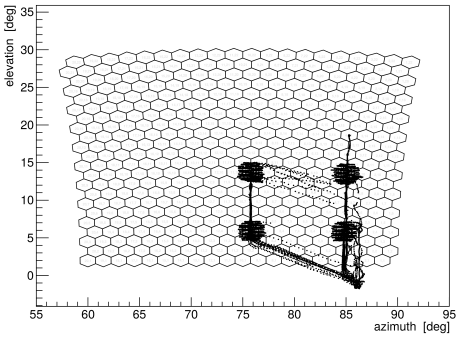

(B) November 2015

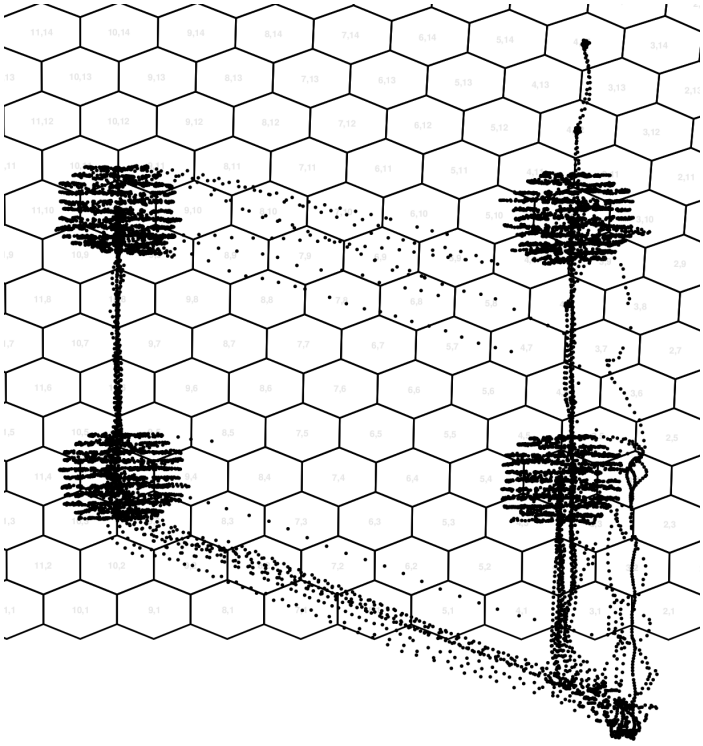

(C) November 2015 – zoom

FIG. 6.5 Pixel coverage during the November 2014 and 2015 campaigns. Each point represents the projection of a position from which a light pulse was fired onto the camera and data from all flights at LL3 during the respective campaign are superposed. The bottom panel contains a zoom of the flight paths of the November 2015 campaign, with the elevation scan clearly visible in the right part of the plot.

TAB. 6.1 Overview of absolute calibration campaigns between 2012 and 2015. Pixels are denoted by their row and column coordinates r and c on the camera (e.g. r04/c17), as well as the absolute pixel number p (e.g. p356).

Campaign	Night	Telescope	Pixel	Flight pattern
Nov 2012	05–06	LL4	r10/c10 p208 r10/c17 p369 r04/c17 p356	one point
	10–11	LL4	r10/c10 p208 r10/c17 p369 r04/c17 p356	one point
		LL3	r10/c10 p208 r10/c04 p076	
Nov 2014	13–14 19–20 21–22	LL3	r04/c04 p070 r04/c04 p070 r10/c10 p208	pixel scan
Nov 2015	05–06 06–07 13–14 17–18	LL3	r10/c10 p208 r10/c04 p076 r04/c04 p070 r04/c10 p202	pixel scan

This work contains the results of both, the 2014 and the 2015 measurement campaigns, the data of which was reconstructed using up-to-date standard FD calibration constants. However, since no aerosol database is available since the beginning of the year 2014, the atmospheric attenuation on the path from the Octocopter to the telescope can only be estimated (see Subsec. 5.5.2).

6.3 Data Reconstruction and Selection

This section outlines basic reconstruction and event selection procedures. First, the data stream logged by the custom-written software of the Octocopter [103, 156] is matched to the individual FD events by time information. For each FD event, uniquely identifiable by its GPS second (as the pulsing rate is 1 Hz), the Octocopter data log is searched for corresponding entries (transmitted and logged at a rate of 5 Hz). Should entries be missing in the Octocopter data log, e.g. due to transmission problems during flight, the matching algorithm will accept entries within ± 2 s of the GPS second of the FD event. The time window can be set arbitrarily, but was not needed at all for the analysis of the 2014 and 2015 campaigns, as the Octocopter data logs were complete for all flights.

The primary output of the FD camera is the ADC trace recorded by each pixel, i.e. the number of ADC counts per 100 ns time bins. The quantity of interest is the number of photons at the aperture, which is obtained by applying the following steps:

TAB. 6.2 Average temperature, humidity, wind speed and air pressure during the Octocopter measurement nights in November 2014 and 2015. For 2014, data recorded by the ground weather station at Los Leones are shown. Since this weather station was malfunctioning in November 2015, data from the CLF station are shown for that period.

Night	Temp. (°C)	Humidity (%)	Wind speed (m/s)	Press. (mmHg)
November 2014, Los Leones weather station				
13–14	11.4	26.3	1.7	863
19–20	10.3	44.5	2.3	861
20–21	9.7	63.5	0.1	862
November 2015, CLF weather station				
5–6	5.7	82.2		866
6–7	8.3	73.1	4.5	862
13–14	8.7	79.5	3.1	861
17–18	6.3	75.0	3.8	858

1. Convert the electronic signal in ADC counts to 375 nm-equivalent photons at the aperture by applying the corresponding standard FD absolute calibration constant.
2. Identify the hottest pixel, i.e. the pixel receiving the highest photon count.
3. Search for the pulse start and end in the hottest-pixel photon trace using the standard FD reconstruction procedure.
4. Integrate the gross photon number within the pulse.
5. Subtract the baseline to obtain the net number of photons.

This procedure yields the total number of 375 nm-equivalent photons arriving at the aperture detected by the hottest pixel, and is subsequently repeated for all other pixels applying the pulse start and stop times found for the hottest pixel to ensure that we do not integrate over random fluctuations.

The AC-coupled electronics responds to the relatively long and strong light pulses of the Octocopter with an undershoot following the main pulse (Fig. 6.6). Strictly speaking, the baseline changes exponentially, yet the very low AC coupling constants of the order of 0.36 ms allow for a linear fit. To be compatible with the drum pulse integration procedure, we do not account for after-pulsing, which typically contributes about (1.2 ± 0.4) % of the signal in LL3. The estimated uncertainty of the net pulse area is ± 2 %. Note that we always work with the total pulse area, as this is the quantity that is measured during the absolute calibration of the light source, and also ensures we are insensitive to deviations from a perfectly square pulse.

The basic FD data reconstruction, pulse finding and conversion to photons is done using the standard procedures of $\overline{\text{Off}}\underline{\text{line}}$, with the module sequence given in App. E.2. The subtraction of the baseline is handled independently, as the $\overline{\text{Off}}\underline{\text{line}}$

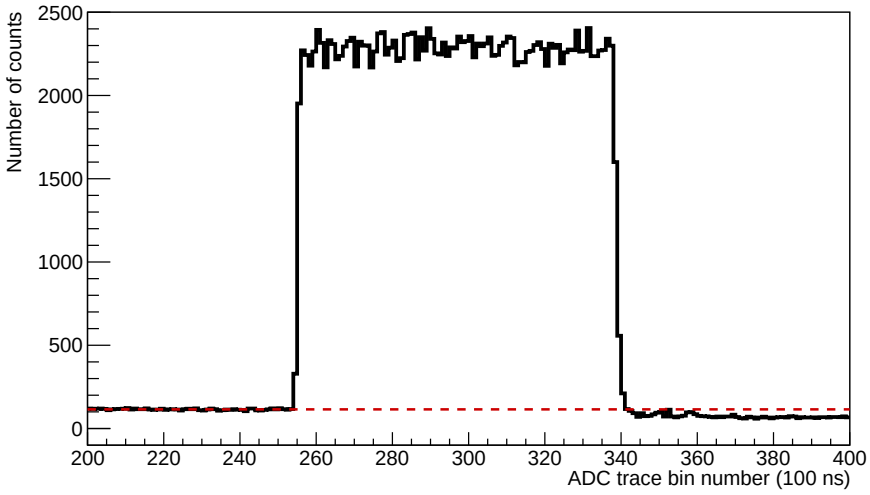

FIG. 6.6 A segment of the ADC trace of the Octocopter light pulse. Each time bin corresponds to 100 ns. The dashed red line marks the mean pre-pulse baseline level and the main pulse is followed by an undershoot.

pulse integration procedures was designed to deal specifically with constant baselines typical for shorter air shower pulses. The output of the reconstruction is a ROOT tree containing a multitude of primary and reconstructed variables referred to as an Advanced Data Structure Tree (ADST) file within the Auger Collaboration [172, 173].

Numerous checks are implemented in the successive Octocopter data analysis to exclude empty events, which may occur for several reasons, but are always tied to the fact that the telescope is triggered externally during Octocopter data acquisition (on top of regular DAQ, which runs concurrently). Commonly encountered situations include the telescope being externally triggered before the Octocopter has reached the FOV, automatic shutter closings, time synchronization problems, which cause the light pulse to fall outside of the read out ADC trace, and self-triggering of the telescope, which leads to Octocopter events becoming part of the regular data stream as opposed to the one reserved for externally triggered events. None of these scenarios are problematic, nor are they in any way related the quality of the Octocopter events. The following selection criteria are applied to filter empty events:

- Only events where the **Octocopter GPS position** is within the FOV of the telescope are considered.
- The **pulse position** is well defined within the ADC trace. In data, the pulse start should occur roughly at bin 250, and the actual observed value is (254 ± 12) ADC bins. In simulation, the position of the pulse is handled slightly differently, with an observed value of (275 ± 24) ADC bins. Only pulses starting in the bin range 150–300 and 180–320 are considered in data and simulation, respectively.

TAB. 6.3 Approximate variance of the ADC trace baseline in ADC counts^2 for different background light conditions.

Light conditions	Variance range (ADC cts.^{2})
Closed shutters	< 10
Low NSB, cloudless night	10–45
Elevated NSB, scattered light	> 45

- The **pulse width** at amplitude $A = 5$ is 8.358 μs, and it is additionally smeared to either side by the anti-aliasing filter. The average observed pulse width is (92 ± 2) ADC bins in both, data and simulation. Only pulses with a width of $\Delta t_{\text{pulse}} = (92\,^{+10}_{-6})$ ADCbins are accepted.
- The average gross **photon number in the hottest pixel** (excluding events at the border of the camera) is $(7.5 \pm 1.8) \times 10^5$. Empty events are excluded by requiring a minimum gross photon number of 5×10^3 photons in the hottest pixel.
- The **variance of the baseline** of the ADC trace is proportional to the NSB photon flux. Tab. 6.3 shows the typical ranges for different background light conditions. By accepting only events with variances in the range 8–65 ADC counts squared, events recorded with high NSB or shutters closed are excluded.

Furthermore, the following basic checks are performed during analysis:

- **Saturation:** Saturated pixels, i.e. those with 4091 ADC counts in any time bin, are checked for. The light source intensity and distance from telescope are chosen such that saturation never occurs for measured data. Saturation may occur in simulation when a clean configuration of the optical components is used and is handled by decreasing the simulated intensity. Saturated simulated events are never simply excluded, as this would bias the results towards low-signal fluctuations.
- **Border of camera:** If the hottest pixel is at the edge or in the corner of the camera, the event is excluded, since the position cannot be reconstructed accurately. This only occurs as the Octocopter is moving into the FOV of the target pixel.
- **Hottest pixel and Octocopter GPS position mismatch.** The difference between the center of the hottest pixel and the projection of the Octocopter GPS position onto the camera is investigated. For proper events, and assuming no glitches occurred in the transmission of the navigational data from the Octocopter, the difference should not exceed the distance between two adjacent pixel centers (1.5°).
- **Hottest pixel and image CG mismatch.** As in the previous point, however, the CG of the image, computed from the signal in the hottest pixel and the surrounding first crown of pixels, is used instead of the Octocopter GPS position.

The last two consistency checks are included mainly to identify any unforeseen failures of the analysis. Without exception, all events of the 2014 and 2015 data set passed those checks after empty events had been excluded.

6.4 Position Determination

A uniform sampling of the telescope response across the entire pixel surface is a prerequisite for a meaningful absolute calibration of the FD and a comparison with the standard drum-based calibration. In this section, various methods for an accurate determination of the Octocopter position are presented and used to assess the uniformity of the sampling.

As discussed in Sec. 5.6, potential systematic offsets in the GPS position of up to 6 m, corresponding to 0.34° on the camera at 1 km flight distance, are not negligible in terms of pixel non-uniformities (cf. Fig. 6.2). While the GPS positions must be used to determine the position along the Octocopter–telescope axis $\mathcal{O}_{\mathrm{Oct-tel}}$, the position in the plane perpendicular to this axis may be deduced from the distribution of the signal on the camera.

Two independent methods were developed. The "constant-offset" method is based on the simplifying assumption that the systematic offset in GPS position remains stable over limited periods of time.[3] While this method fails when its assumptions are not met, it is a valuable simulation-independent cross-check of the second method referred to as "b-conversion", which uses simulation-based factors to obtain the true position from the CG of the image.

[3] *This is a reasonable assumption as long as the satellite configuration remains constant. See App. D for more information.*

The workings and performance of the methods are discussed on the following pages in Subsecs. 6.4.1 and 6.4.2. Both perform well, are able to correct for the systematic GPS position offsets observed in data, and the uncertainty of the position on the camera is determined from the difference in results obtained by applying the two methods.

6.4.1 Constant-offset method

Let us begin by looking at how a systematic offset in GPS position manifests itself in data. The result of selecting all events from a sequence of scanning flights where pixel 208 received the highest photon count and plotting the corresponding GPS positions of the Octocopter relative to the pixel center is shown in Fig. 6.7a. While the image is quite centered in azimuth, it is clearly shifted towards smaller zenith angles. With error-free positioning, we would expect the image to be centered and contained within the indicated pixel boundaries, of course within the accuracy of directional pointing of the telescope of about 0.1°.

It must be emphasized that the two effects – a systematic GPS position offset and a small difference between the actual and nominal pointing of the telescope – cannot be differentiated, certainly not within one flight or night, or using a regular (non-differential) GPS device. This is an important point and having been made, in the following the offset is discussed as if it originated solely from the position inaccuracy. In either case, it does not affect the results of the analysis,

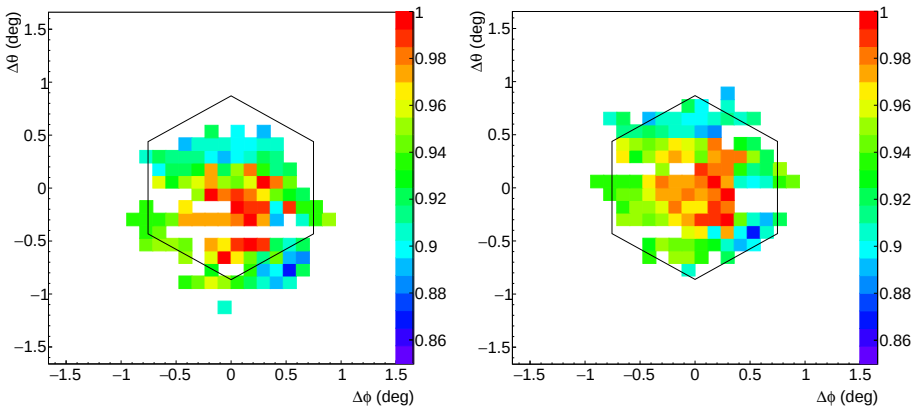

FIG. 6.7 Left: Octocopter GPS positions of all events in a sequence of scanning flights where pixel 208 was the hottest, plotted relative to the pixel center in terms of the zenith and azimuthal angles $\Delta\theta$ and $\Delta\phi$. There is a clear systematic shift towards lower zenith angles. The color scale indicates the relative response of the pixel. Right: After applying a constant correction factor computed based on the GPS positions of events with symmetric signals on the camera.

which effectively eliminates it.

Interestingly, the observed shift appears to be rather constant over the course of three hours during which the flights were completed, which is tied to the fact that satellite coverage itself may remain stable for up to several hours (cf. Fig. D.1). Based on the assumption of a constant offset for a given time interval, a crude GPS position correction factor may be extracted and applied as follows:

1. From all data acquired within one night, select only events producing symmetric FD images on the camera. Those are events where the Octocopter was hovering very close to the central viewing direction of the pixel.

2. Compute the mean of the corresponding GPS positions. Ideally, this value would coincide with the pixel center, yet in practice an offset similar to that in Fig. 6.7 (left) is observed, with typical values for the 2014 campaign listed in Tab. 6.4. Note that the offset in elevation is roughly double that in azimuth, since determining the altitude is more challenging due to geometrical reasons.

3. The difference between the GPS positions of the selected events and the coordinates of the pixel center is the desired correction factor and is applied to correct the position of all events within the relevant time period. The shifted positions are shown in Fig. 6.7 (right).

The typical time interval for which the constant-offset method can be applied is 3–4 hours, i.e. the time it takes to perform about 5 scanning flights. If satellite configuration fluctuates heavily during this period, shorter time intervals must be used. However, in many cases there will not be enough events with symmetric signals to extract the correction factor. Despite the fact that the method only works

TAB. 6.4 The GPS position of events with symmetric signals on the camera relative to the center of the target pixel. Data from the November 2014 campaign were used.

Date	$\Delta\theta$ (°)	$\Delta\phi$ (°)
19–20	0.5	0.2
21–22	0.3	0.0

for nights with stable satellite coverage, it has the immense advantage of being simulation-independent. In the final evaluation, it is used as an independent cross-check to assess the robustness of the results with regards to position uncertainty.

6.4.2 Center-of-gravity method

Using the CG of the image is another option for determining the Octocopter position on the camera, albeit a non-trivial one, as the position of the CG is hardly a linear function of the true positions. Profound non-linearities are caused by the pixelization of the camera and the steep PSF, which drops nearly three orders of magnitude over 3°. The exact functional dependence is defined by the size of the region used to compute the CG and potential weights used to scale the signal in different subregions.

If we include the hottest pixel in the calculation, the CG will be heavily pulled towards the center of the hottest pixel due to the steeply falling distribution of the image. For the very same reason, the CG will be pulled towards the nearest neighboring pixel if we exclude the hottest pixel. This is best understood by simulating Octocopter pulses fired from well-defined positions. Fig. 6.8 illustrates the situation using CG coordinates computed from the signal of all pixels within the first crown and the signal in the hottest pixel scaled by different weights: 0.0, 0.05, 0.1 and 1.0. Larger integration regions of two and three crowns were also investigated, however, the outer crowns were found to be dominated by noise. Consequently, the CG computation region is generally limited to the first crown, unless stated otherwise.

Clearly, no single curve can be used to convert ζ_{CG} to ζ_{true}, as they are either too flat or non-monotonic. The situation is further complicated by the hexagonal shape of the pixel. As can be seen in Fig. 6.9, the conversion function is different when moving from the center of the pixel towards a side or towards a vertex of a light collector. In fact, the non-monotony in Fig. 6.8 results from the spot moving between the two extremes of the side and vertex of the light collector. Also, note that the curves converge to $\zeta_{\mathrm{CG}} = 0.2°$ and not the pixel center at $\zeta = 0°$, which is an artifact of working in polar coordinates where fluctuations around the pixel center never quite cancel out. When elevation and azimuth are handled separately, the curves pass through (or very close to) zero.[4]

[4] *In particular, there is a small (∼0.03°) offset in elevation caused by the shadow of the camera support.*

Since the conversion function from the reconstructed to the true coordinates depends on the two-dimensional position on the pixel surface (θ_{true}, ϕ_{true}), we define the conversion factors

$$b_\theta = \frac{\Delta\theta_{\mathrm{true}}}{\Delta\theta_{\mathrm{CG}}} b_\phi = \frac{\Delta\phi_{\mathrm{true}}}{\Delta\phi_{\mathrm{CG}}}, \tag{6.2}$$

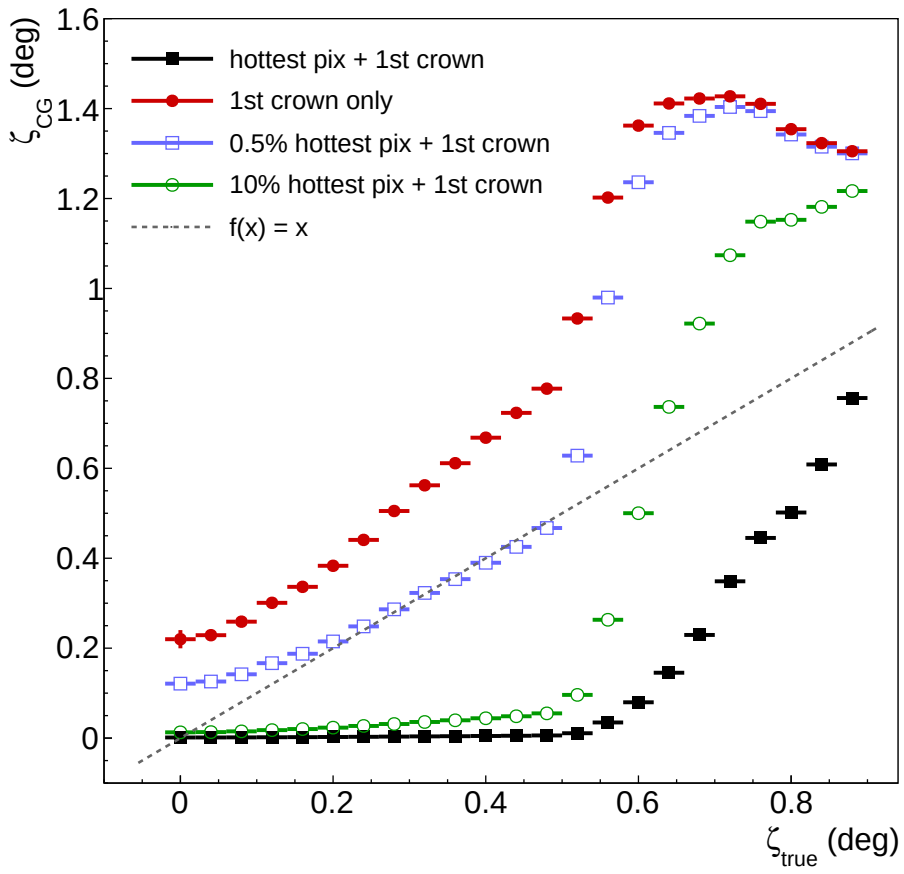

FIG. 6.8 Reconstructed position of the CG (ζ_{CG}) as a function of the true position (ζ_{true}) used in simulation. Both are shown in terms of the angle ζ, denoting the angular distance from the center of the hottest pixel. A 45-degree line was drawn to guide the eyes.

where $\Delta\theta_{CG}$ and $\Delta\phi_{CG}$ are the zenith and azimuthal angles of the image CG computed from the signal of the pixels in the first crown only and excluding the hottest pixel, and $\Delta\theta_{true}$ and $\Delta\phi_{true}$ are the coordinates of the known simulated position, or later, of the unknown true position during flight that we seek to find.

A map of (b_θ, b_ϕ) factors was generated by simulating Octocopter pulses fired from well-defined positions ($\Delta\theta_{true}$, $\Delta\phi_{true}$) on a 0.02° by 0.02° grid, delivering 10 pulses per position and covering the entire pixel surface uniformly. Since the simulated pixel response is azimuthally symmetric (except for pixels at the border of the camera, which are not used in this analysis) and to reduce the already significant computing time, only positions on one half of the pixel were simulated, and the resulting conversion factor half-maps were mirrored about the axis defined by $\Delta\phi = 0°$.

Fig. 6.10a shows all simulated coordinates on and around the target pixel, and Fig. 6.10b the corresponding CG-reconstructed coordinates $\Delta\theta_{CG}$ and $\Delta\phi_{CG}$,

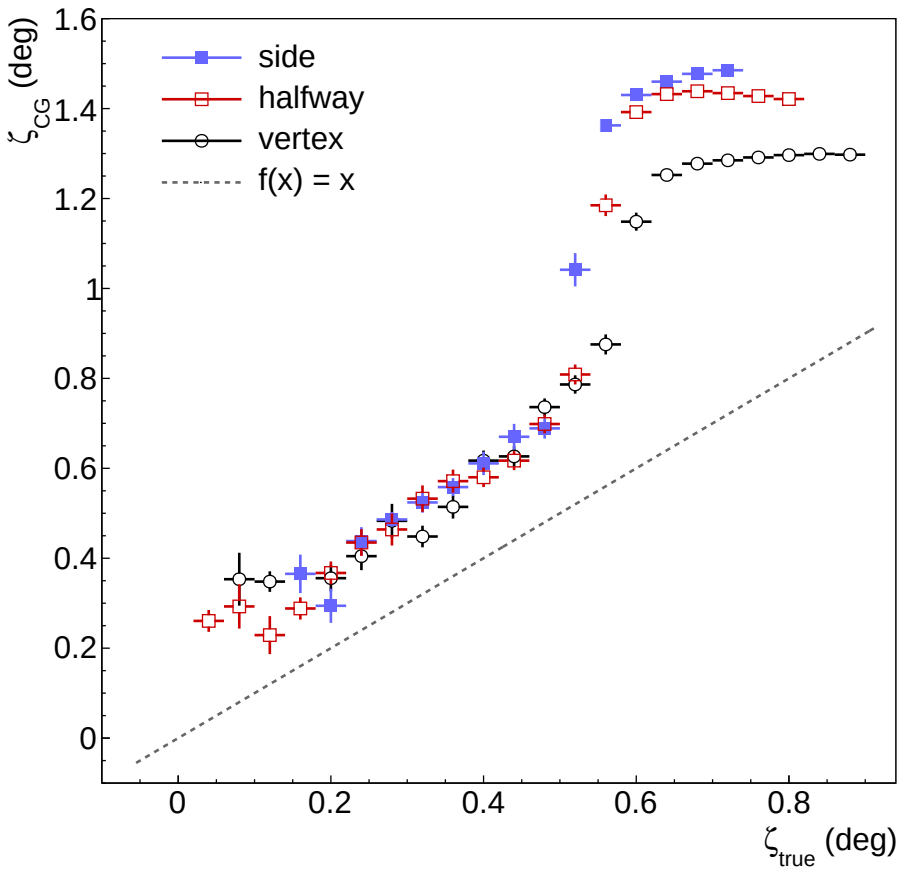

FIG. 6.9 Reconstructed position of the CG (ζ_{CG}), computed from the signal of the pixels in the first crown, as a function of the true position (ζ_{true}) for three different directions of motion from the pixel center: towards the light collector side, vertex and halfway in between. A 45-degree line was drawn to guide the eyes.

selecting only events where the target pixel was the hottest. The reconstructed position is always pulled towards the center of the nearest neighbor, and since the hottest pixel is not included in the computation of the CG, the reconstructed position of events falling just on the side or vertex of the Mercedes star can even coincide with the position of the center of the nearest neighbor. Consider, for example, the "true" right edge of the pixel, which is stretched into a point towards its nearest neighbor at a distance of 1.5° (from center to center). On the other hand, the top vertex of the pixel is flattened as the image squeezes into the corner and the CG is pulled to either side toward two equidistant neighbors.

A potential challenge is the migration of events from one pixel to the neighboring one. In practice this means that even though a particular event originated in the FOV of pixel p, the neighboring pixel q will record the highest signal. While this not an issue in simulation, it will be an issue in measured data and is not

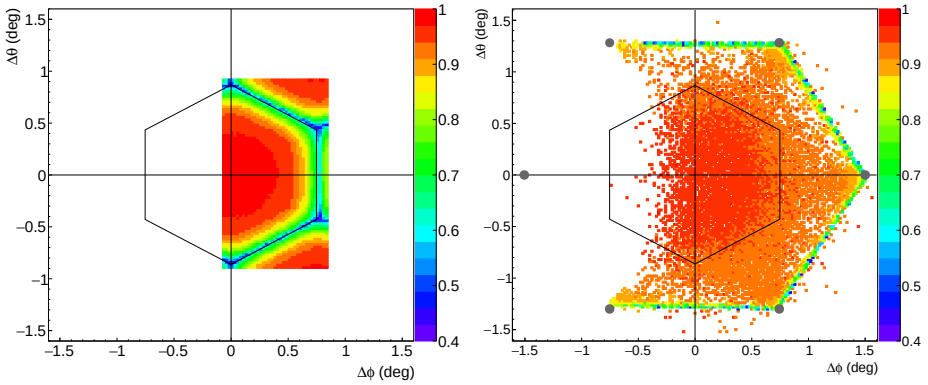

FIG. 6.10 Left: Coordinates of simulated Octocopter pulses $\Delta\theta_{\text{true}}$ and $\Delta\phi_{\text{true}}$ used to generate the map of conversion factors b_θ and b_ϕ. The color scale corresponds to the relative response of the pixel. Right: Reconstructed CG coordinates $\Delta\theta_{\text{CG}}$ and $\Delta\phi_{\text{CG}}$ for the true coordinates $\Delta\theta_{\text{true}}$ and $\Delta\phi_{\text{true}}$. The positions of the centers of the neighboring PMTs are marked by gray solid dots.

easily corrected for. We assume, quite reasonably, that the migration process is symmetric, at least over small regions such as the border of two pixels. This assumption is of course invalid at the borders of the camera, but that is not of concern as those events are de-selected from further analysis.

The final maps of conversion factors generated according to Eq. (6.2) and the corresponding standard deviations are depicted in Fig. 6.11. Focusing on b_θ first (Fig. 6.11c), we see that the standard deviation outside of the central horizontal band of 0.24° is below 0.12°, which is comparable to the bin width of the map (0.12°) as well as the pointing accuracy of the telescopes [174]. The large uncertainty in the central band is caused by the reconstructed coordinate $\Delta\theta_{\text{CG}}$ fluctuating about zero, which in turn causes large fluctuations of the b_θ-factor. For this reason, every event reconstructed in this region is assigned the zenith angle $\Delta\theta = 0°$, i.e. the zenith angle of the pixel center. The factor b_ϕ-factor behaves, and is handled, in the same manner.

The performance of the conversion maps was first tested for consistency on a simulated data set, with results shown in the top panel of Fig. 6.12. Again, only positions covering one half of the pixel were simulated. The reconstructed and b-converted coordinates of 99.6 % of all events for which the target pixel was the hottest fall within ±0.02° of the true position, and over 99.8 % within ±0.12°, i.e. the chosen bin width. This is true for both, the zenith and azimuthal angles. The remaining 2 ‰ fall farther than 0.12° from the true position, but in all cases within 0.75°, i.e. all b-converted coordinates are within the boundaries of the correct PMT. The number of events assigned to other position bins than that corresponding to the true position is negligibly small. Of greater concern is the fact that the simulation does not describe the telescope PSF perfectly and the associated uncertainty will be estimated in Subsec. 6.5.2 in the next chapter.

In Figs. 6.12c to 6.12e, we observe a migration of events to the left part of

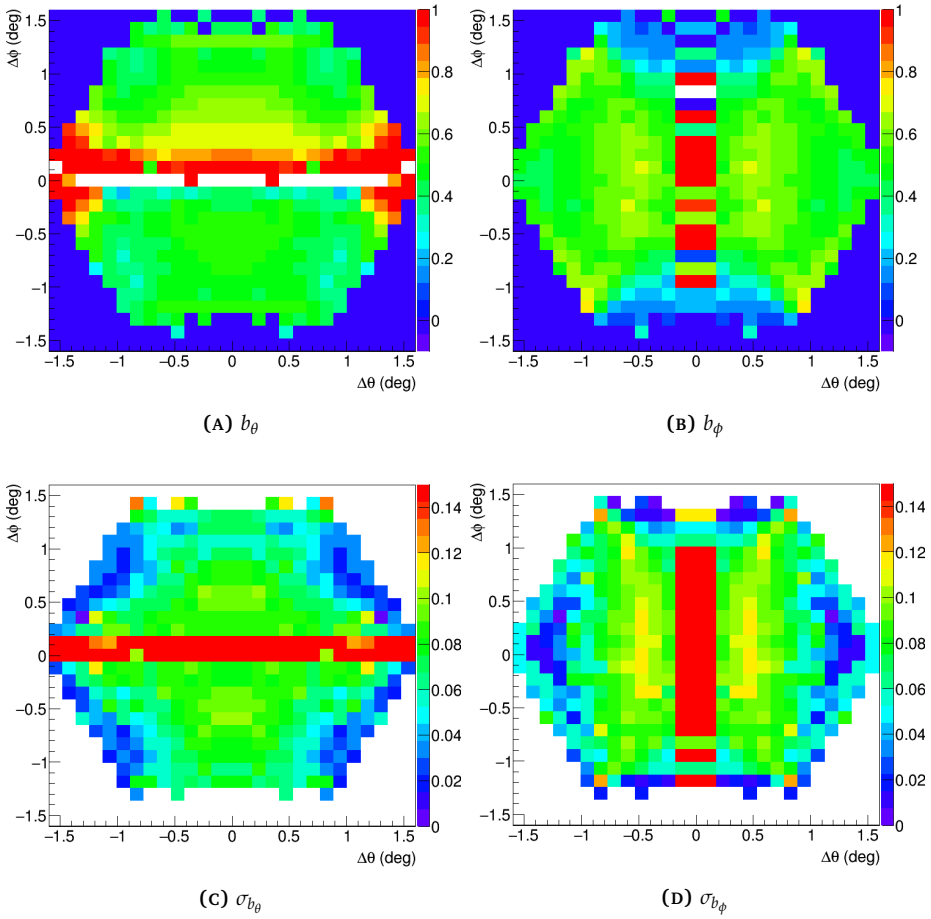

(A) b_θ (B) b_ϕ

(C) σ_{b_θ} (D) σ_{b_ϕ}

FIG. 6.11 Top: b-conversion factors as a function of the CG-reconstructed coordinates $\Delta\theta_{\mathrm{CG}}$ and $\Delta\phi_{\mathrm{CG}}$, shown relative to the coordinates of the pixel center. The color scale indicates the value of the parameter. White regions in the central bands correspond to values of b-factors exceeding the color scale range, which was optimized to see the variation of the factors across the pixel surface. Bottom: Corresponding standard deviations in units of degrees.

the pixel, which in a full-pixel simulation would be compensated by events from the left part of the pixel migrating to its right part. In the next step, the maps were applied to the November 2014 data. The b-converted coordinates shown in Figs. 6.12b to 6.12f are centered on the pixel and correctly trace its outline.

The b-conversion performs well and is able to compensate for systematic offsets in GPS position as well as reproduce the correct pixel outline. Up to this point, the systematic uncertainty of the ray-tracing simulation stemming from a partially idealized representation of the telescope has not been addressed. Instead, in the following analysis both position determination methods are applied, and the resulting differences are taken as an estimate of the systematic uncertainty.

Other conversion factors were tested, e.g. of the form

$$a_\theta = \frac{\Delta\theta_{\text{true}} - \Delta\theta_{\text{CG7}}}{\Delta\theta_{\text{CG6}}} a_\phi = \frac{\Delta\phi_{\text{true}} - \Delta\phi_{\text{CG7}}}{\Delta\phi_{\text{CG6}}}, \tag{6.3}$$

where the subscripts CG7 and CG6 mark the integration region of the first crown, with and without the hottest pixel, respectively. These factors performed nowhere nearly as good as the b-factor. Also, a simple method based on the distance ζ from the pixel center was investigated. While it correctly reproduced the size of the pixel, it failed to reproduce the shape because the radial asymmetry of the pixel shape was neglected.

6.5 Absolute Calibration Results

6.5.1 Reconstructed light fraction

The output of the Octocopter data reconstruction is the number of 375 nm-equivalent photons at the aperture, symbolically expressed as

$$N^{\text{rec}}_{\gamma 375}(\mathcal{R}) = C_{\text{cal}} S_{\text{ADC}}(\mathcal{R}), \tag{6.4}$$

where $S_{\text{ADC}}(\mathcal{R})$ is the number of ADC counts collected within the integration region $\mathcal{R}$ and C_{cal} is the standard FD absolute calibration constant of the read-out pixel (in units of 375 nm-equivalent photons at the aperture per ADC count).

The integration region may be defined in terms of entire physical pixels or the angle ζ, used to denote distances on the spherical focal surface. In case of the former, Eq. (6.4) becomes

$$N^{\text{rec}}_{\gamma 375}(\mathcal{R}) = \sum_{i=i_0}^{i_{\max}} C^i_{\text{cal}} S^i_{\text{ADC}} \,, \tag{6.5}$$

where the sum runs over the pixels within the desired integration region, i_0 is usually the hottest pixel and at the maximum number of considered pixels is $i_{\max} = 440$, i.e. all pixels of one camera, although in some cases the integration region may cross into the neighboring telescope.

In the latter case, i.e. for an integration region defined by the angle ζ,

$$N^{\text{rec}}_{\gamma 375}(\mathcal{R}) = \sum_{\zeta=\zeta_{\min}}^{\zeta_{\max}} \left(\sum_{i=i_0}^{i_{\max}} C^i_{\text{cal}} S^i_{\text{ADC}} \right) \,, \tag{6.6}$$

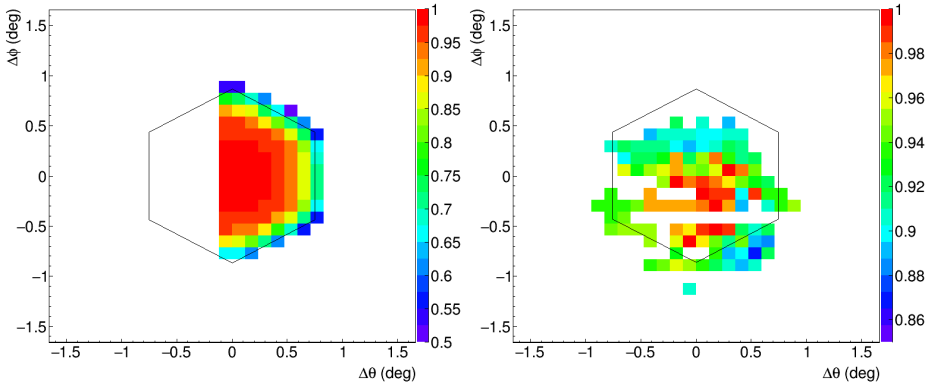

(A) Simulation: true

(B) Octocopter: GPS

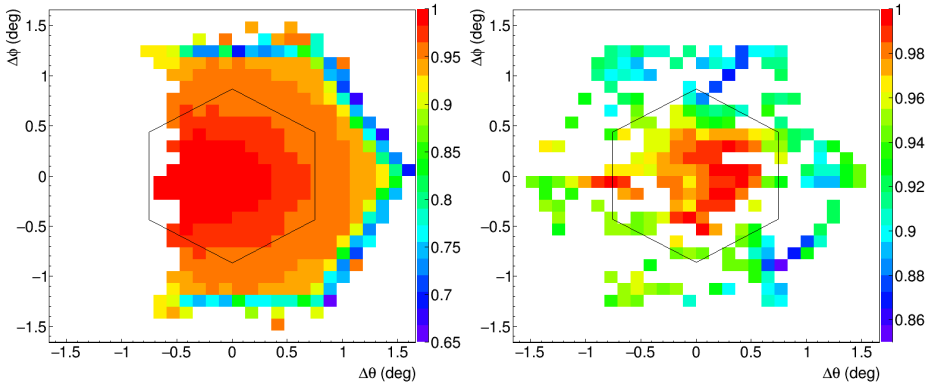

(C) Simulation: CG-reconstructed

(D) Octocopter: CG-reconstructed

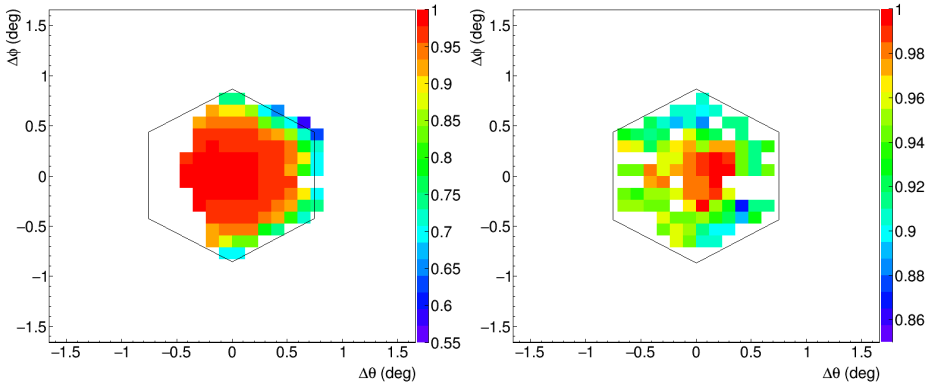

(E) Simulation: *b*-converted

(F) Octocopter: *b*-converted

FIG. 6.12 Left from top to bottom: True, CG-reconstructed and *b*-converted coordinates for a simulated data set. Right from top to bottom: Octocopter GPS, CG-reconstructed and *b*-converted coordinates for the November 2014 data set, pixel 208 in LL3.

where the outer sum runs over the angular distance ζ, usually with a step size of $\Delta\zeta = 0.1°$, $\zeta_{\min} = 0°$ corresponds to the center of the image on the camera and $\zeta_{\max}$ to the angular distance of the most distant pixel, the signal of which is still considered. For pixels 208 and 70, $\zeta_{\max} = 21°$ and 33°, respectively. The inner sum runs over all pixels whose nominal viewing directions[5] fall into the interval $(\zeta + \Delta\zeta)$. This is equivalent to a numerical integration over a spherical surface, except that a pixel's signal always enters as a whole, never as a fractional contribution proportional to the area of the pixel encompassed by $\Delta\zeta$, and it does not run over the full azimuthal phase space of 2π, but only over the part that is physically filled with PMTs.

[5] *Recall the nominal viewing direction of a pixel is defined by the central line of its FOV.*

The value of $N^{\text{rec}}_{\gamma 375}$ is then compared to the number of 375 nm-equivalent photons $N^{\text{ap}}_{\gamma 375}$ arriving at the aperture from the Octocopter obtained as described in Sec. 5.5. The reconstructed light fraction defined as

$$\mathcal{F}(\mathcal{R}) = \frac{N^{\text{rec}}_{\gamma 375}(\mathcal{R})}{N^{\text{ap}}_{\gamma 375}} \tag{6.7}$$

thus quantifies the fraction of photons arriving at the aperture that is reconstructed with the standard FD calibration constant within the integration region $\mathcal{R}$.[6]

[6] *Technically, the calibration constant gives the number of 375 nm-equivalent photons arriving at the aperture as if the source were positioned along the optical axis of the telescope, i.e. the cosine of the angle with respect to the optical axis is automatically taken care of. Therefore, when computing the expected number of photons N^{ap}_{γ} at the aperture using Eq. (5.12), the term $\cos\theta$ is dropped. This is simply a technicality of the implementation.*

Since the value of $\mathcal{F}(\mathcal{R})$ depends on the position (Ω, ϕ) of the event on the pixel surface and we wish to be able to compare the calibration obtained with the Octocopter to that obtained with the drum, the light fractions are additionally averaged over the entire pixel surface, with each position (not event) contributing equally:

$$\mathcal{F}^{\text{pix}}(\mathcal{R}) = \sum_{\Omega} \left(\sum_{\phi} \mathcal{F}(\mathcal{R}, \Omega \pm \Delta\Omega, \phi \pm \Delta\phi) \right) , \tag{6.8}$$

where $\Delta\Omega = \Delta\phi = 0.06°$ give the size of the surface element defined by the coarseness of binning of the b-conversion factors and the sums runs over positions on the pixel surface in 0.12° steps. In the following, we shall refer to $\mathcal{F}^{\text{pix}}(\mathcal{R})$ as the pixel-averaged reconstructed light fraction or simply light fraction. For better readability of the text, we shall also drop the specification of the functional dependence on the integration region $\mathcal{R}$. It is clear that quoting a light fraction without the integration region over which it was obtained is meaningless and the integration region will always be explicitly stated.

The light fraction effectively expresses the Octocopter calibration constant $C^{\text{Octo}}_{\text{cal}}$ in terms of the standard drum-based calibration constant $C^{\text{drum}}_{\text{cal}}$. The Octocopter calibration constant may be easily obtained in absolute units as

$$C^{\text{Octo}}_{\text{cal}} = \frac{C^{\text{drum}}_{\text{cal}}}{\mathcal{F}^{\text{pix}}}, \tag{6.9}$$

where both, the Octocopter and drum calibration constant are given in 375 nm-equivalent photons at the aperture per ADC count.

TAB. 6.5 Relative differences between pixel-averaged light fractions for different integration regions reconstructed using the constant-offset and b-conversion methods.

Integration region	Difference in $\mathcal{F}^{\mathrm{pix}}$ (%)
Hottest pixel	2.1
Hottest pixel–ζ =1.3°	0.4
ζ >1.3°	0.2

6.5.2 November 2014 campaign

Two pixels in LL3 were scanned during the November 2014 absolute calibration campaign: pixel 208 (row 10, column 10) close to the center and pixel 70 (row 4, column 4) close to the corner of the camera. Pixel-averaged reconstructed light fractions $\mathcal{F}^{\mathrm{pix}}$ were computed using both, the constant-offset and b-conversion position determination methods described in Subsecs. 6.4.1 and 6.4.2. The found differences are listed in Tab. 6.5 for different values of ζ.

For $\zeta > 1.3°$, the difference is less than 0.2 %. The discrepancy, though small, grows with decreasing ζ from 0.2 % to a maximum of 2.1 %. This trend results from the way the two methods handle events falling on the boundary between two or three pixels. Nevertheless, given the very good agreement of the two approaches to determining position, only results obtained with the b-conversion method are quoted in the following, with one half of the maximum difference listed in Tab. 6.5 included in the combined systematic uncertainty.

The individual contributions to the total systematic uncertainty of the light fractions $\mathcal{F}^{\mathrm{pix}}$ are summarized in Tab. 6.6. The uncertainty of the standard FD calibration constant[7] enters into the computation of the light fractions during the conversion of the electronic signal to photons at the aperture. As the Octocopter method and the drum calibration use completely different light sources and procedures, their systematic uncertainties are practically uncorrelated and can be added in quadrature. A partial correlation could occur for the uncertainty of the pulse area, in both cases estimated as 2 % and in part related to PMT after-pulsing. This potential small correlation is, however, negligible in the scope of this analysis.

[7] *Unless stated otherwise, the standard drum-based FD calibration constants are meant.*

At 9.9 % [54], the systematic uncertainty of the drum calibration is double that of the Octocopter method. Therefore, in the following the Octocopter-related uncertainty is always quoted first separately, followed by the combined uncertainty of the Octocopter and the FD calibration constant in parentheses. This convention will be maintained throughout the rest of the text. The statistical uncertainty of the light fractions is vanishingly small, so only systematic uncertainties are quoted.

Fig. 6.13 (top) shows the pixel-averaged reconstructed light fractions $\mathcal{F}^{\mathrm{pix}}$ as a function of the size of the integration region, given in terms of the angle ζ relative to the hottest pixel center, for pixels 70 and 208 in LL3. Tab. 6.7 then lists the values for selected benchmark integration regions. All data shown in this section are from the November 2014 campaign.

Whether the observed difference between the two pixels of 3.3 % is significant or not depends on the extent to which the individual uncertainties are correlated

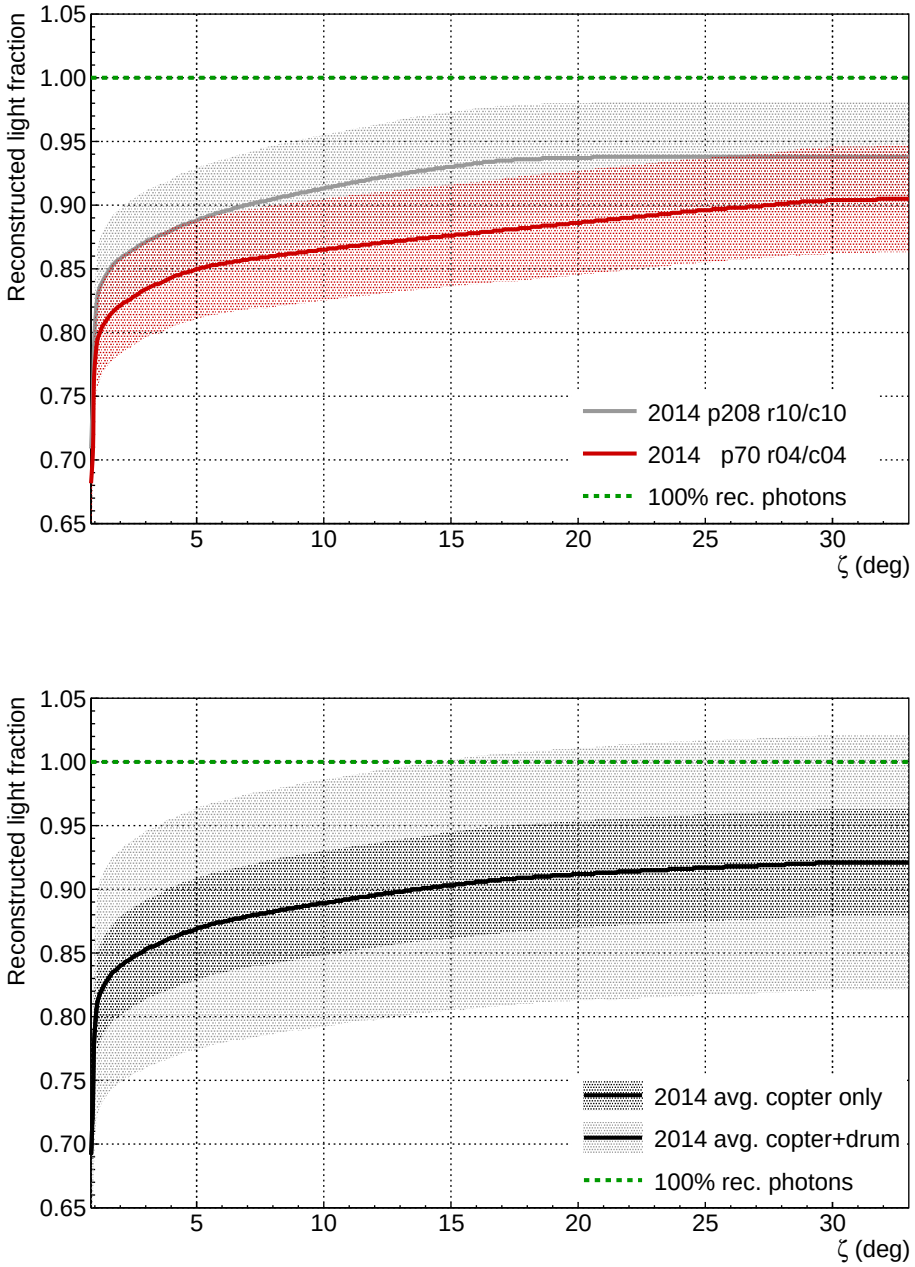

FIG. 6.13 Top: Pixel-averaged reconstructed light fractions $\mathcal{F}^{\text{pix}}$ for pixels 70 and 208 in LL3 as a function of angular distance ζ from the hottest pixel center. The error bands reflect the Octocopter-related systematic uncertainty only and the green line at $\mathcal{F}^{\text{pix}} = 1.0$ corresponds to 100 % reconstructed photons at the aperture. Bottom: Average light fraction for pixels 70 and 208 in LL3. The broader error band (light gray) includes the systematic uncertainty of the FD absolute calibration constant on top of the Octocopter-based uncertainty indicated by the narrower band (dark gray).

TAB. 6.6 Sources of systematic uncertainty of the pixel-averaged reconstructed light fractions $\mathcal{F}^{\mathrm{pix}}$. The uncertainty on the number of photons at the aperture is quoted for the case of using Octocopter sphere temperatures and in parentheses for the case of using weather station temperatures.

Source of uncertainty	Uncertainty (%)
No. of 375 nm-eq. photons at aperture	3.5 (4.0)
Pulse integration	2.0
Position on pixel surface	0.1–1.0
Standard FD calibration constant	9.9
TOTAL *without* FD abs. cal.	4.2 (4.6)
TOTAL *with* FD abs. cal.	10.8 (10.9)

TAB. 6.7 Pixel-averaged reconstructed light fractions $\mathcal{F}^{\mathrm{pix}}$ for pixels 70 and 208 in LL3, and their average, for benchmark integration regions using November 2014 data. The quoted systematic uncertainty is that of the Octocopter method, and the combined systematic uncertainty of the Octocopter and the standard FD calibration constants is given in parentheses.

Integration region	Pixel	
	p208 r10/c10	p70 r04/c04
Hottest pixel	$0.700 \pm 0.032(0.076)$	$0.673 \pm 0.031(0.073)$
$\zeta = 1.14°$	$0.790 \pm 0.036(0.086)$	$0.758 \pm 0.035(0.083)$
$\zeta_{\mathrm{LWC}} = 4.0°$	$0.880 \pm 0.040(0.096)$	$0.843 \pm 0.039(0.092)$
Entire camera	$0.938 \pm 0.043(0.102)$	$0.905 \pm 0.042(0.099)$
	Average	
Hottest pixel	$0.686 \pm 0.032(0.075)$	
$\zeta = 1.14°$	$0.774 \pm 0.036(0.084)$	
$\zeta_{\mathrm{LWC}} = 4.0°$	$0.862 \pm 0.040(0.094)$	
Entire camera	$0.921 \pm 0.042(0.100)$	

(refer to Tab. 5.6 on page 130 for an overview). Even though the covariance matrices are not known, we can begin to understand the degree of correlation at least for some of the sources of uncertainty.

Most of the uncertainties pertaining to the laboratory measurements are fully correlated within one campaign, in particular the uncertainty of: the pulse charge measurement with the Keithley electrometer (2.5 %), the spatial non-uniformity of the sensitive area of the photodiode (0.5 %), the correction for the pulsing rate C_{rate} (0.1 %), the contribution from stray light and multiple reflections (0.1 %) and the effective source–photodiode responsivity R_{eff} (0.5 %). Since the calibration setup remains in place long-term and the light source only has to be affixed to the mount on the optical bench, the source–photodiode distance, and therefore the solid angle Ω_{PD} subtended by the photodiode, remains the same and the associated uncertainty (0.2 %) is fully correlated, too.

Concerning the operation of the Octocopter in the field, the part of the temper-

ature correction uncertainty stemming from the uncertainty of the fit parameters is fully correlated, assuming a constant ambient temperature of 5 °C typical for November Octocopter measurement nights (1.2 %). Also fully correlated is the end-to-end spectral efficiency of the fluorescence detector (0.3 %).

Since the two pixels were flown on different nights, the following sources of uncertainty are believed to be fully or largely uncorrelated: Mie attenuation (1.3 %), short-term stability (0.7 %), the Octocopter–telescope distance (0.6 %), isotropy (0.4 %) and the part of the uncertainty of the temperature correction stemming from the uncertainty of the temperature measurement in the field (again assuming an ambient temperature of 5 °C, 2.0 % for weather station temperatures used in the analysis of the November 2014 campaign data). The uncertainty of the inter-campaign stability of the light source is probably partially correlated between individual nights of one measurement campaign, as the light output is known to drop over the course of one campaign, although it is unclear when and how quickly the drop occurs.

In the Octocopter FD data analysis, the uncertainty of the pulse area is certainly at least partially correlated due to after-pulsing, which is different for the individual PMTs, but in all cases greater than or equal to zero.[8] The uncertainty related to the computation of the position on the camera is also partially correlated. Correlation follows from the design of the method itself, but a random element arises from the actual positions of the Octocopter on a given night.

[8] *Recall that the mean after-pulse ratio in LL3 is (1.2 ± 0.4) %.*

The light fractions are computed using the standard FD absolute calibration constant. It can be safely assumed that the contribution from the uncertainty of the drum calibration is nearly fully correlated, but the uncertainty of the relative CalA constant (2 %) is mostly uncorrelated, as it is dominated by the variations in the electronic gain of the individual PMTs.

To summarize, the following sources of uncertainty were considered as fully uncorrelated for the comparison of the light fractions obtained within the 2014 Octocopter measurement campaign: Mie attenuation (1.3 %), short-term stability of the light source (0.7 %), the part of the temperature correction stemming from the uncertainty of the measurement of the ambient temperature (1.2 % using weather station temperatures and assuming an ambient temperature of 5 °C) and flight distance from the telescope (0.6 %). The inter-campaign stability of the light source was estimated to be 50 % correlated. All in all, only differences in light fractions larger than 3.9 % can be considered as significant.

First, let us consider the limiting case of integrating over the entire camera – the total pixel-averaged light fraction. Summing the photons reconstructed for each of the 440 pixels produces a light fraction of 0.938 ± 0.043 (0.102) and 0.905 ± 0.042 (0.099) for pixel 208 and 70, respectively. Based on the above argumentation concerning the level of correlation of individual sources of uncertainty over the course of one campaign, the difference of 3.3 % is insignificant. In the following discussion, we shall for simplicity use the average light fraction of the two studied pixels, which is shown in Fig. 6.13 (bottom) together with two systematic error bands: with and without the contribution from the FD absolute calibration constant.

The average total light fraction for the two pixels is thus 0.921 ± 0.042 (0.100). If all photons arriving at the aperture were reconstructed, $\mathcal{F}^{\mathrm{pix}}$ would be unity, however, the obtained result is incompatible with 1.0 when the Octocopter-related uncertainty is considered and barely compatible when the combined uncertainty (quoted in parentheses) is considered. Provided the atmospheric attenuation along the path from the Octocopter to the telescope is well described, 8.9 % of photons hitting the aperture are not reconstructed when the standard FD calibration constants are used, either because they do not reach the camera during the measurement, or alternatively, they reach the camera but the calibration constant is off. In practice this number will be even higher, since standard air shower reconstruction algorithms never integrate over the entire camera.

Additional atmospheric attenuation beyond what is described by the currently used mean value is another possible explanation of the observed discrepancy. Increased attenuation would lead to a reduction of the number of photons reaching the aperture N_γ^{ap}, thus boosting the reconstructed light fractions. To confirm or rule out this possibility, a check of the Mie attenuation values once the aerosol database becomes available is necessary.

The other limiting case, i.e. using the hottest pixel only, yields a pixel-averaged light fraction of 0.686 ± 0.032 (0.075). Comparing this to 0.921 obtained for the entire camera, one sees that 23.5 % of photons are detected by pixels other than the target pixel. This is in good agreement with the magnitude of reflections on the PMTs ($\sim$20 %, c.f. Sec. 3.2) and non-specular reflection on the mirror ($\sim$4 %, c.f. Sec. 4.1), both of which are mechanisms that deflect photons from the target pixel. Turning the argument around, we expect that roughly 23 % of the photons that are detected by the target pixel during drum calibration arrive from directions other than the viewing direction of the target pixel.

Air shower images are integrated over regions of variable size. As explained in Sec. 3.3, an optimal integration region is chosen such that its radius ζ_{opt} maximizes the SNR. Next, a phenomenological data-based correction referred to as the LWC is applied. This correction accounts for the photons arriving within the angular interval ζ_{opt} and $\zeta_{\mathrm{LWC}} = 4.0^\circ$ and effectively accounts for the light distribution up this range. However, photons arriving at larger angles from the SDP are not reconstructed. The corresponding light fraction average at ζ_{LWC} is 0.862 ± 0.040 (0.094), indicating that – again, provided that atmospheric attenuation is properly described – the number of photons arriving at the aperture, and consequently the calorimetric energy of an air shower, may be significantly underestimated, in this case by (13.8 ± 0.6) %. This number is commensurate with the total systematic uncertainty of the FD energy scale of 14 % [76].

The integration region $\zeta = 1.14^\circ$ is related to the mean ζ_{opt} for very distant showers that produce a rather narrow image on the camera resembling that of the Octocopter. In Subsec. 6.6.3, this benchmark integration region will be used to investigate the composition of the LWC; for now, it is simply quoted for reference.

6.5.3 Comparison with simulation

In order to check for a reconstruction bias and to verify the correctness of the analysis, the complete reconstruction and analysis chains were run on a simulated data set. The Offline telescope ray-tracing modules are self-consistent in the sense that both, the drum calibration and Octocopter light pulses are simulated using the same hypothetical telescope in the very same configuration, and the absolute normalization in terms of the true (simulated) number of photons at the aperture is known exactly. The expected reconstructed light fraction integrated over the entire camera is thus 1.0 in simulations.

The complete 2014 campaign was simulated for a total of three configurations, using two different simulation modules:

1. TelescopeSimulatorKG_DEV with a clean filter and a clean mirror, i.e. only specular transmission and reflection occur.

2. TelescopeSimulatorKG_DEV with a clean filter and a dusty mirror, which results in non-specular reflection. A height-dependent dust layer described by the CDF given in Sec. 4.1 including a 6 % absorption gradient was used.

3. TelescopeSimulatorKG, a basic ray-tracing code that does not permit multiple reflections between individual optical components and assumes ideal shapes and surfaces of all interfaces.

Unlike the development version TelescopeSimulatorKG_DEV, the standard simulation module TelescopeSimulatorKG neither permits multiple reflections nor non-specular interactions, and thus the resulting PSF is very narrow. Nevertheless, this module is standardly used for official Auger simulations and is used here as a reference and a cross-check.

Fig. 6.14 shows the simulated light fractions obtained for the three different configurations. The total, integrated over the entire camera, lies between 99 % and 99.6 % in all three cases, meaning that with a correct normalization of the drum and Octocopter light sources nearly all photons arriving at the aperture are reconstructed and the reconstruction bias is negligible. This result is of prime importance, for it means that in a self-consistent world, the drum and Octocopter methods are comparable, provided that the spatial inhomogeneity of the pixel is correctly taken into account. This can be achieved either by scanning the surface of the PMT with light pulses as was done here, or the mean sensitivity of the pixel can be related to the sensitivity at some well defined point, e.g. the pixel center. For the latter approach, a differential GPS device is a prerequisite. Furthermore, with the Octocopter method it is not only possible to derive an absolute calibration constant for an entire pixel, but also for sub-regions of one pixel.

The results for different benchmark integration regions are summarized in Tab. 6.8. The total light fraction for configuration 2, i.e. a dusty mirror, is slightly higher (by 0.5 %) than for the other two configurations. While this difference is unimportant, it is a direct result of the variable dust layer on the mirror. The

Tab. 6.8 Pixel-averaged light fractions for benchmark integration regions simulated with three different configurations (refer to page 157 for a description of the configurations).

Integration region	Configuration		
	1	2	3
Hottest pixel	0.808	0.841	0.889
$\zeta = 1.14°$	0.951	0.928	0.990
$\zeta_{\mathrm{LWC}} = 4.0°$	0.959	0.960	0.991
Entire camera	0.990	0.995	0.991

shown light curve is an average for a mid- and low-elevation pixel, which view the cleaner parts of the mirror. If a high-elevation pixel viewing the more dusty parts of the mirror is added to the average, the difference is compensated.

The shape of the light curves reflects the distribution of the signal on the camera. Since the module TelescopeSimulatorKG does not allow any multiple reflections whatsoever, only photons traveling directly from the aperture to the camera are detected and practically all photons strike the target pixel (save for a minimal spread due to spherical aberration). TelescopeSimulatorKG_DEV, on the other hand, allows any combination of reflections between the camera, mirror and aperture, and is limited only by the number of hits of the mirror (10 in this case). PMT-reflected photons define the shape of the light fraction curves in Fig. 6.14 at large angles beyond 4°, non-specular reflection on the mirror dust layer, if activated, at small angles.

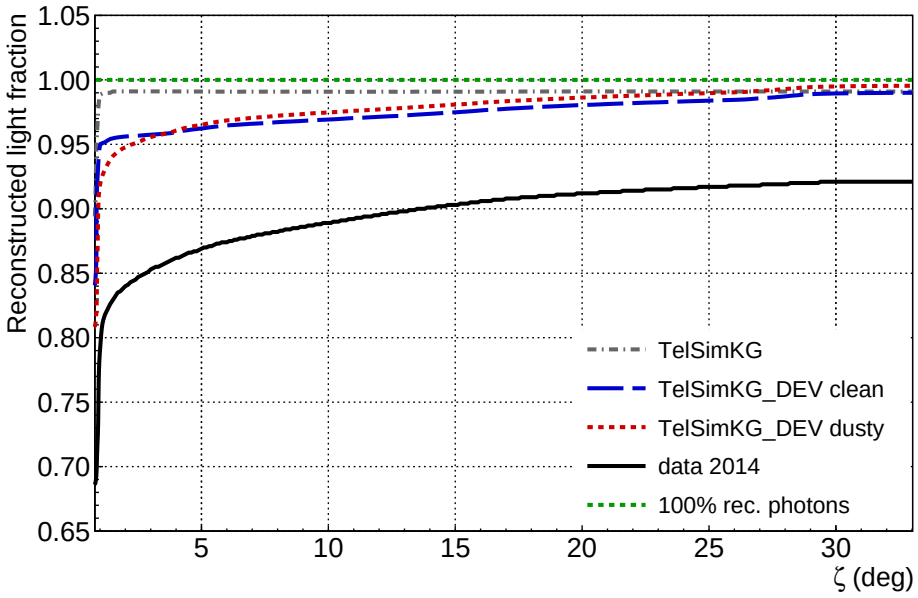

Fig. 6.14 Simulated and measured light fractions as a function of angular distance ζ from the hottest pixel center. The curves for pixels 70 (corner) and 208 (center of the camera) were averaged for simplicity.

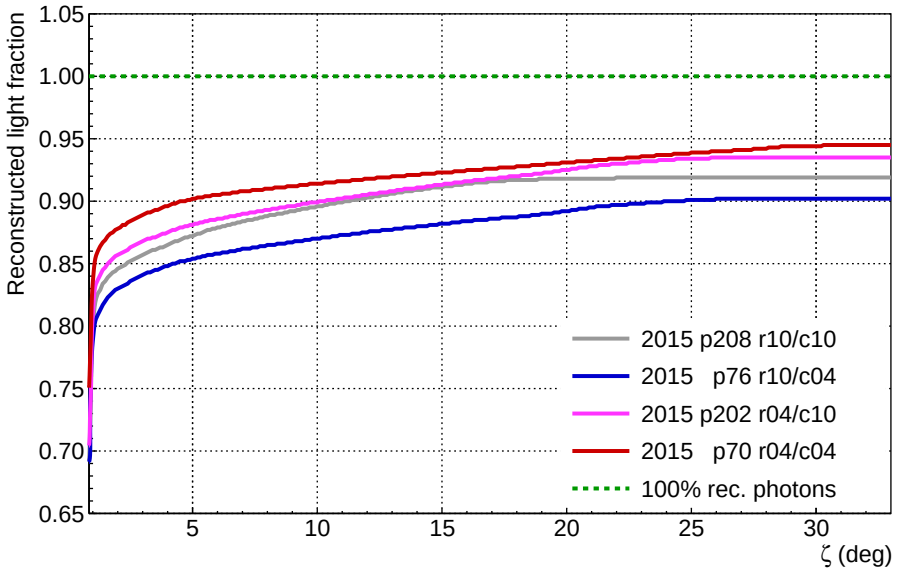

FIG. 6.15 Pixel-averaged reconstructed light fractions $\mathcal{F}^{\text{pix}}$ for pixels 70, 76, 202 and 208 in LL3 for the November 2015 campaign as a function of angular distance ζ from the center of the hottest pixel. The green dotted line at $\mathcal{F}^{\text{pix}} = 1.0$ corresponds to 100 % reconstructed photons.

6.5.4 November 2015 campaign

The November 2015 campaign was similar to its predecessor in design, but more extensive. Four pixels were scanned completely (c.f. Fig. 6.5c). Additionally, an elevation scan was performed, which is described in the following section.

The pixel-averaged light fractions for pixels 70, 76, 202 and 208 in LL3 are displayed in Fig. 6.15 as a function of the angular distance ζ from the center of the hottest pixel. Note that while the x–axis runs to $\zeta = 33°$, there are PMTs at such a large distance only relative to pixel 70, which is located close to the corner of the camera. For pixel 208 in the center of the camera, the farthest pixels are about 21° away, and for pixels 76 and 202 close to the side and bottom edge of the camera, respectively, about 28°. Correspondingly, the light fractions plateau at different angular distances ζ. Light fraction values for benchmark integration regions are listed in Tab. 6.9.

The total light fractions range from 0.902 ± 0.038 (0.097) for pixel 76 to 0.949 ± 0.040 (0.103) for pixel 70, corresponding to a relative difference of 4.7 %.[9] The observed difference between the individual pixels is insignificant with regards to the combined uncertainty of the difference of two light fractions discussed on page 155, even if the slightly lower uncertainty of the sphere temperature measurement in this campaign is taken into account (0.8 % for an ambient temperature of 5 °C). Furthermore, the magnitude of the difference is commensurate with findings in [114], where the stability of the relative calibration was studied by comparing the NSB seen by pixels in the peripheral columns of neighboring telescopes, which partially share the same FOV. The differences in

[9] *Recall the convention of quoting the Octocopter-related systematic uncertainty separately first, and the combined uncertainty of the Octocopter and FD calibration constant in parentheses.*

TAB. 6.9 Pixel-averaged reconstructed light fractions $\mathcal{F}^{\mathrm{pix}}$ for pixels 70, 76, 202 and 208 in LL3, as well as their average, for benchmark integration regions using November 2015 data. The quoted uncertainty is the Octocopter-related systematic, and the total uncertainty including that of the FD calibration constant is printed in parentheses.

Integration region	Pixel	
	p208 r10/c10	p70 r04/c04
Hottest pixel	$0.684 \pm 0.029(0.074)$	$0.741 \pm 0.031(0.080)$
$\zeta = 1.14°$	$0.775 \pm 0.033(0.084)$	$0.819 \pm 0.034(0.088)$
$\zeta_{\mathrm{LWC}} = 4.0°$	$0.865 \pm 0.036(0.093)$	$0.896 \pm 0.038(0.097)$
Entire camera	$0.919 \pm 0.039(0.099)$	$0.949 \pm 0.040(0.103)$
	p76 r10/c04	p202 r04/c10
Hottest pixel	$0.691 \pm 0.029(0.075)$	$0.702 \pm 0.029(0.076)$
$\zeta = 1.14°$	$0.769 \pm 0.032(0.083)$	$0.789 \pm 0.033(0.085)$
$\zeta_{\mathrm{LWC}} = 4.0°$	$0.848 \pm 0.036(0.092)$	$0.875 \pm 0.037(0.095)$
Entire camera	$0.902 \pm 0.038(0.097)$	$0.935 \pm 0.039(0.101)$
	Average	
Hottest pixel	$0.705 \pm 0.030(0.076)$	
$\zeta = 1.14°$	$0.788 \pm 0.033(0.085)$	
$\zeta_{\mathrm{LWC}} = 4.0°$	$0.871 \pm 0.037(0.094)$	
Entire camera	$0.926 \pm 0.039(0.100)$	

the relative response of individual pixels were determined to be 6.7 % on average.

The total light fraction averaged for all four pixels is 0.926 ± 0.039 (0.100), which is 0.5 % higher than 0.921 ± 0.042 (0.100) obtained as the average for pixels 76 and 208 in 2014. Nevertheless, the difference between the two years is again insignificant. The same applies to the reconstructed light fractions at $\zeta_{\mathrm{LWC}} = 4.0°$: 0.862 ± 0.040 (0.094) and 0.871 ± 0.037 (0.094) for the November 2014 and 2015 campaigns, respectively. All in all, the results of the 2015 campaign confirm those from 2014.

The light fractions for pixels 70 and 208 measured in November 2014 and a year later are compared in Fig. 6.16. For pixel 208, the total light fraction was higher in 2014 by 1.9 %. Pixel 70 exhibits the opposite behavior, i.e. the total light fraction was higher in 2015 by 4.4 %. This indicates that the response is dominated either by relatively short-term variations, such as changes in the aerosol concentration over the course of a measurement campaign, or by variations on the level of individual pixels, such as changes in electronic gains of the PMTs. It is not dominated, at least in this case, by comparatively long-term effects, such as the state of the MUG-6 filter. Indeed, if the filter were cleaner, say, during the November 2015 campaign, we would expect to see a higher light fraction in 2015 for both pixels. Incidentally, the filter was cleaned eight and five months before the November 2014 and 2015 measurements, respectively (March 2014 and July 2015).

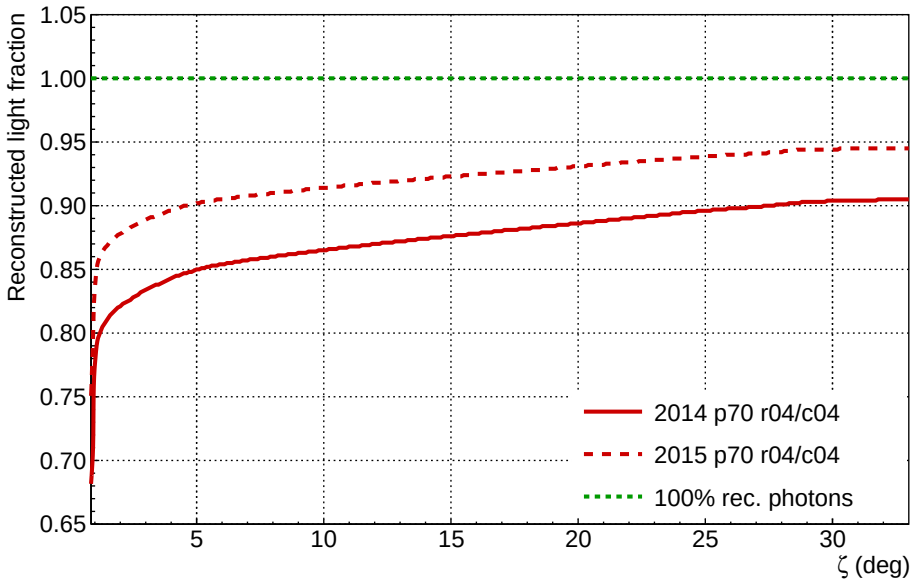

(A) Pixel 70

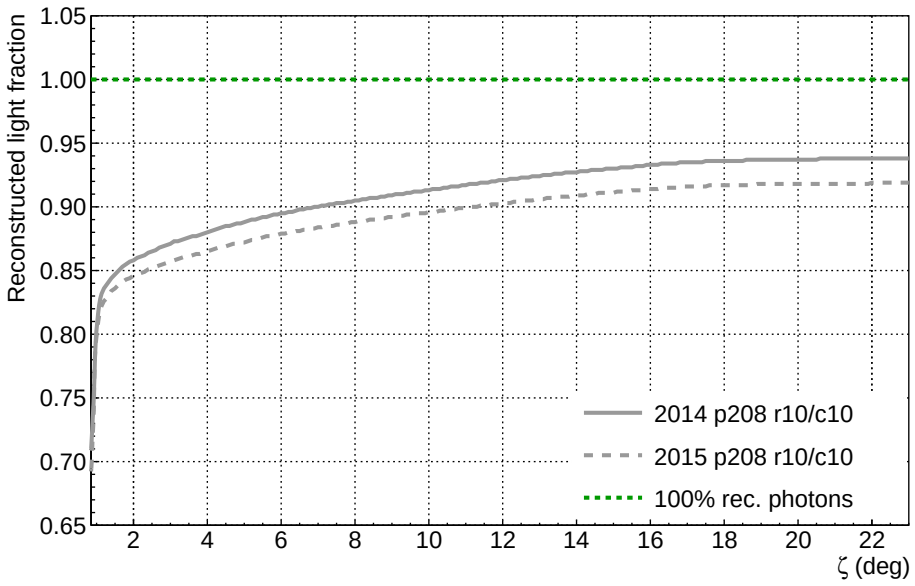

(B) Pixel 208

FIG. 6.16 Pixel-averaged reconstructed light fractions $\mathcal{F}^{\text{pix}}$ for pixels 70 (top) and 208 (bottom) in LL3 found in the November 2014 and 2015 campaigns. The green dotted line at $\mathcal{F}^{\text{pix}} = 1.0$ corresponds to 100 % reconstructed photons.

TAB. 6.10 The pixel-averaged reconstructed light fraction $\mathcal{F}^{\mathrm{pix}}$ averaged over all pixels that were calibrated in the 2014 and 2015 Octocopter campaigns. The quoted uncertainty is the Octocopter-related systematic, and the total uncertainty including that of the FD calibration constant is printed in parentheses.

Integration region	Mean $\mathcal{F}^{\mathrm{pix}}$
Hottest pixel	$0.699 \pm 0.030 (0.075)$
$\zeta = 1.14°$	$0.783 \pm 0.034 (0.085)$
$\zeta_{\mathrm{LWC}} = 4.0°$	$0.868 \pm 0.038 (0.094)$
Entire camera	$0.925 \pm 0.040 (0.100)$

To conclude this section, the light fractions averaged over all pixels calibrated in the 2014 and 2015 Octocopter campaigns are listed in Tab. 6.10. The all-time light fraction for the entire camera is 0.925 ± 0.040 (0.100) and 0.868 ± 0.038 (0.094) for the integration region $\zeta_{\mathrm{LWC}} = 4.0°$, confirming the conclusion drawn based on the results of the 2014 campaign: The number of photons arriving at the aperture, and consequently the calorimetric energy of an air shower, may be significantly underestimated, on average by (13.2 ± 0.6) %.

6.5.5 Elevation scan

In an attempt to identify a potential elevation dependence of the FD signal, an elevation scan was performed during the November 2015 campaign. On the night of 13–14 November, the Octocopter was programmed to target pixels in the following rows of column 4 of the LL3 camera: 4, 8, 12 and 14.[10] The Octocopter first flew into the FOV of the low-elevation pixel in row 4 and after delivering 200 pulses ascended to row 8, again delivering 200 pulses, and so forth up to row 14. All rows were covered within one flight and the entire procedure was repeated in a successive flight (see Fig. 6.5c for the flight paths). The advantage of this approach is that since all events were acquired over a period of about 40 minutes, conditions such as light source intensity, ambient outside temperature or aerosol concentration can be assumed to be stable, or certainly more so than over periods of days or longer.

[10] *The optical axis of the telescope passes between rows 11 and 12.*

Using the data obtained in the elevation scan, the following questions can be addressed:

1. Does the height-dependent dust layer on the mirror introduce an elevation dependence into the signal?
2. Could the albedo of the Pampa Amarilla contribute observably to the signal at low elevations?
3. Is the assumption of a constant mixing layer a realistic description of the bottom-most 400 m of the atmosphere?

A signal dominated by the effect of a height-dependent dust layer on the mirror (described in Sec. 4.1) would gradually decrease with elevation and row number,

since the upper clean parts of the mirror correspond to lower elevations and vice versa. A sizable albedo of the Pampa Amarilla would affect the signal in a similar manner. Concerning question 3., the term "constant mixing layer" describes an aerosol model in which the aerosol concentration is assumed to be constant in the bottom-most $\sim$1000 m of the atmosphere, unlike for higher altitudes, where it decreases gradually. A monotonic change in the aerosol concentration in the bottom-most 400 m covered by the Octocopter in the column scan would manifest as a monotonic elevation dependence of the reconstructed signal. Of course, if the spatial non-uniformity of aerosol concentration dominates, no elevation dependence will be observed.

To isolate any potential elevation-dependent effects, ambient conditions must remain as stable as possible during the measurement. The duration of the elevation scan was thus kept to a minimum by targeting only the center of each pixel and not performing a full pixel scan. The dependence of the reconstructed light fraction on the actual position of the Octocopter within the FOV of the pixel, in this case elevation, is shown in Fig. 6.17 (top). Because the light source keeps flashing once per second even as the platform is changing positions, data are in principle available for different elevations, but reasonably large samples of approximately 175 events are only available for the targeted pixel centers. The characteristic arcs seen in Fig. 6.17 (top), e.g. between 10° and 15°, reflect the changing sensitivity across the pixel surface, with the maxima corresponding to the central pixel area and the minima to the light collectors.

To be able to directly compare the light fractions of pixels viewing different elevations, only events close to the center of the target pixel were selected by imposing the following cut on position: $\Delta\Omega < 0.12°$ and $\Delta\phi < 0.12°$, where $\Delta\Omega$ and $\Delta\phi$ are the elevation and azimuthal angles with respect to the center of the target pixel. The particular choice of 0.12° was motivated by the spatial sensitivity of a pixel shown in Fig. 6.2, which varies by $\sim$1 % within this region. Furthermore, by requesting that the velocity of the platform be less than 1 m/s, only events during which the Octocopter was hovering on-target were selected.

Looking at Fig. 6.17 (bottom), in which the light fractions are plotted as a function of pixel row number, there appears to be neither a monotonic change of response with elevation, nor a symmetry with respect to the optical axis. The standard deviation of the response of a pixel in a particular row is 2.8 % and must be dominated by effects other than those just discussed, possibly by variations in the electronic gains of the PMTs as observed by continuous CalA and discussed in Subsec. 3.1.2, or spatial non-uniformities of the aerosol concentration. There is a jump of nearly 8 % as the Octocopter moves from row 8 to row 12, which is not understood and further studies would be required to confirm and explain this observation. It is, for example, possible that a small cloud or patch of fog, which was not visible by eye, blocked the path between the Octocopter and pixel 78 in LL3.

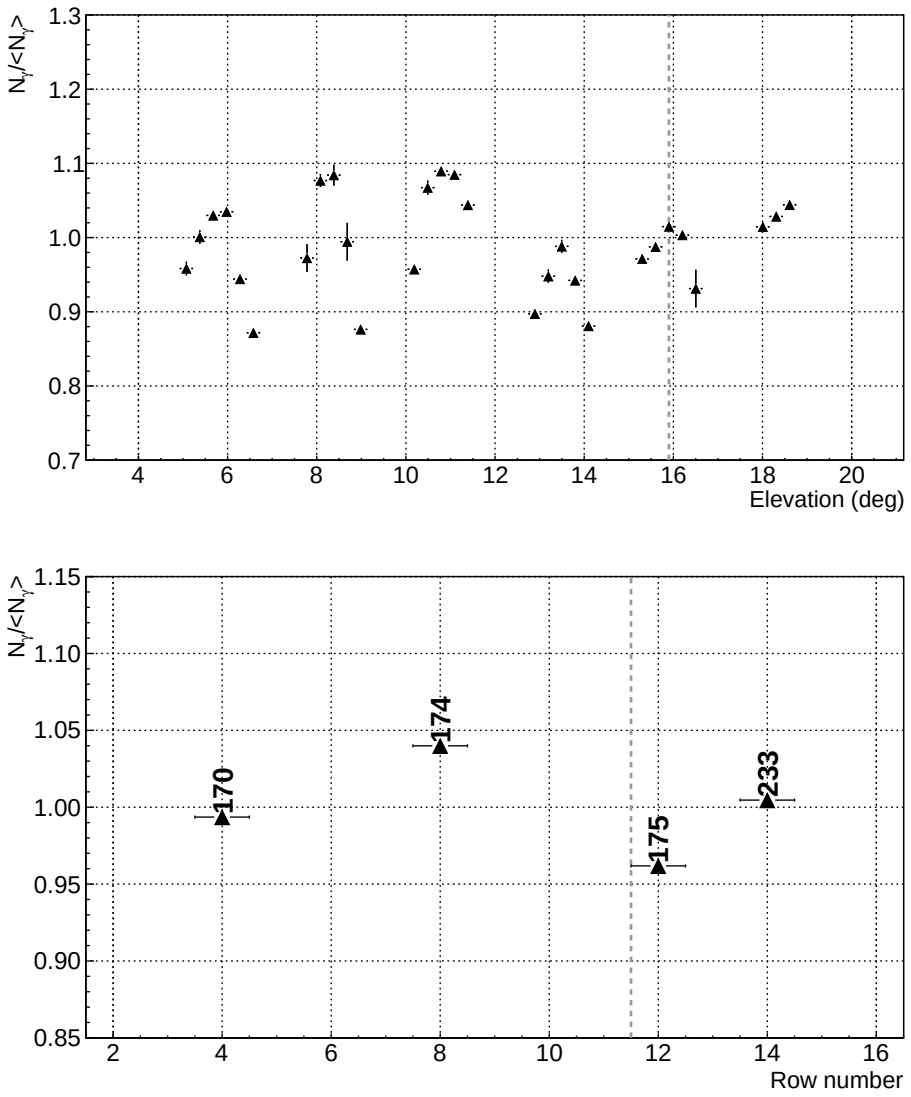

FIG. 6.17 Relative light fraction as a function of elevation angle (top) and row number (bottom) for pixels in column 4 of LL3. The signal was summed over the first three crowns of pixels surrounding the hottest pixel and is shown relative to the average for all data points. The elevation of the optical axis is marked by the gray dashed line. Top: The characteristic arc shape is a direct consequence of the different sensitivity of the central part of the pixel and the light collectors. Bottom: Only events within 0.12° of the pixel center fired when the platform was hovering on-target were accepted. The numbers printed above the data points are the number of events passing the aforementioned cuts.

6.6 Discussion of Results

6.6.1 A check of the standard FD calibration constants

Since standard absolute FD calibration constants are used for the reconstruction of the Octocopter signal, the obvious question is: What if there was something wrong with the calibration constants on the Octocopter measurement nights? In this section, the standard calibration constants are investigated and even the continuous CalA constants, presented in Subsec. 3.1.2 but not yet implemented in the reconstruction procedures, are called on for more insight.

Based on Fig. 6.18a, which shows the standard absolute calibration constants for pixel 70, 208 and the mean for all 440 pixels of the LL3 camera throughout the November 2014 FD shift, there appears to be nothing unusual. CalA was performed for both pixels as usual on all three measurement nights, which are indicated by gray arrows. The variation in the calibration constants throughout the shift is about $\sim$3 % and is typical for the relatively short measurement nights of the late austral spring. In short, there is no indication that the discrepant light fractions result from corrupted or unreliable FD calibration constants. An analogue plot is shown in Fig. 6.18b for pixels 70, 76, 202 and 208 in LL3 in November 2015. Again, no anomalous behavior is observed.

Incidentally, November 2014 was the first month during which full final implementation of continuous CalA was run on all telescopes, and data for both pixels are available. While raw data for the pixels calibrated during the November 2015 campaign are also available, they had not been processed at the time of writing of this manuscript. Therefore, the following discussion focuses on continuous CalA during the 2014 campaign.

Fig. 6.19 shows an example of the evolution of the sensitivity of pixel 70 throughout the first measurement night in November 2014. Notice that in this case the *response* of the pixel is shown, which is simply the inverse of the calibration constant. Over the course of the night, the continuous CalA response grows by 2.4 %, yet the average response throughout the night is only 0.6 % lower than during the morning CalA run – the data point used in standard reconstruction procedure. There is no significant drift of the response or periods of unusually low responsivity that could explain the discrepant light fraction.

Similar plots for pixel 70 during the second measurement night and pixel 208 during the third measurement night are shown in App. F. Qualitatively both behave very similarly. The mean response of pixel 70 throughout the second measurement night is within 0.5 % the same as its response to the morning calibration run. For pixel 208, the average response throughout the night is 1 % higher than in the morning CalA run. Again, this cannot explain the significantly less-than-one light fractions. In fact, a higher response throughout the night compared to the morning calibration run results in an overestimation of the number of photons at the aperture and may at best aid in explaining the difference of $\sim$4 % between the light fractions of the two pixels.

To conclude, there is no indication that the standard FD calibration constants

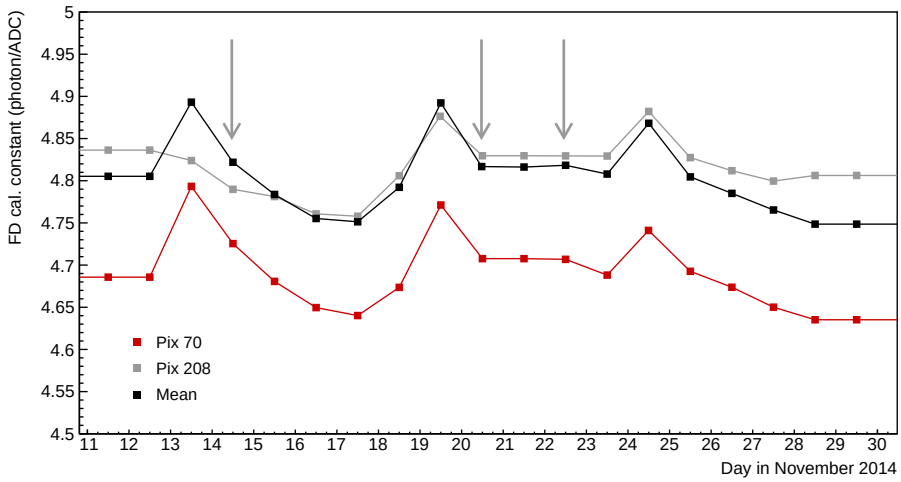

November 2014

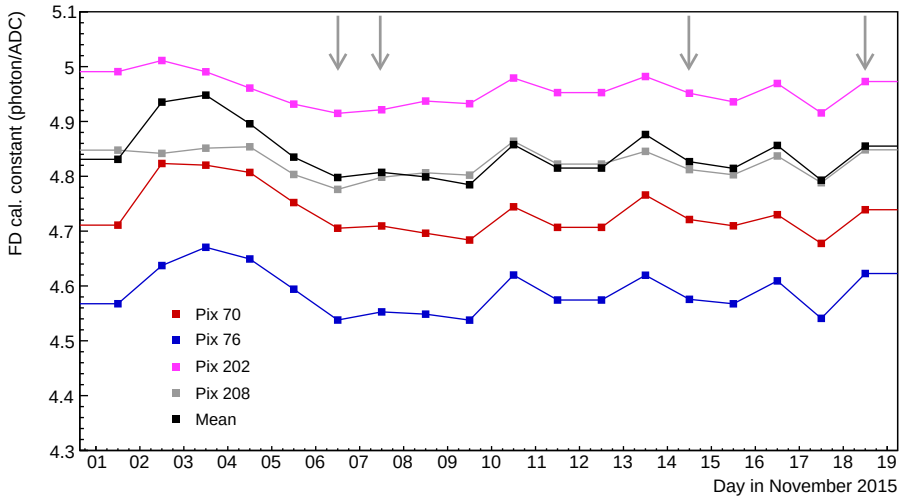

November 2015

FIG. 6.18 Standard absolute FD calibration constants in 375 nm-equivalent photons at the aperture per ADC count. Shown are the progressions for the entire November shifts in 2014 and 2015, with the Octocopter measurement nights indicated by gray arrows. The mean of the constants for all 440 PMTs is also shown.

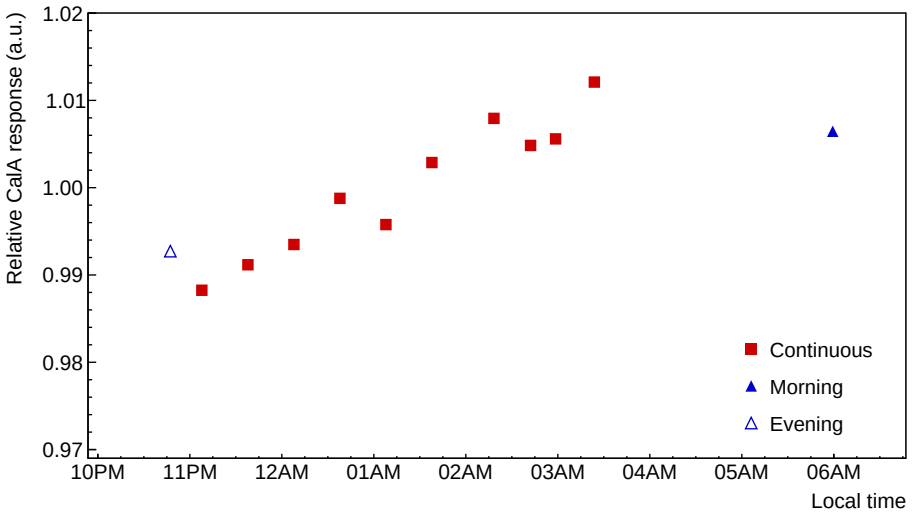

FIG. 6.19 Evolution of the sensitivity of pixel 70 in LL3 throughout the first measurement night in November 2014. The solid red squares indicate the continuous CalA response, while the open and solid blue triangles at the beginning and end of the sequence represent the standard evening and morning CalA, respectively. The response on the y-axis is shown relative to the mean of all responses to allow for an easy estimate of the magnitude of the drifts and fluctuations.

used for the reconstruction of the Octocopter signal are not representative of the sensitivity of the telescope at the relevant time. Furthermore, only small drifts of maximum 1 % with respect to the morning calibration run were observed in continuous CalA. The reconstructed light fractions are thus not an artifact of problems with the calibration system or unusual responses of the studied pixels during the relevant time intervals.

6.6.2 Comparison to drum calibration

The reconstructed light fractions are consistently lower than unity for all integration regions, meaning that the number of photons at the aperture is underreconstructed when using the standard FD calibration constants. Even though we strive to make the Octotoper-to-drum comparison as realistic as possible by averaging the response to Octocopter pulses over the entire pixel surface, major differences between the drum and the Octocopter methods nonetheless remain. In particular, there are effects, including those that are PSF-related, to which the drum calibration is not sensitive, whereas the Octocopter as well as air shower measurements are. These include the following:

Non-specular reflection and transmission: In particular, the drum calibration is not sensitive to non-specular reflection and non-specular transmission on the dust layers on the mirror and filter, respectively. During drum calibration, photons that are scattered away from the target PMT are simply detected by its neighbors, as the entire camera is illuminated and read out simultaneously.

For point-like sources like the Octocopter or an air shower, scattering leads to a widening of the image on the camera.

By using large integration regions, e.g. the entire camera, scattered photons can be recovered, save for those that are scattered off the camera completely. This is, however, only applicable for externally triggered events with a full-camera read-out, as is the case for Octocopter measurements. In air shower detection, only parts of the camera are read out and used for reconstruction, thus some light is inevitably lost. The effect is particularly severe for the case of a very dusty mirror, where about 8 % of all reflected photons land outside the target pixel (c.f. Sec. 4.1). Unlike scattering, absorption by the dust on the mirror is to a large degree properly encompassed by the drum calibration constants.

Reflections on the PMT faces: This mechanism, already discussed in Sec. 3.2, is responsible for producing the flat tail of the PSF. While photons that undergo multiple reflections between the camera and the mirror (or to a lesser degree the aperture) contribute to the drum calibration response of individual pixels, in air shower detection those photons will generally strike the camera at large distances from the main image, possibly landing in pixels that will not pass the three trigger levels or will not fall within the optimum integration region defined by ζ_{opt}.

A +3.5 % correction (see Sec. 3.2) was applied to the standard FD calibration constants to account for the halo produced by PMT reflections. However, based on the light fractions derived with the Octocopter method, the fraction of all reconstructed photons that fall outside $\zeta_{\mathrm{LWC}} = 4.0°$ is 0.057 ± 0.003. This value of course combines all contributions to the telescope PSF and not just the multiple reflections between the camera and the aperture. Nevertheless, it appears that the aforementioned +3.5 % correction to the drum-derived calibration constants fails to account for the full impact of the PSF.

Large-angle scattering and reflections on the MUG-6 filter: The reflectivity of the MUG-6 filter, based solely on its index of refraction $n = 1.52$, is about 8.5 % for normal incidence. In air shower and Octocopter measurements, photons reflected on the aperture will be permanently lost to the outside environment. Not so in drum calibration, where a significant fraction of back-scattered photons re-enters the drum, undergoes multiple reflections and is re-emitted, making the drum effectively brighter. Such a recycling process is, of course, not available during air shower and Octocopter measurements and may lead to an underestimation of the number of photons at the aperture, if not properly accounted for. While a constant +4 % correction is applied to the drum calibration constants to compensate for back-reflections on the MUG-6 filter (see Subsec. 3.1.1), it is unclear to what extent this correction changes with the condition, i.e. the dust layer, of the filter.

Furthermore, significant attenuation of light by the dust layer on the filter was observed in a dedicated shower-like measurement discussed in Sec. 4.3. The effect is of the order of 10 % and was confirmed by independent measurements [140].

Most importantly, the drum method appears to be only half as sensitive to the attenuation by the dust layer on the filter as the aforementioned measurements (refer to Subsec. 4.3.4), plausibly because part of the photons are scattered at large angles and subsequently re-injected into the telescope by the drum. This mechanism could account for up to 7 % of the gap between the actually measured total light fraction and unity.

6.6.3 Thoughts on the composition of the LWC

The lateral width correction (LWC) [132], already discussed in Sec. 3.3, is a data-based correction designed to account for the photon fraction falling outside of the optimum integration region defined in terms of the angle ζ_{opt}, but still within $\zeta_{\mathrm{LWC}} = 4.0°$. It is a function of ζ_{opt}, and is parametrized in terms of shower age and distance.[11] Example values for distances of 10 km and 30 km, and ages 0.8, 1.0 and 1.2 are plotted in Fig. 6.20.

[11] *Recall that the age* s *of a shower describes its stage of development with respect to the depth of the shower maximum* X_{max}*, at which* $s = 1$*, and the distance refers to the distance of closest approach of the shower axis to the telescope.*

Being a phenomenological construct, the LWC does not give any microscopic or physical explanation of the composition of the light it corrects for. There is, however, strong evidence that the light excess outside of ζ_{opt} is a direct consequence of the PSF of the telescopes (see Sec. 3.2 and Subsec. 4.2.2). As of the time of writing this work, multiple scattering had been ruled out as the source [132].

Estimating an effective ζ_{opt} for the Octocopter image and comparing the corresponding LWC value to the light fraction between ζ_{opt} and $\zeta_{\mathrm{LWC}} = 4.0°$ may allow us to isolate the PSF-related fraction of the correction. With a geometric angular size of 0.006° at the standard flight distance of 1 km, the Octocopter really is a point source to the telescope, thus any considerable widening of its

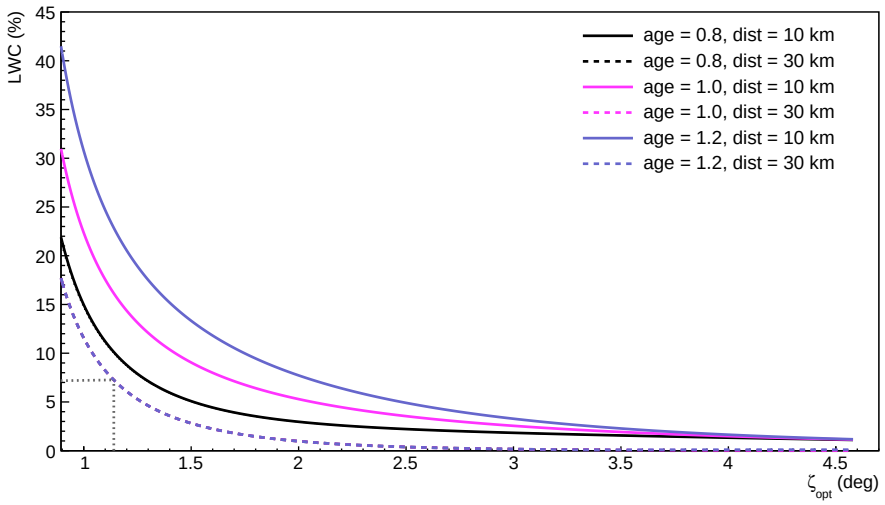

FIG. 6.20 The LWC as a function of ζ_{opt} for different shower ages and distances. At a distance of 30 km all three curves overlap, regardless of shower age. The dotted gray line marks the mean value of ζ_{opt} for very distant showers (1.14°).

image is caused by the PSF itself and potentially by multiple scattering. The challenge now lies in estimating a realistic ζ_{opt} value, and an effective shower distance and age for the Octocopter image.

We argue that the Octocopter image is best approximated by that of distant young showers, which are laterally well contained within the FOV of one or two pixels. In this context, "young" refers to a relatively narrow intrinsic width of the shower as well as a small depth in the atmosphere, so that light propagates to the telescope through less dense layers of the atmosphere and is subject to comparatively less multiple scattering. As can be seen in Fig. 6.21, the value of ζ_{opt} asymptotically goes to 1.14° for shower distances of 20 km and more, and the corresponding all-time light fraction at this angle is $\mathcal{F}^{\mathrm{pix}}(1.14°) = 0.783 \pm 0.034(0.085)$.

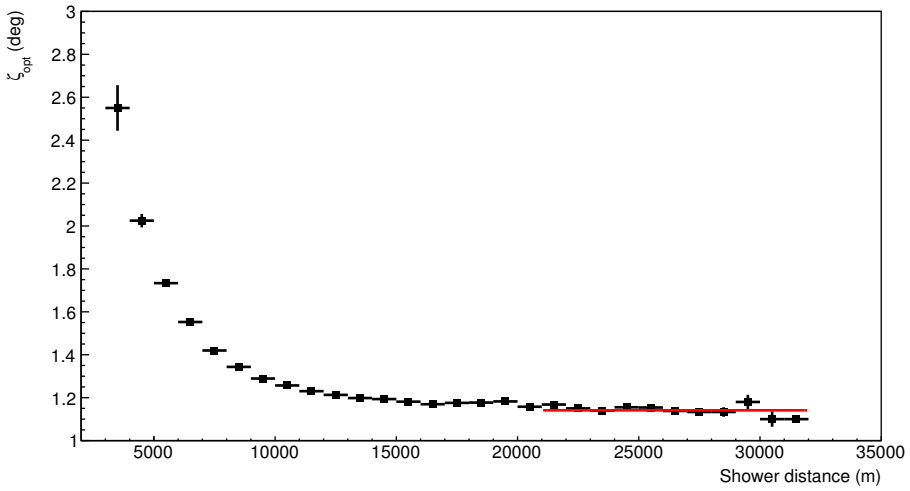

FIG. 6.21 The value of ζ_{opt} as a function of shower distance goes asymptotically to 1.14°, as is indicated by the red line. The data set shown here consists of nearly 20 000 measured air showers in the energy range $10^{17.7}$–$10^{19.9}$ eV. For a plot of energy vs. distance, refer to Fig. 3.17. Data from [83].

The need for estimating an effective age of the Octocopter image is made obsolete by the fact that at large distances, the LWC is no longer sensitive to shower age (c.f. Fig. 6.20). Applying the LWC value of 7.3 % corresponding to a distance of 30 km, the corrected light fraction becomes 0.839 ± 0.054 (0.103), which is in reasonable agreement with 0.868 ± 0.038 (0.094) obtained when integrating up to 4.0°.[12]

[12] *The error on the LWC-corrected fraction includes the systematic uncertainty of the LWC of 4.7 % [132].*

Assuming that the choice of ζ_{opt} is realistic, this result indicates that the light excess observed between ζ_{opt} and $\zeta_{\mathrm{LWC}} = 4.0°$ for distant showers is dominated by the telescope PSF and is, within the accuracy of the calculation, properly accounted for. It is, however, not clear whether this observation can be extended to nearby showers, as the composition of the light that the LWC corrects for may change with shower distance. In particular, at close distance the LWC may correct for a convolution of the intrinsic lateral width with the PSF.

In this exercise, the contribution from multiple scattering was neglected. Since multiple scattering has been eliminated as the source of the observed light excess

between ζ_{opt} and $\zeta_{\mathrm{LWC}} = 4.0°$ for air showers, and is only a minimal contribution for the Octocopter method due to the small flight distance from the telescope, this simplification is not expected to change the conclusion reached here.

The fact that the Octocopter light source is point-like and the resultant image on the camera resembles that of distant showers raises the question whether the light fractions obtained at $\zeta_{\mathrm{opt}} = 4.0°$ are equally valid for nearby showers with considerably larger optimal integration regions (up to $\zeta_{\mathrm{opt}} \sim 2.7°$). This question is directly linked to the just discussed composition of the LWC and cannot be answered based on Octocopter data alone. It is, however, conceivable that the light fractions at ζ_{LWC} of nearby and distant showers are commensurate. Certainly, a global distance-independent offset in the reconstructed energy of (7.5 ± 0.3) percent, corresponding to the all-time average of the total light fraction of 0.925 ± 0.040 (0.100), is present and may be regarded as a lower limit.

6.6.4 Concluding remarks on the Octocopter method

In this chapter, the full procedure for calibrating the fluorescence detector of the Pierre Auger Observatory using the Octocopter method was presented. The key features and findings are the following:

- The estimated systematic uncertainty of the measured light fractions is 4.2 % if Octocopter sphere temperatures are used to correct for the temperature-dependence of the light source, and 4.6 % if weather station temperatures are used in lieu of the sphere temperatures.

- Using an isotropic point-like source, the Octocopter method is a shower-like measurement and as such is affected by different properties of the telescopes in the same way as an air shower would be, e.g. it is sensitive to the telescope PSF and to large-angle scattering of photons on the aperture. The method does not suffer from methodological weaknesses of on-shower-like measurements, which rely on placing a reflector directly into the aperture.

- The point-like light source is perfectly suited for the study of the telescope PSF on sub-pixel level, e.g. in the pixel center or the side or vertex of a light collector.

- To obtain the mean calibration constant for a pixel, the spatial inhomogeneities must be averaged over. This can be achieved by either covering the pixel surface uniformly with Octocopter shots, as was done in this work, or deriving factors to convert the responsivity of a small surface element to the mean responsivity of the pixel, using e.g. the data set plotted in Fig. 6.2 or Fig. 6.7. Alternatively, position-dependent calibration constants could be derived on the level of one pixel.

- A new avenue for simulating the fluorescence detector opens up, circumventing ray-tracing completely. The Octocopter data are in principle a set of conversion maps from the number of photons impinging on the aperture at a given angle

to the number of ADC counts for individual pixels of the camera. Hence, knowing the angular distribution of photons arriving at the aperture, the distribution of the signal on the camera can be produced immediately based on the Octocopter-measured conversion maps alone. An extended light source can be simply treated as a superposition of several point sources.

- While scanning individual pixels is time-consuming, the results for one or a few pixels can be replicated over the full camera, e.g. by a flat-fielding procedure. The term flat-fielding refers to the process of compensating for variations in pixel-to-pixel sensitivity, caused in particular by different PMT gains and dark currents, and a flat-fielded camera will yield a uniform response to a uniform signal. As long as the responsivity ratio between the pixels is known from e.g. a previous drum calibration or CalA, the Octocopter calibration constant of one pixel can be transferred to other pixels. Additionally, if the spatial responsivity of a pixel is well known, it is sufficient to target one position on the pixel with the Octocopter, e.g. the center, and subsequently map the obtained response over the entire pixel.

The Octocopter method would greatly benefit from an upgrade to a differential GPS device and a temperature-stabilized light source. Within the Pierre Auger Observatory, potential future measurements include calibration of different telescopes at different sites, calibration at short distance to maximally reduce the possible influence of the uncertainty of Mie attenuation and scattering[13] , and at different distances to probe the dependence of atmospheric and aerosol effects on distance. Further applications include e.g. the energy and timing cross-calibration of the Coihueco telescopes and HEAT, which share a common FOV and have been found to reconstruct energies of the same air showers with a difference of $(5.3 \pm 0.6)\,\%$ [175].

[13] *a differential GPS device is a prerequisite to achieve sufficient position accuracy*

7 Summary and Outlook

The Pierre Auger Observatory combines the surface array and air-fluorescence detection methods to measure extensive air showers initiated by ultra-high energy cosmic rays (UHECRs) in the Earth's atmosphere. Due to its calorimetric nature and model-independence, the fluorescence measurement is used to set the energy scale of the Observatory, making an accurate energy calibration of the fluorescence detector (FD) of utmost importance. The goal of the work presented in this thesis was to perform an absolute calibration of the FD with the following key features: a very high accuracy, resemblance of an actual air shower measurement and full independence of the current standard calibration system (drum calibration and CalA).

In the first step, existing calibration systems were reviewed (Chap. 3), starting with CalA that monitors night-to-night variations of the PMT gain, but not intra-night variations. To study those, an extended CalA scheme that records the PMT response throughout each measurement night in 30-minute intervals – the so-called continuous CalA – was developed (Sec. 3.1). Already early test measurements revealed significant gain drifts of up to 6 % occurring within one measurement night, which are neither accounted for by the standard CalA scheme, nor can they be reliably predicted due to their dependence on various external factors. If not properly handled, they deteriorate the energy resolution and may even introduce a systematic bias into the reconstructed energies. Following this realization, the continuous CalA scheme was extensively tested and implemented in all telescopes, and is now in the process of being incorporated into standard air shower reconstruction procedures.

In the second step, the imaging properties of the fluorescence detector were investigated. Solid understanding of the point spread function (PSF) is required for the interpretation of both, the standard drum calibration procedure, in which all pixels of one camera are illuminated simultaneously, as well as shower-like methods like the Octocopter. In fact, at the time this thesis project began, there had been a long-standing discrepancy between the experimentally measured and the simulated PSF (Sec. 3.2), which motivated a series of dedicated measurements of the properties of the aperture MUG-6 filter and the mirror (Chap. 4).

An in situ measurement of the angular distribution of mirror-reflected light was carried out (Sec. 4.1), taking advantage of the special geometrical properties of the center of curvature of the mirror. It was found that the dust layer on the mirror scatters photons substantially, shaping the hitherto not understood region of the PSF at small angles $\zeta < 5°$. For a dusty mirror, over 7 % of photons are scattered outside of the target pixel, i.e. to angles larger than $\sim$0.75°. Due to the 16° tilt of the spherical mirror with respect to the vertical, dust only accumulates in its

bottom bowl-like part. The upper parts of the mirror are quite clean, scattering less than 1 % outside of the target pixel.

The measured angular distribution functions of mirror-reflected light were implemented into telescope simulation codes to achieve more realistic ray-tracing (Sec. 4.2), leading to significant improvement in the agreement between the measured a simulated PSF. Simulations with and without the dust layer on the mirror confirmed that the drum calibration is nearly blind to scattering, while air shower measurements are fully sensitive to it. This is an important distinction, since the extent to which the drum calibration is sensitive to different telescope properties directly determines the impact those properties have on reconstructed shower variables. Both, the drum calibration and air shower measurements are fully sensitive to pure absorption on optical components.

Assuming that the state of the mirror is frozen in time, energies are reconstructed on average by (3.3 ± 0.1) % lower when the dust layer is activated in the simulation. Provided that the empirically introduced lateral width correction (LWC), currently applied to compensate for the photon fraction falling outside the optimum integration region ζ_{opt} but still within $\zeta_{\mathrm{LWC}} = 4.0°$, is PSF-dominated, the effect of scattering on the mirror is properly accounted for in energy reconstruction. Additional discrepancy between the generated and reconstructed energies arises if the dust layer changes between the time the drum calibration was performed and the detection of the actual event.

As the height-dependence of the dust layer on the mirror is likely to introduce an elevation dependence into the reconstructed signal, the depth of maximum shower development X_{max} was investigated as well. For protons and iron nuclei alike, the activation of the dust layer pushed the reconstructed X_{max} (2.9 ± 0.9) g/cm^2 deeper into the atmosphere. While the shift is small, it is significant and is to be regarded as an additional contribution to the systematic uncertainty of the X_{max} measurement, which is estimated to be less than 10 g/cm^2 for all energies.

The MUG-6 filter was studied in a separate measurement using a modified laser pointer as the light source (Sec. 4.3). Unexpectedly, it was found that the dust layer on the outside of the filter can, depending on its thickness, easily attenuate 11 % of incoming light. This result was confirmed by independent measurements based on the detection of laser shots from the Central Laser Facility. On the other hand, the drum calibration had been previously shown to be only half as sensitive to the attenuation on the dust layer, because unlike the laser pointer it is a non-shower-like measurement. The reflective drum covers the aperture fully, thus effectively re-injecting a fraction of photons that are back-reflected on the MUG-6 filter into the telescope. Such back-reflected photons are, of course, lost during actual air shower measurements, resulting in an underestimation of the number of photons at the aperture in shower reconstruction.

Finally, a fully independent calibration of selected pixels of an FD camera was carried out using the Octocopter method – a remotely controlled drone that lifts an isotropic UV light source into the FOV of a telescope (Chap. 6). First, the light source was calibrated to a very high accuracy: the number of photons arriving

at the telescope aperture is known to better than 4 % (Chap. 5). To enable a comparison of the derived calibration constants to the standard drum-based ones (Sec. 6.1), the spatial inhomogeneity of the camera pixels was averaged over by covering the studied pixel with Octocopter shots as uniformly as possible.

Two extensive calibration campaigns were flown in telescope 3 of Los Leones (Sec. 6.2). In November 2014, two pixels were calibrated. Those very same pixels and additionally two other ones were calibrated a year later in November 2015. The number of photons reconstructed using standard drum-based calibration constants was compared to the number of photons expected to arrive at the aperture from the Octocopter (referred to as the light fraction) (Sec. 6.5). The average light fraction (over all pixels and both years) summed over the entire camera was found to be 0.925 ± 0.040. Air shower signals are, however, never integrated over the entire camera, but effectively up to $\zeta_{\mathrm{LWC}} = 4.0°$, where the ratio of reconstructed and expected signals amounts to 0.868 ± 0.038.

The difference between the total light fractions averaged over all calibrated pixels in 2014 and 2015 is only 0.5 %, indicating that the discrepancy found between the reconstructed and generated signals is a long-term one. The difference in the response of any two pixels measured on different nights but within one campaign was found to be 3.3 % and 4.7 %, and is commensurate in magnitude to intra-night PMT gain drifts (now addressed through the continuous CalA) and the uncertainty in Mie attenuation. The change in the response of the two pixels that were measured in both years was found to be 1.9 % and 4.4 %, suggesting that on top of a long-term offset the pixel response is dominated by relatively short-term effects, such as the just mentioned nightly PMT gain drifts or uncertainty in aerosol concentration.

The implication of those findings is a global shift of the energy scale of the Pierre Auger Observatory of +7.5 %, and additionally a potentially distance-dependent shift, which amounts to +5.7 % for distant, and thus primarily ultra-high energy, showers. Such a significant change would play a pivotal role in the astrophysical interpretations of the origin of the flux suppression, combined Auger–TA searches for anisotropy in cosmic-ray arrival directions and the underlying UHECR source candidates. It is, furthermore, expected to considerably improve the long-standing discrepancy between simulated and measured ground signals of the surface detector. Nevertheless, further studies and cross-checks are required before an energy shift is actually performed.

Indisputable advantages of the Octocopter method, which has been under development at KIT since 2009, are:

- *very high accuracy* – individual pixels can be calibrated to an accuracy better than 4.6 %, which is significantly less than the uncertainty of the standard absolute calibration of 9.9 %,

- *shower-like nature* – the method is sensitive to the PSF of the telescope in the same way as an air shower is,

- *wide applicability* – the Octocopter can be used for absolute calibration, to

probe the PSF of the telescopes or to produce end-to-end conversion maps from the number of photons of a given direction at the aperture to ADC counts in different pixels of the camera, thus allowing one to obtain a realistic telescope simulation and even to circumvent ray-tracing codes completely,

- *easy portability* – both the platform and the light source can be easily fitted into a standard airplane carry-on luggage, opening up the possibility for use at different observatories, such as the Pierre Auger Observatory and the Telescope Array [152], and
- *versatility* – the option to exchange the light source for e.g. a radio emitter expands the application horizons to other instruments [150].

The key feature and advantage of the Octocopter method, namely its point-like isotropic light source, is at the same time its biggest drawback: Because pixels must be calibrated individually, the method is time-consuming. Moreover, high-quality flights require good weather conditions with wind speeds below 10 m/s. Even though the calibration constants obtained for a few pixels can be mapped over the entire camera of one telescope, it is unlikely that the Octocopter could replace the standard calibration procedure in the near future. It is, however, a very valuable complementary method, the results of which can be used to correct for the methodological deficiencies of non-shower-like calibration methods, as was shown in this work.

Acknowledgements

I owe thanks to many people who have supported me generously throughout the creation of this work.

First and foremost, I am grateful to Prof. Johannes Blümer for making this research project possible in the first place and Prof. Thomas Müller for allowing me to finish. Furthermore, I wish to thank Prof. Blümer for acting as referee and Prof. Ulrich Husemann for taking on the role of the co-referee, providing many helpful insights as the manuscript was taking shape.

I thank Ralph Engel for directly supervising my work, the perpetual and patient guidance he has provided and the many opportunities he has granted me to do work at the Pierre Auger Observatory and present my work to the Collaboration.

Special thanks go to Kai Daumiller for his incredible work on the Octocopter, for tens upon tens of crash-free flights (and letting me keep my fingers), countless hours spent in the laboratory calibrating the light source, extended Python support and his frequent presence during the in situ telescope measurements. Thanks are also due to Felix Werner for building such an amazing flying platform during his Master's project.

I owe heartfelt thanks to Radomír Šmída for his unwavering encouragement and support during the past three years, his encyclopedic knowledge of the FD and the many fruitful discussions we have shared. I highly appreciate the great commitment with which he approached the in situ telescope measurements as well as the Octocopter campaigns.

Many thanks go to Michael Unger for his continuous assistance with all things related to FD analysis and simulation, nearly in real time even across the Atlantic. I owe sincere thanks to Hermann-Josef Mathes and Kai Daumiller for all the amazing work they have done on continuous CalA, reaching from the design to the final implementation stages, and to Hermann-Josef for the last-minute stream of data.

Further thanks belong to my colleagues, past and present, at KIT and within the Pierre Auger Collaboration, in particular to Hans Klages for his deep involvement in many of the measurement campaigns, Ralf Ulrich for his reinforcement in battling the telescope simulations, Bianca Keilhauer for her help with the atmosphere, Mariano del Río for his assistance during FD measurement campaigns, María Micheletti for making the aerosol measurement at Los Leones possible and Sabine Bucher for navigating the administrative jungle.

I am grateful to Ralph Engel, Prof. Husemann, Radomír Šmída, Ivana Tománková, Kai Daumiller, Michael Unger, Hans Klages and Hermann-Josef Mathes for proofreading the manuscript, in part or whole, and providing sharp and insightful editorial comments.

Over the past three years, I have had the honor to be a member of the graduate school KSETA. I am truly grateful for the ample learning opportunities and the stimulating learning environment this school has provided.

Most importantly, my most sincere gratitude goes to those dearest to me, my family and friends, without whom none of this would matter.

Appendix

A Distributions of Mirror-Reflected Light

Tab. A.1 The cumulative distribution functions (CDFs) describing non-specular reflection on the upper clean and lower dusty parts of the mirror, based on the measurement in Sec. 4.1. The angle δ is the angular deviation from the specular direction of reflection on the mirror.

δ (°)	CDF	δ (°)	CDF	δ (°)	CDF	δ (°)	CDF
Upper part of mirror							
0.000	0.909	0.313	0.977	0.628	0.991	1.198	0.996
0.063	0.952	0.376	0.981	0.691	0.992	4.110	0.997
0.125	0.961	0.439	0.985	0.754	0.993	6.456	0.998
0.188	0.967	0.502	0.988	0.880	0.994	10.333	0.999
0.250	0.972	0.565	0.990	1.134	0.995	15.023	1.000
Lower part of mirror							
0.000	0.837	1.134	0.943	2.350	0.964	4.506	0.982
0.063	0.863	1.198	0.944	2.479	0.965	4.705	0.983
0.125	0.874	1.261	0.946	2.544	0.966	4.838	0.984
0.188	0.882	1.325	0.947	2.608	0.967	5.037	0.985
0.250	0.890	1.388	0.949	2.738	0.968	5.237	0.986
0.313	0.897	1.452	0.950	2.803	0.969	5.438	0.987
0.376	0.904	1.516	0.951	2.933	0.970	5.638	0.988
0.439	0.910	1.580	0.952	2.998	0.971	5.893	0.989
0.502	0.915	1.644	0.953	3.128	0.972	6.143	0.990
0.565	0.919	1.708	0.954	3.258	0.973	6.393	0.991
0.628	0.923	1.772	0.956	3.389	0.974	6.706	0.992
0.691	0.926	1.836	0.957	3.519	0.975	7.081	0.993
0.754	0.929	1.900	0.958	3.650	0.976	7.456	0.994
0.817	0.932	2.028	0.959	3.782	0.977	7.894	0.995
0.880	0.934	2.092	0.960	3.913	0.978	8.457	0.996
0.944	0.937	2.157	0.961	4.044	0.979	9.207	0.997
1.007	0.939	2.221	0.962	4.176	0.980	10.270	0.998
1.071	0.941	2.286	0.963	4.374	0.981	12.209	0.999
						15.023	1.000

B Shower Simulation Quality Cuts

The following basic geometry- and profile-related cuts were applied to the simulated shower samples in Subsec. 4.2.4:

```
maxCoreTankDist 1500.0 # max. shower plane distance core-hybrid-tank
nAxisPixels        5   # min. number of pixels used in axis fit
xMaxInFOV        0.0   # max. distance of xMax to borders
xMaxError       40.0   # max. error on xMax [g/cm^2]
energyError      0.2   # max. error on energy (relative)
profileChi2      2.5   # max. reduced GH chi2
minViewAngle    20.0   # min. viewing angle
```

C Light Source Calibration: Corrections

C.1 Temperature

LED light output is known to vary inversely with junction temperature, which in turn is a function of

▷ ambient temperature,

▷ junction current, and

▷ heat sinking.

The light source is calibrated at a stable ambient temperature in the range 21.5–25.0 °C. In the field, however, the temperatures are typically 15 °C to 25 °C lower. In fact, on any given measurement night the Octocopter will have sat in the open for about one hour before its first flight, thus fully adapting to the ambient temperature. Even though InGaN-based LEDs tend to have relatively weak temperature dependences (compared to e.g. AlGaInP-based LEDs used in the red region [176, 177]), the intensity gain due to the temperature difference in the laboratory and during flight must be taken into account properly.

We measured the light output of the *L2b* in standard calibration configuration[1] as a function of ambient temperature under laboratory conditions. The complete light source including the electronic board, i.e. all parts that are exposed to the ambient temperature in the field, was placed in a climate chamber equipped with a UV-transparent quartz window. A photodiode (of a different type than that used for the absolute charge measurement, IRD-UVG100) was positioned to view the quartz window at close distance and read out by the Keithley 6514 electrometer. Keeping the measurement instruments outside the chamber at a stable temperature ensures that we observe the temperature behavior of the light source, and not that of the photodiode or the electrometer. Since the measurement was relative and the only varying quantity was the chamber temperature, factors such as the quartz window transmissivity and the photodiode spectral responsivity are not needed for further analysis.

[1] *Amplitude $A = 5$ corresponding to 997 DAC, pulse width $\Delta t = 8\ \mu s$ and pulsing rate $f = 1\ kHz$.*

Fig. C.1 depicts the relative measured light output as a function of the difference T_{offset} between the current and calibration temperatures T and T_{cal}, where $T_{\text{cal}} = 22.0\,^{\circ}\text{C}$. The y-error bars include the statistical uncertainty and an uncertainty related to the short-term instability of the light source, which is discussed in detail in Sec. 5.6. In short, the measured light output varies by $\pm 0.7\,\%$ on the time scale of days. Since the origin of this behavior is not quite understood and the light output–temperature curve was measured over the course of two days, this variation is fully included. All other systematic uncertainties are correlated

and, assuming they are of the form of a constant offset, they would simply shift the entire curve up or down, either way leaving the gradient unchanged. The estimated uncertainty of the temperature measurement is $\pm 0.1\,^{\circ}\mathrm{C}$.

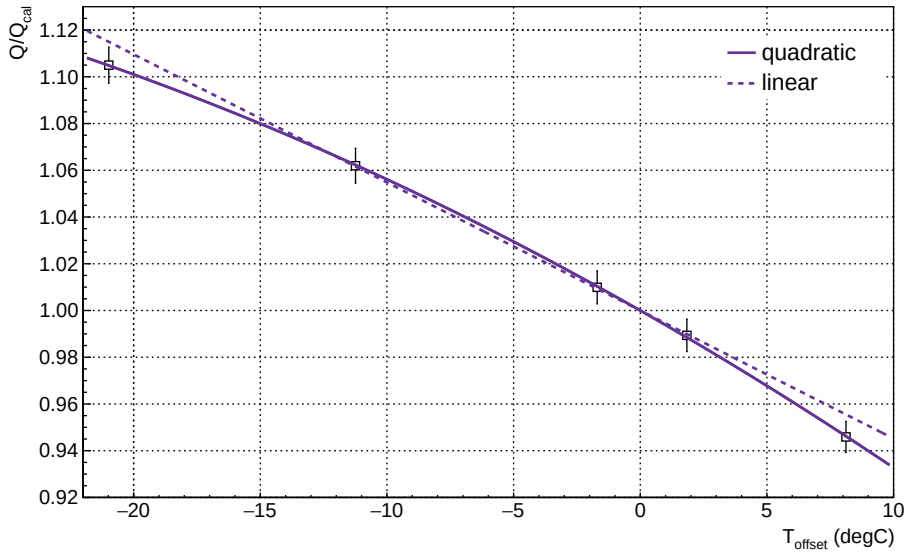

FIG. C.1 Measured pulse charge Q as a function of the difference T_{offset} between the current and the standard calibration temperature T and $T_{\mathrm{cal}} = 22.0\,^{\circ}\mathrm{C}$. All points are shown relative to the calibration measurement Q_{cal} recorded at T_{cal}, i.e. at $T_{\mathrm{offset}} = 0\,^{\circ}\mathrm{C}$. Linear (dashed) and quadratic fits (solid line) to the data are also shown.

Four different functions were tried to fit the data (linearly and quadratically proportional, exponential and power law), the best result in terms of the χ^2 being the quadratic form

$$f(T_{\mathrm{offset}}) = 1.0 + p_1 T_{\mathrm{offset}} + p_2 T_{\mathrm{offset}}^2\,, \tag{C.1}$$

where p_1 and p_2 are free parameters. The linear form

$$f(T_{\mathrm{offset}}) = 1.0 + p_1 T_{\mathrm{offset}} \tag{C.2}$$

is included for comparison (see Fig. C.1) and the fit results are summarized in Tab. C.1.

The reduced χ^2 is lower than unity for both selected fit functions: 0.6 and $8 \cdot 10^{-3}$ for the linear and the quadratic form, respectively. This indicates that the uncertainty of the measurement is overestimated, possibly due to factoring in the short-term instability of the light source. However, since the uncertainty of the fit parameters is only used to estimate the uncertainty associated with the temperature correction and does not in any way affect the computation of the number of photons at the aperture, this simply means that the uncertainty estimate is on the conservative side.

TAB. C.1 Parameters of the linear and quadratic fits to the light output vs. temperature curve of the light source *L2b*.

	linear	quadratic
p_1 (1/°C)	$(-5.5 \pm 0.3) \cdot 10^{-3}$	$(-6.2 \pm 0.5) \cdot 10^{-3}$
p_2 (1/°C^2)		$(-5.6 \pm 3.0) \cdot 10^{-5}$
$\mathcal{X}^2/NdF$	0.6	$8.4 \cdot 10^{-3}$

TAB. C.2 Example values of the temperature correction factor C_{temp} and associated uncertainties for two different flight temperatures.

T (°C)	T_{offset} (°C)	C_{temp}	ΔC_{temp}	$\Delta C_{\text{temp}}/C_{\text{temp}}$ (%)
10.0	−12.0	1.066	0.019	1.7
0.0	−22.0	1.109	0.008	0.7

We choose to describe the temperature correction with the quadratic form and note that a similar functional dependence was observed e.g. in [176]. The resulting correction function then becomes

$$f(T_{\text{offset}}) = p_1 T_{\text{offset}} - p_2 T_{\text{offset}}^2 \tag{C.3}$$

$$= -6.158 \cdot 10^{-3} T_{\text{offset}} - 5.413 \cdot 10^{-5} T_{\text{offset}}^2 , \tag{C.4}$$

and the multiplicative factor C_{temp} used to correct the calibration pulse charge Q_{cal} is obtained by evaluating Eq. (C.3) at a particular T_{offset} defined by the ambient temperature during the Octocopter flight. In all further calculations and analyses, the temperature-corrected pulse charge is used.

The uncertainties σ_{p_1} and σ_{p_2} of the fit parameters p_1 and p_2 propagate into the correction factor C_{temp} as

$$\Delta C_{\text{temp}} = \left[\left(\frac{\partial C_{\text{temp}}}{\partial p_1} \sigma_{p_1} \right)^2 + \left(\frac{\partial C_{\text{temp}}}{\partial p_2} \sigma_{p_2} \right)^2 \right]^{\frac{1}{2}} = \left[(T_{\text{offset}} \sigma_{p_1})^2 + (T_{\text{offset}}^2 \sigma_{p_2})^2 \right]^{\frac{1}{2}} . \tag{C.5}$$

To get a feeling for the magnitude of the uncertainty tied to this correction, results of an example calculation for flight temperatures of 0 °C and 10 °C are given in Tab. C.2.

The uncertainty of the ambient temperature measurement during flight, discussed in Subsec. 5.6.2, results in an additional term in the combined uncertainty of C_{temp}

$$(p_1 + 2 p_2 T_{\text{offset}}) \Delta T_{\text{offset}} , \tag{C.6}$$

where $\Delta_{T_{\text{offset}}}$ is the uncertainty of the temperature difference between calibration and flight, although in practice just the latter. Eq. (C.5) then becomes

$$\Delta C_{\text{temp}} = \left\{ (T_{\text{offset}} \sigma_{p_1})^2 + (T_{\text{offset}}^2 \sigma_{p_2})^2 + [(p_1 + 2 p_2 T_{\text{offset}}) \Delta T_{\text{offset}}]^2 \right\}^{\frac{1}{2}} . \tag{C.7}$$

C.2 Pulsing rate

For reasons of practicality, stability and measurement uncertainty, the light source is pulsed at different rates during calibration and actual FD measurements. In case of the latter, the telescope is triggered externally for every single light pulse and, in contrast to an air shower, all 440 pixels of the camera are read out. The chosen pulsing rate of 1 Hz is matched to the maximum full-camera readout speed and ensures that neither the light source nor the FD electronics warm up in a significant, non-correctable way. At the same time, we are still able to record hundreds of light pulses in one flight.

During calibration, conditions are less restrictive and we strive for maximum accuracy and precision. At a pulsing rate of 1 kHz, large data samples can be collected within short periods of time, over which the light source, the measurement instruments and ambient conditions remain stable. Moreover, as already explained in Subsec. 5.3.1, by measuring the cumulative charge of 100 pulses, we avoid cutting into the noise floor of the Keithley electrometer. In the following paragraphs, the effect of the pulsing rate on measured pulse charge at a set nominal amplitude is investigated.

Similarly to the standard calibration procedure, the pulse charge Q_{pulse} was measured for nine different pulsing rates spanning the range 1–1000 Hz. To ensure sufficient signal at the lower rates, the standard source–photodiode distance of 243.6 cm was reduced to 25 cm. Fig. C.2 shows how the relative pulse charge Q_{pulse} increases with the pulsing rate at a constant nominal amplitude setting $A = 5$. The dependence is approximately linear, with a slope of $\sim$3.5 %/kHz. To account for this behavior, a multiplicative correction factor $C_{\text{rate}} = 96.6 \pm 0.1$ is applied to the pulse charge Q_{pulse} measured during calibration. The uncertainty of C_{rate} was computed as the standard deviation of all 10 measurements acquired at 1 Hz.

One may wonder whether the observed dependence could be caused by the measurement instruments themselves and not be the light source and its driving electronics, in which case the correction would be moot. As described in Subsec. 5.3.1, we observe a small warm-up effect in the shape of the pulse at 1 kHz and correct for it immediately during pulse processing. While in principle there could still be another warm-up component that only affects the pulse amplitude and not the shape, we refer to the absolute calibration of the drum by Brack et al. [92]. In this measurement, the driving electronics and the LED of the drum were maintained at a stable temperature by a Peltier circuit, and similar instruments as in the calibration of the Octocopter light source, i.e. a silicon photodiode read out by a Keithley 6514 electrometer, were used to measure the light output. No dependence on pulsing rate was observed in the range 1–400 Hz. We conclude that the rate dependence indeed originates from the light source, specifically its driving electronics, since the light output of the LEDs themselves decreases with temperature.

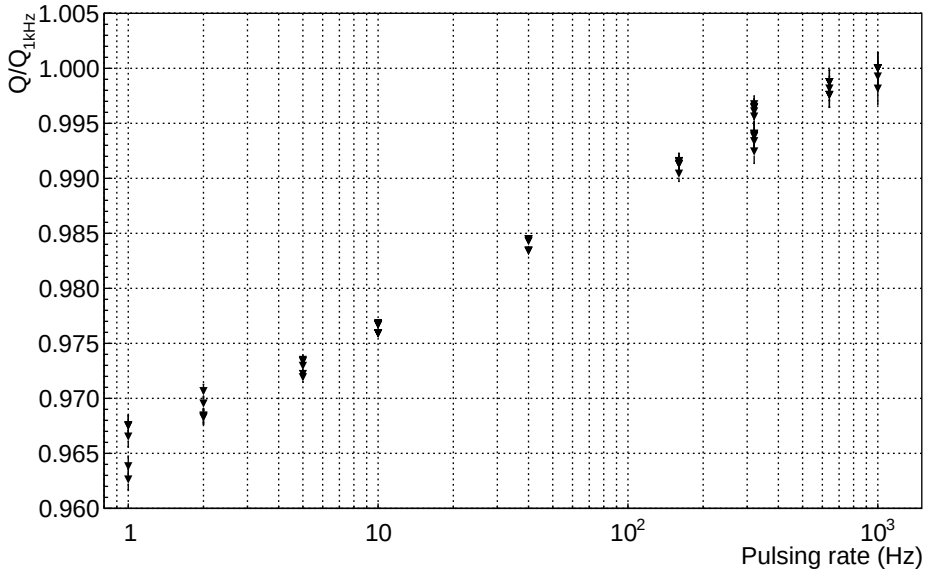

FIG. C.2 Measured pulse charge relative to the reference value Q_{1kHz} at 1 kHz vs. pulsing rate. The dependence was measured at a constant nominal amplitude setting $A = 5$.

C.3 Pulse width

Nominal pulse width settings range from 2 to 64 μs, 8 μs being the standard value used in the November 2012, 2014 and 2015, as well as many other campaigns. However, the actually produced pulse width as measured with an oscilloscope differs slightly from the nominal value and, as Fig. C.3 illustrates, increases with pulse amplitude and levels off at large values. The effect is of the order of a few tenths of μs. For the standard light source configuration, the deviation from the nominal pulse width of 8 μs is 0.358 μs.

Since the analysis of the Octoctoper light pulses recorded by the FD camera operates with the total photon number at the aperture and not the photon flux, the final results will not be affected by this correction. Nevertheless, it is relevant for a realistic simulation of Octocopter light pulses.

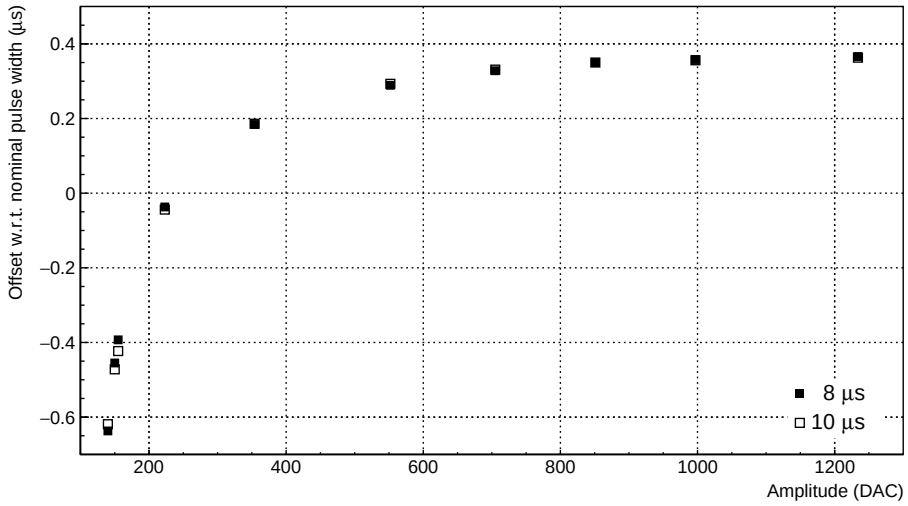

FIG. C.3 The difference between the measured and nominal pulse width as a function of DAC counts (see Tab. 5.2 for the relation between DAC counts and amplitude setting) for two nominal pulse widths: 8 μs and 10 μs. The points overlap above 300 DAC counts.

D Octocopter GPS Position Uncertainty

Different causes contribute to the total uncertainty of the GPS position [153], including:

- ▷ finite precision of satellite clocks,
- ▷ limited knowledge of satellite orbits,
- ▷ changes in the speed of light as the signal traverses different layers of the atmosphere,
- ▷ receiver ability to determine the time of the incoming signal,
- ▷ reception of reflected signals, and
- ▷ satellite geometry with respect to the receiver.

Typical uncertainties are listed in Tab. D.1 and add up to 3.9 m. The uncertainty is further multiplied by a scalar factor referred to as dilution of precision (DOP), which quantifies just how favorable the geometrical configuration of the visible satellites is. In general, the larger the distances between the individual satellites used in the measurement, the lower the DOP and the better the final position accuracy. At high satellite coverage, DOP values rarely exceed 2.0, but may skyrocket to 20.0 and above in areas with major satellite obstruction. Satellite coverage and DOP values may be retrieved using the Trimble Global Navigation Satellite System (GNSS) Online Planning tool [178]. An example for a campaign night in November 2012 at LL is shown in Fig. D.1. Eleven satellites were visible on average and the positional DOP varied between 1.1 and 1.8, with a short spike of 2.0 resulting from the number of satellites dropping to ten. No horizon obstruction was considered, which is a reasonable approximation of the flat terrain of the Pampa Amarilla. Moreover, in [103] DOP values at the Pierre Auger Observatory were measured to be approximately 1.5, which is in excellent agreement with the Trimble data. For the combined uncertainty analysis, we

Source	**Uncertainty (m)**
Effect of the atmosphere	3.1
Ephemeris data	1.5
Satellite clocks	1.5
Multipath reception	1.0
Effect of the receiver	0.5
TOTAL	**3.9**

TAB. D.1 Typical uncertainties on horizontal GPS position coming from different sources. Adapted from [153].

adopt a mean DOP value of 1.5 and a corresponding GPS position uncertainty of 6 m.

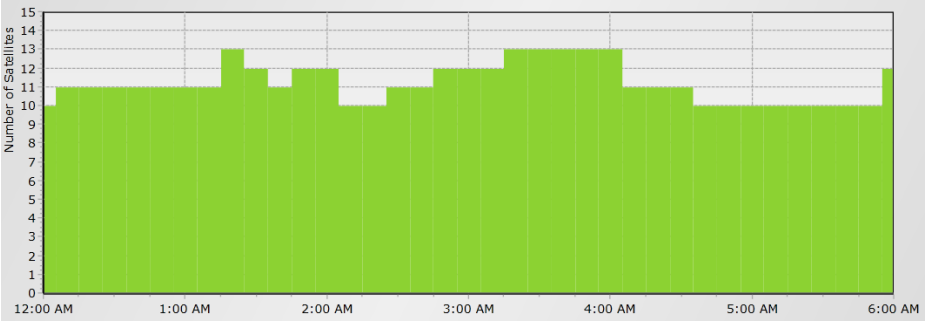

(A) Number of visible satellites

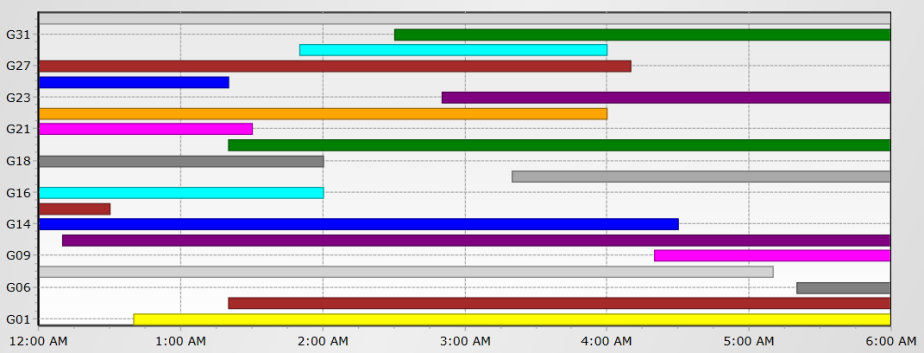

(B) Satellite coverage

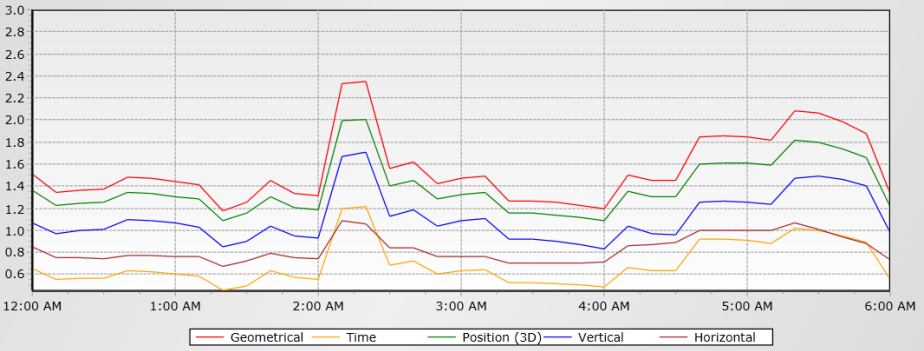

(C) DOP values (Position (3D) is relevant for our case)

FIG. D.1 Satellite data during the night hours of 06 November 2015 (times shown are in local Argentina Time (ART)) assuming no horizon obstruction. The DOP values strongly correlate with the number of visible satellites. From [178].

E Offline Module Sequences

E.1 Drum Simulation

```
<sequenceFile>

   <enableTiming/>

   <moduleControl>

      <loop numTimes="1">
         <!-- set the detector time -->
         <module> EventGeneratorOG      </module>

         <!-- the drum photon loop -->
         <loop numTimes="unbounded">
            <module> DrumPhotonGeneratorOG </module>
            <module> TelescopeSimulatorKG_DEV </module>
         </loop>

         <!-- calculate the calibration constants -->
         <module> DrumPhotonGeneratorOG </module>
         <!-- the drum electronics sim -->
         <module> FdElectronicsSimulatorOG </module>
         <module> FdTriggerSimulatorOG </module>
         <module> EventFileExporterOG </module>
      </loop>

   </moduleControl>

</sequenceFile>
```

E.2 Octocopter FD Data Reconstruction

```
<sequenceFile>

   <enableTiming/>
   <enableModuleTracing/>

   <moduleControl>

      <loop numTimes="unbounded">
         <module> EventFileReaderOG </module>

         <loop numTimes="1">
            <module> FdCalibratorOG  </module>
            <module> FdPulseFinderOG </module>
            <module> FdSDPFinderOG   </module>
         </loop>

         <module> RecDataWriterNG </module>
      </loop>

   </moduleControl>

</sequenceFile>
```

F Continuous CalA for Octocopter Nights

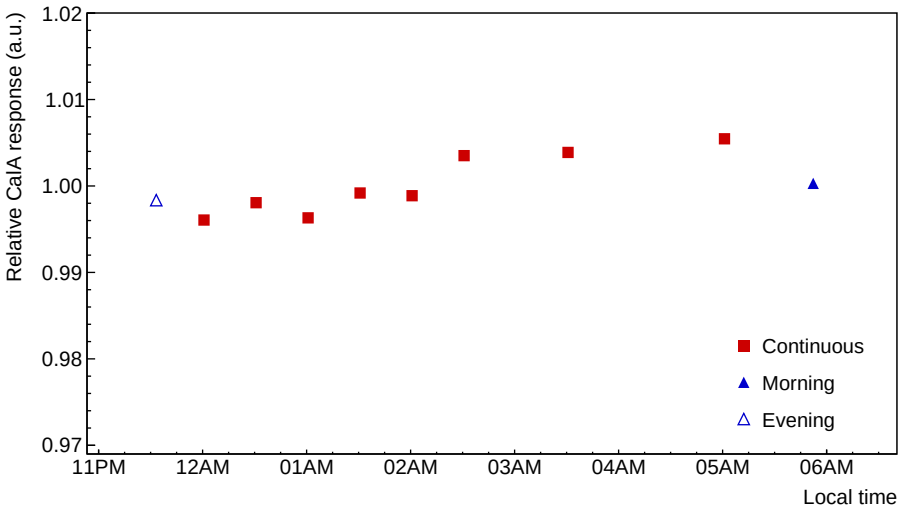

Pixel 70, second measurement night (19–20 November 2014)

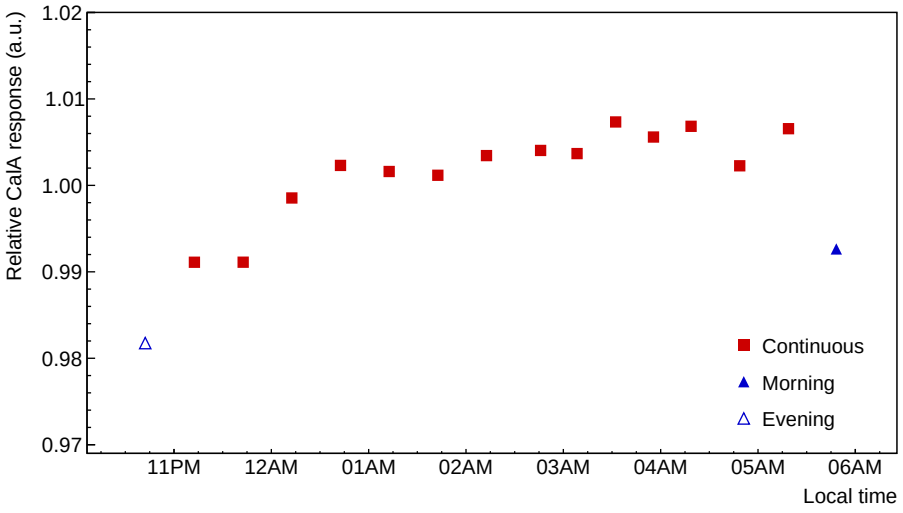

Pixel 208, third measurement night (20–21 November 2014)

FIG. F.1 Temporal evolution of the sensitivity of pixels 70 and 208 throughout the relevant measurement nights of the November 2014 campaign. The solid red squares indicate the continuous CalA response, the open and solid blue triangles at the beginning and end of the sequence represent the standard evening and morning CalA, respectively. The response on the y-axis is shown relative to the mean of all responses to allow for an easy estimate of the magnitude of the drifts and fluctuations.

Bibliography

[1] A. Gockel, "Luftelektrische Beobachtungen bei einer Ballonfahrt," *Physik. Zeitschr.* XI (1910) 280–282.

[2] A. Gockel, "Messungen der durchdringenden Strahlung bei Ballonfahrten," *Physik. Zeitschr.* XII (1911) 595–597.

[3] T. Wulf, "Beobachtungen über die Strahlung hoher Durchdringungsfähigkeit auf dem Eiffelturm," *Physik. Zeitschr.* XI (1910) 811–813.

[4] W. Kolhörster, "Über eine Neukonstruktion des Apparates zur Messung der durchdringenden Strahlung nach Wulf und die damit bisher gewonnenen Ergebnisse," *Physik. Zeitschr.* XIV (1913) 1066–1069.

[5] V. Hess, "Über Beobachtungen der durchdringenden Strahlung bei sieben Freiballonfahrten," *Physik. Zeitschr.* XIII (1912) 1084–1091.

[6] M. F. L'Annunziata, *Radioactivity: Introduction and History*. Elsevier, 2007.

[7] F. W. Stecker and S. T. Scully, "Searching for new physics with ultrahigh energy cosmic rays," *New J. Phys.* 11 (2009) 085003, arXiv:0906.1735 [astro-ph.HE].

[8] S. T. Scully and F. W. Stecker, "Lorentz invariance violation and the observed spectrum of ultrahigh energy cosmic rays," *Astropart. Phys.* 31 (2009) 220–225, arXiv:0811.2230 [astro-ph].

[9] A. Saveliev, L. Maccione, and G. Sigl, "Lorentz invariance violation and chemical composition of ultra high energy cosmic rays," *JCAP* 1103 (2011) 046, arXiv:1101.2903 [astro-ph.HE].

[10] R. Engel, D. Heck, and T. Pierog, "Extensive air showers and hadronic interactions at high energy," *Ann. Rev. Nucl. Part. Sci.* 61 (2011) 467–489.

[11] A. Schulz, Pierre Auger Collab., "The measurement of the energy spectrum of cosmic rays above $3x10^{17}$ eV with the Pierre Auger Observatory," in *Proceedings, 33rd International Cosmic Ray Conference (ICRC2013): Rio de Janeiro, Brazil, July 2-9, 2013*, p. 0769. http://www.cbpf.br/%7Eicrc2013/papers/icrc2013-0769.pdf.

[12] T. Abu-Zayyad *et al.*, Telescope Array Collab., "The cosmic-ray energy spectrum observed with the surface detector of the Telescope Array experiment," *Astrophys. J.* 768 (2013) L1, arXiv:1205.5067 [astro-ph.HE].

[13] R. Abbasi *et al.*, IceCube Collab., "Cosmic ray composition and energy spectrum from 1–30 PeV using the 40-string configuration of IceTop and IceCube," *Astropart. Phys.* 42 (2013) 15–32, arXiv:1207.3455 [astro-ph.HE].

[14] R. Abbasi *et al.*, IceCube Collab., "All-particle cosmic ray energy spectrum measured with 26 IceTop stations," *Astropart. Phys.* 44 (2013) 40–58, arXiv:1202.3039 [astro-ph.HE].

[15] L. O. Drury, "Origin of cosmic rays," *Astropart. Phys.* 39-40 (2012) 52–60, arXiv:1203.3681 [astro-ph.HE].

[16] J. R. Hörandel, "Models of the knee in the energy spectrum of cosmic rays," *Astropart. Phys.* 21 (2004) 241–265, arXiv:astro-ph/0402356 [astro-ph].

[17] W. D. Apel *et al.*, "KASCADE-Grande measurements of energy spectra for elemental groups of cosmic rays," *Astropart. Phys.* 47 (2013) 54–66, arXiv:1306.6283 [astro-ph.HE].

[18] V. S. Berezinsky and S. I. Grigor'eva, "A bump in the ultrahigh-energy cosmic ray spectrum," *Astron. Astrophys.* 199 (1988) 1–12.

[19] V. Berezinsky, A. Z. Gazizov, and S. I. Grigorieva, "Dip in UHECR spectrum as signature of proton interaction with CMB," *Phys. Lett.* B612 (2005) 147–153, arXiv:astro-ph/0502550 [astro-ph].

[20] K. Kotera and A. V. Olinto, "The astrophysics of ultrahigh energy cosmic rays," *Ann. Rev. Astron. Astrophys.* 49 (2011) 119–153, arXiv:1101.4256 [astro-ph.HE].

[21] J. Abraham *et al.*, Pierre Auger Collab., "Observation of the suppression of the flux of cosmic rays above 4×10^{19} eV," *Phys. Rev. Lett.* 101 (2008) 061101, arXiv:0806.4302 [astro-ph].

[22] T. Abu-Zayyad *et al.*, Telescope Array Collab., "The cosmic ray energy spectrum observed with the surface detector of the Telescope Array experiment," *Astrophys. J.* 768 (2013) L1, arXiv:1205.5067 [astro-ph.HE].

[23] R. Abbasi *et al.*, "First observation of the Greisen-Zatsepin-Kuzmin suppression," *Phys. Rev. Lett.* 100 no. 10, (2008) 101101–101106.

[24] K. Greisen, "End to the cosmic-ray spectrum," *Phys. Rev. Lett.* 16 no. 17, (1966) 748–750.

[25] G. Zatsepin and V. Kuz'min, "Upper limit of the spectrum of cosmic rays," *ZhETF Pis'ma* 4 no. 3, (1966) 114–117.

[26] M. Nagano and A. A. Watson, "Observations and implications of ultra-high energy cosmic rays," *Rev. Mod. Phys.* 72 no. 3, (2000) 689–732.

[27] B. Sarkar, K.-H. Kampert, and J. Kulbartz, "Ultra-high energy photon and neutrino fluxes in realistic astrophysical scenarios," in *Proceedings, 32nd International Cosmic Ray Conference (ICRC 2011)*, vol. 2, p. 198. https://inspirehep.net/record/1352272/files/v2_1087.pdf.

[28] J. W. Cronin, "The highest-energy cosmic rays," *Nucl. Phys. Proc. Suppl.* 138 (2005) 465–491, arXiv:astro-ph/0402487 [astro-ph].

[29] E. Fermi, "On the origin of cosmic radiation," *Phys. Rev.* 75 no. 8, (1949) 1169–1174.

[30] A. R. Bell, "The acceleration of cosmic rays in shock fronts. I," *Mon. Not. Roy. Astron. Soc.* 182 (1978) 147–156.

[31] G. F. Krymsky, A. I. Kuzmin, and S. I. Petukhov, "A formation of cosmic ray spectrum by a regular acceleration mechanism in the supernova shell," in *Proceedings, 16th International Cosmic Ray Conference (ICRC1979): Kyoto, Japan, 1979*, vol. 2, pp. 44–48. 1979.

[32] P. Bhattacharjee and G. Sigl, "Origin and propagation of extremely high-energy cosmic rays," *Physics Reports* 327 (2000) 109–247.

[33] J. Abraham *et al.*, Pierre Auger Collab., "Upper limit on the cosmic-ray photon fraction at EeV energies from the Pierre Auger Observatory," *Astropart. Phys.* 31 (2009) 399–406, arXiv:0903.1127 [astro-ph.HE].

[34] T. Abu-Zayyad *et al.*, Telescope Array Collab., "Upper limit on the flux of photons with energies above 10^{19} eV using the Telescope Array surface detector," *Phys. Rev.* D88 no. 11, (2013) 112005, arXiv:1304.5614 [astro-ph.HE].

[35] A. Aab *et al.*, Pierre Auger Collab., "Improved limit to the diffuse flux of ultrahigh energy neutrinos from the Pierre Auger Observatory," *Phys. Rev.* D91 no. 9, (2015) 092008, arXiv:1504.05397 [astro-ph.HE].

[36] A. Haungs *et al.*, "KCDC - The KASCADE Cosmic-ray Data Centre," *J. Phys. Conf. Ser.* 632 no. 1, (2015) 012011, arXiv:1504.06696 [astro-ph.IM].

[37] J. Matthews, "A Heitler model of extensive air showers," *Astropart. Phys.* 22 (2005) 387–397.

[38] W. Heitler, *Quantum theory of radiation*. Oxford University Press, 1944.

[39] T. K. Gaisser, *Cosmic rays and particle physics*. Cambridge University Press, 1990.

[40] P. Abreu *et al.*, Pierre Auger Collab., "Interpretation of the depths of maximum of extensive air showers measured by the Pierre Auger Observatory," *JCAP* 1302 (2013) 026, arXiv:1301.6637 [astro-ph.HE].

[41] A. Ferrari, P. R. Sala, A. Fasso, and J. Ranft, "FLUKA: A multi-particle transport code (Program version 2005)," *CERN-2005-010* (2005) .

[42] D. Heck, G. Schatz, T. Thouw, J. Knapp, and J. N. Capdevielle, "CORSIKA: A Monte Carlo code to simulate extensive air showers," *Report FZKA 6019, Forschungszentrum Karlsruhe* (1998) .

[43] S. J. Sciutto, "AIRES: A system for air shower simulations. User's guide and reference manual. Version 2.2.0," arXiv:astro-ph/9911331 [astro-ph].

[44] E.-J. Ahn, R. Engel, T. K. Gaisser, P. Lipari, and T. Stanev, "Cosmic ray interaction event generator SIBYLL 2.1," *Phys. Rev.* D80 (2009) 094003, arXiv:0906.4113 [hep-ph].

[45] S. Ostapchenko, "QGSJET-II: Towards reliable description of very high energy hadronic interactions," *Nucl. Phys. Proc. Suppl.* 151 (2006) 143–146, arXiv:hep-ph/0412332 [hep-ph].

[46] T. Pierog, I. Karpenko, J. M. Katzy, E. Yatsenko, and K. Werner, "EPOS LHC: Test of collective hadronization with data measured at the CERN Large Hadron Collider," *Phys. Rev.* C92 no. 3, (2015) 034906, arXiv:1306.0121 [hep-ph].

[47] A. Letessier-Selvon and T. Stanev, "Ultrahigh-energy cosmic rays," *Rev. Mod. Phys.* 83 no. 3, (2011) 907–942.

[48] J. J. Beatty and S. Westerhoff, "The highest-energy cosmic rays," *Ann. Rev. Nucl. Part. Sci.* 59 (2009) 319–345.

[49] F. Kakimoto *et al.*, "A measurement of the air fluorescence yield," *Nucl. Instr. and Meth. in Phys. Res. A* 372 (1996) 527–533.

[50] M. Nagano *et al.*, "New measurement on photon yields from air and the application to the energy estimation of primary cosmic rays," *Astropart. Phys.* 22 (2004) 235–248.

[51] M. Ave *et al.*, "A novel method for the absolute fluorescence yield measurement by AIRFLY," *Nucl. Instr. and Meth. in Phys. Res. Section A* 597 no. 1, (2008) 55–60.

[52] M. Ave *et al.*, "Precise measurement of the absolute yield of fluorescence photons in atmospheric gases," *Nucl. Phys. B Proc. Suppl.* 212–213 (2011) 356–361.

[53] M. Ave *et al.*, AIRFLY Collab., "Spectrally resolved pressure dependence measurements of air fluorescence emission with AIRFLY," *Nucl. Instrum. Meth.* A597 (2008) 41–45.

[54] A. Aab *et al.*, Pierre Auger Collab., "The Pierre Auger Cosmic Ray Observatory," *Nucl. Instrum. Meth.* A798 (2015) 172–213, arXiv:1502.01323 [astro-ph.IM].

[55] J. Abraham *et al.*, Pierre Auger Collaboration Collab., "The Fluorescence Detector of the Pierre Auger Observatory," *Nuclear Instruments and Methods in Physics Research A* 620 (2010) 227–251.

[56] T. Waldenmaier, *Spectral resolved measurement of the nitrogen fluorescence yield in air induced by electrons*. PhD thesis, Universität Karlsruhe (TH), 2006.

[57] "Pics about space." http://permetix.com/samurize/img/azimuth_elevation.gif. Retrieved on Apr 30, 2016.

[58] "MUG-6 special filter glass, 3.25 mm thick, Schott Glaswerke, Mainz, Germany." http://www.schott.com. Retrieved on 09 May, 2014.

[59] J. A. Matthews, "Optical calibration of the Auger fluorescence telescopes." Pierre Auger Note: GAP 2002-029.

[60] "PHOTONIS XP3062, High PHR, 8-stage, 40 mm hexagonal tube." http://photonis.com. Retrieved on 09 May, 2014.

[61] C. Aramo *et al.*, "The camera of the Auger fluorescence detector." Pierre Auger Note: GAP 1999-027.

[62] P. Facal and P. Privitera, "Measurement of the FD camera light collection efficiency and uniformity." Pierre Auger Note: GAP 2000-010.

[63] P. Abreu *et al.*, Pierre Auger Collab., "The Pierre Auger Observatory V: Enhancements," in *Proceedings, 32nd International Cosmic Ray Conference (ICRC 2011)*. 2011. arXiv:1107.4807 [astro-ph.IM]. http://inspirehep.net/record/919727/files/arXiv:1107.4807.pdf.

[64] A. Aab *et al.*, Pierre Auger Collab., "The Pierre Auger Observatory upgrade – preliminary design report," arXiv:1604.03637 [astro-ph.IM].

[65] R. Engel, Pierre Auger Collab., "Upgrade of the Pierre Auger Observatory (AugerPrime)," in *Proceedings, 34rd International Cosmic Ray Conference (ICRC2015): Hague, Netherlands, July 30–August 6, 2015*. http://arxiv.org/pdf/1509.03732.pdf.

[66] J. Abraham *et al.*, Pierre Auger Collab., "A study of the effect of molecular and aerosol conditions in the atmosphere on air fluorescence measurements at the Pierre Auger Observatory," *Astropart. Phys.* 33 (2010) 108–129, arXiv:1002.0366 [astro-ph.IM].

[67] P. Abreu *et al.*, Pierre Auger Collab., "Techniques for measuring aerosol attenuation using the Central Laser Facility at the Pierre Auger Observatory," *JINST* 8 (2013) P04009, arXiv:1303.5576 [astro-ph.IM].

[68] M. G. Winnick, *Cloud cameras at the Pierre Auger Observatory*. PhD thesis, University of Adelaide, 2010. Available online at http://digital.library.adelaide.edu.au/dspace/handle/2440/67198.

[69] S. Y. BenZvi *et al.*, "The lidar system of the Pierre Auger Observatory," *Nucl. Instrum. Meth.* A574 (2007) 171–184, arXiv:astro-ph/0609063 [astro-ph].

[70] V. Rizi, A. Tonachini, M. Iarlori, and G. Visconti, Pierre Auger Collab., "Atmospheric monitoring with LIDARs at the Pierre Auger Observatory," *Eur. Phys. J. Plus* 127 (2012) 92.

[71] P. Abreu *et al.*, Pierre Auger Collab., "The rapid atmospheric monitoring system of the Pierre Auger Observatory," *JINST* 7 (2012) P09001, arXiv:1208.1675 [astro-ph.HE].

[72] P. Trávníček *et al.*, Pierre Auger Collab., "New method for atmospheric calibration at the Pierre Auger Observatory using FRAM, a robotic astronomical telescope," in *Proceedings, 30th International Cosmic Ray Conference (ICRC 2007)*, vol. 4, pp. 347–350. 2007. arXiv:0706.1710 [astro-ph]. http://lss.fnal.gov/cgi-bin/find_paper.pl?conf-07-377.

[73] M. Roth. Private communication, 2016.

[74] I. Valiño, Pierre Auger Collab., "The flux of ultra-high energy cosmic rays after ten years of operation of the Pierre Auger Observatory," in *Proceedings, 34rd International Cosmic Ray Conference (ICRC2015): Hague, Netherlands, July 30–August 6, 2015*. http://arxiv.org/pdf/1509.03732.pdf.

[75] D. Mockler. Private communication, 2016.

[76] V. Verzi, Pierre Auger Collab., "The energy scale of the Pierre Auger Observatory," in *Proceedings, 33rd International Cosmic Ray Conference (ICRC2013): Rio de Janeiro, Brazil, July 2-9, 2013*, p. 0928. http://www.cbpf.br/%7Eicrc2013/papers/icrc2013-0928.pdf.

[77] T. Abu-Zayyad *et al.*, Telescope Array Collab., "The surface detector array of the Telescope Array experiment," *Nucl. Instrum. Meth.* A689 (2013) 87–97, arXiv:1201.4964 [astro-ph.IM].

[78] A. Schulz, *Measurement of the energy spectrum and mass composition of ultra-high energy cosmic rays*. PhD thesis, Karlsruhe Institute of Technology, 2016.

[79] A. Aab *et al.*, Pierre Auger Collab., "Searches for anisotropies in the arrival directions of the highest energy cosmic rays detected by the Pierre Auger Observatory," *Astrophys. J.* 804 no. 1, (2015) 15, arXiv:1411.6111 [astro-ph.HE].

[80] A. Aab *et al.*, Pierre Auger Collab., "Large scale distribution of ultra high energy cosmic rays detected at the Pierre Auger Observatory with zenith angles up to 80°," *Astrophys. J.* 802 no. 2, (2015) 111, arXiv:1411.6953 [astro-ph.HE].

[81] R. U. Abbasi *et al.*, Telescope Array Collab., "Indications of intermediate-scale anisotropy of cosmic rays with energy greater than 57 EeV in the Northern sky measured with the Surface Detector of the Telescope Array Experiment," *Astrophys. J.* 790 (2014) L21, arXiv:1404.5890 [astro-ph.HE].

[82] A. Aab *et al.*, Pierre Auger, Telescope Array Collab., "Searches for large-scale anisotropy in the arrival directions of cosmic rays detected above energy of 10^{19} eV at the Pierre Auger Observatory and the Telescope Array," *Astrophys. J.* 794 no. 2, (2014) 172, arXiv:1409.3128 [astro-ph.HE].

[83] A. Aab *et al.*, Pierre Auger Collab., "Depth of maximum of air-shower profiles at the Pierre Auger Observatory. I. Measurements at energies above $10^{17.8}$ eV," *Phys. Rev.* D90 no. 12, (2014) 122005, arXiv:1409.4809 [astro-ph.HE].

[84] J. Allen *et al.*, Yakutsk, Pierre Auger, Telescope Array Collab., "Air shower simulation and hadronic interactions," *EPJ Web Conf.* 53 (2013) 01007, arXiv:1306.6090 [astro-ph.HE].

[85] A. Aab *et al.*, Pierre Auger, Telescope Array Collab., "Testing hadronic interactions at ultra-high energies with air showers measured by the Pierre Auger Observatory,". Submitted for publication.

[86] C. D. Fratte *et al.*, "On the stability of the FD cameras." Pierre Auger Note: GAP 2007-111.

[87] C. D. Fratte *et al.*, "On the stability of the FD cameras - update #1." Pierre Auger Note: GAP 2008-129.

[88] L. Tománková, "The Pierre Auger Fluorescence Detector – Analysis of relative calibration data," Master's thesis, Czech Technical University in Prague, 2012.

[89] R. Šmída, "Nights suitable for measurement with fluorescence detector." Pierre Auger Note: GAP 2011-039.

[90] A. Segreto, "Nightly variability of PMT gains as measured by the UVscope and calibration A." Talk at Pierre Auger Collaboration meeting in Malargüe, Nov 2010.

[91] J. T. Brack, R. Meyhandan, G. J. Hofman, and J. Matthews, "Absolute photometric calibration of large aperture optical systems," *Astropart. Phys.* 20 (2004) 653–659.

[92] J. T. Brack, R. Cope, A. Dorofeev, B. Gookin, J. L. Harton, Y. Petrov, and A. C. Rovero, "Absolute calibration of a large-diameter light source," *Journal of Instrumentation* 8 no. 05, (May, 2013) P05014, arXiv:1305.1329 [astro-ph.IM]. http://stacks.iop.org/1748-0221/8/i=05/a=P05014.

[93] Nichia, "NSHU550 UV LED, Nichia America Corp., 48561 Alpha Dr., Wixom, MI.".

[94] J. Brack *et al.*, "Auger fluorescence detector absolute calibration January and June 2010." Pierre Auger Note: GAP 2010-118.

[95] B. Gookin, *Calibration of the Pierre Auger Observatory fluorescence detectors and the effect on measurements*. PhD thesis, Colorado State University, 2015.

[96] B. Gookin. Private communication, 2016.

[97] J. Brack and M. Sutherland, "Fluorescence detector absolute calibration database update." Pierre Auger Note: GAP 2012-095.

[98] A. C. Rovero, P. Bauleo, J. T. Brack, J. L. Harton, and R. Knapik, Pierre Auger Collab., "Multi-wavelength calibration procedure for the Pierre Auger Observatory fluorescence detectors," *Astropart. Phys.* 31 (2009) 305, arXiv:0811.1518 [astro-ph].

[99] B. Gookin, A. Dorofeev, J. Brack, J. Harton, and A. Rovero, "Multi-wavelength calibration, March 2014." Pierre Auger Note: GAP 2014-091.

[100] R. Knapik *et al.*, Pierre Auger Collab., "The absolute, relative and multi-wavelength calibration of the Pierre Auger Observatory fluorescence detectors," in *Proceedings, 30th International Cosmic Ray Conference (ICRC 2007)*, vol. 4, pp. 343–346. 2007. arXiv:0708.1924 [astro-ph]. http://lss.fnal.gov/cgi-bin/find_paper.pl?conf-07-425.

[101] A. Dorofeev *et al.*, "FD absolute calibration, April 2013." Pierre Auger Note: GAP 2013-058.

[102] A. Menshikov, "LED Calibration Unit user manual, Revision 1.1." http://fuzzy.fzk.de/bscw/bscw.cgi/d153232/LCUUsermanual.pdf. Retrieved on 11 Jan, 2016.

[103] F. Werner, "Design and test of a flying light source for the calibration of the Auger fluorescence telescopes," Master's thesis, Karlsruhe Institute of Technology, 2011.

[104] P. Bauleo *et al.*, "The generation of relative calibration constants for the FD." Pierre Auger Note: GAP 2009-076.

[105] P. Nguyen and B. Dawson, "Update on seasonal variations of the energy scale." Talk at Pierre Auger Collaboration meeting, Malargüe, Nov 2014.

[106] R. Clay, B. Dawson, N. Wild, and B. Whelan, "Ageing and other gain variations of Auger fluorescence detector photomultipliers." Pierre Auger Note: GAP 2009-026.

[107] J. Zorn *et al.*, "The first measurement with the FD operated at a reduced PMT gain." Pierre Auger Note: GAP 2015-021.

[108] L. Tománková, R. Engel, H.-J. Mathes, M. del Río, and R. Šmída, "CalA during data taking." Talk at Pierre Auger Collaboration meeting in Malargüe, Feb 2013.

[109] L. Tománková, K. Daumiller, R. Engel, H.-J. Mathes, M. del Río, and R. Šmída, "On the status of continuous CalA." Talk at Pierre Auger Collaboration meeting in Malargüe, Feb 2015.

[110] J. Bellido, "Measuring the energy scale stability of the surface and fluorescence detectors." Pierre Auger Note: GAP 2010-014.

[111] K. Daumiller, M. del Río, H.-J. Mathes, R. Šmída, and L. Tománková, "Towards a continuous calibration A during FD data taking." Pierre Auger Note: GAP 2016-009.

[112] C. de Donato, F. Sanchez, M. Santander, D. Camin, B. Garcia, and V. Grassi, "Using star tracks to determine the absolute pointing of the fluorescence detector telescopes." Pierre Auger Note: GAP 2005-008.

[113] M. Prouza *et al.*, "Star tracking using background data of FD telescopes – whole star track optimization method." Pierre Auger Note: GAP 2005-041.

[114] P. Nguyen, B. Dawson, and J. Bellido, "Cross-check of the fluorescence detector calibration using the night sky background." Pierre Auger Note: GAP 2016-005.

[115] A. Segreto *et al.*, "Verification of the FD absolute calibration using stars." Talk at Pierre Auger analysis meeting, Prague, Jun 2012.

[116] R. Ulrich, D. Pearson, and P. Sommers, "Relative FD-calibration: calibration system and its stability." Pierre Auger Note: GAP 2010-116.

[117] "LS-1130-4 1100 Series FlashPac with FX-1160 xenon flash lamp with reflector and borosilicate window from Perkin Elmer Opto-electronics, 35 Congress St., Salem, MA 01970." `http://www.perkinelmer.com`. Retrieved on 07 Mar 2015.

[118] "Rm-3700 single channel universal radiometer with RjP-465 silicon energy probe with UV-enhanced response from Laser Probe Inc., 23 Wells ave., Utica, NY 13502." `www.laserprobeinc.com`. Retrieved on 07 Mar 2015.

[119] J. Zorn, "Preparation of an extended measurement cycle of the fluorescence telescopes of the Pierre Auger Observatory," Master's thesis, Karlsruhe Institute of Technology, 2015.

[120] J. Abraham *et al.*, Pierre Auger Collab., "Properties and performance of the prototype instrument for the Pierre Auger Observatory," *Nucl. Instrum. Meth.* A523 (2004) 50–95.

[121] J. R. Becker, "Untersuchung der optischen Eigenschaften der Fluoreszenzteleskope des Pierre Auger Observatoriums," Master's thesis, Universität Karlsruhe (TH), 2005.

[122] J. M. Parrisius, "Test of the calibration of the Auger fluorescence telescopes with an isotropic UV light source," Master's thesis, Universität Karlsruhe (TH), 2009.

[123] P. Assis *et al.*, "Analysis of 2011 roving laser data." Talk at Pierre Auger analysis meeting, Santiago de Compostela, Jun 2011.

[124] P. Assis *et al.*, "Reference manual of fluorescence detector simulation in $\overline{\text{Off}}\underline{\text{line}}$." Pierre Auger Note: GAP 2008-014.

[125] S. Argiro, S. L. C. Barroso, J. Gonzalez, L. Nellen, T. C. Paul, T. A. Porter, L. Prado, Jr., M. Roth, R. Ulrich, and D. Veberič, Pierre Auger Collab., "The Offline software framework of the Pierre Auger Observatory," in *2005 IEEE Nuclear Science Symposium and Medical Imaging Conference El Conquistador Resort, Puerto Rico, October 23-29, 2005*. 2006. arXiv:astro-ph/0601016 [astro-ph].

[126] S. Argiro *et al.*, Pierre Auger Collab., "The Offline software framework of the Pierre Auger Observatory," in *29th International Cosmic Ray Conference (ICRC 2005) Pune, India, August 3-11, 2005*. 2005. http://lss.fnal.gov/cgi-bin/find_paper.pl?conf-05-311.

[127] J. G. Gonzalez, Pierre Auger Collab., "The Offline software of the Pierre Auger Observatory: Lessons learned," arXiv:1208.2154 [astro-ph.IM].

[128] D. Mandát *et al.*, "Measurements of PMT's reflectivity." Talk given by R. Šmída at Pierre Auger Analysis Meeting, Lecce, Jun 2010.

[129] D. Motta and S. Schonert, "Optical properties of bialkali photocathodes," *Nucl. Instrum. Meth.* A539 (2005) 217–235, arXiv:physics/0408075 [physics.ins-det].

[130] M. Unger. Private communication, 2014.

[131] B. Dawson, M. Debes, and P. Sommers, "Shower profile reconstruction with Engineering Array FD data." Pierre Auger Note: GAP 2001-016.

[132] B. R. Dawson *et al.*, "Proposal for an update of the Auger energy scale." Pierre Auger Note: GAP 2012-124.

[133] L. Nožka *et al.*, "Condition of mirror segments after 5 years of operation in Pierre Auger Observatory." Pierre Auger Note: GAP 2010-040.

[134] D. Mandát *et al.*, "Mirror cleaning of Coihueco telescopes in March 2011 – bays 1, 4 and 6." Pierre Auger Note: GAP 2011-077.

[135] D. Mandát. Private communication, 2016.

[136] L. Nožka *et al.*, "Scatter measurements of selected mirror segments – examination of dust contamination." Pierre Auger Note: GAP 2012-048.

[137] Roithner LaserTechnik GmbH. http://www.roithner-laser.com/. Retrieved on 09 Jan, 2016.

[138] PCO, "SensiCam operating instructions." http://www.pco.de/fileadmin/user_upload/db/download/MA_SCOPIE_0411.pdf. Retrieved on 14 Feb, 2016.

[139] A. L. Read, "Linear interpolation of histograms," *Nucl. Instrum. Meth.* A425 (1999) 357–360.

[140] J. Debatin, "Investigation of optical properties of the fluorescence telescopes of the Pierre Auger Observatory," Master's thesis, Karlsruhe Institute of Technology, 2015.

[141] T. Bergmann *et al.*, "One-dimensional hybrid approach to extensive air shower simulation," *Astropart. Phys.* 26 (2007) 420–432, arXiv:astro-ph/0606564 [astro-ph].

[142] K.-H. Kampert and M. Unger, "Measurements of the cosmic ray composition with air shower experiments," *Astropart. Phys.* 35 (2012) 660–678, arXiv:1201.0018 [astro-ph.HE].

[143] Pierre Auger Collaboration, "List of cleanings." https://www.auger.unam.mx/AugerWiki/ListOfCleanings. Retrieved on 30 Jan, 2016.

[144] D. Mandát *et al.*, "Optical properties of MUG-6 filter and the halo problem." Pierre Auger Note: GAP 2009-164.

[145] D. Veberič, K. Daumiller, and D. Gonzalez, "Filter contribution to the FD halo." Pierre Auger Note: GAP 2012-153.

[146] Grimm Technologies Inc., "Portable aerosol spectrometer Grimm 1.109." http://www.dustmonitor.com/Research/1109.htm. Retrieved on Feb 2016, 2016.

[147] R. Engel, L. Tománková, J. Debatin, *et al.*, "Brief status report on study of importance of dust on optical surfaces." Talk at Pierre Auger analysis meeting, Golden, Colorado, Jun 2014.

[148] R. Šmída. Private communication, 2014.

[149] M. Radosz, "Untersuchung der Abbildungseigenschaften eines Auger-Fluoreszenzteleskopes mit einer künstlichen UV-Lichtquelle," Master's thesis, Universität Karlsruhe (TH), 2006.

[150] R. Šmída *et al.*, "First experimental characterization of microwave emission from cosmic ray air showers," *Phys. Rev. Lett.* 113 no. 22, (2014) 221101, arXiv:1410.8291 [astro-ph.IM].

[151] MikroKopter. http://wiki.mikrokopter.de/en/MikroKopter. Retrieved on 07 Dec, 2015.

[152] J. Matthews, "Progress towards a cross-calibration of the Auger and Telescope Array fluorescence telescopes via an air-borne light source," in *Proceedings, 33rd International Cosmic Ray Conference (ICRC2013): Rio de Janeiro, Brazil, July 2–9, 2013*, p. 1218. http://www.cbpf.br/%7Eicrc2013/papers/icrc2013-1218.pdf.

[153] u-blox AG, "GPS, Compendium." https://www.u-blox.com/en/technology/GPS-X-02007.pdf, 2009. Retrieved on 30 Nov, 2015.

[154] V. Ahuja, N. Gentry, V. Gokhale, and O. Staton, "Multi-rotor autonomous vehicle." https://engineering.purdue.edu/ece477/Archive/2011/Spring/S11-Grp09/images_oliver/RollPitchYaw.bmp. Retrieved on Apr 30, 2016.

[155] F. Werner. Private communication, 2015.

[156] K. Daumiller. Private communication, 2015.

[157] OSI Optoelectronics, "UV enhanced photodiodes." http://www.osioptoelectronics.com/standard-products/silicon-photodiodes/uv-enhanced-photodiodes/uv-enhanced-photodiodes-overview.aspx. Retrieved on 15 Dec, 2015.

[158] J. M. Houston, T. C. Larason, and E. Shirley, "Report of calibration," tech. rep., National Institute of Standards and Technology, 2010.

[159] Tektronix. http://tek.com. Retrieved on 09 Dec, 2015.

[160] K. Machida, "Octocopter light source test at the Telescope Array site," in *Proceedings, 33rd International Cosmic Ray Conference (ICRC2013): Rio de Janeiro, Brazil, July 2-9, 2013*, p. 0504. http://www.cbpf.br/%7Eicrc2013/papers/icrc2013-0504.pdf.

[161] S. Thomas. Private communication, 2013.

[162] Ocean Optics Inc. http://oceanoptics.com. Retrieved on 09 Jan, 2016.

[163] "Wavelength calibration data sheet," tech. rep., Ocean Optics Inc., 2000.

[164] A. Bucholtz, "Rayleigh-scattering calculations for the terrestrial atmosphere," *Applied Optics* 34 (1995) 2765–2773.

[165] B. Dawson, "New Rayleigh scattering implementation in the $\overline{\text{Off}}\underline{\text{line}}$." Pierre Auger Note: GAP 2006-007.

[166] F. Werner, *Detection of microwave emission of extensive air showers with the CROME experiment*. PhD thesis, Karlsruhe Institute of Technology, 2013.

[167] "National Oceanic and Atmospheric Administration." https://www.ncdc.noaa.gov/data-access/model-data/model-datasets/global-data-assimilation-system-gdas. Retrieved on 19 Jan, 2016.

[168] B. Keilhauer and M. Will, "Data from the Global Data Assimilation System (GDAS) for the Pierre Auger Observatory." Pierre Auger Note: GAP 2011-015.

[169] A. Criss. Private communication, 2015.

[170] MSR. http://www.msr.ch/en/. Retrieved on 29 Jan, 2016.

[171] Pierre Auger Collab., "Conventions of the Pierre Auger Observatory, version 2 draft." https://edms.cern.ch/ui/file/317390/1/ConventionsRevisedMay2005Draft.pdf, 2005.

[172] I. C. Mariş, S. Müller, F. Schüssler, R. Ulrich, and M. Unger, "ADST-analysis manual: Utilities for ADST-analysis." Pierre Auger Note: GAP 2009-012.

[173] I. C. Mariş, F. Schüssler, R. Ulrich, and M. Unger, "ADST and EventBrowser reference manual: Data summary trees and shower visualization for reconstructed Auger events." Pierre Auger Note: GAP 2006-081.

[174] S. Falk, R. Engel, R. Ulrich, and M. Unger, "Telescope alignment studies." Pierre Auger Note: GAP 2011-123.

[175] A. Porcelli, *Measurement of the depth of shower maximum in the transition region between galactic and extragalactic cosmic rays with the Pierre Auger Observatory*. PhD thesis, Karlsruhe Institute of Technology, 2014.

[176] T. Mukai, M. Yamada, and S. Nakamura, "Characteristics of InGaN-based UV/blue/green/amber/red light-emitting diodes," *Japanese Journal of Applied Physics* 38 no. 7A, (Jul, 1999) 3976. http://stacks.iop.org/1347-4065/38/i=7R/a=3976.

[177] G. Weling, J. Xuejiao, Y. Fei, C. Bifeng, G. Wei, L. Ying, and Y. Weiwei, "Characteristics of high power LEDs at high and low temperature," *Journal of Semiconductors* 32 no. 4, (Apr, 2011) 044007–1–3. http://www.jos.ac.cn/bdtxben/ch/reader/create_pdf.aspx?file_no=10092702.

[178] Trimble, "GNSS Planning Online." http://www.trimble.com/gnssplanningonline. Retrieved on 11 Jan, 2016.